Synthesis, characterization and electrochemistry of phthalocyanine derivatives with biomedical applications

A dissertation submitted in accordance with the requirements for the degree

Magister Scientiae

in the

Department of Chemistry

Faculty of Natural and Agricultural Sciences

at the

University of the Free State

by

Dina Naudé Oosthuizen

Supervisor

Dr. E. Fourie

Co-supervisors

Prof J.C. Swarts and Prof. J. Conradie

Table of Contents

Acknowledgements i

List of compounds ii

List of Abbreviations vi

Chapter 1: Introduction and Aims

1.1 Introduction 1

1.2 Aims of this study 2

Chapter 2: Literature Survey

2.1 Introduction 4

2.2 History and structural determination of phthalocyanines 4

2.3 General Applications of phthalocyanines 5

2.4 The synthesis of unsubstituted phthalocyanines 6

2.4.1 Metal-free phthalocyanine (H_2Pc) 6

2.4.2 Metallated phthalocyanine (MPc) 7

2.5 The synthesis of substituted phthalocyanines 8

2.5.1 The synthesis of monosubstituted phthalonitriles 10

2.5.2 The synthesis of 3,6-disubstituted phthalonitriles 12

2.5.3 Axially Substituted Phthalocyanines 13

2.6 Electrochemical studies 14

2.6.1 Cyclic Voltammetry 14

2.7 UV-Visible spectroscopy of phthalocyanines 20

2.8 Computational Chemistry 22
2.8.1 Introduction 22
2.8.2 Quantum Mechanics 22
2.8.3 Density Functional Theory (DFT) 23
2.8.4 Exchange correlation functionals 24
2.8.5 Amsterdam density functional (ADF) 24
2.8.6 Basis Sets 25
2.8.7 Molecular Orbitals (MO) 25
2.8.8 Symmetry operations and point groups, 26
2.8.9 Phthalocyanine 28
2.9 Reaction calorimetry (RC1 reactor) 29
2.9.1 Heat and Mass transfer in the RC1 reactor 32
2.9.2 Kinetics and Thermodynamics 33

Chapter 3: Results and Discussion

3.1 Introduction 43
3.2 Synthesis and characterization of phthalocyanine derivatives 43
3.2.1 Synthesis of substituted phthalonitriles 43
3.2.2 Synthesis of substituted metal-free phthalocyanine 48
3.3 RC1 synthesis 55
3.3.1 General 55
3.3.2 Determination of Mass Transfer coefficient, k_La 56
3.3.3 Synthesis performed on the RC1 reactor 60
3.3.4 Calorimetric and kinetic investigations on the RC1 62

3.4 Computational Chemistry 77

3.4.1 Oxidation of thiophene derivatives 77

3.4.2 Reduction of nitrobenzene and 4-nitrophthalonitrile 79

3.4.3 Comparison of Computational and RC1 study 80

3.5 Electrochemistry 82

3.5.1 General 82

3.5.2 Metal-free phthalocyanines with various ethylene glycol and alkyl substituents, **9, 11-12** 84

3.5.3 Various ruthenium phthalocyanines with carbonyl axial ligand, **23-29** 91

3.6 Computational study of the ruthenium phthalocyanines, **23-29** 106

3.6.1 Simplified phthalocyanines, **23a-29a** 108

3.6.2 Full experimental phthalocyanines, **23-29** 110

3.6.3 Frontier Orbital Energies 113

3.6.4 Molecular Orbital view of phthalocyanines, **23a-29a** 116

3.7 Comparison of the ruthenium phthalocyanine derivatives 118

3.7.1 Oxidation potential relationships 118

3.8 Conclusion 119

Chapter 4: Experimental

4.1 Introduction 121

4.2 Materials 121

4.3 Spectroscopic measurements 121

4.4 Synthesis 121

4.4.1 Phthalonitrile derivatives 122

4.4.2 Synthesis of Metal-free substituted phthalocyanines 125

4.5 RC1 Reactor synthesis 127

4.5.1 General 127

4.5.2 Experimental determination of Mass Transfer coefficient, k_La 128

4.5.3 Oxidation of thiophene derivatives 129

4.5.4 Reduction of 4-nitrophthalonitrile, **16** 129

4.6 Thermal analysis with the RC1 calorimeter 129

4.7 Computational Chemistry 130

4.7.1 Method 130

4.8 Electrochemistry 130

4.7.1 Synthesis of Tetrabutylammonium tetrakis(pentafluorophenyl)borate, $[^nBu_4N][B(C_6F_5)_4]$, **22** 131

Chapter 5: Summary, Conclusions and Future Perspectives

5.1 Summary and Concluding remarks 132

5.2 Future perspectives 133

Appendix

A. ^{1}H NMR Spectra 135

B. FT-IR Spectra 143

C. Cyclic Voltammetry Data 146

D. Molecular Orbital Views 149

Abstract 150

Opsomming 151

Acknowledgements

I would like to thank all my friends, family and colleagues for their support, friendship and guidance throughout the period of my studies. Special appreciation must be made to the following people:

To my promotor and co-promotors (Dr. Eleanor Fourie, Prof. Jannie Swarts and Prof. Jeanet Conradie), thank you for all your guidance, support and leadership throughout the course of this study.

To my parents (Thinus Oosthuizen and Tokkie Oosthuizen) and three sisters (Angenita, Elana and Hettie), thank you for all the love, support and understanding during these few years.

To my Polish colleague and friend (Jasiu Lewtak), thank you for all the motivation and encouragement in and out of the lab, it will always be a fond memory.

To my friend (Maretha Scheepers), thank you for all the support and encouragement throughout this study.

To my Daniel Freiner, from Switzerland thank you for your guidance and support on the RC1 reactor.

To the Physical Chemistry group, thank you all for support and quick laughs when it all felt a bit too much.

To the Chemistry department and the University of the Free State, thank you for available facilities.

To the National Research Foundation and the University of the Free State, thank you for the financial support.

List of Compounds

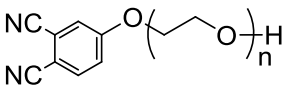

1: n =2,
2: n = 3

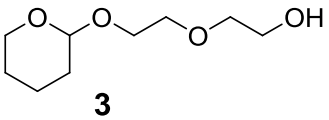

3

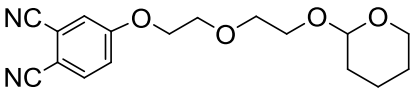

4

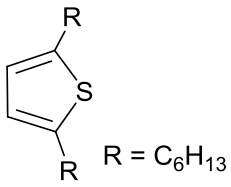

5

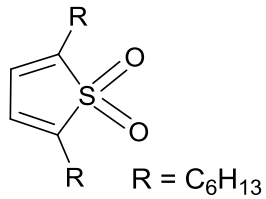

6

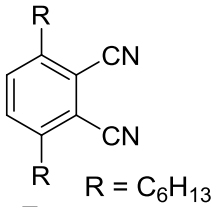

7

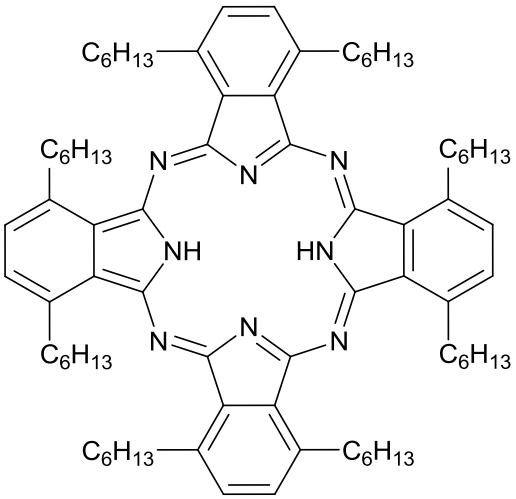

8

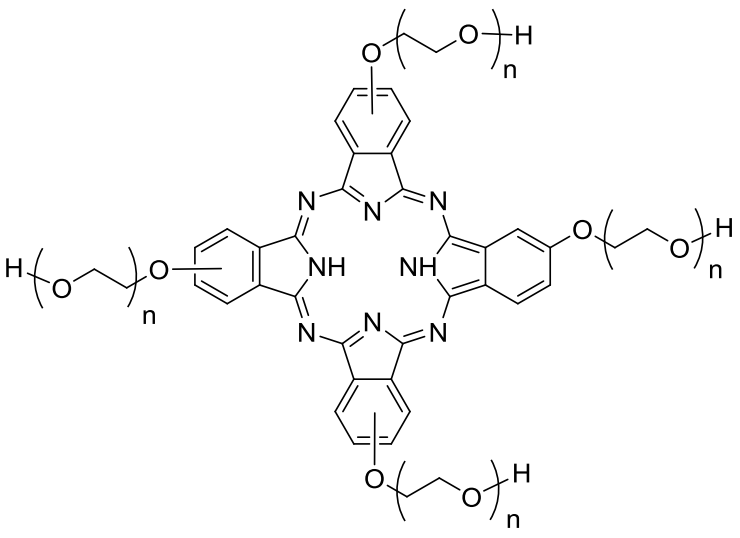

9: n = 2,
10: n =3

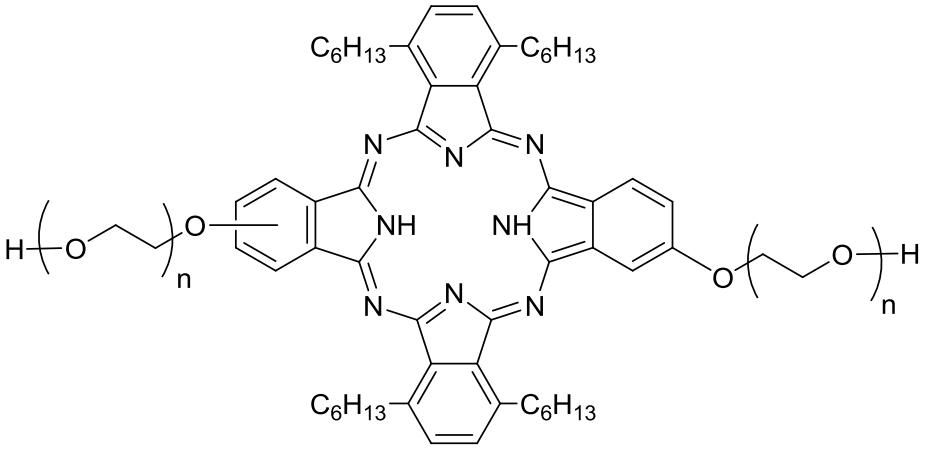

11: n = 2,
12: n =3

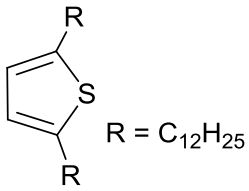

R = $C_{12}H_{25}$

13

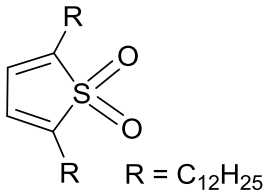

R = $C_{12}H_{25}$

14

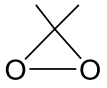

15

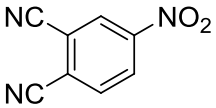

16

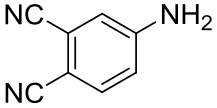

17

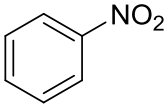

18

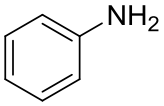

19

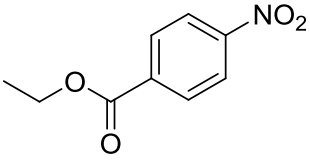

20

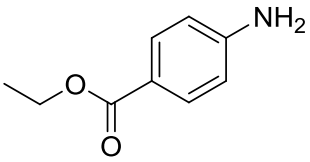

21

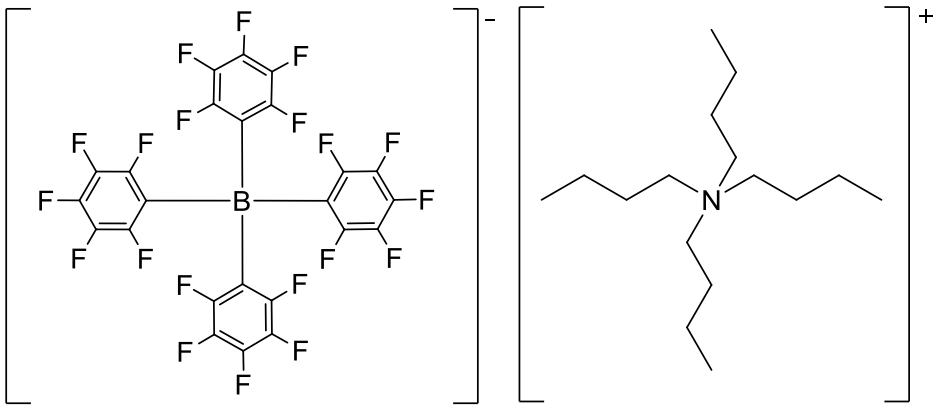

22

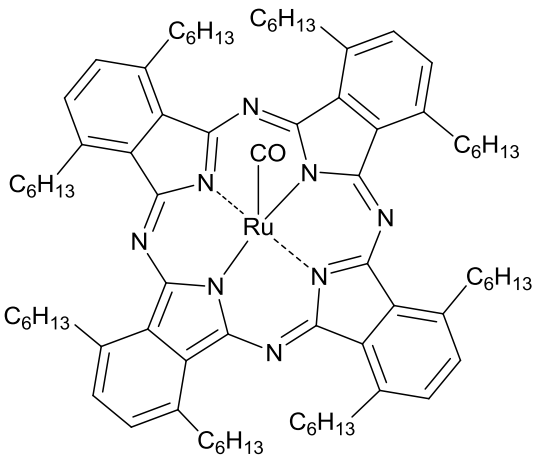

23

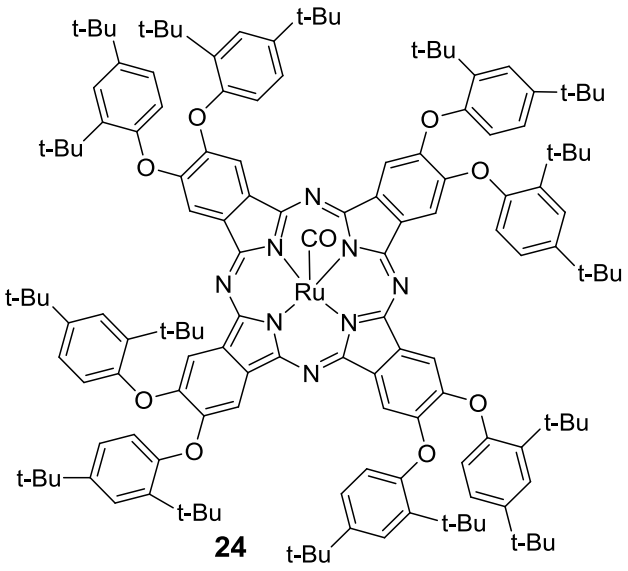

24

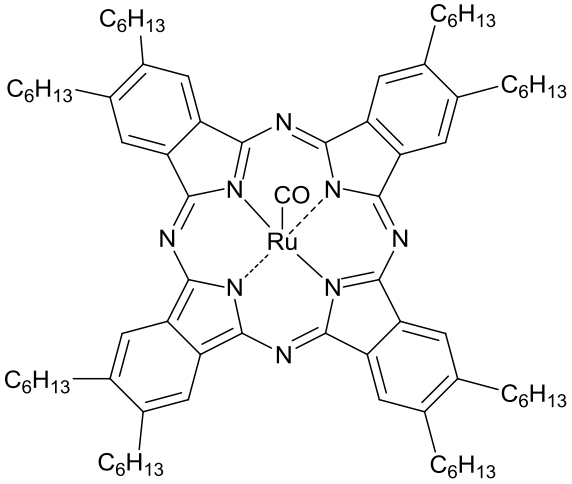

25

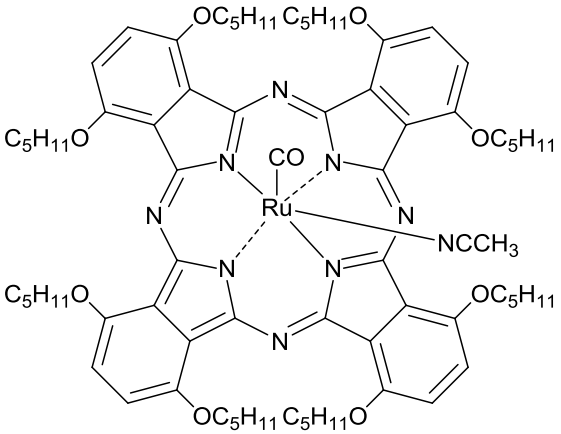

26

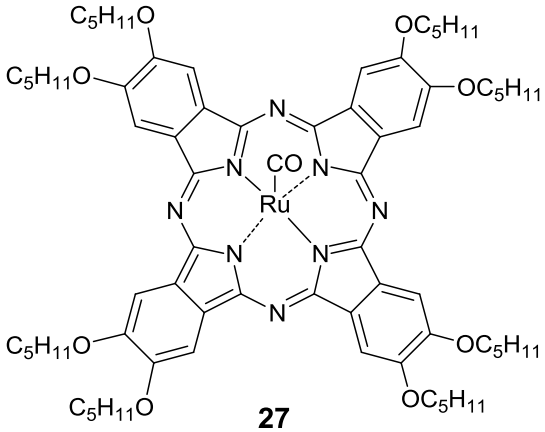

27

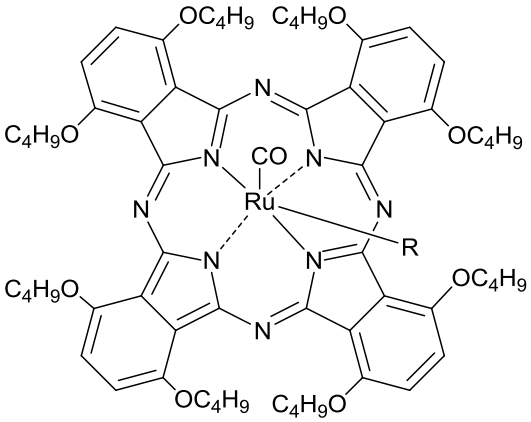

28: R = *py* (pyridine)

29: R = $NH(CH(CH_3)_2)_2$

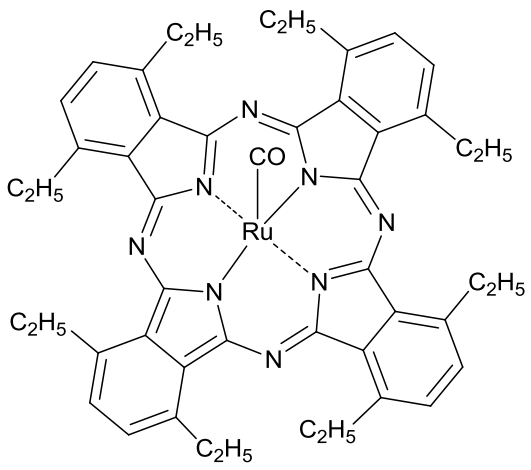

23a

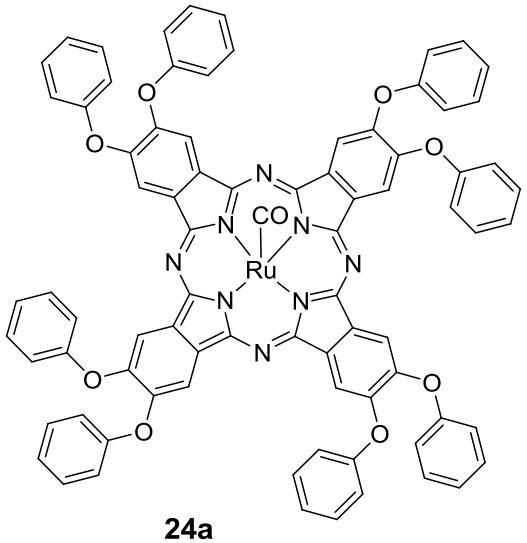

24a

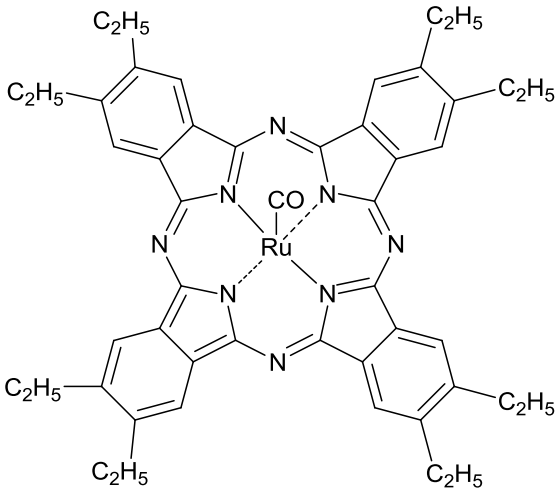

25a

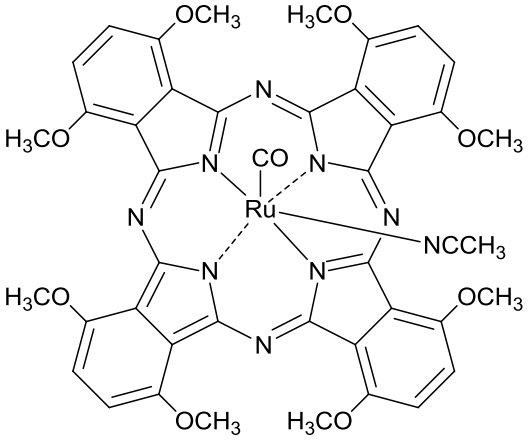

26a

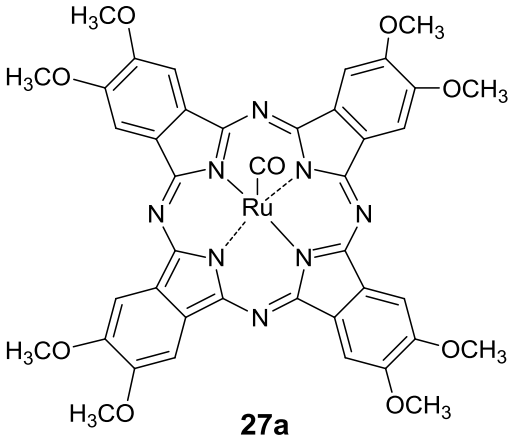

27a

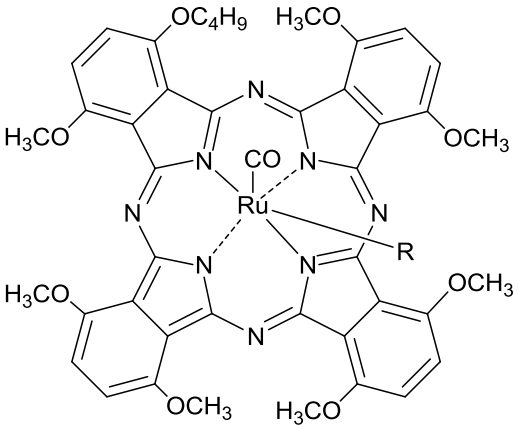

28a: R = *py* (pyridine)

29a: R = $NH(CH(CH_3)_2)_2$

List of Abbreviations

k_La	Mass transfer coefficient

Chemicals

m-CPBA	*m*-chloroperoxybenzoic acid
PPTS	pyridinium p-toluenesulfonate
NEt_3	Triethylamine

Cyclic Voltammetry

CV	cyclic voltammetry
$E^{0'}$	formal reduction potential
E_{pa}	anodic peak potential
E_{pc}	cathodic peak potential
ΔE_p	separation of anodic and cathodic peak potentials
i_{pa}	anodic peak current
i_{pc}	cathodic peak current
SCE	saturated calomel electrode
$[^nBu_4N][B(C_6F_5)_4]$	Tetrabutylammonium tetrakis(pentafluorophenyl)borate,

CHAPTER 1

INTRODUCTION AND AIMS

1.1 Introduction

Phthalocyanines (Pc's), **1**, are macrocycles which are structurally related to the naturally occurring porphyrins, **2**, Figure 1.1. Phthalocyanines, however, do not occur in nature. The synthetically available phthalocyanines are more stable and robust than most porphyrins and thus have a wider application range.

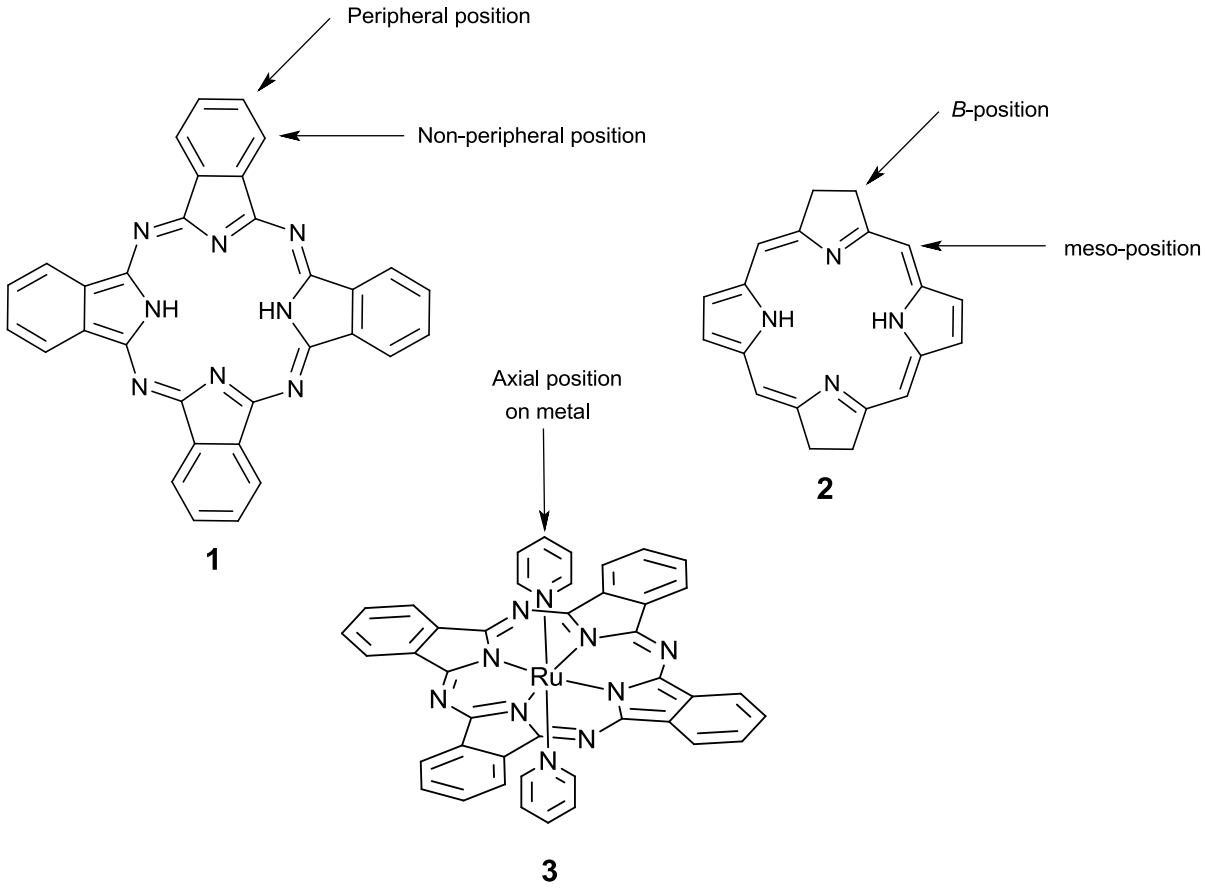

Figure 1.1: Structures of phthalocyanine, **1**, and porphyrin, **2**, showing the possible ring-substitution sites, and an axially substituted ruthenium (II) phthalocyanine complex, **3**.[1]

Metallophthalocyanines (MPc) complexes in particular have attracted much attention due to their potential applications. They are very versatile compounds due to their 18-π electronic structure, which makes them chemically and thermally stable. Phthalocyanine compounds have been studied due to their diverse range of applications such as photodynamic therapy,[2] semiconductors,[3] photovoltaic devices[4] and catalysts.[5] Unsubstituted metallophthalocyanines aggregate in solutions even in low concentrations ($< 10^{-5}$ M) due to strong π-stacking. This lowers the solubility of these compounds, which in turn hampers their effectiveness in applications. Many studies are focused on improving the solubility for these compounds. The

solubility of these compounds can be increased by derivitising the peripheral or non-peripheral positions of the phthalocyanine macrocycle. Non-ionic functional groups, like polyethylene glycol,[6,7] carbohydrate[8] and other polyhydroxylated[9] substituents may be able to confer water-solubility to phthalocyanines. For instance, oligomeric ethylene glycol–quinoline substituted zinc(II) phthalocyanine derivatives are promising aqueous compatible antitumor agents for photodynamic therapy.[10] The addition of axial ligands on the central metal also helps to disrupt the π-stacking and increase solubility.

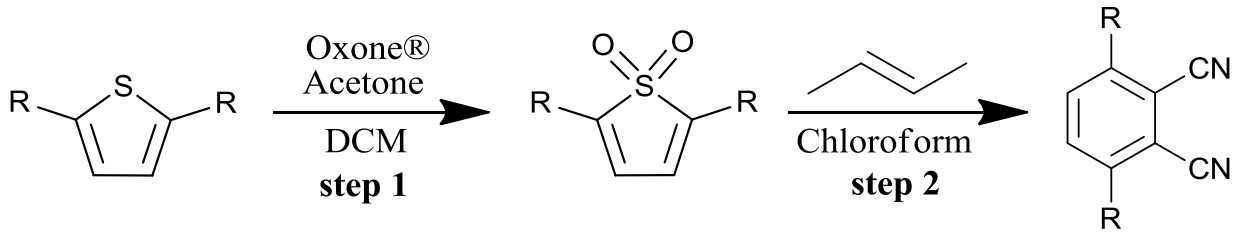

Figure 1.2: Conversion of a substituted thiophene to a substituted phthalonitrile.

Phthalocyanines are produced from phthalonitrile precursors. The steps to obtain suitable phthalonitrile precursors are tedious due to various multiple reaction steps and reaction times. For instances, to obtain 3,6-dihexylphthalonitrile, thiophene needs to undergo an alkylation step, an oxidation step, was well as a Diels-Alder reaction. A RC1-reactor is capable of measuring thermal event in batch reactor mode for reactions. It can be utilized to optimize reaction conditions, including stirring speed and reaction temperature, for example for the oxidation step the alkylated thiophenes (Figure 1.2, step 1). Thermodynamic and kinetic insights into this oxidation reaction may be obtained as well as information of intermediates during the course of the reaction.

1.2 Aims of this study

With this background, the following aims were set for this study:

1. The synthesis of non-peripherally substituted alkyl- and ethylene glycol-containing phthalocyanines.
2. The characterization of the synthesized non-peripherally substituted alkyl and ethylene glycol-containing phthalocyanines with a variety of methods, including ^{1}H and ^{13}C NMR, FT-IR and UV/vis spectroscopy.

3. Thermodynamic and kinetic studies utilizing an RC1 reaction calorimeter, for the oxidation reaction of alkylated thiophenes suitable for conversion to alkylated thiophene-1,1-dioxides. Alkylated thiophene-1,1-dioxides can then be converted to phthalonitriles that can be used to cyclize to phthalocyanines, as well as in a reduction reaction of 4-nitrophthalonitriles.
4. Calculation of the reaction enthalpy (ΔH) and Gibbs Free energies (ΔG), for the oxidation of alkylated thiophene by means of DFT computational methods.
5. Determination of relationships between the experimental and calculated thermodynamic results of thiophene oxidation and phthalonitrile substituent reductions.
6. An investigation of the electrochemical behaviour of PcRu(CO)(L) complexes, with various axial ligands, by utilizing cyclic voltammetry, square wave voltammetry and linear sweep voltammetry.
7. Determination of the three dimensional geometry and relative energies of the PcRu(CO)(L) complexes by means of DFT computational methods.
8. Determination of relationships between the electrochemical and computational results for experimental results for PcRu(CO)(L) complexes.

---

[1] Dolphin, D., James, B., Murray, A., & Thornback, J., *Can J. Chem.,* 1980, 58, 1125-1132

[2] Miller, J.D., Elma D. Baron, E.D., Heather Scull, H., Hsia, A., Jeffrey C. Berlin, J.C, McCormick, T., Colussi, V., Kenney, M.E., Cooper, K.D, and Oleinick, N.L., *Toxicol. Appl. Pharmacol*., 2007, 224, 290–299

[3] Murtaza, I., Qazi, I., Karimov, K.S., Sayyad M.H., *Physica B*., 2011, 406, 1238–1241

[4] Senthilarasu, S., Velumani, S., Sathyamoorthy, R., Subbarayan, A., Ascencio, J., Canizal, G., et al. *Appl. Phys. A*., 2003, 383-389

[5] Kluson, P., Drobek, M., Zsigmond, A., Bata, P., Kalaji, A., Baranji, J., et al., *Appl. Catal. B,*. 2009, 605–609

[6] Karabork, M., & Serin, S., *Synth. React. Inorg., Met.-Org., Nano-Met. Chem.*, 2002, 32, 1635-1647

[7] Tuncel, S., Dumoulin, F., Gailer, J., Sooriyaarachchi, M., Atilla, D., Durmus, M., et al.. *J. Chem. Soc., Dalton Trans*., 2011, 40, 4067–4079

[8] Berthold, H. J., Franke, S., Thiem, J., & Schotten, T., *J. Org. Chem.*, 2010, 75, 3859-3862

[9] Dumoulina, F., Durmus, M., Ahsena, V., Nyokong, T., *Coord. Chem. Rev*., 2010, 254, 2792–2847

[10] Jia, X., Yang, F., Li, J., Liu, J.Y., & Xue, J.P., *J. Med. Chem.*, 2013, 56, 5797-5805

CHAPTER 2

LITERATURE SURVEY

2.1 Introduction

This chapter provides a literature survey of topics pertinent to this study. It is arranged to firstly give a background of the synthetic reactions relevant to the study of phthalocyanines, followed by a discussion of the physical techniques applied to characterize and fully describe the compounds related to this study.

2.2 History and structural determination of phthalocyanines

In 1907, the first phthalocyanine (Pc) was isolated as an accidental by-product during a preparation of *o*-cyanobenzamide from phthalimide and acetic anhydride.[1, 2] The students, Tscherniak and Braun observed a highly coloured, insoluble by-product forming. Comprehensive studies were performed by Linstead and co-workers[3] that led to the determination of the phthalocyanine structure in the early 1930's. Robertson later confirmed the structure *via* X-ray diffraction techniques.[4]

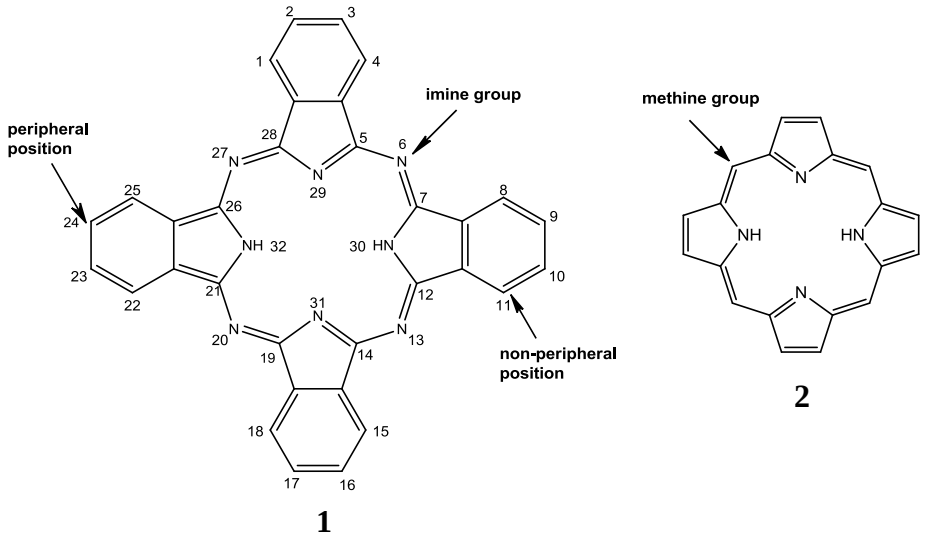

1 **2**

Figure 2.1: Comparison of the phthalocyanine, **1** and porphyrin, **2**, structures. The numbering system and substitution positions on phthalocyanines are also shown.[1, 2]

The similarity between phthalocyanine, **1**, and porphyrin, **2**, which form the basic structure of many natural occurring compounds such as haemoglobin, is evident in Figure 2.1. The systems differ in that the four pyrrole units of the phthalocyanine are linked by aza (imine)

groups, instead of the methine groups as in a porphyrin. Therefore, phthalocyanines can also be referred to as tetrabenzotetraazaporphyrins. Phthalocyanines are 18 π-electron planar aromatic macrocycles consisting of four isoindole units that link together their 1,3-positions by aza bridges, an arrangement of alternated carbon and nitrogen atoms. There are sixteen possible sites for macrocycle substitution associated with the four benzo rings shown in Figure 2.1. These substitutions are divided into two categories, the 2,3,9,10,16,17,23,24 carbon atoms are referred to as the peripheral sites due to the position on the outer edge of phthalocyanine and the 1,4,8,11,15,18,22,25 carbon atoms are denoted as the non-peripheral sites.[1, 2] The phthalocyanine contains a central cavity of sufficient size to accommodate various metal ions.

The phthalocyanine macrocycle ligand (formally a Pc^{2-} anion) can coordinate over 70 different elements in its central cavity and some transition metal ions (e.g. Cu^{2+}, Ni^{2+} and Zn^{2+}).[5] The choice of central metal cation can strongly influence its physical properties.[6] Most metal containing phthalocyanine complexes possess a remarkably planar structure. However, the presence of a large central metal cation, such as lead and tin, is known to distort the geometry, forming a domed conformation.[7] The essentially planar conformation of phthalocyanines can also be significantly distorted by axial substituents on a metal through conformational stress.[8] Phthalocyanines with a metal or a semi-metal centre are referred to as metallophthalocyanines (MPc's). Both free base and metal containing phthalocyanines are known for their intense blue/green colours and their stability towards heat, acids and bases.

2.3 General Applications of phthalocyanines

Phthalocyanines (Pcs) possess remarkable properties (e.g. thermal and chemical stability) which render them important commercial commodities. Their unique properties stem mostly from their planar structure and aromaticity.[2] Phthalocyanines possess a dark green-blue colour and strongly absorb light in the visible range, between 620-750 nm.[9] For this reason they have been employed for many years as dyestuffs for textiles and as inks.[2]

The optical, electronic and photo-electronic[10, 11, 12] properties of phthalocyanines are also extensively investigated. Metal phthalocyanines (MPc, M = Zn, Ni, Co, Cu and H_2) as sensors[13] show promise as robust, inexpensive chemiresistors for incorporation into electronic-noise type applications. It contains properties that make it viable for use as liquid

crystal displays[14] and laser printers,[10, 14] transistors,[15, 16] detection of sulphur in cosmetic products,[17] and as heterogeneous and homogeneous catalysts for a number of industrial processes.[18, 19]

Phthalocyanines are well-known organic semiconductors[20] and are suitable for use in photovoltaic devices[21] because of its very high physical and chemical durability. Zinc phthalocyanine (ZnPc) is a promising candidate for solar-cell applications,[22] because it is easily synthesized and is non-toxic to the environment. Phthalocyanines are also recognized as having excellent potential in photodynamic therapy for certain types of cancer.[23, 24, 25] Biological and medical applications of phthalocyanines, however, is enhanced by water-solubility in various concentration and pH ranges.[26, 27] Aqueous solubility is thus an important goal nowadays in Pc synthesis.

2.4 The synthesis of unsubstituted phthalocyanines

Unsubstituted metal-free phthalocyanine and metal containing phthalocyanines (MPcs) can be prepared from ortho-disubstituted benzene derivatives, like 1,2-dicyanobenzene or isoidoline-1,3-diimine, which acts as phthalocyanine precursors. One of the aims for this study is the synthesis of phthalocyanine derivatives.

2.4.1 Metal-free phthalocyanine (H_2Pc)

Metal-free phthalocyanines are prepared by the removal of labile metal ions such as Li^+ or Mg^{2+} after cyclotetramerization.[1, 2] There are several methods of cyclotetramerization (Scheme 2.1) of ortho-disubstituted benzene derivatives to form 2H-phthalocyanine (H_2Pc):

i) 2H-phthalocaynine is conveniently prepared from phthalonitrile using a refluxing solution of lithium metal dissolved in pentanol (forming lithium pentyloxide) to yield 2Li-phthalocyanine, which can be demetallated using dilute aqueous acid.[28]

ii) The metal-free preparation of 2H-phthalocyanine can be accomplished by cyclotetramerization of phthalonitrile with hydroquinone as the necessary reducing agent.[29] Cyclotetramerization of phthalonitrile can also be achieved in a pentanol solution with a non-nucleophilic hindered base such as with 1,8-diazabicyclo[4.3.0]non-5-ene.[30]

iii) It can also be achieved by the reaction of phthalonitrile with ammonia forming isoidoline-1,3-diimine. Isoindoline-1,3-diimine condenses under relatively mild conditions to form 2H-phthalocyanine.[31] The use of dimethylaminoethanol (DMAE) during the condensation of a substituted isoidoline-1,3-diimine can produce a metal-free phthalocyanine.[32]

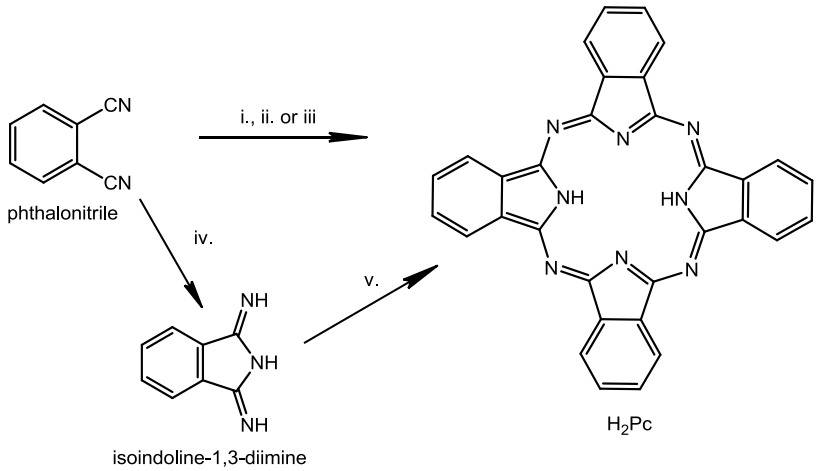

Scheme 2.1: Synthetic routes to H_2Pc. Reagents and conditions: (i) Lithium, refluxing pentanol, followed by aqueous hydrolysis. (ii) Fuse with hydroquinone. (iii) Heat with 1,8-diazabicyclo[4.3.0]non-5-ene (DBN) in a melt or in pentanol solution. (iv) Ammonia (NH_3), refluxing methanol, sodium methoxide. (v) Reflux in a high-boiling-point alcohol.[2]

2.4.2 Metallated phthalocyanine (MPc)

The most common synthetic routes towards metal containing phthalocyanines (MPcs) are shown in Scheme 2.2. MPcs are often prepared directly from phthalonitrile or isoidoline-1,3-diimine using the metal ion as a template for the cyclotetramerization. Phthalic anhydride or phthalimide can also be used as a precursor in the presence of a source of nitrogen (urea) and a metal salt. Alternatively, the reaction between 2H-phthalocyanine or 2Li-phthalocyanine and the appropriate metal salt can produce most metallated phthalocyanines.[1, 2]

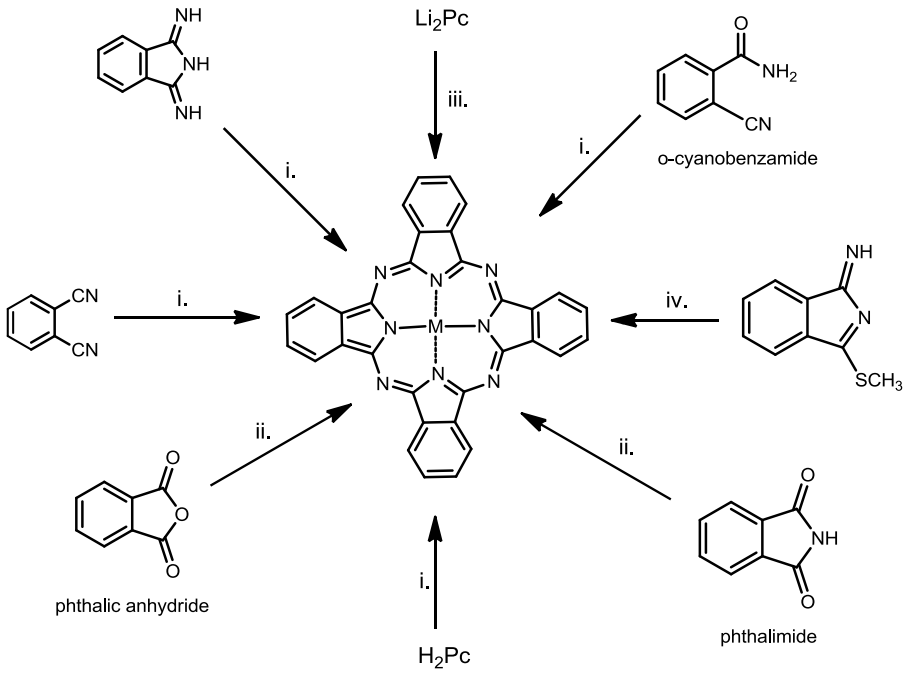

Scheme 2.2: Synthetic routes to MPc. Reagents and conditions: (i) Heat in a high-boiling-point solvent (quinolone) with metal salt. (ii) Heat in a high-boiling-point solvent with urea and metal salt. (iii) Heat in ethanol with metal salt. (iv) -15 to -20 °C in DMF with metal salt.[2]

2.5 The synthesis of substituted phthalocyanines

The preparation of phthalonitrile precursors with the desired substituents is a critical step in phthalocyanine synthesis. A challenge is the introduction of a large variety of substituents in peripheral and non-peripheral positions of the benzene rings which directs phthalocyanine properties in the direction of tailor-made phthalocyanines.[10] The solubility of neutral phthalocyanines can be improved by synthesizing phthalocyanines with substituents on the peripheral and non-peripheral positions or in the axial directions. It is a continuous effort to circumvent the problem of poor solubility, due to strong intermolecular π–π stacking in planar phthalocyanines, and tune the steric effects and electronic features of phthalocyanines.[8]

There are three major routes to obtain asymmetrical substituted phthalocyanines namely:

i) The statistical condensation of two different phthalonitriles, **A** and **B** (as seen in Scheme 2.3);
ii) Ring expansion of subphthalocyanines;
iii) The use of a polymer in a template-assisted synthesis.

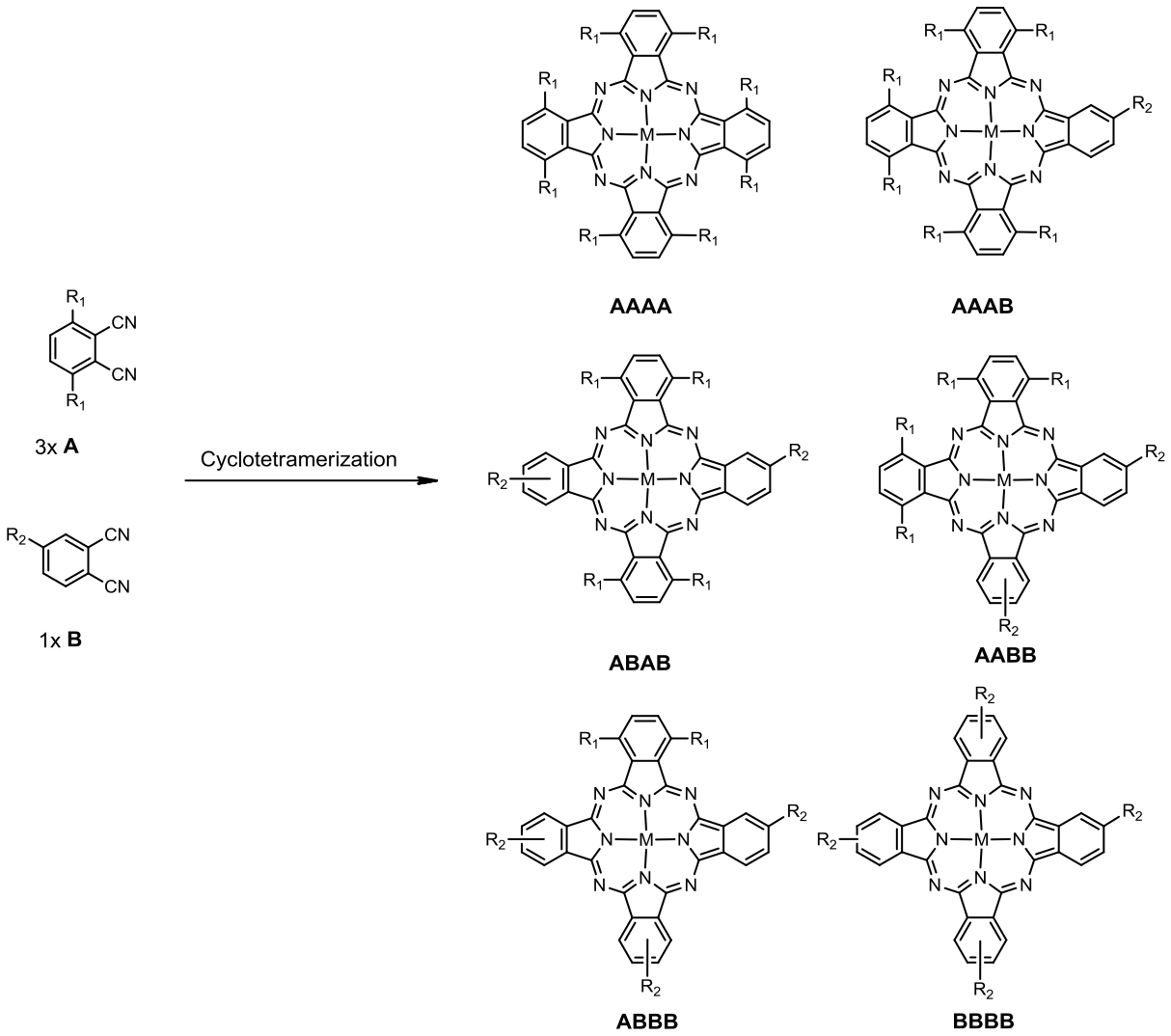

Scheme 2.3: The statistical condensation reaction of 2 different phthalonitrile with the resulting products. Reagents and conditions: Lithium, refluxing pentanol, followed by aqueous hydrolysis. ‘‘Reproduced from [McKeown, N. B., Chambrier, I., & Cook, M. J.; *J. Chem. Soc., Perkin Trans*. 1,. 1990, 1169] with permission of The Royal Society of Chemistry’’

Statistical condensation is the most common route to asymmetrical phthalocyanines. It involves the cyclotetramerization of two differently functionalized phthalonitrile. This study is only concerned with the synthesis of asymmetrical phthalocyanines containing two differently functionalized phthalonitrile: A – a unit possessing two similar substituents (R_1) and B – a unit with one substituent (R_2). In Scheme 2.3 the six different substituent patterns are shown, whereas Table 2.1 shows the expected mixture of products.

Table 2.1: Expected relative portions from the statistical condensation of two different phthalonitriles **A** and **B** to form a mixture of products (%). "Reproduced from [McKeown, N. B., Chambrier, I., & Cook, M.; J., *J. Chem. Soc., Perkin Trans*. 1,. 1990, 1169] with permission of The Royal Society of Chemistry"

A:B	Pcs (Type AAAA)	Pcs (Type AAAB)	Other Pcs (Types ABAB, AABB, ABBB, BBBB)
1:1	6	25	69
3:1	33	44	23
9:1	66	29	5

2.5.1 The synthesis of monosubstituted phthalonitriles

The improvement of phthalocyanine aqueous compatibility is an important goal of this study. As stated in section 2.5, phthalocyanine solubility can be improved through substituents on the peripheral and non-peripheral positions and/or in the axial directions.[2, 10] There are several types of non-ionic functional groups that are able to confer water-solubility or at least impart compatibility to phthalocyanines, namely polyethylene glycol, carbohydrate[33] and other polyhydroxylated[34] substituted derivatives. These phthalocyanines are known as non-ionic water soluble phthalocyanines and are rather rare.[35] Polyethylene glycol substituents are a classical means to confer water-solubility to many molecular materials. The attachment of polyethylene glycol moieties[26, 36] to the macrocycle greatly increased the solubility of the phthalocyanines in highly polar solvents (*e.g.* DMSO), but was insufficient to increase their water-solubility except in one previously reported instance.[37] Ng *et al.* prepared a series of asymmetric methylated polyethylene glycol zinc phthalocyanines, which proved to have high cytotoxic properties despite their water-insolubility.[38] Free hydroxyl groups at the end of the polyoxo chain were reported to considerably increase the water-solubility of the phthalocyanine[27, 39] and phthalocyanine-related compounds such as porphyrazine.[40, 41]

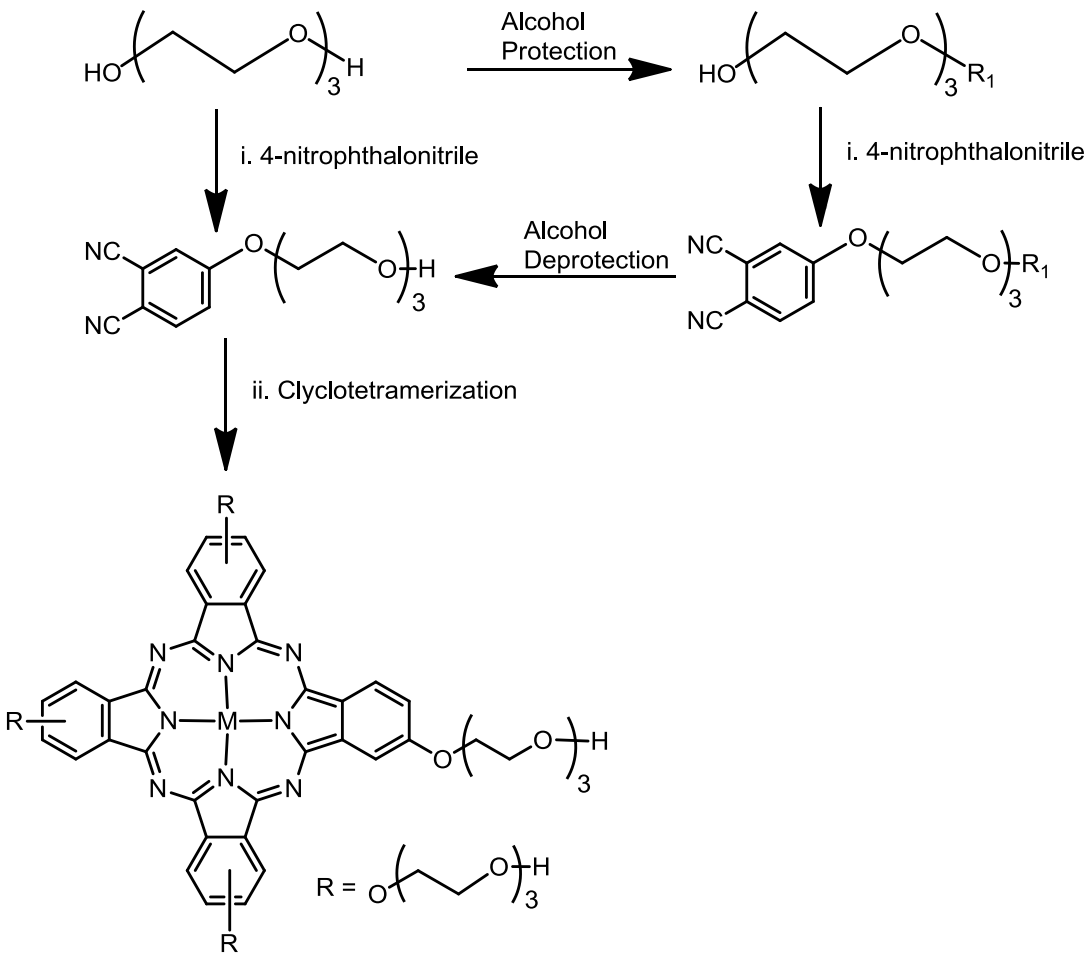

Scheme 2.4: Synthetic routes to phthalonitrile, Reagents and Conditions: (i) Base-catalysed (K_2CO_3) reaction in DMF at various temperatures (ii) Cyclotetramerization with reagents, $Zn(OAc)_2.H_2O$, DBU and n-pentanol at 150 °C for 12 hours. "Adapted from [Tuncel, S., Dumoulin, F., Gailer, J., Sooriyaarachchi, M., Atilla, D., Durmus, M., *J. Chem. Soc., Dalton Trans*., 2011, 40, 4067] with permission from The Royal Society of Chemistry.

There are two different ways to obtain these precursory phthalonitriles as seen in Scheme 2.4. Firstly, and the more common method is by the direct condensation of the suitable dialcohol on 4-nitrophthalonitrile.[26, 27, 39] Secondly, the monosubstituted phthalonitrile can be obtained by prior selective protection or selective substitution of the diol after which the remaining hydroxyl is reacted with the 4-nitrophthalonitrile by nucleophilic condensation.[26] These reactions mentioned occur in polar solvents (e.g. DMSO and DMF) in the presence of a base catalyst namely potassium carbonate at various reaction conditions (temperature and reaction time) depending on the nucleophile.[26, 27, 39]

2.5.2 The synthesis of 3,6-disubstituted phthalonitriles

The incorporation of long aliphatic chains as substituents for octa-substituted phthalocyanines have received considerable attention and dates back to the 1980's. These long chains enhance solubility in organic solvents and also promote discotic columnar liquid crystal behaviour.[28, 42] Scheme 2.5 shows the synthetic route to dialkylated phthalonitrile, which is thoroughly discussed in sections (i)- (iii) below.

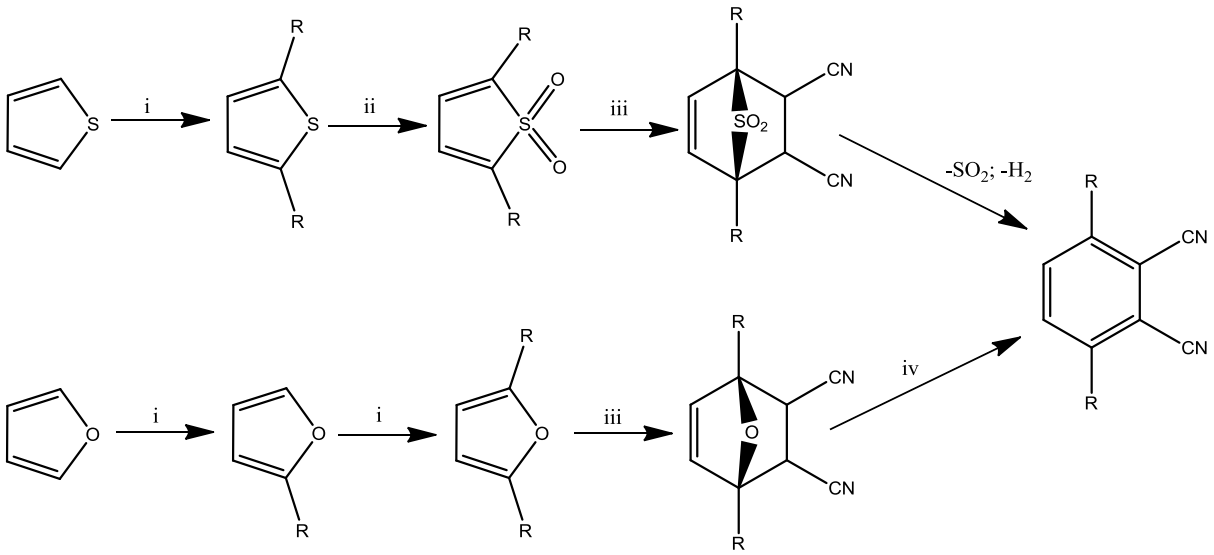

Scheme 2.5: Synthetic routes to dialkylated phthalonitrile, Reagents: (i) Reaction with BuLi and RBr, where R is the appropriate alkyl chain desired. (ii) Oxidation of dialkylated thiophene with $NaBO_3$, *m*-chloroperoxybenzoic acid (m-CPBA) or dimethyldioxirane. (iii) Diels-Alder reaction with fumaronitrile and chloroform at 160 °C. (iv) React with $LiN(SiMe_3)_2$ in THF at -78 °C. "Reproduced from [McKeown, N. B., Chambrier, I., & Cook, M. J.; *J. Chem. Soc., Perkin Trans. 1*, 1990, 1169] with permission of The Royal Society of Chemistry"

(i) *Alkylation of furan and thiophenes*

The potential ease of preparing 2,5-dialkylfurans and 2,5-dialkylthiophene via lithiation of the aromatic ring led to the investigation of the chemistry depicted in Scheme 2.5. The alkylation of furan was achieved using butyl-lithium in hexane-THF initially to deprotonate the furan ring. The two-step procedure gave first the monoalkyl and then the dialkyl furan derivatives. The near complete disubstitution of thiophene was achieved in one step using 2.5 equivalents of butyl-lithium in hexane-THF and long reaction times by McKeown and co-workers.[28] Thiophene is firstly dilithiated followed by the immediate dialkylation to produce 2,5-dialkylthiophene as shown in Scheme 2.5 (step i).

(ii) *Oxidation of substituted thiophenes*

Oxidation of the 2,5-dialkylated thiophene (step ii) can be achieved by the use of a peracid as oxidizing agent as reported by Langner and Swarts in 2001 and depicted in Scheme 2.5.[43] 2,5-dialkylated thiophenes can be converted into the corresponding thiophene-1,1-dioxides in moderate yields (41 %) using *m*-chloroperbenzoic acid (*m*-CPBA), yields lower than 20 % using sodium perborate irrespective of alkyl chain length or using dimethyldioxirane that afford superior yields (94 %) compared to other reagents.[43] Dimethyldioxirane is routinely prepared by oxidizing acetone with Oxone® (the Aldrich trade name for $2KHSO_5.KHSO_4.K_2SO_4$) in the presence of a base such as sodium bicarbonate.[43, 44, 45]

(iii) *Diels-Alder conversion of substituted thiophene-1,1-dioxides*

Fumaronitrile has been used as dienophile in reactions with various conjugated dienes, the products being subsequently dehydrogenated over sulphur. Alternatively, dicyanoacetylene has been added across both furans[46] and thiophenes.[47] The Diels-Alder reactions of furans is reversible and the adduct formation is encouraged using high pressure, or under low pressure, low temperature.[48, 49] Fumaronitrile have been given preference over dicyanoacetylene, due to better accessibility. McKeown[28] and co-workers reported a one-pot sealed tube reaction for the conversion of thiophene-1,1-dioxides into phthalonitrile, involving a Diels-Alder condensation reaction with fumaronitrile (step iii), followed by the subsequent *in situ* SO_2 extrusion and dehydrogenation as depicted in Scheme 2.5.

2.5.3 Axially Substituted Phthalocyanines

It is well-known that phthalocyanines tend to aggregate at high concentrations. These aggregates are usually depicted as a coplanar association of rings progressing from monomer to dimer and higher order complexes, and are driven by enhanced Van der Waal's and π-stacking attractive forces between phthalocyanine rings.[50] The tendency to aggregate is lessened in axially-substituted phthalocyanines, since the intermolecular interactions have to work over longer distances and therefore are weaker than in those without axial substituents.[51] Axial substitution in phthalocyanines involves the complexation of additional ligands to the central metal ion in a general direction perpendicular to the macrocyclic plane (Figure 2.2, where L_1 and L_2 may be identical or different).

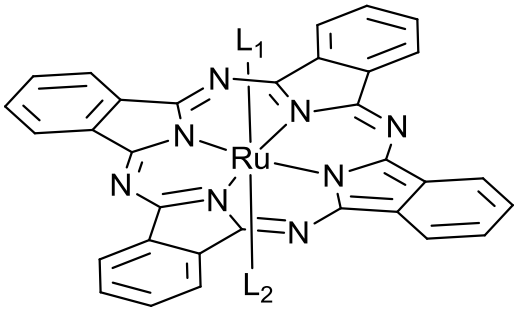

Figure 2.2: The structure of a metallated phthalocyanine with axial ligands, L_1 and L_2.

Depending on the oxidation number of the central metal ion, M, only one, L_1, or two ligands, L_1 and L_2, may be coordinated. The enhanced solubility of the resultant compounds show that the usual tendency of phthalocyanines to aggregate can be effectively suppressed by axial substitution.[52]

2.6 Electrochemical studies

Several reviews are available to give a good background on the theory and techniques relating to electroanalytical chemistry. In this section only some of the most important parameters and definitions utilized in the electrochemical section of Chapter 3 will be highlighted. In addition, some aspects of phthalocyanine electrochemistry will be explored. A considerable part of this study concerns the electrochemistry (by means of voltammetry) of selected and newly synthesized phthalocyanines.[53, 54, 55]

2.6.1 Cyclic Voltammetry

Voltammetry includes a group of electroanalytical techniques in which information about an analyte is derived from the measurement of current as a function of applied potential. The three most commonly used types of voltammetry, and the only ones utilized in this study, are cyclic voltammetry (CV), square wave voltammetry (SWV) and linear sweep voltammetry (LSV). Cyclic voltammetry is possible the simplest and most versatile electroanalytical technique for the study of electroactive species and produces a typical cyclic voltammogram as shown in Figure 2.3. The most important parameters pertaining to cyclic voltammetry are the peak anodic potential (E_{pa}), peak cathodic potential (E_{pc}) and the magnitudes of the peak anodic current (i_{pa}) and peak cathodic current (i_{pc}), Figure 2.3.[54, 55]

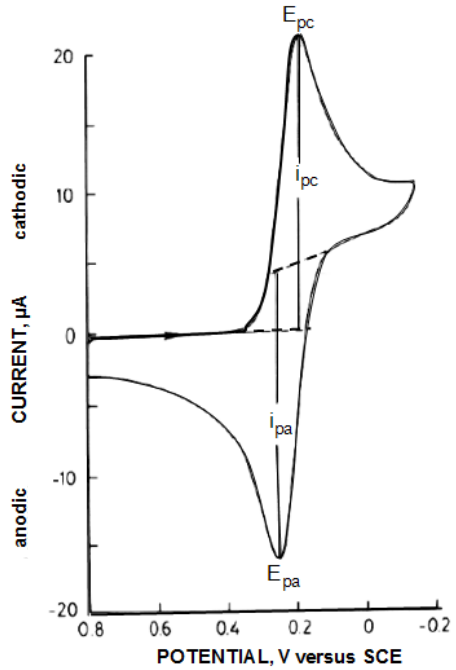

Figure 2.3: A generic cyclic voltammogram. "Reprinted with permission from [Mabbott, G. A.; *J. Chem. Educ.*; 1983, 60, 697). Copyright (1983) American Chemical Society."

By utilizing these parameters, valuable information regarding the chemical and electrochemical reversibility of each redox process of the analyte can be obtained. Theoretically, electrochemical reversibility implies that the peak potential difference ΔE_p = E_{pa} - E_{pc}, of a one-electron redox processes at 25 °C should, in the absence of coupled chemical processes, be 59 mV. Peak current ratios, i_{pc}/i_{pa} for anodic (oxidation) processes or i_{pa}/i_{pc} for cathodic (reduction) processes should be one in order to indicate chemical reversibility.[55]

2.6.1.1 Ferrocene

The electrochemistry of ferrocene and its derivatives (e.g. decamethylferrocene) is normally reversible and seldom undergoes chemical side-reactions. The electron transfer reaction observed is a chemically and electrochemically reversible one-electron step centred at the iron core of the ferrocenyl moiety. The central iron atom can either be in a two (ferro) or three (ferri) oxidation state. The resting state, however, is the reduced ferrocene, which contains an Fe(II) nucleus. As a functional group, this species is abbreviated as Fc (ferrocenyl) and carries no charge. During cyclic voltammetry the iron core is reversibly oxidized to Fe(III), the positively charged ferricenium species, and the reaction summarized as follows: $Fc^+ + e^- \rightleftharpoons$

Fc.[55, 56] Ferrocene (FcH) is the internal standard against which all redox potentials by IUPAC convention, are reported.

2.6.1.2 Phthalocyanines

The electrochemistry of phthalocyanines is very rich with as many as six ring-based redox processes. The redox processes occurring in phthalocyanine complexes may be centred at the central metal or at the phthalocyanine ring. The processes are affected by: [57, 58]

i) The nature and oxidation state of the central metal.
ii) The nature of the substituents on the phthalocyanine.
iii) The nature of the axial ligands co-ordinated to the central metal.

Figure 2.4 contains five overlayed cyclic voltammograms that illustrates the four redox processes (waves I, II, III and IV) of 1,4,8,11,15,18,22,25-octadodecylphthalocyanine (8 substituents on the non-peripheral positions).[43]

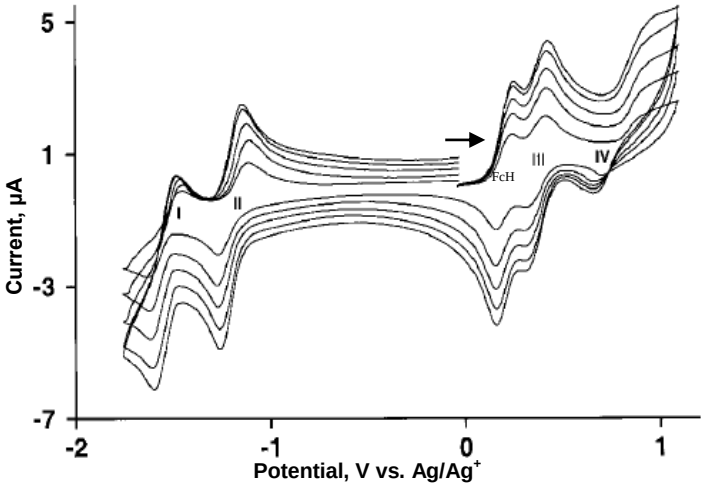

Figure 2.4: Cyclic voltammogram (CV) of 1,4,8,11,15,18,22,25-octadodecylphthalocyanine, in 1,2-dichloroethane (1 mmol dm^{-3}) containing [$^{n}Bu_4N$][PF_6] at scan rates of 50, 100, 150, 200, 250 mV s^{-1} on a platinum working electrode at 25 °C. The CV shows two ring-centered reversible oxidation peaks (III and IV) and two reversible reduction peaks (I and II). Two more reduction peaks lie outside the solvent window. The peak label Fc is that of ferrocene that has been added as an internal reference. "Adapted and reprinted from [Swarts, J. C., Langner, E. H. G., Krokeide-Hove, N. & Cook, M. J.; *J. Mater. Chem.*, 2001, 11, 434] with permission of The Royal Society of Chemistry"

Four ring-based processes for the metal-free macrocycles as well as the Fc/Fc^{+} couple of the internal standard can be identified in the potential range -1.8 V to 1.2 V *vs.* Ag/Ag^{+} in dichloroethane (DCE). The potential scan starts at a potential where the system is redox silent

and continues in a positive direction. Two ring-based oxidations occur at 418 mV and 929 mV, peaks III and IV, respectively. The scan direction is reversed at 1000 mV and reduction of oxidized species takes place. Further reduction takes place at -1265 mV and -1619 mV, peaks I and II, respectively. The scan direction is reversed at -1800 mV, oxidizing the reduced species. Each peak represents an electrochemical reversible one-electron transfer process.

The electrochemical processes represented by the various peaks in Figure 2.4 can be explained by the following electrochemical scheme:

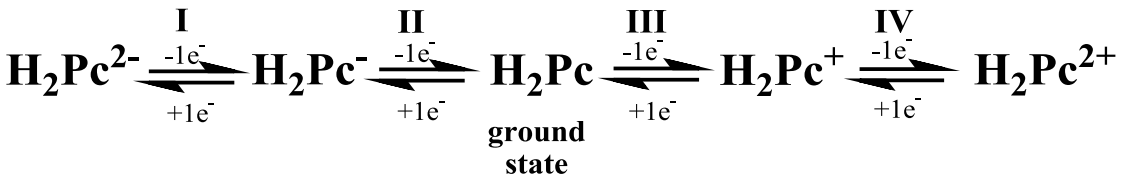

Scheme 2.6: The proposed electrochemical scheme for 1,4,8,11,15,18,22,25-octadodecylphthalocyanine.

The electrochemical properties of phthalocyanine complexes can be adjusted by a number of methods. Adding electron-withdrawing or -donating substituents on the periphery and non-periphery of the phthalocyanine ring have a substantial effect on redox potentials.[59, 60, 61] Electron-donating groups increase electron density on the macrocycle, and redox processes occur at more negative potentials; the opposite effect occurs when electron-withdrawing groups are used. Incorporation of different metals into the core of the ring and the ability to vary the axial ligands can also help to adjust redox potentials.[58, 62]

In 2006 an extensive survey was reported on the electrochemical effect of various electron-withdrawing and -donating substituents on the electrochemistry of metal-free phthalocyanines. Of particular interest, to this study, are the alkyl and alkoxy substituents as illustrated in Figure 2.5.

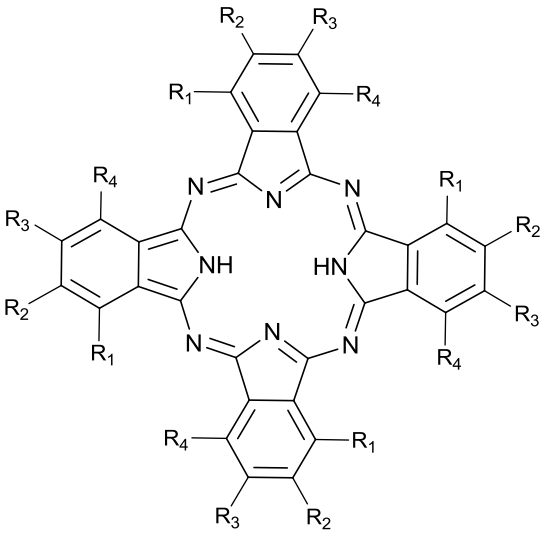

Compound	Substituents
H_2Pc	$R_1=R_2=R_3=R_4=H$
$H_2Pc(C_5H_{11})_8$	$R_1=R_4=H$; $R_2=R_3=C_5H_{11}$
$H_2Pc(OC_5H_{11})_4$	$R_1=R_4=H$;$R_2\neq R_3=H,OC_5H_{11}$
$H_2Pc(\alpha\text{-}OC_5H_{11})_4$	$R_1\neq R_4=H$, OC_5H_{11};$R_2=R_3=H$
$H_2Pc(OC_5H_{11})_8$	$R_1=R_4=H$;$R_2=R_3=$ OC_5H_{11}
$H_2Pc(\alpha\text{-}OC_5H_{11})_8$	$R_1=R_4=OC_5H_{11}$; $R_2=R_3=H$

Figure 2.5: A series of alkyl (electron-donating) and alkoxy (electron-withdrawing) substituted phthalocyanines. "Adapted and reprinted with permission from [Li, R., Zhang, X., Zhu, P., Ng, D.K., Kobayashi N., & Jiang, J.; *Inorg. Chem.*, 2006, 45, 2327] Copyright (2006) American Chemical Society."

The series of alkyl (electron-donating) and alkoxy (electron-withdrawing) substituted phthalocyanines show two one-electron oxidations and up to four quasireversible one-electron reductions, (where the separation of the reduction and oxidation potentials for each process is 60 to 95 mV), were reported within the electrochemical window of CH_2Cl_2 for the metal-free Pc derivatives. All processes were attributed to the removal of electrons from, or addition of electrons to the macrocycle orbitals. The effects of substituent species and positions were clearly reflected by the shift in the half-wave potentials of the first oxidation and first reduction, together with their difference. Both the first oxidation and the first reduction of $H_2Pc(C_5H_{11})_8$, 0.94 and -0.77 V vs. SCE remain almost unchanged relative to those of H_2Pc, 0.93 and -0.78 V vs. SCE. The substitution of alkoxy groups at the peripheral and non-peripheral positions of phthalocyanines, $H_2Pc(OC_5H_{11})_4$ and $H_2Pc(OC_5H_{11})_8$, induces a shift in the negative direction for both the first oxidation, 0.85 and 0.72 V vs. SCE, and the first reduction, -0.86 and -0.97 V vs. SCE, when compared to the first oxidation and the first reduction of H_2Pc, 0.93 and -0.78 V vs. SCE, respectively. It is important to note that the substitution on non-peripheral positions afforded a more significant shift in the negative direction than that of the peripheral positions.[63]

Ruthenium exhibits a number of formal metal oxidation states when complexed to phthalocyanines.[64, 65, 66, 67] The majority of reported ruthenium phthalocyanines (RuPcs) have

Ru^{II} metal centres[68, 69], although some Ru^{III} and Ru^{IV} complexes have been reported.[67] The oxidation potentials of RuPcs can also depend on the nature of the axial ligand. Axial ligands with a higher donating character imply that the ruthenium centre should be easier to oxidize, than a ruthenium centre connected to axial ligands that have high electron withdrawing characteristics.[68, 70]

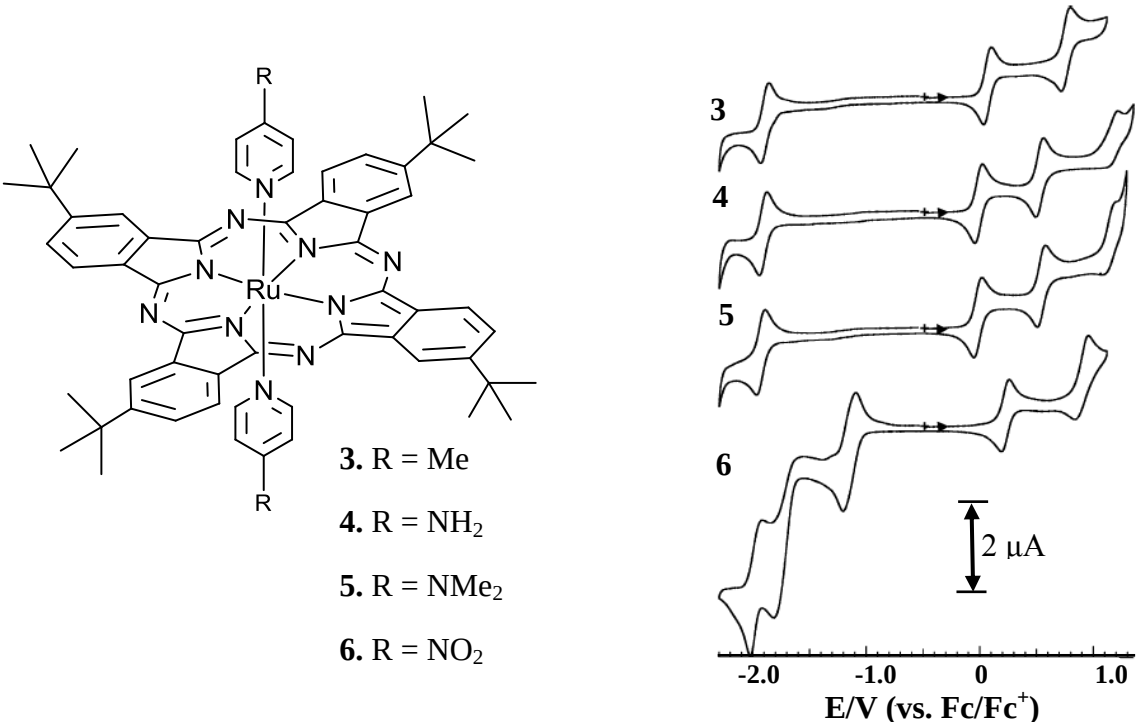

Figure 2.6: Left: The structure of the various [{(t-Bu)$_4$Pc}Ru(4-Rpy)$_2$] complexes. **Right:** Cyclic voltammograms of these complexes in dichloromethane solution with 0.1 M [Bu_4N][PF_6] electrolyte with a scan rate = 100 mV.s^{-1}.[70] "Adapted and reprinted with permission from [Rawling, T., Xiao, H., Lee, S.-T.; Colbran, S. B. & McDonagh, A. M.; *Inorg.Chem.*, 2007, 46, 2805] Copyright (2007) American Chemical Society."

Figure 2.6 shows the electrochemical data of (t-Bu)$_4$-$RuPcL_2$, where L is a axial ligand with para-substituted pyridine groups. The first oxidation potential for the amino-pyridine complexes, **4** and **5**, were found to be the same with a potential of -0.02 V versus Fc/Fc$^+$. A third one-electron oxidation process was observed for the amino-pyridine complexes, **4** and **5**, with values of 1.17 and 1.13 V. The oxidation potential for the nitro-pyridine complexes, **6** in Figure 2.6, was found to have a significantly larger first oxidation potential, 0.22 V, than the amino-pyridine complex, **4** and **5**, -0.02 V. The difference between the oxidation potential of the 4-methylpyridine complex, **3**, and the amino-pyridine complexes, **4** and **5**, are less significant, 0.07 V and -0.02 V, respectively.[70] In 2014, it was showed that (t-Bu)$_4$-PcRu(CO) undergoes two oxidation and two reduction processes, but that only the first oxidation and first reduction processes are reversible in CH_2Cl_2. All four redox processes of (t-Bu)$_4$-

PcRu(CO) were assigned to processes on the phthalocyanine ring and not the ruthenium metal centre.[71, 72]

Spectroelectrochemical studies for $PcRu(py)_2$[73] and $PcRu(3\text{-}Clpy)_2$[74] showed that the first and second oxidation processes both involve oxidation of the phthalocyanine macrocycle, which gave $[Pc^{-}Ru^{II}L_2]^{+}$ and $[Pc^{0}Ru^{II}L_2]^{2+}$ species, respectively. The first one-electron reduction process, for both complexes, $PcRu(py)_2$ and $PcRu(3\text{-}Clpy)_2$, have been observed at approximately -1.8 V and were assigned to the reduction of the macrocycle.[73, 74] Typically a difference of 2 V was reported between the first oxidation and reduction processes for $PcRuL_2$ complexes, however substitution of the periphery of the macrocycle also had a significant effect on the potential of the first and second oxidation processes.[69, 74] Complexes of the type PcRu(CO)L, where L = py, or 4-Mepy, showed a more positive oxidation potential than the corresponding $PcRuL_2$ complexes, where L = py or 4-Mepy. This effect was reported to be due to π-backbonding of ligated CO when compared to pyridine-containing ligands.[68, 70]

2.7 UV-Visible spectroscopy of phthalocyanines

The UV-vis spectrum of a metallated phthalocyanine is characterized by a strong band, the Q band and the B (or Soret) band which is slightly weaker as shown is Figure 2.7. The changes in UV-vis spectra of phthalocyanines can be analysed as a function of four different parameters, namely:

i) the nature of the central metal,
ii) the sequential addition of fused benzene rings,
iii) the nature and position of the peripheral and axial substituents, and
iv) the deviation from planarity.[1, 2]

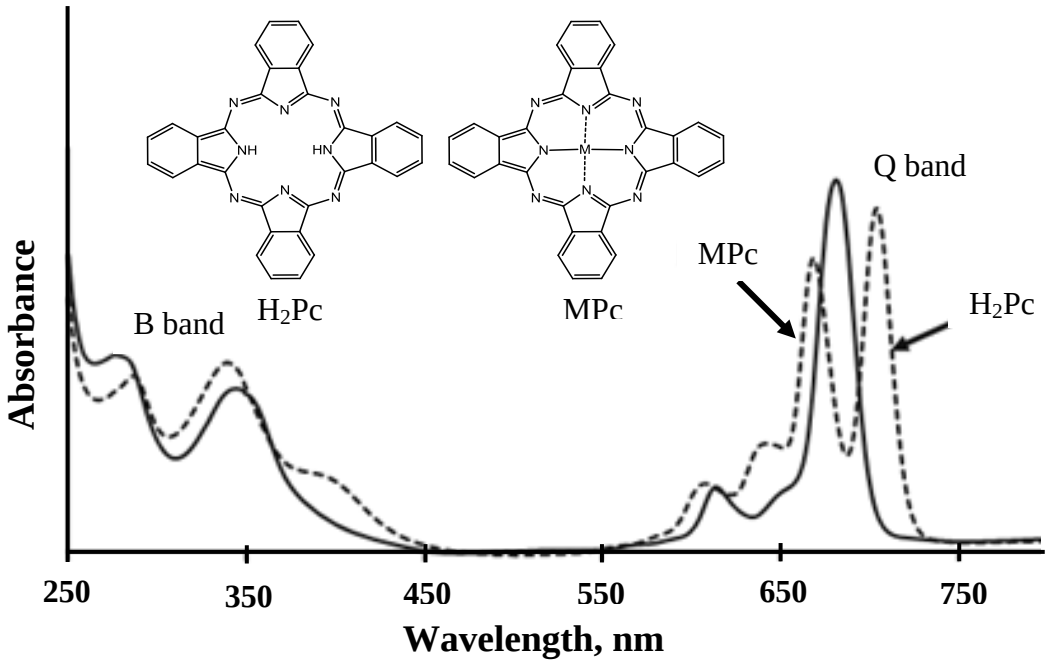

Figure 2.7: Typical UV-vis spectra of metal free (dotted line) and metallated (solid line) phthalocyanines. Reproduced from [Rio, Y., Rodríguez-Morgade, S. & Torres, T.; *Org. Biomol. Chem*., 2008, 6, 1877] with permission from The Royal Society of Chemistry

The electronic spectrum of unsubstituted metal-free phthalocyanines (H_2Pc) is characterized by a split Q-band (Q_x and Q_y) where absorbance maxima (λ_{max}) appear at 698 and 664 nm, respectively.[9] Splitting of the Q-band onto x and y components occurs as a result of the reduction of symmetry from D_{4h} to D_{2h}, going from metal macrocycles to demetallated macrocycles (Figure 2.7). The UV/vis spectrum of metal-free tetra(2-hydroxyethyleneoxy)phthalocyanine is characterized by a split Q-band, appearing at λ_{max} (Q_x) = 710 and λ_{max} (Q_y) = 681 nm.[39] The species with closed-shell metals, for example magnesium (II), lithium (II) or zinc (II) show λ_{max} values around 670 nm. Species with open-shell metal ions that interact strongly with the phthalocyanine ring, such as iron (II), cobalt (II) or ruthenium (II) have Q-bands shifts with λ_{max} at around 630 to 650 nm. A remarkable exception is found by the titanium and manganese phthalocyanines that have been reported with Q-band maxima at strongly shifted values of Q_y = 808 nm, and Q_x = 828 and 893 nm, respectively.[2, 38]

2.8 Computational Chemistry

2.8.1 Introduction

Computational chemistry, also known as molecular modelling, is a set of techniques for exploring chemical phenomena on a computer. The following questions are commonly investigated computationally:

i. Geometry optimization, which consists of the bond lengths, bond angles and dihedral angles.
ii. Molecular energies, structures and orbitals
iii. Chemical reactivity: Excited states, transition states and reaction pathways.
iv. Spectroscopy: Infrared (IR), ultraviolet and visible (UV/Vis) and nuclear magnetic resonance (NMR), Raman and circular dichroism (CD).

This branch of chemistry, which consists of calculating the strain-free bond lengths, is becoming more and more accessible, because computer hardware becomes cheaper and powerful software become readily available for inexpensive personal computers. The combination of theoretical and experimental chemistry can lead to the interpretation of conflicting results, better understanding and the prediction of properties for compounds that are dangerous or difficult to obtain experimentally.[75, 76]

2.8.2 Quantum Mechanics

Quantum Mechanics is used to describe the behaviour of electrons mathematically. The Schrödinger equation is the basis of nearly all computational chemistry methods.[76] This equation is a differential equation depending on time and all of the spatial coordinates necessary to describe the system. The general time dependent Schrödinger equation is:

$$\hat{H}\Psi = E\Psi \qquad \textbf{Equation 2.1}$$

where $\hat{H}$ is the Hamiltonian operator, Ψ a wave function and E the energy. The wave function Ψ is a function of the electron and nuclear positions. The Hamiltonian operator $\hat{H}$ is, in general:

$$\hat{H} = -\sum_i^{particles} \frac{\nabla_i^2}{2m_i} + \sum_{i<j}^{particles} \sum \frac{q_i q_j}{r_{ij}} \qquad \textbf{Equation 2.2}$$

$$\nabla^2 = \frac{\partial^2}{\partial x_i^2} + \frac{\partial^2}{\partial y_i^2} + \frac{\partial^2}{\partial z_i^2} \qquad \textbf{Equation 2.3}$$

where ∇ is the Laplacian operator acting on particle *i*. The particles consist of electrons and nuclei. The mass and charge of particle *i* is m_i and q_i, respectively. The kinetic energy of the particle is within a wave function and the potential energy is due to the Coulomb interaction between the particles. The Hamiltonian for a molecule with stationary nuclei is given below.

$$\hat{H} = -\sum_i^{electrons} \frac{\nabla_i^2}{2} - \sum_i^{nuclei} \sum_j^{electrons} \frac{Z_i}{r_{ij}} + \sum_{i<j}^{electrons} \sum \frac{1}{r_{ij}} \qquad \textbf{Equation 2.4}$$

Here, the first term is the kinetic energy of the electrons only. The second term is the attraction of the electron to nuclei. The third term is the repulsion between electrons.[75, 76, 77,] The solution of the Schrödinger equation gives a wave function and quantized energies. The square of the wave function gives the probability of finding the electron at a specific position in space.

2.8.3 Density Functional Theory (DFT)

Density Functional Theory (DFT) operates on the principle that the energy of a molecule can be determined from the electron density, ρ, instead of a wave function, ψ. Kohn and Sham developed a practical application of this theory. This technique that has gained significant ground in recent years to become one of the most widely used techniques for the calculation of molecular structure.[80] Its advantages include less demanding computational effort, less computer time, and—in some cases (particularly *d*-metal complexes)—better agreement with experimental values than is obtained from Hartree–Fock procedures.[77]

The energy of the molecule is a function of the electron density, written E[ρ], and the electron density is a function of position, ρ(r).

$$\rho(\boldsymbol{r}) = \sum_{i=1}^{N} \psi_i(\boldsymbol{r})^2 \qquad \textbf{Equation 2.5}$$

The exact ground-state energy of an n-electron molecule is:

$$E[\rho] = E_K + E_{P;e,N} + E_{P;e,e} + E_{XC}[\rho] \qquad \textbf{Equation 2.6}$$

where E_K is the total electron kinetic energy, $E_{P;e,N}$ the electron–nucleus potential energy, $E_{P;e,e}$ the electron–electron potential energy, and $E_{XC}[\rho]$ the exchange–correlation energy, which takes into account all the effects due to spin. The biggest advantage of DFT is that it is the most cost-effective method to achieve a given accuracy. No systematic way of improving DFT calculations exists as DFT results can only be improved by using better functionals.[77, 80]

2.8.4 Exchange correlation functionals

The exchange-correlation functional is also known as the density functional.[80] There are four well-known functionals, namely local density approximation (LDA), generalized gradient approximation (GGA), meta-GGA methods and hybrid-GGA methods. This study will utilize GGA, as well as hybrid-GGA, therefore, further discussion will focus on these functionals.

The generalized gradient approximation (GGA) for the exchange functional in density-functional theory (DFT) in conjunction with accurate expressions for the correlation functional include PW91, from Perdew and Wang in 1991, BLYP, where B denotes Becke's 1988 exchange functional and LYP denotes the Lee–Yang–Parr correlation functional. The correlation functionals of B3PW91 and B3LYP are based on PW91 and LYP, respectively, but are optimized specifically for the use in a hybrid functional where B3 denotes three Becke's parameter. The combination of OPTX and LYP, yields the combined corrections functional OLYP. M06L is a functional that combines thermochemistry, thermochemical kinetics, metallochemical and noncovalent interactions, bond lengths, and vibrational frequencies.[75, 76, 80, 78]

2.8.5 Amsterdam density functional (ADF)

Amsterdam density functional (ADF) is a DFT programme. It was created four decades ago and is still being improved. ADF is also known as Hartree-Fock-Slater (HFS). ADF can be used to study geometry optimization, transition states, spectroscopy characteristics, transition states and many more properties. Calculations on atoms and molecules can be done in gas or solution phases.[79]

2.8.6 Basis Sets

The computational chemistry method, DFT, requires some understanding of basis sets and basis functions. A basis set is a linear combination of basis functions to create atomic orbitals (AOs). There are two types of basis functions commonly used in electronic structure calculations: Slater Type Orbitals (STO) and Gaussian Type Orbitals (GTO). Amsterdam density functional theory (ADF), unlike any other density functional theory programme, uses STO instead of GTO. Minimal basis set are defined as one function (STO or GTO) per atomic orbitals.[80] GTO needs more functionals than STO to achieve the same level of basis set quality.

The ADF has a large basis set database. The minimum basis set is single-zeta (SZ) with the smallest amount of functions. Triple-zeta (TZ) has three times the amount of functions than the minimum basis (SZ). Polarization functions are the combination of radial correlation and angular correlation. Radial correlation is where one electron is close to the nucleus and the other one far from it. Angular correlation refers to the phenomenon when two electrons are on opposite sides of the nucleus. These polarization functions can be combined with the different zeta basis sets for instance, triple-zeta plus polarization (TZP).[80, 79]

2.8.7 Molecular Orbitals (MO)

Visualization of molecular orbitals illustrates the location of those regions where the highest- and lowest-energy electrons are concentrated. The highest-energy electrons will be in the highest occupied MO, the HOMO. The region which offers the lowest-energy accommodation to any donated electrons is called the lowest unoccupied MO, the LUMO[75, 80] Electrophiles should bond to the atom where the HOMO is "strongest" (where the electron density due to the highest-energy electron pair is greatest) and nucleophiles to the atom where the LUMO is strongest, at least as seen on the van der Waals surface by an approaching reagent.[75, 80] Figure 2.8 shows the visualisation of the HOMO and LUMO of demetalled phthalocyanine, H_2Pc.[81] The difference between the HOMO and LUMO energies are known as the HOMO-LUMO gap, which indicates the lowest energy electronic excitation.

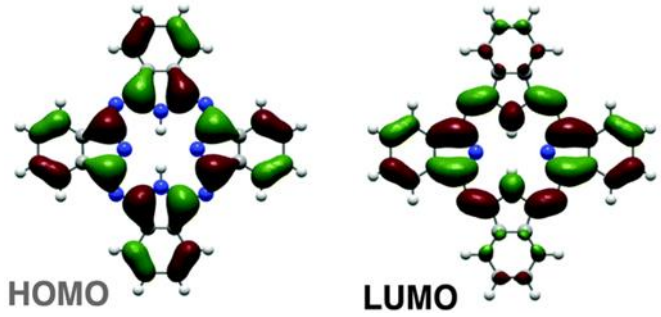

Figure 2.8: Visualisation of HOMO and LUMO of H_2Pc generated by DFT calculations at the B3LYP/6-31G(d,p) level. [Ikeda, T., Iino, R., & Noji, H.; *Chem. Commun.*, 2014, 50, 9443] - Published by The Royal Society of Chemistry.

2.8.8 Symmetry operations and point groups[82, 83]

Each molecule has a set of symmetry operations that describes the molecule's overall symmetry. This set of operations defines the point group of the molecule. Symmetry operations are actions where a part of the molecule can be interchanged with other parts of the molecule without changing the identity or the orientation of the molecule. The parts that interchange in this manner are equivalent to one another by symmetry. Every symmetry operation has a symmetry element (a point, line or plane) to which the symmetry operation is performed. At least one point of the molecule stays unchanged when performing these symmetry operations and that is why they are known as the operations of point group symmetry. The five important point group symmetry operations are:

i. **Identity (E)** – the operation where no action is performed on the molecule. Therefore, each molecule at least has one symmetry operation by which they can be classified. This is needed if all molecules are to be classified by symmetry.

ii. **Proper rotation (C_n)** –the operation where rotation around an axis, which goes through a molecule, with an angle of 360°/*n* is performed and has a virtually unchanged molecule as a result. If this rotation is repeated *n* times the molecule will be in its original orientation. This operation is also known as an *n*-fold rotation axis abbreviated as C_n. A molecule can have more than one proper rotation operation. The operation with the highest order (*n*) is called the principal axis. The principal axis is normally defined as the z-axis.

iii. **Reflection (σ)** –the operation where all the atoms of a molecule can be reflected through a plane that passes through the molecule. This reflection operation (σ) is also

known as a mirror plane. There are three reflection operations possible. The first is a mirror plane parallel to the principal axis and is called vertical (σ_v). The second is called horizontal (σ_h) since the mirror plane is perpendicular to the principal axis. The third reflection operation is called dihedral which consists of a mirror plane that bisects the angle between two 2-fold rotational axes.

iv. **Centre of inversion (i)** – the operation where each atom of a molecule is projected through a single point to an equal distance on the other side.

v. **Improper rotation (Sn)** – this operation is defined as a rotation around an axis that goes through a molecule with an angle of 360°/*n* and then reflects all the atoms through a plane that is perpendicular to the axis. The same result will be obtained if the operation is carried out in reverse (first the reflection and then the rotations around the axis).

Different combinations of the symmetry operations give different point groups. For this study C_2 and C_s point groups are important, as illustrated by Figure 2.9 for H_2Pc.

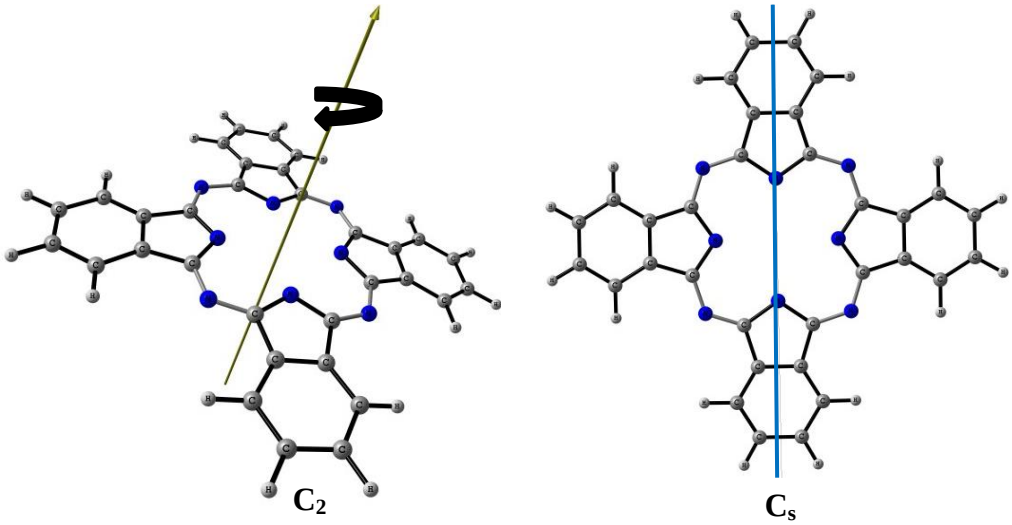

Figure 2.9: Illustration of the C_2 (rotation axis indicated with line and arrow) and C_s (blue line indicates a mirror plane) point groups for H_2Pc.

The C_2 point group is defined as a molecule that has both an identity and a C_2 proper rotation operation. This implies that the molecule has a rotation axis through the molecule where the molecule can rotate with an angle of 180° (360°/2). The C_s point group describes the symmetry of bilateral objects that lack any symmetry other than E and σ_h.

2.8.9 Phthalocyanine

Different functionals and basis sets can be employed during DFT calculations for phthalocyanines. A study was done by Che et al. on $Ru^{II}(Pc)(HNQu)_2$ where HNQu is N-phenyl-1,4-benzoquinonediimine, as shown in Figure 2.10. All calculations were performed using the M06L functional. Stuttgart effective-core potentials with their accompanying basis set were used for the Ru atom, and the 6-31G(d) basis set was used for all the other atoms (H, C, N, and O). Geometry optimization showed a bond length of 2.071 Å for Ru-N_{ax} bond (N_{ax} is the nitrogen atom of the axial ligand bonding to the Ru), 1.318 Å for N_{ax}-C_{Qu} bond and 2.017 and 2.018 Å for Ru-N_{eq} bond, where N_{eq} is the nitrogen atoms on the phthalocyanine ring. All these bond lengths were in accordance with the experimental values obtained through crystal X-ray analysis. According to the results obtained, the LUMO was described as an antibonding π* (d_{xz}(Ru)–p_x(N)) orbital, whereas the HOMO was phthalocyanine-based.[66]

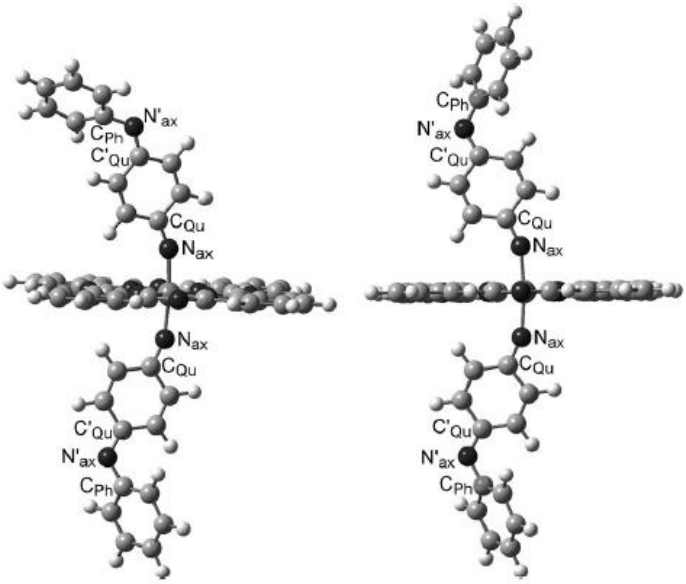

Figure 2.10: DFT-optimized structures of $Ru^{II}(Pc)(R\text{-}py)_2$, where R = pyridine, **left:** *anti* isomer; **right:** *syn* isomer. "Reprinted from [Huang, J., Wong, K., Chan, S., Tso, K., Jiang, T., & Che, C.; *Asian J. Chem*.,2014, 9, 338] with permission from John Wiley and Son"

In 2009, DFT calculations were carried out on two tetra-(tert-butyl)RuPc(4-carboxypyridine)(R-pyridine), where R is 4-carboxy for **7** and R is an electron-donor substituent, triphenylamine for **8**, as showed in Figure 2.11. B3LYP was employed using a general basis set with 6-31G(d) for C, N, and O atoms, 6-31G for H atoms and an effective

core potential basis set LANL2DZ for the Ru atom. The effect of the axial ligands on the nature of the HOMO was investigated for both these compounds. In both cases, the HOMO was exclusively located in the phthalocyanine ring, not on the metal centre or the axial ligands.[68]

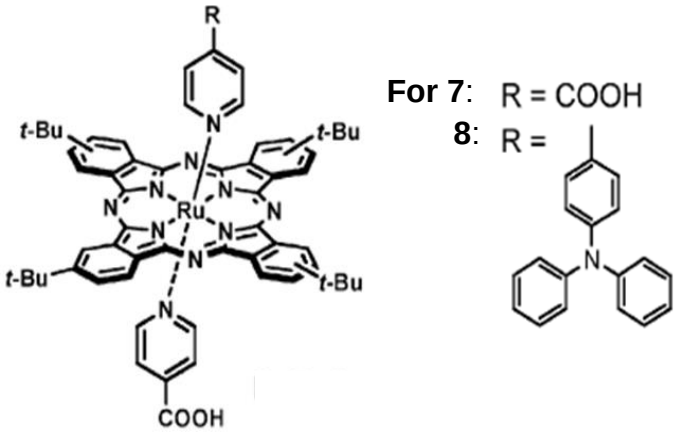

Figure 2.11: Molecular structure of the tetra-(tert-butyl)RuPc(4-carboxypyridine)(R-pyridine). "Adapted and reprinted from [Morandeira, A., Lopez-Duarte, I., O'Regan, B., Martìnez-Dìaz, V., Forneli, A. & Palomares, E.; *J. Mater. Chem.*; 2009, 19, 5016] with permission of The Royal Society of Chemistry"

2.9 Reaction calorimetry (RC1 reactor)

Reaction calorimetry measures the heat, *q*, released from a chemical reaction or physical process under process-like conditions and provides the fundamentals of the thermochemistry of a reaction. Calorimetric information is crucial when determining how chemical reactions can be transferred safely from lab to plant. Reaction calorimetry helps to identify issues related to heat and mass transfer or mixing, and allows the determination of the correct temperature, stirring or dosing profile. It also uncovers unexpected behaviour and makes other scalability issues visible and quantifiable.[84]

The Mettler Toledo RC1 process development workstation enables such calometric studies through precise temperature measurement and control, to within 0.1 °C, of either the reaction vessel or the reaction mixture. The RC1 reactor vessel has a specific volume (for example 2 000 cm^3) cylindrical tank that is equipped with an impeller, or stirrer (able to stir at up to 1 000 rpm), as well as three different temperature sensors, two pressure sensors, a pH sensor and a mass controlled feed pump. Additionally, the RC1 reactor is also equipped with an *in situ* FT-IR. Thus the RC1 enables exceptional control over all reaction conditions (temperature, pressure, pH and stirring rate), it provides precise thermodynamic data of the

reaction, and also allows the kinetic study through FT-IR. Figure 2.12 shows a schematic of the RC1-reatcor, while Figure 2.13 highlights the temperature measuring probes utilized in the reactor as well as the principle of heat flow balance during measurements.[85]

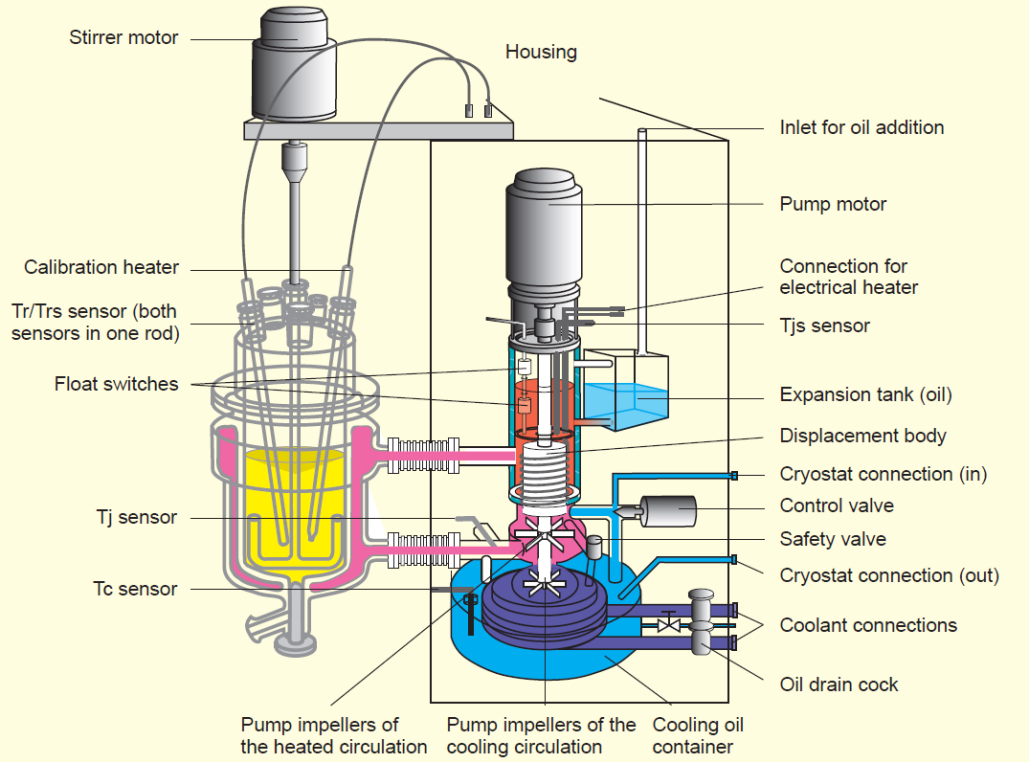

Figure 2.12: Cross section highlighting the design of the Mettler Toledo RC1 reactor. Reproduced from (Mettler Toledo – Operating Instructions – RC1) with permission of Mettler Toledo.

In most cases it is useful to add a baffle to the reaction vessel stirring mechanism. This prevents a circular flow pattern inside the vessel and inhibits the formation of a free surface vortex which is always present in unbaffled tanks. The inhibitions of vortex formation as well as circular flow pattern, improves total reaction mixing.

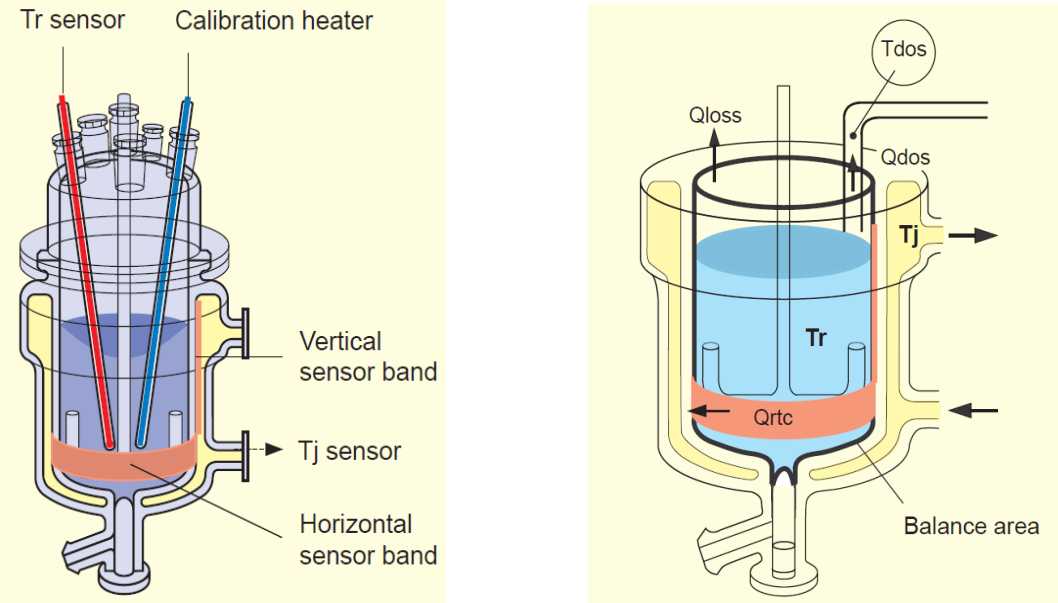

Figure 2.13: The RC1 used with heat flux sensors attached to the outer wall of the reaction vessel. These measure the specific heat flow through the horizontal sensor band. The fill level is determined by the vertical sensor band. This allows the heat flow through the reactor wall to be calculated. Reproduced from (Mettler Toledo – Operating Instructions – RC1) with permission of Mettler Toledo.

Q_{RTC} =	A. q_{s0}	
Q_{RTC}:	Heat flow through the part of the reaction vessel wall wetted by its contents.	W
A:	Effective heat exchange area, determined by the sensors of the vertical band.	m^2
Q_{s0}:	Specific heat flow through the horizontal sensor band.	W/m^2

The heat flow balance over the reactor is as follows:

Inflow = Accumulation + Outflow of the heat

$(Qr_{\_est})$ = (Q_{accu}) + $(Q_{rtc} + Q_{dos} + Q_{loss} + \ldots)$

Q_{rtc}: heat flow through the reactor wall (rtc: real time calorimetry)

Q_{accu}: heat storage (accumulation) by the reaction mass and through the inserts

Q_{dos}: heat input due to dosing: power that is needed to bring the inflow from T_{dos} to T_r

Q_{loss}: heat flows through the reactor head assembly (radiation, conduction)

Q_{r_est} is the estimated heat generation rate of all individual heat effects in the reaction medium that are caused by all chemical reactions running simultaneously and through phase changes such as evaporation, crystallization, dissolution and mixing.

Mixing inside the system can take place in one of two ways namely laminar and turbulent flow, Figure 2.14:

- Laminar (or streamlined) flow[86] is the most predictable type of flow and is an orderly type of flow; it occurs at stable, low flow rates.
- Turbulent flow[87, 88] is a type of flow that occurs at faster flow rates or through disruption of normal flow patterns. Distortions take place in flow result through vortexes and random fragmentation, causing blending of the tiers within the fluid.

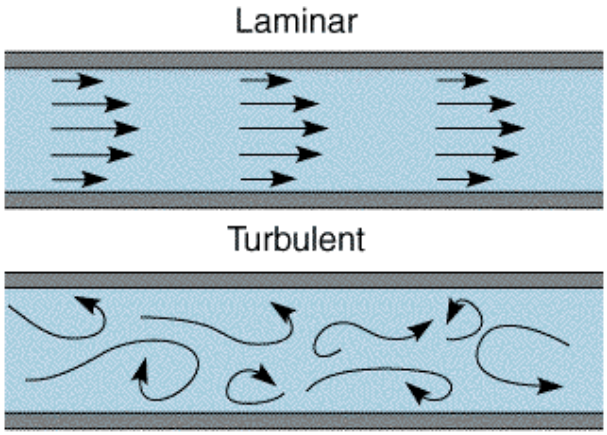

Figure 2.14: Depiction of laminar and turbulent flow patterns.

Mass transfer[88] (section 2.9.1) is the movement of mass from one area to another, and offers a way to quantify the effectiveness of the stirring process. Mass transfer in laminar flow is mainly due to molecular diffusion due to the orderly movement of the system, while in case of turbulent flow, random movement occurs in all directions; giving rise to transport rates that may be orders of magnitude higher than those solely due to molecular effects.

2.9.1 Heat and Mass transfer in the RC1 reactor

The process by which molecules, ions, or other small particles spontaneously mix, moving from regions of relatively high concentration into regions of lower concentration are known as diffusion or molecular diffusion. Molecular diffusion can be analysed in two ways. Firstly it can be described by means of Fick's law and diffusion coefficient[89] and secondly by means of a mass transfer coefficient.[90]

A conversion profile of a chemical reaction can be optimized for given operating conditions by understanding the factors that influence. In order to obtain the best possible chemical conversion, it is expected that heat and mass transfer should occur optimally as well. Heat and mass transfer in a stirred vessel can be quantified by the coefficients name, Heat Transfer, U and Mass Transfer, k_La.

When looking specifically at the transfer of gas molecules in a solution, the gas (oxygen, nitrogen etc.) concentration in the gas phase (C_g) in a small-scale system is determined by the gas consumption in the liquid phase and by the mass transfer resistance of the barrier

applied.[90, 91] Factors influencing Gas–Liquid Transfer Systems are the composition of the liquid medium, i.e., the concentration of dissolved compounds, which in turn influences the gas–liquid mass transfer characteristics. Higher concentrations or ionic strength lead to a lower gas solubility (L_g) and lower mass transfer coefficients (k_La) due to smaller diffusion coefficients. Considering all parameters, including reactor set-up are important to consider, because this will ensure that further experiments are done under optimal mass transfer conditions.[90, 92, 93]

2.9.2 Kinetics and Thermodynamics

The RC1 additionally offers the unique ability of *in situ* product identification and determination of the reaction kinetics through the combination of the ReactIR FT-IR instrument. In the system used, an ATR-IR probe (ATR = attenuated total reflectance) with Si as active surface material was used. If a diamond crystal is used, due to the strong IR active vibrational band between 1800 and 2400 cm^{-1} that it possesses, this region would not be useful for measurements. Although this technique enables direct *in situ* measurements during the course of reactions, it does suffer from some limitations which are good to take note of. First of all, if the extinction coefficient of the sample to be measured is too low, obviously it will be an IR blind system and no meaningful measurements would be possible. Secondly, measurements are made at the surface of the Si crystal from a thin layer (film thickness is in the range of only a few μm) in the liquid phase. The thickness of this layer will vary with temperature. This means the IR light path length is not constant. Therefor measurements should preferably always be at constant temperature. In addition, with varying thin film thickness, application of the Beer Lambert law may fail, especially if the absorption bands are intense. Any solids which do not dissolve in the solvent utilized will also not be detected by this measuring technique. This usually is regarded as a limitation, but in the present study it was an advantage. It meant no solids (of which there were many in the reaction mixture, see Chapter 3) could interfere with measurements. The desired products (oxidised thiophene and reduced nitrophenyl derivative) could be detected at unique IR vibration frequencies without interfering contributions from other species in the system. Other components that could also be uniquely identified in this study were acetone and dimethyldioxirane, and they could also be measured with only a little interference during the course of reactions. Although the film constitution at the surface of the Si crystal may not

have been constant in terms of *all* components in the reaction mixture, it was constant for the identification of the desired dissolved species and measured products because of efficient stirring.[92] The work described by Crump and co-workers are very useful to highlight the above aspects. It also is very instructive for kinetic measurements with devices such as the RC1 reactor.[92]

Determining the kinetics of a chemical reaction is an essential characteristic, especially when going from lab to plant, and also provides information regarding the reaction mechanism. Factors affecting reaction rates include physical state of the reactants, concentration of reactants, temperature, pressure and the presence of a catalyst. [94, 95]

The first order kinetic equations in differential form is: [80]

$$\frac{dA}{dt} = -kt \qquad \textbf{Equation 2.7}$$

where A is the concentration of the analyte, t is the time of the reaction and *k* is the reaction rate constant. The integrated first order rate equations can be written as:

$$ln(\frac{A}{A0}) = -kt \qquad \textbf{Equation 2.8}$$

$$ln\,[A]_t - ln\,[A]_0 = -kt$$

$$ln\,[A]_t = -kt + ln\,[A]_0 \qquad \textbf{Equation 2.9}$$

Thermodynamics focusses on the relationship between heat and other forms of energy. Heat is the energy that is transferred between substances or systems due to a temperature difference between these substances or systems. The first law of thermodynamics states that energy cannot be created or destroyed, energy can only be converted from one form to another. Enthalpy, *H*, and entropy, *S*, is thermodynamic properties of a system (reaction) related to the system's internal energy and the degree of disorder of the system.[77, 94, 95]

The enthalpy, *H*, is defined as

$$H = U + PV \qquad \textbf{Equation 2.10}$$

where P is the pressure of the system, V is its volume and U is the internal energy. The change in enthalpy, ΔH, between any pair of initial and final states is independent of the path between them.

$$\Delta H = \Delta U + P\Delta V$$

The change in internal energy can also be define by:

$$\Delta U = q + w$$

where $w = -P\Delta V$ and q is the heat flow. At constant pressure or constant volume $w = 0$, change in internal energy, ΔU, is equal to heat flow, q. Thus the change in enthalpy is:

$$\Delta H = \int_0^\infty q_{react} dt \qquad \textbf{Equation 2. 11}$$

The enthalpy of a perfect gas is related to its internal energy by using $PV = nRT$ in the definition of H:

$$H = U + PV = U + nRT$$

This relation implies that the change of enthalpy in a reaction that produces or consumes gas is

$$\Delta H = \Delta U + \Delta n_g RT \qquad \textbf{Equation 2.12}$$

where ΔU is the change in internal energy and Δn_g is the change in the amount of gas molecules in the reaction. The change in enthalpy, ΔH, for a reaction indicates if heat is absorbed or released by the system.

$$\Delta H = \sum H_{product} - \sum H_{reactants} \qquad \textbf{Equation 2.13}$$

When ΔH is negative, heat is liberated and the reaction is exothermic. The reaction is endothermic when ΔH is positive and heat is absorbed.

According to thermodynamics, a process can either be spontaneous or non-spontaneous, as summarized by the Second Law of Thermodynamics. The Second Law of Thermodynamics states that entropy, S, of an isolated system increases over time:

$$\Delta S_{tot} > 0$$

where S_{tot} is the total entropy of the system and its surroundings. A negative change in entropy, ΔS_{tot}, indicates that the products formed in the reaction are less disordered than reactants, while positive change in entropy, ΔS_{tot}, indicates the opposite.

Gibbs free energy, G, is defined by the following equation:

$$G = H - TS \qquad \textbf{Equation 2.14}$$

The Gibbs free of a system predicts if a reaction would occur spontaneously, when the system is at constant temperature and pressure. The following equation defines the change in Gibbs free energy of a system:

$$\Delta G = \Delta H - T\Delta S \qquad \textbf{Equation 2.15}$$

The system or reaction is spontaneous (but not necessary fast) if ΔG is negative.[77, 95]

Determining the kinetics of a chemical reaction is an essential characteristic, especially when going from lab to plant, and also provides information regarding the reaction mechanism. Factors affecting reaction rates include physical state of the reactants, concentration of reactants, temperature, pressure and the presence of a catalyst.[94, 95]

In 2006 a hydrogenation study on nitrobenzene and ethyl-4-nitrobenzoate, utilizing a small-scale, pressure-resistant reaction calorimeter (CRC.v4) fitted with an integrated infrared-attenuated total reflection (FT-IR-ATR) probe, was performed.[96] During this study measurements of calorimetric and FT-IR signals were gathered to optimize the reaction conditions.

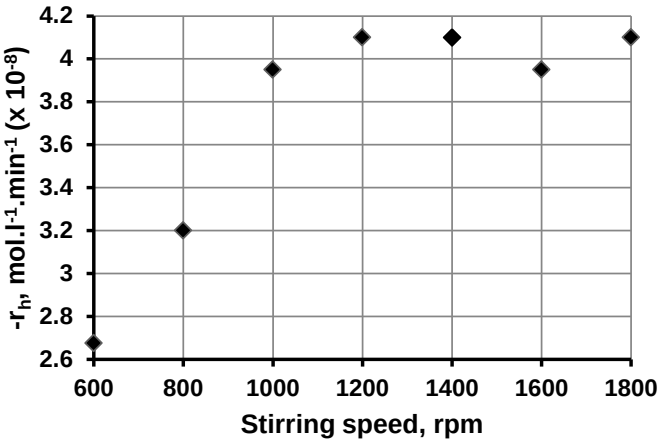

Figure 2.15: Effect of the change in the stirrer speed (600-1800 rpm) on the reaction rate of the hydrogenation of nitrobenzene. "Reprinted (adapted) with permission from (Visentin, F., Puxty, G., Kut, O. & Hungerbühler, K., *Ind. Eng. Chem. Res,*. 2006, 45 (13), 4544-4553. DOI: 10.1021/ie0509591). Copyright (2006) American Chemical Society."

The role of the external mass transfer on the reaction was assessed, by studying the effect of the stirring speed (Figure 2.15). During this study the stirring speed was varied from 600 to 1800 rpm. It was found that increasing the stirrer speed increased the rate of the reaction; however mass-transfer effects did not influence the reaction above 1200 rpm. Therefore all further reactions were carried out at 1200 rpm where the external mass transfer did not influence the observed kinetics.

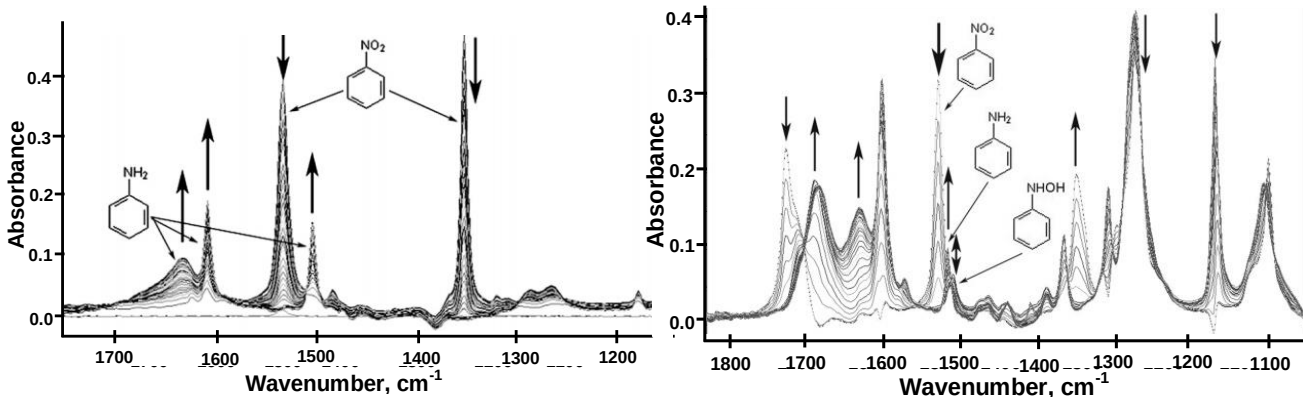

Figure 2.16: Part of the IR spectra recorded as a function of time during the hydrogenation of; **Left:** Nitrobenzene at 50 °C; **Right:** Ethyl-4-nitrobenzoate at 50 °C. "Adapted and reprinted with permission from (Visentin, F., Puxty, G., Kut, O. & Hungerbühler, K., *Ind. Eng. Chem. Res,*. 2006, 45 (13), 4544-4553. DOI: 10.1021/ie0509591). Copyright (2006) American Chemical Society."

The IR spectra were measured over the range 1100-1800 cm^{-1}. For the IR spectra of nitrobenzene (Figure 2.16, Left), the peak at 1505 cm^{-1} corresponds to C-H bending, the peaks at 1605 and 1630 cm^{-1} correspond to the NH_2 bending absorption of aniline, while the peak at

1530 cm^{-1} corresponds to the NO_2 asymmetric stretch absorption, and the peak at 1350 cm^{-1} corresponds to the NO_2 symmetric stretch absorption of nitrobenzene. The IR spectra of the hydrogenation of ethyl-4-nitrobenzoate were found to be more complicated (Figure 2.16, Right). The peak at 1530 cm^{-1} corresponds to the NO_2 asymmetric stretch absorption of ethyl-4-nitrobenzoate, the peak at 1510 cm^{-1} corresponds to the C-H bending absorption of ethyl-4-hydroxylaminobenzoate, and the peak at 1518 cm^{-1}, which corresponds to the C-H bending absorption of ethyl-4-aminobenzoate, was chosen in a range between 1460 and 1560 cm^{-1}.

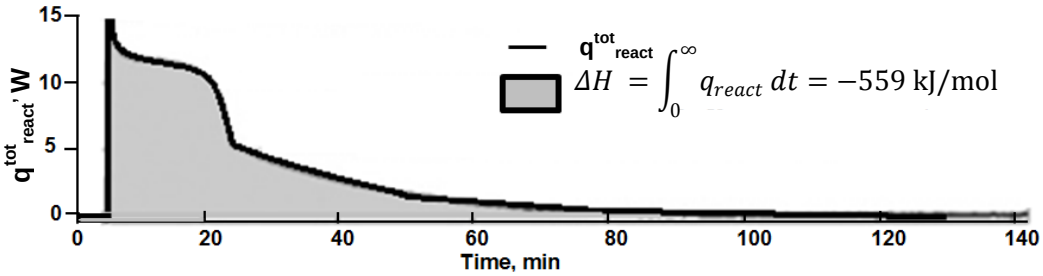

Figure 2.17: Heat flow of the reaction and reaction enthalpy of ethyl-4-nitrobenzoate hydrogenation. "Reprinted with permission from (Visentin, F., Puxty, G., Kut, O. & Hungerbühler, K., *Ind. Eng. Chem. Res*,. 2006, 45 (13), 4544-4553. DOI: 10.1021/ie0509591). Copyright (2006) American Chemical Society."

Figure 2.17 is heat flow diagram generated by reactor software during the hydrogenation of ethyl-4-nitrobenzoate as well as the total reaction enthalpy determined by integration of heat flow. The hydrogenation reaction of nitrobenzene and ethyl-4-nitrobenzoate were both repeated three times. The integration of the q^{tot}_{React} for the reaction of nitrobenzene and ethyl-4-nitrobenzoate gave a total reaction enthalpy of -530 kJ/mol and -559 kJ/mol, respectively.[96]

[1] Leznoff, C. C., Lever, A. B. P., Phthalocyanine. Properties and Applications; Eds.; VCH Publications: New York, 1989; Vol. 1, 1993; Vols. 2 and 3, 1996; Vol. 4.

[2] McKeown, N. B. (1998). Phthalocyanine Materials: Synthesis, Structure and Function. United Kingdom: Cambridge University Press.

[3] Linstead, R.P.; *J. Chem. Soc*., 1934, 1016; (b) Linstead, R.P., Lowe, A.R.; *J. Chem. Soc*., 1934, 1031.; (c) Barrett, P.A.; Frye, A.A.; Linstead, R.P.; *J. Chem. Soc*. 1938, 1157.

[4] (a) Robertson, J.M.; *J. Chem. Soc*., 1935, 615; (b) Robertson, J. M.; *J. Chem. Soc*., 1936, 1195.

[5] Bian, Y., Li, L., Dou, J., Cheng, D.-Y., Li, R., Ma, C.; *Inorg. Chem.*, 2004, 43, 7539.

[6] Woosung, L., Yuk, S. B., Choi, J., Jung, D. H., Choi, S.-H., Park, J.; *Dyes Pigm.*, 2012, 942.

[7] Chambrier, I., Cook, M.J., Wood, P.T.; *Chem. Comm*., 2000, 2133-2134.

[8] Ni, Z., Li, R., Jiang, J.: *Structure and Bonding*,. 2009, 121.

[9] Yannick Rio, M., Rodríguez-Morgade, S., Torres, T.; *Org. & Biomol. Chem*., 2008, 6, 1877.

[10] Wöhrle, D., Schnurpfeil, G., Makarov, S. G., Kazarin, A., & Suvorova, O. N.; *Macroheterocycles*, 2012, 191.

[11] Shuai Zhang, Toshiyuki Abe, Tomokazu Iyoda & Keiji Nagai.; *Molecules*., 2012, 17, 10801.

[12] Georgij, L., Pakhomov Lev., G. Pakhomov Vlad, V., Travkin Mikhail, V., Abanin Pavlo, Y., Stakhira Vladyslav, V.; *J. Mater. Sci*., 2010, 45, 1854–1858.

[13] Bohrer, F. I., Colesniuc, C. M., Park, J., Ruidiaz, M. E., Schuller, I. K., Kummel, A. C., *J. Am. Chem.Soc*., 2009, 131, 479.

[14] Faulkner, E. B., & Schwartz, R. J. (2009). High Performance Pigments. John Wiley & Sons.

[15] Chaure, N.B., Pal, C., Barard, S., Kreouzis, T., Ray, A.K., Cammidge, A.N., Cambrier, I., Cook, M.J., Murphy, E.C., Cainc, M. G.; *J. Mater. Chem*., 2012, 22, 19179.

[16] Yaorong Su, Ming Ouyang, Pengyi Liu, Zhi Luo, Weiguang Xie & Jianbin Xu.; *Appl. Mater. Interfaces*., 2013, 5, 4960.

[17] Chen, P.-Y., Luo, C.-H., Chen, M.-C., Tsai, F.-J., Chang, N.-F., & Shih, Y.; *Int. J. Mol. Sci*,. 2011, 12, 3810.

[18] Kluson, P., Drobek, M., Zsigmond, A., Bata, P., Kalaji, A., Baranji, J.; *Appl. Catal. B*,. 2009, 605.

[19] Sorokin, A.B.; *Chem. Rev*., 2013, 8152.

[20] Murtaza, I., Qazi, I., Karimov, K.S., Sayyad M.H.; *Physica B*., 2011, 406, 1238.

[21] Senthilarasu, S., Velumani, S., Sathyamoorthy, R., Subbarayan, A., Ascencio, J., Canizal, G.; *Appl. Phys. A*., 2003, 383.

[22] Walter, M. G., Rudine, A. B., & Wamser, C. C.; *J. Porphyrins Phthalocyanines*, 2010, 14, 759.

[23] Bonnett, R.; *Chem. Soc. Rev*., 1995, 19.

[24] Chunhui, Xia., Yu, Wang., Wei, Chen., Wenxue, Yu., Baiqi, Wang., and Tao Li,; *Molecules*, 2011, 16, 1389.

[25] Miller, J.D., Elma D. Baron, E.D., Heather Scull, H., Hsia, A., Jeffrey C. Berlin, J.C, McCormick, T., Colussi, V., Kenney, M.E., Cooper, K.D, and Oleinick, N.L.; *Toxicol. Appl. Pharmacol*., 2007, 224, 290.

[26] Jia, X., Yang, F., Li, J., Liu, J.Y., & Xue, J.P.; *J. Med. Chem*., 2013, 56, 5797.

[27] Tuncel, S., Dumoulin, F., Gailer, J., Sooriyaarachchi, M., Atilla, D., Durmus, M.; *J. Chem. Soc., Dalton Trans*., 2011, 40, 4067.

[28] McKeown, N. B., Chambrier, I., & Cook, M. J.; *J. Chem. Soc., Perkin Trans*. 1,. 1990, 1169.

[29] Thompson, J.A., Murata, K., Miller, D.C., Stanton, J.L., Broderick, W.E., Hoffman, B.M., Ibers, J.A.; *Inorg. Chem*., 1993, 32, 3546.

[30] Wöhrle, D., Eskes, M., Shigehara, K., Yamada, A.; *Synthesis*, 1993, 194.

[31] Leznoff, C.C., Hall, T.W.; *Tetrahedron Lett.*, 1982, 112, 9640.

[32] Maya, EM., Haisch P., Vazquez P., Torres T.; *Tetrahedron*, 1998, 54, 4397.

[33] a) Maillard, P., Guerquin-Kern, J.-L. & Momenteau, M.; *J. Am. Chem. Soc*., 1989, 111, 9125; (b) X. Alvarez-Mico, M. J. F. Calvete, Hanack, M. & Ziegler, T.; *Tetrahedron Lett*., 2006, 47, 3283; (c) Ribeiro, A.O., Tome, J. P. C., Neves, M. G. P. M. S., Tome, A.C., Cavaleiro, J.A.S., Iamamoto, Y. &Torres, T.; *Tetrahedron Lett.*, 2006, 47, 9177; (d) Iqbal, Z., Hanack, M., & Ziegler, T.; *Tetrahedron Lett.*, 2009, 50, 873; (e) Choi, C.F., Huang, J.D., Lo, P.C., Fong, W.P., & Ng, D. K. P.; *Org. Biomol. Chem*., 2008, 6, 2173; (f) Liu, J.Y., Lo, P.C., Fong, W. & Ng, D. K. P.; *Org. Biomol. Chem.*, 2009, 7, 1583; (g) Berthold, H. J., Franke, S., Thiem, J., & Schotten, T.; *J.*

Org. Chem., 2010, 75, 3859; (h) Alvarez-Mico, Z., Calvete, M. J. F., Hanack, M., & Ziegler, T.; *Synthesis*, 2007, 14, 2186.

[34] Dumoulina, F., Durmus, M., Ahsena, V., Nyokong, T.; *Coord. Chem. Rev.*, 2010, 254, 2792.

[35] (a) Zorlu, Y., Ermeydan, M. A., Dumoulin, F., Ahsen, V., Savoie H., & Boyle, R.W.; *Photochem. Photobiol. Sci.*, 2009, 8, 312; (b) Boyle, R. W., Leznoff, C. C., & van Lier, J. E.; *Br. J. Cancer*, 1993, 67, 1177.

[36] (a) McKeown, N. B., & Painter, J., *J. Mater. Chem.*, 1994, 4, 1153; (b) Kroon, J. M., Koehorst, R. B. M., von Dijk, M., Sanders, G. M., & Sudhölter, E. J. R.; *J. Mater. Chem*., 1997, 7, 615;(c). Atilla, D., Durmus, M., Gürek, A. G., Ahsen, V., & Nyokong, T.; *Eur. J. Inorg. Chem*., 2007, 3573; (d) Liu, J.-Y., Lo, P.-C., Jiang, X.-J., Fong, W.-P.; & Ng, D. K. P.; *Dalton Trans*., 2009, 4129.

[37] Atilla, D., Saydan, N., Durmus¸ M., Gürek, A. G., Khan, T., Rück, A., Walt, H., Nyokong, T., & Ahsen, V.; *J. Photochem. Photobiol., A*, 2007, 186, 298.

[38] Liu, J.-Y., Jiang, X.-J., Fong, W., & Ng, D. K. P.; *Org. Biomol. Chem.*, 2008, 6, 4560.

[39] Karabork, M., & Serin, S.; *Synth. React. Inorg., Met.-Org., Nano-Met. Chem.*, 2002, 32, 1635.

[40] Lee, S., Vesper, B. J., Zong, H., Hammer, N. D., Elseth, K. M., Barrett, A. G. M., Hoffman, B. M., &.Radosevich, J.A.; *Met.-Based Drugs*, 2008, DOI: 10.1155/2008/391418.

[41] Kandaz, M., Koca, A., & Salih, B.; *Dyes Pigm*., 2007, 74, 483.

[42] Piechocki, C.; Simon, J.; Skoulios, D.; Guillon, D.; Weber, P.; J. Am. Chem. Soc., 1982, 104, 5245.

[43] Swarts, J.C., Langner, E.H., Krokeide-Hoveb, N. & Cook, M.J.; *J. Mater. Chem.*, 2001, 11, 434.

[44] Murray, R. W., & Jeyaraman, R.; *J. Org. Chem.*, 1985, 50, 2847.

[45] Adam, W., Bialas, J. & Hadjiarapoglou, L.; *Chem. Ber.* 1991, 124, 2377.

[46] Hovegeen, H., Middelkoop, TB.; *Tetrahedron Lett.*, 1973, 3671.

[47] Helder, R., Wynberg, H.; *Tetrahedron Lett.*, 1972, 605.

[48] Kotsuki, H., Nishizawa, H.; *Heterocycles*., 1981, 16, 1281.

[49] Kienzle, F.; *Helv. Chim. Acta.*, 1975, 58, 1180.

[50] Snow, A.W., Shirk, J.S., Peebles, L.H. Jr., *in Proceedings to the International Conference on Porphyrins and Phthalocyanines-Symposium Lectures*, Dijon, France, June 25-30, 2000, p. 177.

[51] Hanack, M., Schneider, T., Barthel, M., Shirk, J.S., Flom, S.R., Pong, R.G.S.; *Coord. Chem. Rev.*, 2001, 219/221, 235.

[52] Chen, Y.; Hanack, M.; Blau, W.J.; Dini, D.; Liu, Y.; Bai, J.; *J. Mater. Sci.*, 2006, 41, 2169.

[53] Kissiger, P.T.; Heineman, W.R.; *J. Chem. Educ*., 1983, 60, 290.

[54] Mobbot, G.A.; *J. Chem. Educ.*, 1983, 60, 697.

[55] Gericke, H.J.; Barnard, N.I.; Erasmus, E.; Swarts, J.C.; Cook, M.J.; Aquino, M.A.S.; *Inorg. Chim. Acta,*, 2010, 363, 2222.

[56] Gagne, R.R;, Koval, C.A.; Licensky, G.C.; *Inorg. Chem.*, 1980, 19, 2854.

[57] Nyokong, T., *Polyherdron.*, 1993, 12, 375.

[58] Alexiou, C.; Lever, A. B. P., Coord. Chem. Rev., 2001, 45, 216.

[59] Yilmaz, I.; Guerek, A.; Ahsen, V. *Polyhedron*., 2005, 24, 791.

[60] Louati, A.; El Meray, M.; Andre, J. J.; Simon, J.; Kadish, K. M.; Gross, M.; Giraudeau, A.; *Inorg. Chem.*, 1985, 24, 1175.

[61] Christendat, D.; David, M.-A.; Morin, S.; Lever, A. B. P.; Kadish, K.M.; Shao, J.; *J. Porphyrins Phthalocyanines.*, 2005, 9, 626.

[62] Nyokong, T.; *S. Afr. J. Chem.*, 1995, 48, 23.

[63] Li, R.; Zhang, X..; Zhu, P.; Ng, D.K.P.; Kobayashi, N.; & Jiang, J., *Inorg. Chem*., 2006, 45, 2327.

[64] Cotton, S.; (2012). *Chemistry of Precious Metals*Springer Science & Business Media.

[65] Martynov, A., Gorbunova, Y., & Tsivadz, A.; *Russian J. Inorg. Chem.*, 2014, 59, 1635.

[66] Huang, J., Wong, K., Chan, S., Tso, K., Jiang, T., & Che, C.; *Asian J. Chem*.,2014, 9, 338.

[67] Sievertsen, S., Schlehahn, H., & Homborg, H.; *Zeitschrift für anorganische und allgemeine Chemie Z. anorg. allg. Chem.*, 1993, 619, 1064.

[68] Morandeira, A., Lopez-Duarte, I., O'Regan, B., Martìnez-Dìaz, V., Forneli, A., Palomares, E.; *J. Mater. Chem.*, 2009, 19, 5016.

[69] Rawling, T.; *Coord. Chem. Rev.*, 2007, 251, 1128.

[70] Rawling, T., Xiao, H., Lee, S.T., Colbran, S.B., McDonagh, A.M.; *Inorg. Chem*., 2007, 46, 2805.

[71] Jiménez, A., Grimm, B., Gunderson, V., Vagnini, M., Calderon, S., Rodríguez-Morgade, M.; *Chem. Eur. J*,. 2011 17, 5024.

[72] Manowong, M., Van Caemelbecke, E., Rodríguez-Morgade, M., Bear, J., Kadish, K., & Torres, T.; *J. Porphyrins Phthalocyanines*., 2014, 18, 49.

[73] Dolphin, D., James, B., Murray, A., & Thornback, J.; *Can J. Chem.*, 1980, 58, 1125.

[74] Hanack, M., & Dürr, K..; *J. Porphyrins Phthalocynaines*., 1999, 3, 224.

[75] Lewars, E. G., (2011). *Computational Chemistry: Introduction to the Theory and Applications of Molecular and Quantum Mechanics* (2nd ed.)., New York: Springer.

[76] Young, D., *Computational Chemistry: A Practical Guide for Applying Techniques to Real World Problems.*, 2001, Canada: John Wiley & Sons, Inc., Publication.

[77] Atkins, P., & De Paula, J. (2006). *Atkins' Physical Chemistry* (8th ed.). New York: W. H. Freeman and Company.

[78] Cramer, C., & Truhlar, D.; *Phys. Chem. Chem. Phys*., 2009, 11, 10757.

[79] Te Velde, G., Bickelhaupt, F.M., Baerends. E.J., Guerra, C.F., Van Gisbergen, S.J.A., Snijders, J.G., Ziegler, T.; *J. Comput. Chem.*, 2001, 22, 931.

[80] Jensen, F. (2007). *Introduction to Computational Chemistry* (2nd ed.). England: John Wiley & Sons Ltd.

[81] Ikeda, T., Iino, R., & Noji, H.; *Chem. Commun.*, 2014, 50, 9443.

[82] Cotton, F.A., Wilkinson, G., Gaus, P.L., (1995). *Basic Inorganic Chemistry*, (3rd ed.). New York, John Wiley & Sons Ltd, p. 785.

[83] Atkins, P.W., Overton, T.L., Rourke, J.P., Weller, M.T., Armstrong, F.A., Hageman, M., (2010). *Shriver & Atkins' Inorganic Chemistry*, (5th ed.). Great Britain, Oxford University Press, p179.

[84] Mettler website: http://us.mt.com/us/en/home/products/L1_AutochemProducts/Reaction-Calorimeters-RC1-HFCal.tabs.custom5.html Accessed on 18/08/2015.

[85] RC1$_e$ with RTcal option, Operating Instructions, Mettler Toledo.

[86] Bakker, A., Myers, K., Ward, R., & Lee, C.; *IChemE.*, 1996, 76, 485.

[87] Painmanakul, P., Wachirasak, J., Jamnongwong, M., & Hébrard, G. (2009). *Theoretical Prediction Of Volumetric Mass Transfer Coefficient (kLa) For Designing An Aeration Tank. Engineering*, p. 13.

[88] Frost, W., Moulden, T., & Garner, A. (1977*). Handbook of Turbulence: Fundamentals and Applications* (Vol. 1). New York: Springer US.

[89] Fick, A.; *J. Mem. Sci.*, 1995, 100, 33.

[90] Deimling, A., Karandikar, B.M., Shah, Y.T., and Carr, N.L.; *The Chem. Eng. J*., 1984, 29, 127.

[91] Lemoine, R., Fillion, B., Behkish, A., Smith A.E. and Morsi, B.I.; *Chem. Eng. Proc.*, 2003, 42, 621.

[92] U.P. Fringeli in Internal Reflection Spectroscopy. Marcel Dekker. New York (1992).

[93] Crump, B.R. Goss, C. Lovelace, T. Lewis, R. Peterson, J.; *Org. Process Res. Dev*. 2013, 17, 1277.

[94] Chang, R. (2010). *Chemistry* (10th ed.). New York: McGraw-Hill.

[95] Laidler, K., Meiser, J., & Sanctuary, B. (2003). *Physical Chemistry* (4th ed.). Boston: Houghton Mifflin Company.

[96] Visentin, F., Puxty, G., Kut, O. & Hungerbühler, K.; *Ind. Eng. Chem. Res,*. 2006, 45, 4544.

CHAPTER 3

RESULTS AND DISCUSSION

3.1 Introduction

This chapter consists of a detailed discussion of all experimental results obtained during this study. Firstly, the synthesis and characterization of substituted metal-free phthalocyanines are described, including the synthesis of all precursors utilized during this study. Certain precursors were prepared by making use of an RC1 reactor. Kinetic and thermodynamic studies of the *in situ* formation of the oxidizing agent (dimethyldioxirane) utilized in thiophene oxidation as well as the hydrogenation of 4-nitrophthalonitrile are then presented. Results from a computational chemistry study calculating the enthalpy involved in the oxidation reaction of thiophene derivatives and the hydrogenation of 4-nitrophthalonitrile then compliments the experimental studies done on the RC1 reactor. The chapter concludes with results from a computational and electrochemical study of peripherally and non-peripherally substituted phthalocyanato ruthenium metal complexes, PcRu(CO)(R), with one or two axial ligands.

3.2 Synthesis and characterization of phthalocyanine derivatives

3.2.1 Synthesis of substituted phthalonitriles

As a precursor to the envisaged phthalocyanines of goal 1 of this study (Chapter 1) phthalonitriles are required with substituents containing ethylene glycol as well as alkyl fragments. The synthesis of these substituted phthalonitriles was quite challenging.

3.2.1.1 4-Glycolated phthalonitriles, 1 and 2

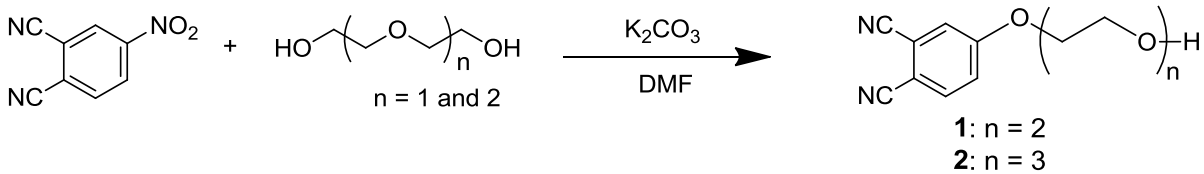

Scheme 3.1: Synthetic route to 4-glycolated phthalonitriles, performed at room temperature (25 °C) for 24 hours under inert atmosphere.

To synthesize a phthalocyanine with a side chain containing ethylene glycol with a hydroxyl functional group, the side chain was introduced into the phthalonitrile structure. This functional group will provide a site for linking the phthalocyanine to suitable compound, e.g. carboxylic acid. The reaction between 4-nitrophthalonitrile and a large excess diethylene or triethylene glycol (2 eq.) was achieved through a base catalyzed reaction in dimethylformaldehyde (DMF) as solvent. For these reactions, potassium carbonate (K_2CO_3) was the chosen base to enhance nucleophilic aromatic displacement.[1] The synthesis progressed successfully, however, separating the product from the excess DMF proved difficult. Due to the high polarity of the products, it could not be isolated through extraction without lowering the yield dramatically. Yields as low as 5% for the desired phthalonitrile products, **1** and **2**, were obtained. Before altering the work-up procedure for this synthesis, a different synthetic pathway was investigated, see section 3.2.1.2.

Ultimately, it was more effective to first; remove the unreacted base by filtering the reaction mixture, followed by removal of the DMF by vacuum distillation, using a strong vacuum pump (< 3 mmHg). This method resulted in yields of 49% for 4-(2-(2-hydroxyethoxy)ethoxy)phthalonitrile, **1**, and 45% for 4-[2-(2-(2-hydroxyethoxy)ethoxy)ethoxy]phthalonitrile, **2**. A unique Ar-OC**H_2** resonance in the ^{1}H NMR spectra of **1** and **2** confirmed successful glycolation (Spectrum A1 and A2: see Appendix A at the end of this thesis). The ether protons closest to the aromatic ring (Ar-OC**H_2**) was observed at 4.25 ppm, compared to 3.95, 3.74 and 3.6 ppm for the free diethylene glycol and 3.84, 3.78 and 3.62 ppm for the free triethylene glycol.

3.2.1.2 Protected 4-glycolated phthalonitrile, 4

As a result of the difficult isolation of the 4-glycolated phthalonitriles, **1** and **2**, described in section 3.2.1.1, another synthetic route was also investigated wherein one of the hydroxyl groups on diethylene glycol was first protected by tetrahydropyranylation. Diethylene glycol and triethylene glycol are inexpensive starting material relative to 4-nitrophthalonitrile. The removal, by protection, of one of the two hydroxyl groups on di- and triethylene glycol, would decrease the polarity of the protected alcohol which should enhance isolation with extraction. It would also prevent side reactions where two 4-nitrolphthalonitrile units may react with one dihydroxy glycolated precursor.

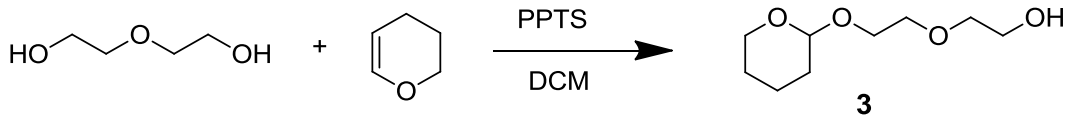

Scheme 3.2: The tetrahydropyranylation of diethylene glycol with 3,4-dihydro-2H-pyran, in the presence of pyridinium *p*-toluenesulfonate (PPTS) as catalyst.

Selective protection of one of the hydroxyl groups on diethylene glycol was performed in dichloromethane (DCM) in the presence of pyridinium *p*-toluenesulfonate (PPTS) as catalyst, as shown in Scheme 3.2, by using a slight excess of glycolated substance over the protecting agent, 3,4-dihydro-2H-pyran. Protection of the diethylene glycol, **3**, was confirmed by ^{1}H NMR spectroscopy (Spectrum A3, Appendix A). The ^{1}H NMR spectra showed the cyclic alkyl protons of the pyran unit at 1.90-1.50 ppm and the first ether protons next to the phthalonitrile ring (Ar-OC**H$_2$**) at 4.65 ppm.

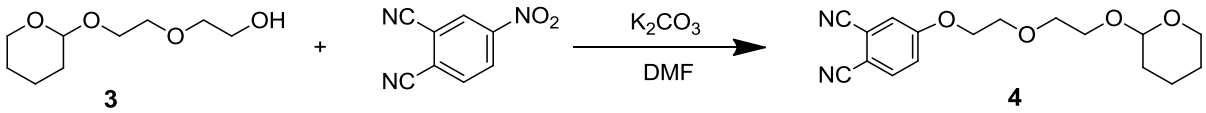

Scheme 3.3: The synthetic route of the protected glycol phthalonitrile formation.

The protected diethylene glycol unit was reacted with 4-nitrophthalonitrile as shown in Scheme 3.3. The reaction conditions were the same as described in section 3.2.1.1 for **1** and **2**, with K_2CO_3 as catalyst and DMF as solvent. The isolation of the product, **4**, was performed through extraction; however the addition of the protection step did not improve yields as hoped. Complex, **4**, was isolated only in 6.6% yield. ^{1}H NMR spectrum confirmed the formation of **4**, 4-(2-(2-((tetrahydro-2H-pyran-2-yl)oxy)ethoxy)ethoxy)phthalonitrile, (Spectrum A4, Appendix A).

3.2.1.3 3,6-Dihexylphthalonitrile, 7

The synthesis of 3,6-dihexyl-substituted phthalonitriles as precursor is shown in Scheme 3.4. This involves a four step synthetic route, starting from thiophene. Thiophene is firstly lithiated and subsequently dihexylated in the 2,5-positions. The hexyl substituted thiophene is then oxidized to the corresponding substituted thiophene-1,1-dioxide. Finally, the substituted

thiophene-1,1-dioxide, is subjected to a Diels-Alder condensation reaction with fumaronitrile to afford 3,6-dihexylphthalonitrile, **7**.

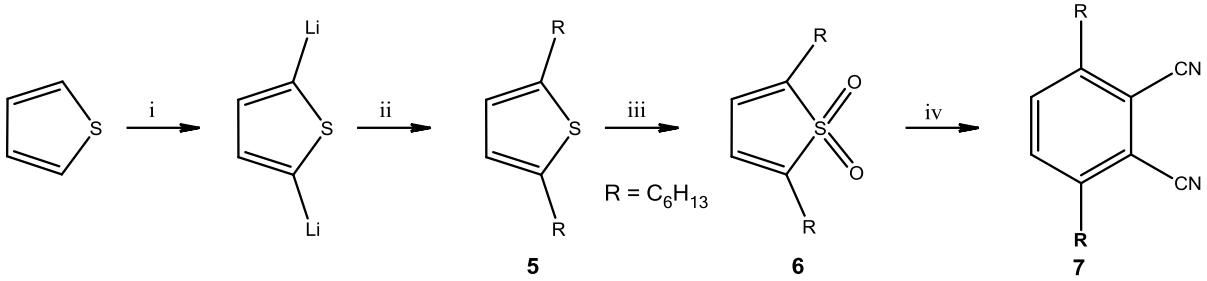

Scheme 3.4: Synthetic route to dialkylated phthalonitrile, Reagents: (i) Reaction with n-BuLi for 24 hours (ii) RBr for 24 hours, where R is a hexyl chain. (iii) Oxidation of dialkylated thiophene with m-CPBA or dimethyldioxirane. (iv) Diels-Alder reaction with fumaronitrile and chloroform at 160 °C, where after spontaneous SO_2 extrusion and dehydrogenation take place.[3]

Lithiation and hexylation of thiophene (Scheme 3.4, step i and ii) are performed without the isolation of the intermediate dilithiated thiophene. The reaction gives 2,5-dihexylthiophene, **5**, in high yields (76%), provided the alkyl bromide is added to the lithiated thiophene at -65 °C. 2,5-Dihexylthiophene, **5**, was obtained as a dark brown oil and was purified by vacuum distillation. The infrared spectrum (Figure 3.1) of **5** showed sharp peaks at 2953 and 1463 cm^{-1} consistent with the presence of the alkyl chain on the thiophene ring. Two characteristic resonances on the ^1H NMR spectrum of **5** (Spectrum A5, Appendix A), are the signals at 6.58 ppm representing two aromatic thiophene protons ($C_4\mathbf{H_2}R_2S$), and a triplet at 0.88 ppm representing the two methyl groups.

The oxidation of 2,5-dihexylthiophene (Scheme 3.4, step iii) was performed with *m*-chloroperoxybenzoic acid (*m*-CPBA) in DCM. After recrystallization from ethanol (EtOH), 2,5-dihexylthiophene-1,1-dioxide, **6**, white neelde-like crystals was obtained in 31% yield. This is a crucial intermediate product in the synthesis of the phthalonitrile, **6**, since it provides the SO_2 which is a good leaving group in the ensuing Diels Alder reaction. The formation of 2,5-dihexylthiophene-1,1-dioxide, **6**, was also performed under different reaction conditions utilizing a RC1 reactor that will be discussed in section 3.3.3. The presence of the SO_2-group was confirmed by infrared (Figure 3.1), which showed two S=O stretching frequencies at 1275 and 1140 cm^{-1}. The chemical shifts of the non-aromatic thiophene-1,1-dioxide resonating protons ($C_4\mathbf{H_2}R_2SO_2$) in the ^1H NMR (spectrum A6, Appendix A) of 2,5-dihexylthiophene-1,1-dioxide are at 6.28 ppm, 0.3 ppm more upfield than that of the 2,5-

dihexylthiophene precursor (see Spectrum A5, Appendix A). The upfield shift is due to the charge from aromaticity of **5**, compared to non-aromaticity of **6**.

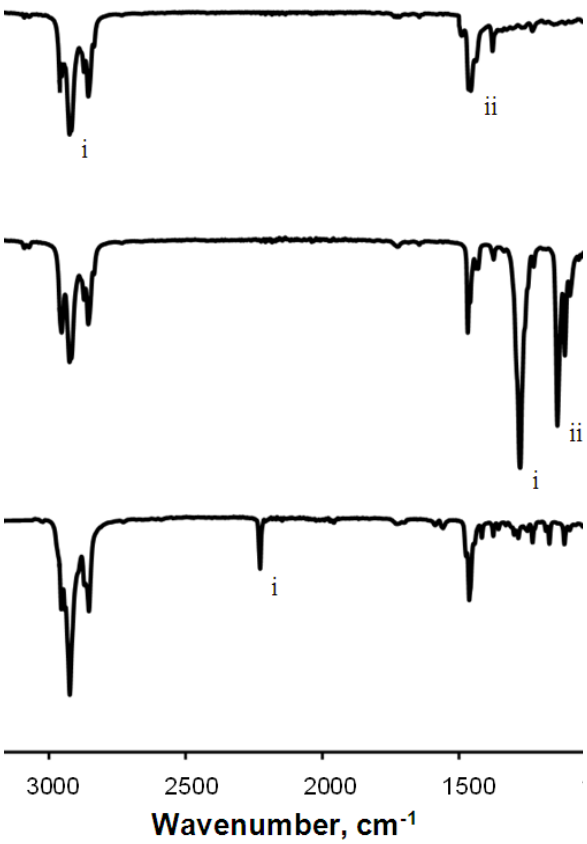

IR assignments (cm^{-1})

2,5-dihexylthiophene, **5**

i) 2953 (C-H)

ii) 1463 (CH_3)

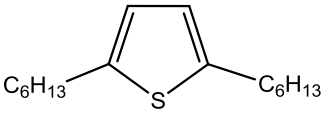

2,5-dihexylthiophene-1,1-dioxide, **6**

i) 1275 ($-SO_2$)

ii) 1140 ($-SO_2$)

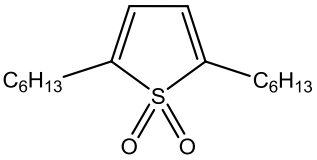

3,6-dihexylphthalonitrile, **7**

i) 2228 (C≡N)

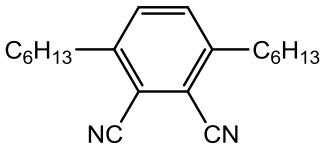

Figure 3.1: Infrared spectra for all compounds obtained during the synthesis is of 3,6-dihexylphthalonitrile.

The Diels-Alder condensation (Scheme 3.4, step iv) between fumaronitrile and 2,5-dihexylthiophene-1,1-dioxide, **6**, proceed in a sealed tube over 16 hours at 160 °C, in the presence of a minimal amount of chloroform[i]. This leads to the spontaneous elimination of SO_2 and hydrogen. 3,6-Dihexylphthalonitrile, **7**, was obtained in 21.6% yield. The formation of the benzene ring during the Diels-Alder condensation resulted in the downfield shift to 7.47 ppm of the aromatic protons signals in the ^{1}H NMR (Spectrum A7, Appendix A). An infrared signal with a stretching frequency of 2228 cm^{-1} (Figure 3.1) confirmed the presence of the nitrile groups (C≡N) for **7**.

[i] A minimum amount of chloroform (between 1.0 and 1.5 cm^3), the amount needed to wash the reactants through the nozzle of the tube, is necessary since larger quantities reduces the yield of the desired phthalonitrile dramatically.

3.2.2 Synthesis of substituted metal-free phthalocyanine

After the synthesis of the, 4-(2-(2-hydroxyethoxy)ethoxy)-, 4-[2-(2-(2-hydroxyethoxy)ethoxy)ethoxy]phthalonitriles and 3,6-dihexyl-, **1**, **2** and **7**, respectively, attention was focused on phthalocyanine synthesis. Two types of phthalocyanines were targeted for synthesis during this study:

a. The first consisted of symmetrically non-peripheral octahexyl substituted and symmetrically peripheral tetra-ethylene glycol substituted phthalocyanines.
b. The second consisted of asymmetrically dihexyl- hydroxyethoxy substituted phthalocyanine, whereby 2-(2-hydroxyethoxy)ethoxy or 2-(2-(2-hydroxyethoxy)ethoxy)ethoxy groups on the peripheral position via statistical condensation between two different phthalonitriles took the place of two hexyl chains on the non-peripheral positions.

3.2.2.1 1,4,8,11,15,18,22,25-Octahexylphthalocyanine, 8

To obtain 1,4,8,11,15,18,22,25-octahexylphthalocyanine, **8**, 3,6-dihexylphthalonitrile, **7**, was refluxed for 16 hours in 1-pentanol under inert atmosphere in the presence of a small excess of lithium metal (5 eq), Scheme 3.5. The lithium metal aids the cyclotetramerization of the phthalonitrile into a dilithium phthalocyanine. The dilithium phthalocyanine intermediate was then converted into the metal-free derivative through acid work-up, yielding **8** as a dark green solid in a yield of 10%.

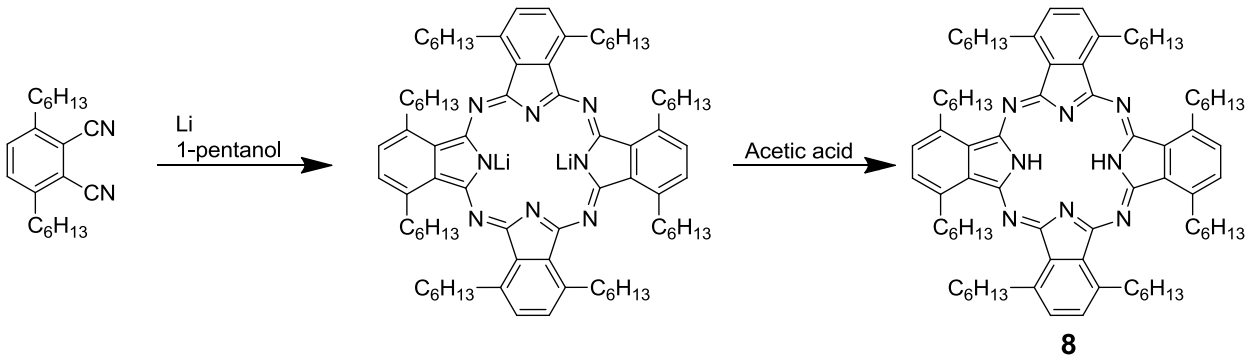

Scheme 3.5: Synthesis of 1,4,8,11,15,18,22,25-Octahexylphthalocyanine, **8**.

The ^{1}H NMR spectrum of **8** (Spectrum A8, Appendix A) showed the ring-based aromatic protons resonate at 7.89 ppm, 0.42 ppm downfield from the aromatic proton resonance position of the phthalonitrile precursor, **7**. In addition the benzylic protons of 3,6-dihexylphthalonitrile resonate at 2.86 ppm, while the equivalent protons of the phthalocyanine **8** resonate at 4.47 ppm, this is 1.61 ppm more downfield for the phthalocyanine complex. The larger size of the aromatic ring is considered to be the reason for this dramatic shift as it will distort the magnetic field of the NMR to a greater extent than the phthalonitrile precursor.

The disappearance of the IR stretching peak for the nitrile groups of **7** at 2228 cm^{-1} and the appearance of a peak at ~3300 cm^{-1} (Spectrum B1, Appendix B) due to the presence of the cavity protons (N-H) of **8** also diagnostically confirms the phthalonitrile, **7**, to the metal-free phthalocyanine, **8**, conversion. The UV-Vis spectrum, Figure 3.2, of **8** in tetrahydrofuran (THF) showed two strong characteristic Q-band absorption peaks of metal-free phthalocyanines in the Q-band region at Q_y = 697 and Q_x = 728 nm. The Soret band was observed as a broad peak with λ_{max} at 356 nm.

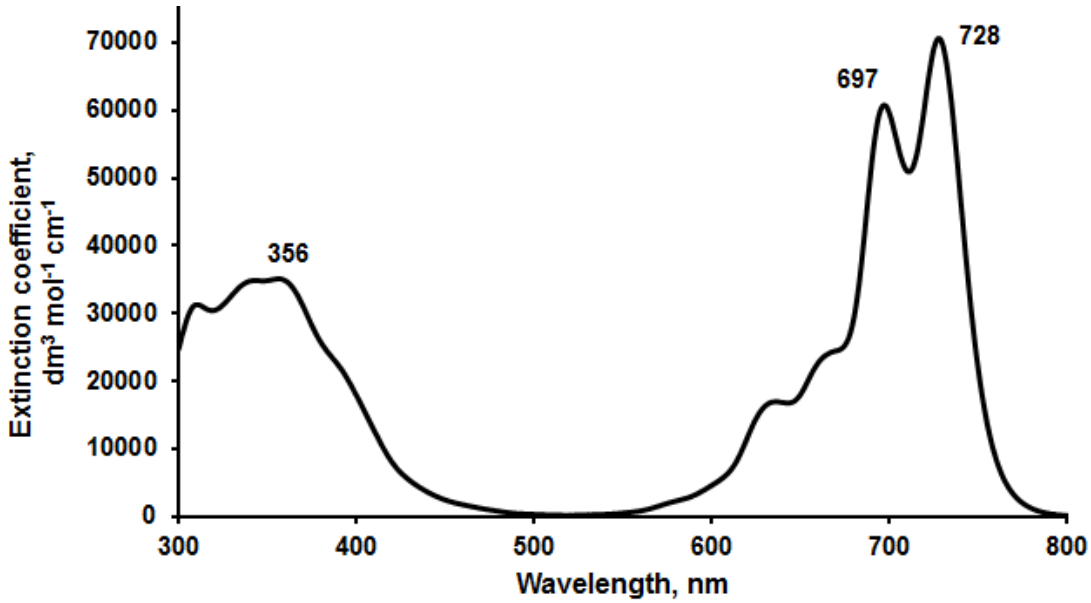

Figure 3.2: UV-Vis spectrum of 1,4,8,11,15,18,22,25-Octahexylphthalocyanine, **8**, in THF.

3.2.2.2 Tetra-ethylene glycolated phthalocyanines

To obtain 2,9,16,23-tetra[2-(2-hydroxyethoxy)ethoxy]phthalocyanine, [ii] **9** and 2,9,16,23-tetra[2-(2-(2-hydroxyethoxy)ethoxy)ethoxy]phthalocyanine,[ii] **10**, the respective phthalonitriles, 4-[2-(2-hydroxyethoxy)ethoxy]phthalonitrile, **1**, and 4-[2-(2-(2-hydroxyethoxy)ethoxy)ethoxy]phthalonitrile, **2**, were placed in a sealed glass tube with hydroquinone and kept at 160 °C for 22 hours. Hydroquinone acts as a solvent as well as a reducing agent, which aids in the cyclotetramerization of the 4-substituted phthalonitrile into metal-free phthalocyanine.[2]

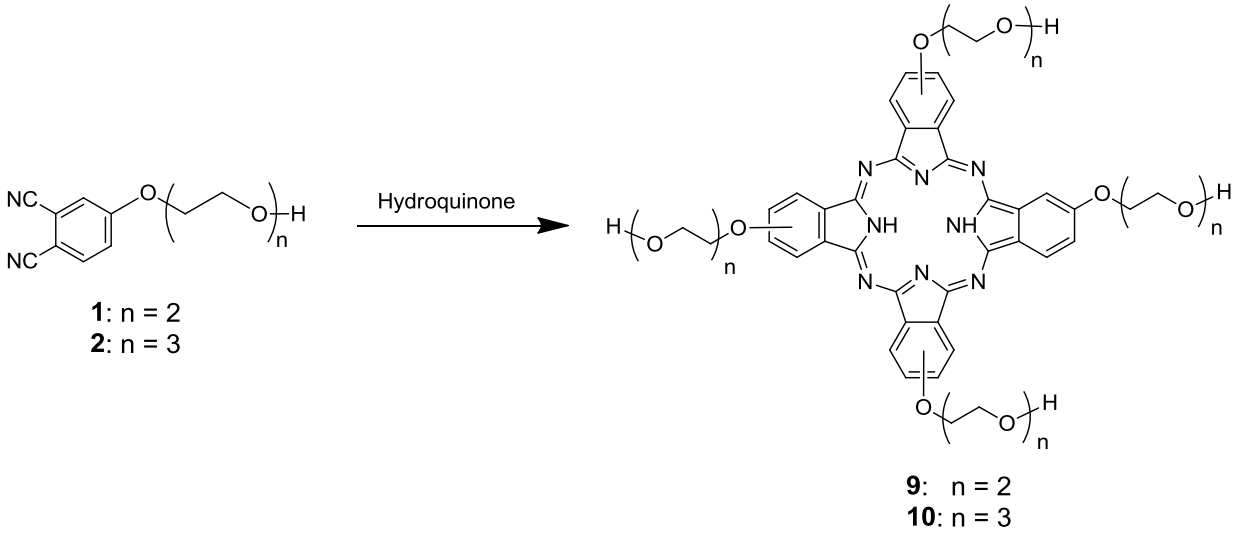

Scheme 3.6: Synthesis of ethylene glycol containing metal-free phthalocyanines, **9** and **10**, tetra[2-(2-hydroxyethoxy)ethoxy]phthalocyanine and tetra[2-(2-(2-hydroxyethoxy)ethoxy)ethoxy]phthalocyanine, respectively.

The reaction mixture containing compound **9** was washed with EtOH to remove all side products as well as residual hydroquinone and quinone. 2,9,16,23-tetra[2-(2-hydroxyethoxy)ethoxy]phthalocyanine, **9**, was then recrystallized from a mixture of hot methanol (MeOH) and triethylamine (NEt_3) (1% of amine) by precipitating it with diluted HCl (3% in H_2O) and slowly cooling down the mixture. Compound **10** containing the shorter ethylene glycol chain was isolated by precipitation from hot EtOH as a blue-green powder. Compounds **9** and **10** are tetra-substituted phthalocyanines which contain mixtures of four positional isomers; isolation of these isomers proved impossible. Although the ethylene

[ii] Although it is recognized that cyclization of the phthalonitriles in Scheme 3.6 will give a multitude of isomers (5), for writing simplicity the numbering assignment for **9** and **10**, in this thesis will continuously be 2,9,16,23, see Chapter 2, Section 2.2 for numbering system.

glycol fragment[2] can confer water-solubility to some compounds, these phthalocyanines, **9** and **10**, however are not water-soluble, but they are highly soluble in aprotic polar solvents like DMF and dimethyl sulfoxide (DMSO).

The ^{1}H NMR spectrum of **9** and **10** (Spectra A9 and A10, respectively in Appendix A) showed the ring-based aromatic protons resonate at 7.54-6.64 and 7.59-7.49 ppm and the ether protons bonded to the aromatic ring was observed resonating at 3.57-3.20 and 3.21-2.8 ppm. The IR transmission peaks for compounds **9** and **10** (Spectra B2 and B3, respectively in Appendix B) with stretching frequencies at 3290 and 3202 cm^{-1} correspond to the cavity protons (N-H), those at 2927 and 2938 cm^{-1} are associated with the aromatic protons and those at 2871 and 2866 cm^{-1} belong to the C-H stretches. The broad transmission peak observed between 3200 and 3300 cm^{-1} were assigned to the OH-bond. The UV-Vis spectra, Figure 3.3, of **9** and **10** in DMSO showed two strong absorption peaks in the Q-band region at Q_y = 676; 673 nm and Q_x = 705, 706 nm, respectively. The broad Soret band for **9** and **10** was observed at 337 and 334 nm.

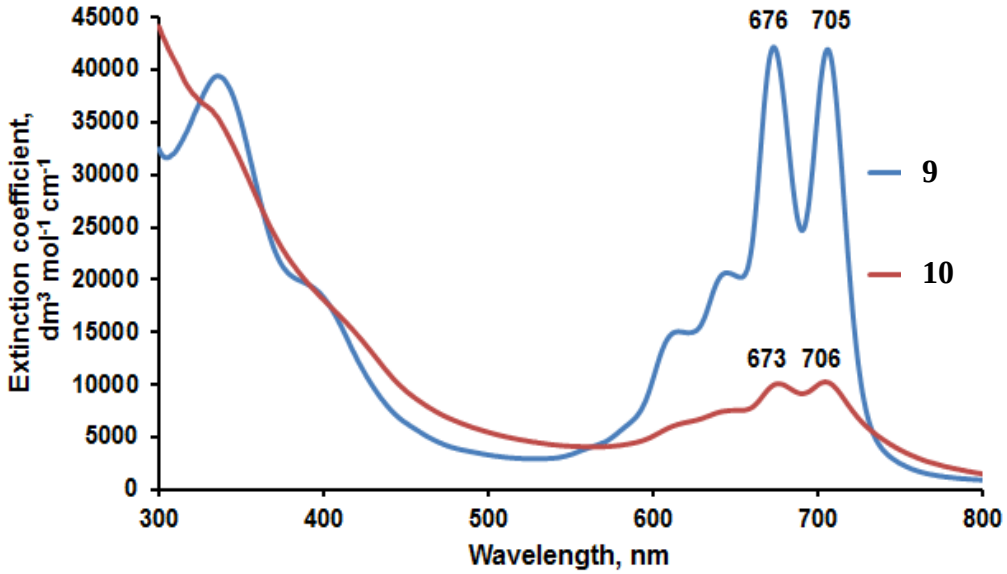

Figure 3.3: UV-Vis absorption spectra of a 10 µM solution of the symmetrically substituted metal-free phthalocyanines, **9** and **10**, in DMSO showing the increased extinction coefficient of **9** compared to **10** ($\varepsilon_{max706,\,\mathbf{9}}$ = 10 111; $\varepsilon_{max705,\,\mathbf{10}}$ = 42.171).

The UV-vis spectra are in agreement with results for similar ethylene glycolated metal-free phthalocyanines, 2,9,16,23-tetra(2-hydroxyethoxy)phthalocyanine and 2,9,16,23-tetra{2-[2-(2-(2-hydroxyethoxy)ethoxy)ethoxy]ethoxy}phthalocyanine, found in literature, where two strong absorption peaks are observed in the Q-band region.[2] From these results it can be

concluded that the position of the Q-band value (Q_y and Q_x) decreases as the ethylene glycol chains increases, see Table 3.1.

Table 3.1: UV/vis data comparison of the synthesized compounds, **9** and **10**, to other data for similar compounds found in literature.[2]

Compounds with	Band Q_y	Band Q_x
a: ethylene glycol units[2]	681[e]	710[e]
b: diethylene glycol units	676	705
c: triethylene glycol units	673	706
d: tetraethylene glycol units[2]	611[e]	681[e]

a: 2,9,16,23-tetra(2-hydroxyethoxy)phthalocyanine containing four ethylene glycol units from literature, reference 2.
b: 2,9,16,23-tetra[2-(2-hydroxyethoxy)ethoxy]phthalocyanine, 9, containing four diethylene glycol units
c: 2,9,16,23-tetra[2-(2-(2-hydroxyethoxy)ethoxy)ethoxy]phthalocyanine, 10, containing four triethylene glycol units
d: 2,9,16,23-tetra{2-[2-(2-(2-hydroxyethoxy)ethoxy)ethoxy]ethoxy}phthalocyaninecontaining four tetraethylene glycol units from literature, reference 2.
e: Data from literature as found in reference 2.

3.2.2.3 Asymmetrically substituted phthalocyanines, 11 and 12

Statistical condensation, in an 1:1 ratio, of 3,6-dihexylphthalonitrile, **7**, with either ethylene glycol containing phthalonitriles, **1**, or **2** was performed in 1-pentanol in the presence of lithium metal (22 eq.) under inert condition for 20 hours. The reaction mixture was allowed to cool down before the addition of acetone and DCM followed by MeOH to rinse off all solid residues. The acetic acid work-up[3] usually used to remove the lithium from the macrocycle to yield metal-free phthalocyanines, should not be followed for these phthalocyanines because it can initiate decomposition of the ether bonds in the ethylene glycol chains attached to the phthalocyanine rings.

During this procedure (Scheme 3.7) statistical mixtures of products (AAAA, AAAB, ABABA, ABBA, and BBBB as discussed in Chapter 2 (section 2.5)) were formed. Only the target compound AABB and ABAB were isolated. The A_2B_2 phthalocyanines are mixtures of five positional isomers because of the mono-substituted phthalonitriles, showed as **B** in Scheme 3.7.

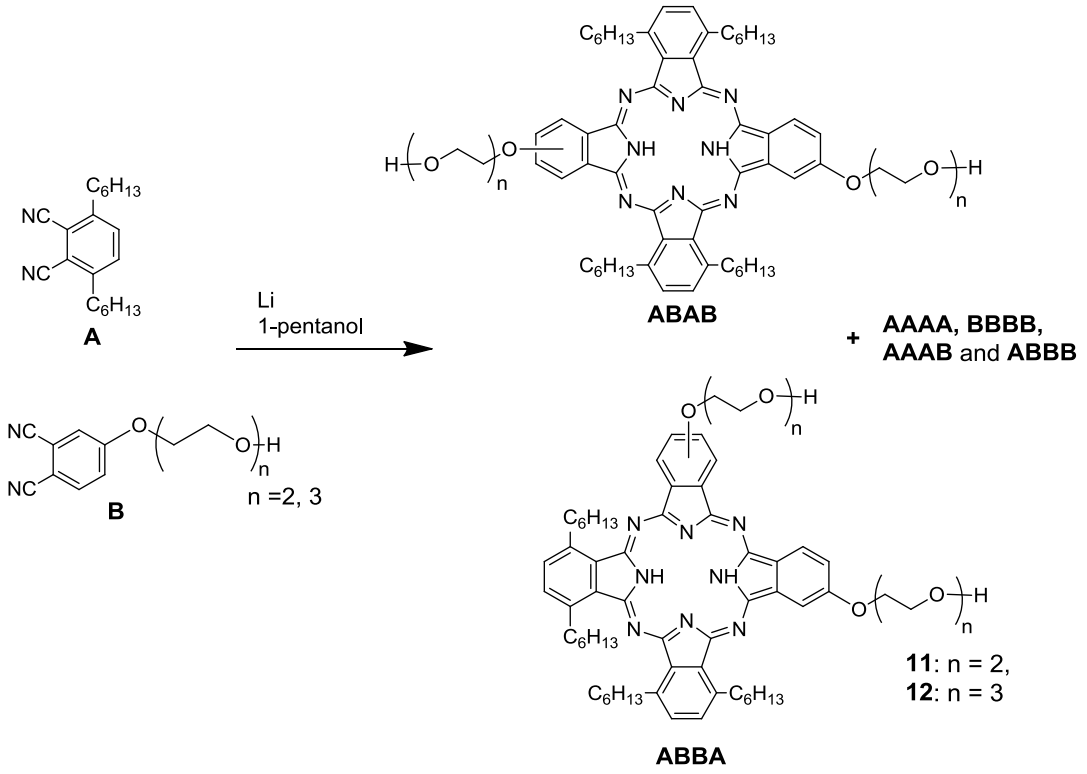

Scheme 3.7: Synthetic route to the desired tetrahexyl-di-[2-(2-hydroxyethoxy)ethoxy]-phthalocyanine, **11**, and tetrahexyl-di-{2-[2-(2-hydroxyethoxy)-ethoxy]-ethoxy}-phthalocyanine, **12**.

The AABB and ABAB structural isomeric phthalocyanines for **11** and 1**2**, were isolated by using preparative silica (SiO_2) TLC, with DCM, MeOH and NEt_3 as eluents. Triethylamine was used to decrease the phthalocyanines ability to bound to the silica. It was also found that the A_2B_2 phthalocyanines were not stable once loaded on SiO_2 or when kept in solution. To minimize the decomposition, the chamber (in which the preparative TLC plates were placed) was purged with inert gas prior to elution as well as kept away from direct light. Although NEt_3 decreased the binding of the phthalocyanines to the SiO_2, some difficulty was still experienced removing all phthalocyanines from the SiO_2. It was found that washing the phthalocyanine SiO_2 with DCM and MeOH, interchangeably, resulted in the removal of almost all phthalocyanines from the SiO_2 while filtering.

The ^{1}H NMR spectrum of **11** and **12** (Spectra A11 and A12, respectively in Appendix A) showed the ring-based aromatic protons resonate at between 7.5 ppm and the ether protons bonded to the aromatic ring was observed at 4.5-3.75 ppm and alkyl protons at 2.25-0.9 and the cavity protons (N-H) of **11** at -1.38 and -1.84 ppm for **12**. The IR transmission peaks for compounds **11** and **12** (Spectra B4 and B5, respectively in Appendix B) with stretching frequencies at 3281 and 3282 cm^{-1} correspond to the cavity protons (N-H), those at 2955 and

2953 cm^{-1} associated with the aromatic protons and those at 2918 and 2919 cm^{-1} belong to the C-H stretches. The UV-Vis spectrum, Figure 3.4, of **12**, $H_2Pc[(-(OCH_2CH_2)_2OH)_2(C_6H_{13})_4]$ in THF showed two strong absorption peaks in the Q-band region at Q_y = 684 and Q_x = 717 nm, while for **11** Q_y = 684 and Q_x = 718 nm. The Soret band for **11** and **12** was observed as a broad peak with λ_{max} at 341 and 331 nm, respectively.

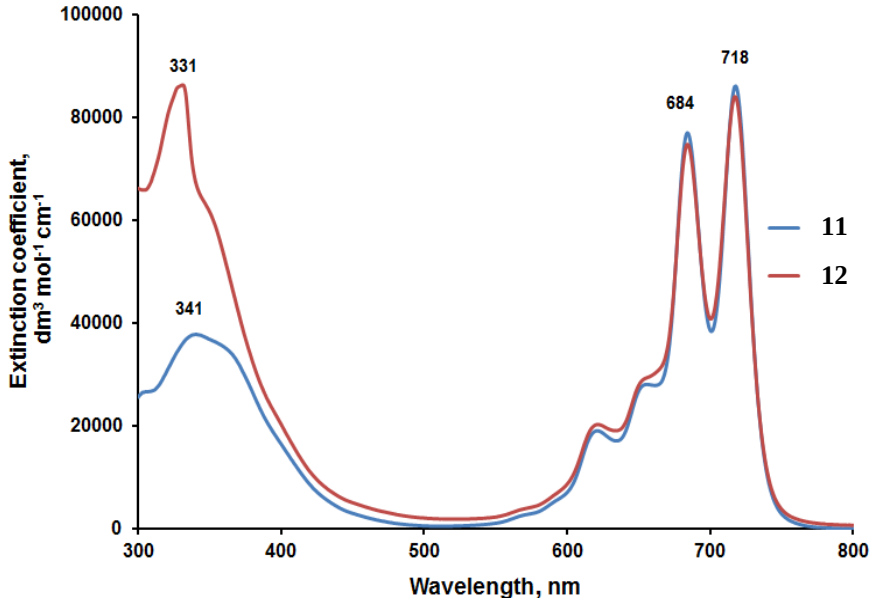

Figure 3.4: UV-Vis absorption spectra of the 6 µM asymmetrically substituted metal-free phthalocyanines, **11** and **12**, in THF ($\varepsilon_{max718,\ \mathbf{11}}$ =86 871; $\varepsilon_{max717,\ \mathbf{12}}$ = 82 955).

To conclude Section 3.2 (Synthesis and characterization of phthalocyanine derivatives), in order for compounds to be suitable for photodynamic therapy (PDT), the compounds should have hydrophilic properties. Unsubstituted phthalocyanines are insoluble compounds, but the solubility can be improved by synthesizing phthalocyanines with substituents on the peripheral and non-peripheral position. In this study, the addition of hexyl and glycol chains peripheral and non-peripheral position on the macrocycle, decreased aggregation dramatically, which led to these compounds being highly soluble in aprotic polar solvents like DMF and DMSO. Metal insertion of Zn or Al will be ideally suited for PDT, although metals like Ru and Co will lead to catalytic applications.

3.3 RC1 synthesis

3.3.1 General

The RC1 reactor (designed for synthesis and calometric control during synthesis) provides excellent temperature, pressure, stirring speed and other experimental parameter control.

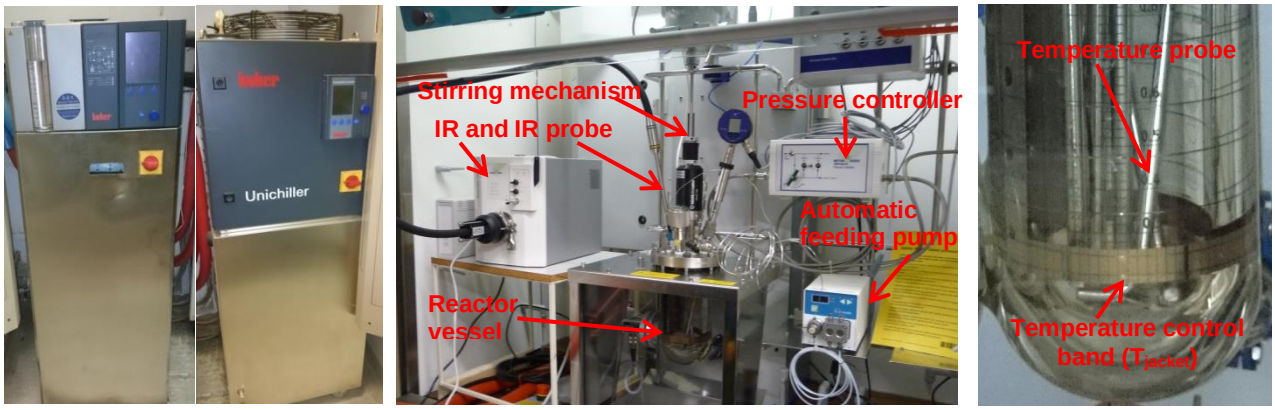

Figure 3.5: **Left:** Extreme cooling/heating facility that enables real-time calorimetric (temperature) measurements. **Middle:** The RC1 reactor with some of its attachments. **Right:** A close-up of the reactor vessel showing the temperature control band (copper-coloured metal band) and temperature probe (internal).

The temperature control and measuring system consists of a measuring probe inside the reactor to measure $T_{reaction}$ as well as a band to measure the temperature of the jacket, T_{jacket} around the reactor vessel. By comparing these two temperatures, and with the capability of keeping the temperature of the either jacket or the reaction mixture constant even for highly exothermic or endothermic reactions, one can determine heat of reactions, q, in real time. It is possible to convert q to ΔH by the determination of the area under a graph of q vs. time. This area is the reaction enthalpy, ΔH, for the quantities inside the reaction vessel. The simultaneous measurement of IR absorbances (in absorbance transmittance or reflective mode) with time, leads to data can be used for kinetic purposes.

By performing reaction synthesis in this apparatus, it enables better control over these reaction conditions. Reaction temperatures are controlled to within 0.1 °C, even when dealing with highly exothermic (or endothermic) reactions. Thus, real time calorimetric data is one set of reaction results that may be obtained for all reactions. Stirring of viscous

reaction mixtures is also possible and highly controllable. By combining the RC1 reactor with the *in situ* iCIR, (*intelligent* Control Infra Red sampling system for the RC1 reactor) it is possible to follow the reaction under non-ideal, experimental conditions kinetically by IR, which allows the simultaneous thermodynamic and kinetic studies for all reactions.

All rate constants for the kinetic studies in this study were determined under pseudo first conditions, utilizing the first order kinetic rate law:

$$A_{obs} = A_1 - (A_1 - A_0)(exp^{-k_{obs}.t})$$

Equation 3.1

For Equation 3.1, A_0 is the initial absorbance, A_1 is the final absorbance, A_{obs} is the measured absorbance at specific time, t is time, and k_{obs} is the observed experimental pseudo first order rate constant. In the RC1 part of the present research program:

a. synthetic reactions were performed under optimised reactor conditions,
b. where possible kinetic and calorimetric data (especially rate constants, ΔH-values and activation energies) were collected from it, and
c. calorimetric values were compared with theoretical DFT-calculated values.

3.3.2 Determination of Mass Transfer coefficient, k_La

Before the RC1 reactor can be used optimally with reactions in which one reactant component is a gas, it is necessary to determine the optimum condition of gas dissolution and dispersion through the reaction mixture as a function of stirring speed at the reaction temperature. To establish this, determination of the mass transfer coefficient, k_La, is required.

The mass transfer coefficient, k_La is used to quantify how well a gas is distributed through a solution in the reactor. In order to determine the mass transfer coefficient during a reaction in the RC1 reactor, the dispersion of nitrogen in toluene and THF was studied at stirring speeds, 600, 700 and 800 rpm. During these experiments, the amount of solvent was kept constant at 700 cm^3 (the reactor vessel has a capacity of 1 200 cm^3). Some experiments were repeated on the presence of a baffle. A baffle is an obstruction in the reactor vessel that prevents vortexes in the reacting solution and ensures efficient mixing during stirring. Data sampling takes place every 2 seconds by the RC1 reactor. Figure 3.6 shows the nitrogen pressure

decrease in the reactor vessel above the solvent over time for THF and toluene, as the solvent becomes saturated by the nitrogen gas. Both THF and toluene slowly absorbed the nitrogen gas at 600 rpm, but the rate of N_2 absorption increased as the stirring rate increased.

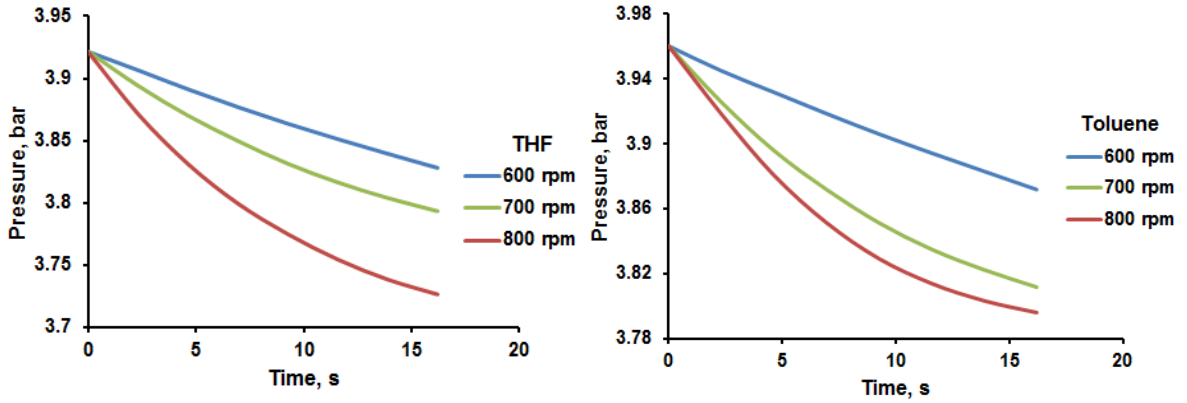

Figure 3.6: Pressure versus time graphs for the absorption of N_2 by THF **(Left)** and Toluene **(Right)** in a sealed vessel.

In Figure 3.7 it is shown that that at 800 rpm, toluene has a higher rate of absorption than THF. The apparent end of the gas absorption process ("apparent" because it is a dynamic process, and at equilibrium the rate of absorption and desorption is equal) is denoted by a constant pressure in the dead volume above the solvent after a specific time. THF absorbed more gas than toluene as shown in Figure 3.7, but toluene is much closer to the asymptotic infinite value of absorption after 14 seconds.

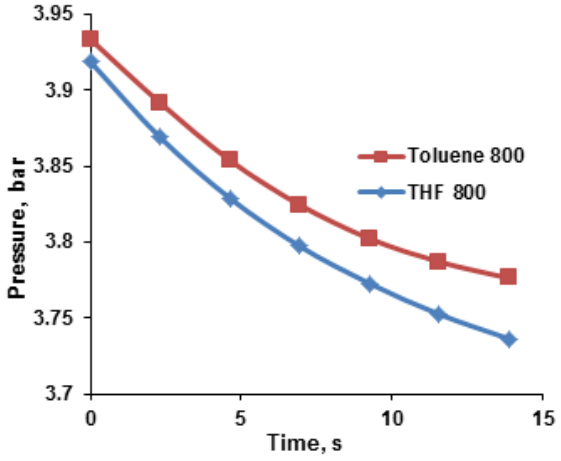

Figure 3.7: Comparison of saturation by THF and Toluene at 800 rpm and 25 °C.

By monitoring the rate of absorption of a gas into a solvent, in this case THF and toluene, it is possible to determine k_La-values. The absorption rate is monitored by measuring pressure

differences with time in the dead volume of the reactor above the solvent in a sealed reactor. The k_La-values for THF and toluene in this study were obtained by fitting measured real time RC1 P(pressure) - t(time) data to equation 3.1. The volumetric mass transfer coefficient (k_La) constants so obtained are summarized in Table 3.2.

Table 3.2: Summary of the k_La-values for N_2 in toluene and THF.

Stirring Speed (rpm)	k_La (s^{-1}) for toluene (density 0.867 g/mol; viscosity 0.586 cP)	k_La (s^{-1}) for THF (density 0.8892 g/mol; viscosity 0.48 cP)
600	0.0261(8)	0.0233(3)
600 (Equipped with Baffle)	-	0.075(2)
700	0.106(3)	0.0733(5)
800	0.13(1)	0.100(1)

For both solvents, the mass transfer coefficient varies logarithmically with stirring speed within the utilized stirring speed region, Figure 3.8. From the data it is clear that toluene has a near optimal k_La value at a stirring speed of 800 rpm, but in THF at 800 rpm stirring speed the k_La value is still far from the infinite value. From Figure 3.8, *left*, THF will have the same k_La value as toluene approaching the asymptotic value of 0.135 s^{-1} at a stirring speed of *ca*. 1000 rpm.

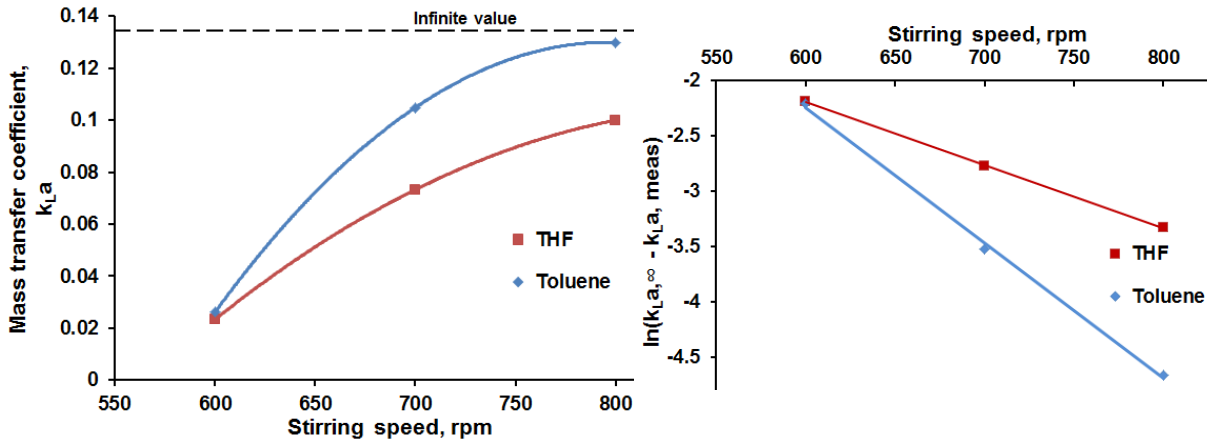

Figure 3.8: Left: k_La values versus stirrer speed for toluene and THF. **Right:** the logarithmic relationship between k_La and stirring speed.

Other factors influencing the gas uptake of solvents were also investigated, on THF only as a model system; one of these factors was the addition of a baffle to the reaction vessel. The baffle is expected to increase the mass transfer coefficient (k_La), by changing the flow in the reactor from laminar to turbulent flow. Figure 3.9 highlights the increased uptake in N_2 gas by the THF in the presence of a baffle. It should be noted that that uptake of N_2 gas by

toluene in the presence of a baffle was so rapid; it could not be tracked by the instrument. From Table 3.2 the baffle increased k_La slightly more than three-fold compared to the value in the absence of a baffle.

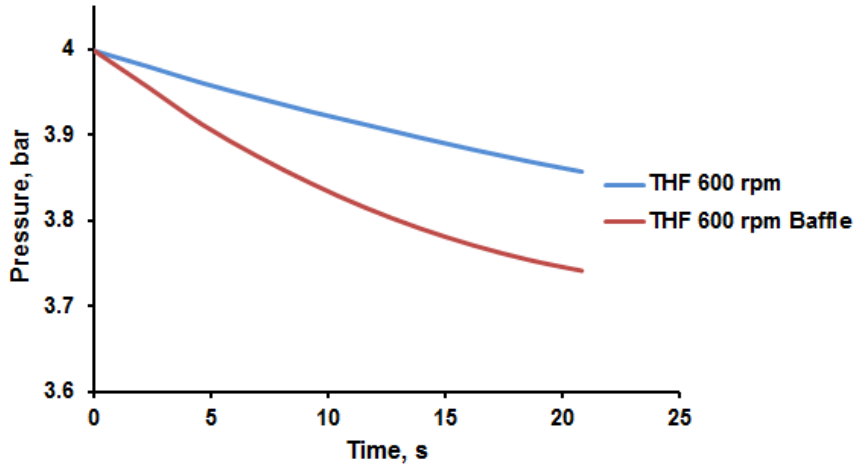

Figure 3.9: Comparison of N_2 gas absorption by THF at 600 rpm with and without a baffle added to the reaction vessel.

The results described above indicate that, given sufficient time, e.g. 200 seconds, all (or at least most of) the gasses above the liquid reaction medium will have reached dynamic gas-solvent exchange equilibrium expressed as the infinite k_La value. Most reactions take place over much longer time scales than these 200 seconds required for dynamic equilibrium. This implies also that one does not have to "drive" the rotating mechanism of the reactor to high (e.g. 1000 rpm) values. It will be "softer" on the instrument to rotate at slower (600 rpm) stirring speeds and just allow slightly longer times to obtain k_La(infinite).

Determination of k_La and the factors that influence it should ideally be performed at the start of every reactor study, not only for RC1. Kinetic and thermal characterization can be performed under the experimental conditions of RC1 experiments. Variables influencing k_La include stirrer speed, stirrer type, baffling, temperature etc.; all need to be considered, especially in cases where gases acts as reactants in the reaction being studied (e.g. hydrogenation of alkenes).

3.3.3 Synthesis performed on the RC1 reactor

3.3.3.1 Oxidation of thiophene derivatives

Dimethyldioxirane (bp = 8 ^{o}C) was utilized for the oxidation of 2,5-dihexylthiophene, **5**, and 2,5-didodecylthiophene, **13**, in an RC1 reactor on synthetic scale. The reaction is given in Scheme 3.8.

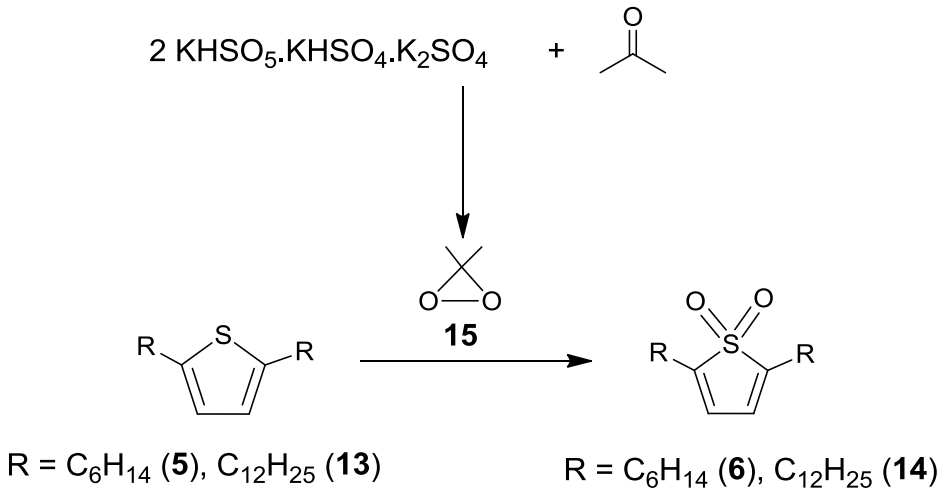

Scheme 3.8: Dimethyldioxirane, **15**, was utilized for the oxidation of thiophene derivatives, **5** and **13**.

Dimethyldioxirane was generated *in situ*, by reacting acetone with Oxone® ($2KHSO_5.KHSO_4.K_2SO_4$ a Aldrich product) at either 0 or 5 °C, in the presence of $NaHCO_3$ in the heterogeneous mixed-solvent system of water: DCM = 1.25: 1 by volume. The order of addition in which acetone and Oxone® was added to the solvent system was investigated. It was found that by adding the acetone last, better yields are obtained. Different experiments showed that by adding acetone to Oxone® and not visa versa, yields of **6** increased from 22 to 87%. It also allowed better resolution between calorimetric measurements for the different reaction steps. After dimethyldioxirane has formed (as indicated by heat flow and IR measurements which will be discussed later), 2,5-dihexylthiophene, **5**, or 2,5-didodecylthiophene, **13**, was added to the reaction vessel. The reaction mixture was stirred (different experiments used different stirring speeds: 500, 700 or 1000 rpm in the presence of a baffle) continuously for the duration of the reaction. After 6 to 24 h, yields of up to 87% were obtained for **6** and **14**. Reactions that were terminated after 6 hours gave 52% yield of **6** but 83 to 87% yield after 18 – 24 hours. For the C_{12} compound, **14**, yields increased from 66

to 85% when the reaction time increased from 18 to 24 hours. Because a dynamic equilibrium of evaporated dimethyldioxirane being re-absorbed by the H_2O-DCM solvent reaction mixture is setting in quickly, stirring speeds between 500 and 1000 rpm does not influence yields noticeably. In the workup, the crude products were recrystallized from ethanol to provide white needle-like crystals for both **6** and **14**. Spectroscopic and other characterisation data are as discussed in section 3.2.1.3 and summarized in the experimental section (Chapter 4).

In section 3.2.1.3, utilizing *m*-chloroperoxybenzoic acid (*m*-CPBA) as oxidant and traditional round-bottom flasks yields were much lower (32%).

3.3.3.2 Reduction of 4-nitrophthalonitrile

The RC1 reactor was also utilized to synthesise 4-aminophthalonitrile, **17**, by reducing 4-nitrophthalonitrile, **16**, in methanol with H_2 gas over 10% Pd/C as indicated by Scheme 3.9.

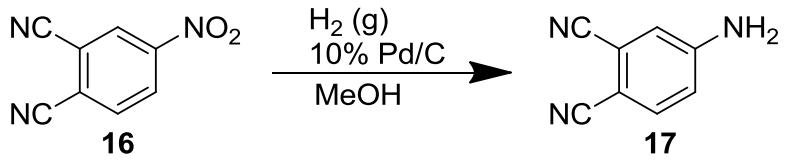

Scheme 3.9: Hydrogenation of 4-nitrophthalonitrile, **16**, performed at 50 °C under H_2-gas.

The reactor vessel was kept under H_2 pressure at 1 bar throughout the reaction. The temperature of the reaction was kept at 50 °C, while stirring the mixture at 400 rpm. To minimize temperature gradients between reaction vessel, reaction mixture and reactor head, the Hasteloy head of the reactor, was heated to 45 ^{o}C. This ensured that no condensation takes place on a cold reactor head. The system was flushed with N_2 before opening the reactor vessel. Yield approached 86% for this reaction. The ^{1}H NMR spectra showed the ring-based aromatic protons resonate at 7.55, 6.97 and 6.87 ppm.

3.3.4 Calorimetric and kinetic investigations on the RC1

3.3.4.1 The oxidation of thiophene derivatives

A. Calorimetry

The oxidation of thiophene derivatives with dimethyldioxirane (a very volatile compound with b.p. = 8 °C) takes place over long periods of time (24 hour time scale), thus stirring speed and other reactor parameters were not regarded as very important because these have influences on a "second" time scale. The focus of this part of the study was to obtain calorimetric data and kinetic data of the reaction in real time (not post synthesis) under actual reactor conditions. The dimethyldioxirane oxidation of thiophenes, **5** and **13**, takes place in two distinct separate reaction steps:

a. The *in situ* generation of dimethyldioxirane from acetone. This reaction step was from a calorimetric point of view very energetic because much work had to be done by the reactor temperature control units to keep the temperature of the reaction medium constant. The generation of dimethyldioxirane can be followed by monitoring FT-IR stretching frequencies at 1063 to 1068 and 1208 to 1248 cm^{-1}.
b. The actual oxidation of the thiophene derivatives, **5** and **13**, were with respect to the calorimetric efficiency of the RC1 reactor, on the lower edge of its measuring capability. It was also not possible to measure the formation of thiophene dioxide products by IR directly as the S=O IR stretching frequencies were interfered with by vibrations of other components in the system. Rather, the reaction was followed by monitoring the disappearance of dimethyldioxirane with time.

It is important to recognize that calorimetric and kinetic studies are normally performed under "ideal" conditions. This implies low concentrations (mM range), transparent and homogeneous solvents and reactions between reactants which are in the same phase (usually a dissolved phase). Furthermore, calometric measurements are normally performed by measuring the reactant thermal properties before mixing, and then long after the reaction again, i.e. a post reaction measurement. From these two sets of data the reaction enthalpy may be obtained. The challenge of the present study lies therein that it was attempted to

obtain the reaction enthalpy in real time, i.e. as the reaction progressed, as well as the non-ideal conditions that was employed. These included:

a. the solvent is biphasic (a 1.4: 1 mixture of DCM and water, *ca*. total volume = 300 cm^3).
b. The reaction mixture (initially) contained in excess of 210 g of solids (oxone® and $NaHCO_3$).
c. To this reaction mixture 108 cm^3 liquid acetone was added (*ca*. 1.5 mol; volume = 658 cm^3, 2.3 M concentration) to always have an excess of *in situ* formed dimethyldioxirane in the reaction medium. This ensured pseudo first order kinetic conditions for the process.
d. Finally, the thiophene derivatives (*ca*. 1 g, giving a total concentration of 5 to 6.5 mM) were added to this reaction medium to allow oxidation.

It is clear that these condition are very far from ideal but measurements on such "real" systems is important for any industrial process. For this reason it was attempted (with an unexpectedly large amount of success) to measure calorimetric and kinetic parameters under real reactor conditions.

The reaction temperature was always maintained at 0, or 2 or 5 °C with an accuracy of 0.1 °C. Colder reactions than 0 °C were avoided to prevent ice formation (the solvent contained *ca*. 150 cm^3, while higher temperatures than 5 °C were avoided to prevent dimethyldioxirane from beginning to boil. If boiling occurred, the thermodynamic picture would be much more complicated because phase changes would have to be compensated for in all calorimetric measurements by means of the third law of thermodynamics. The reactions taking place is shown in Scheme 3.10

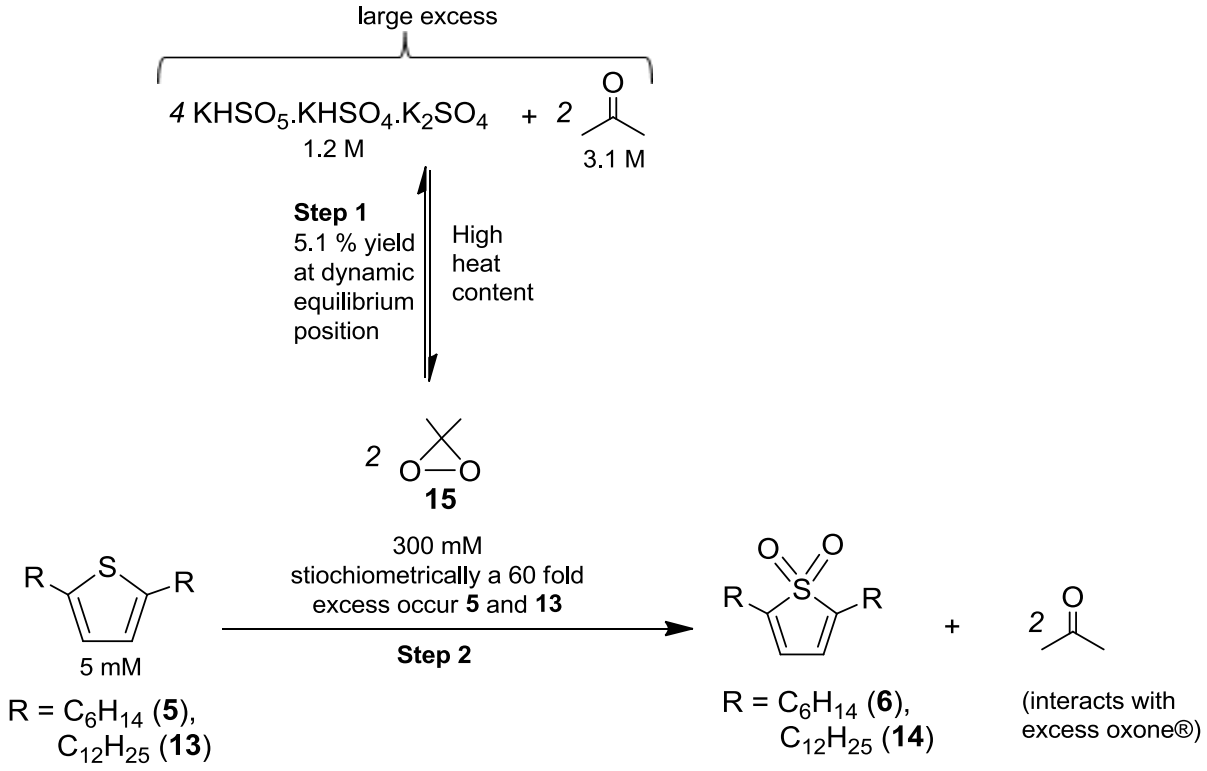

Scheme 3.10: Reaction scheme for the initial formation of the oxidizing agent (**step 1**) and the subsequent oxidation of the thiophene derivatives (**step 2**).

Figure 3.10 provides graphs highlighting the real time heat of reactions that was measured for the formation of dimethyldioxirane (Conditions as per reaction 3 in Table 3.3). In Table 3.3, reaction enthalpies of different reactions at different reaction conditions are summarized.

Table 3.3: Summary of the reaction conditions and reaction enthalpies (kJ/mol) for the dimethyldioxirane, **15**, formation and thiophene derivatives, **5** and **13**, oxidation, including rate of formation and disappearance. (Abbreviations used in this table: N/D - not determined, N/A - not applicable)

				ΔH, (kJ)[a]	ΔH, (kJ/mol)[b]	ΔH, (kJ)[c]	ΔH, (kJ/mol)[d]	1063 cm^{-1}		1208 cm^{-1}	
Reaction Number	**Reaction Temp. (Tr, °C)**	**Stirrer Speed (rpm)**	**Baffle**	**Dimethyl-dioxirane enthalpy**	**Dimethyl-dioxirane enthalpy**	**Thiophene-1,1-dioxide enthalpy**	**Thiophene-1,1-dioxide enthalpy**	**Formation of dimethyl-dioxirane (k_{obs}) ($x10^{-3}$ s^{-1})**	**Disappear-ance of dimethyl-dioxirane (k_{obs}) ($x10^{-3}$ s^{-1})**	**Formation of dimethyl-dioxirane (k_{obs}) ($x10^{-3}$ s^{-1})**	**Disappear-ance of dimethyl-dioxirane (k_{obs}) ($x10^{-3}$ s^{-1})**
1[e]	0	1000	Yes	-3.0	-	N/A	N/A	2.03	N/A	3.76	N/A
2[f]	5	500	No	-7.1	-4.8	N/D	N/D	2.15	1.3(1)	1.57	6.27
3[f]	2	500	No	-6.0	-2.9	-1.64[h]	-510	1.85	0.193	0.129	0.409
4[f]	0	1000	Yes	-5.1	-3.8	-3.83[i]	-830	1.79	0.0976	4.83[k]	0.0400[k]
5[g]	0	700	Yes	-3.1	-2.1	N/D	N/D	1.57	0.743	2.01	0.0103
6[g]	0	1000	Yes	-3.8	-3.0	-3.83[j]	-860	6.83[l]	0.367[l]	4.65[m]	0.277[m]

[a] Enthalpy, ΔH measured for the actual masses used in the reactor.
[b] ΔH_{meas} converted to be in units of kJ/mol. Theoretically this value was calculated by DFT techniques as -57.2 kJ/mol see section 3.4.1. Hence it was concluded that at dynamic equilibrium only (-2.9)/(-57.2) x 100 = 5.1% of the theoretical amount of dimethyldioxirane is available for thiophene derivative oxidation.
[c] Enthalpy, ΔH, measured for the actual masses used in the reactor for thiophene-1,1-dioxide derivatives.
[d] ΔH_{meas} converted to be in units of kJ/mol for thiophene-1,1-dioxide derivatives, **6** and **14**.
[e] The formation of dimethyldioxirane, **15**, only, no thiophene derivative was ever introduced to the reaction mixture.
[f] The formation of dimethyldioxirane and subsequent oxidation of 2,5-dihexylthiophene, **5**.
[g] The formation of dimethyldioxirane and subsequent oxidation of 2,5-didodecylthiophene, **13**.
[h] 6.2 mmol 2,5-dihexylthiophene was used, it yielded 52.0% of 2,5-dihexylthiophene-1,1-dioxide, **6**, after work-up.
[i] 5.5 mmol 2,5-dihexylthiophene was used, it yielded 83.9% of 2,5-dihexylthiophene-1,1-dioxide, **6**, after work-up.
[j] 5.2 mmol 2,5-didodecylthiophene was used, it yielded 85.5% of 2,5-didodecylthiophene-1,1-dioxide, **14**, after work-up.
[k] Rate of formation and disappearance collected at 1230 cm^{-1}.
[l] Rate of formation and disappearance collected at 1068 cm^{-1}.
[m] Rate of formation and disappearance collected at 1248 cm^{-1}.

Under condition of reaction 3 (Table 3.3), a large amount of heat is evolved for the formation of dimethyldioxirane within 2 minutes, Figure 3.10 (*bottom right insert*). The heat evolved is due to the relatively quick and energetic formation of dimethyldioxirane. Factors that were studied for this process included stirring speed, 5 °C temperature changes (restricted to temperatures between the freezing point of water and the boiling point of dimethyldioxirane) and the presence or absence of a baffle. Formation enthalpies varied between -3.0 and -7.1 kJ, but should really be constant as efforts were made to always use the same amounts of reactants and solvents. The variations documented in Table 3.3 are ascribed to the extreme non-ideal conditions that were employed, see factors a – d on page 63. Taking this extreme non-ideal reaction conditions into account, a variation of only a factor of two (-7.1/-3.0 = 2.37) is regarded as a remarkably good result.

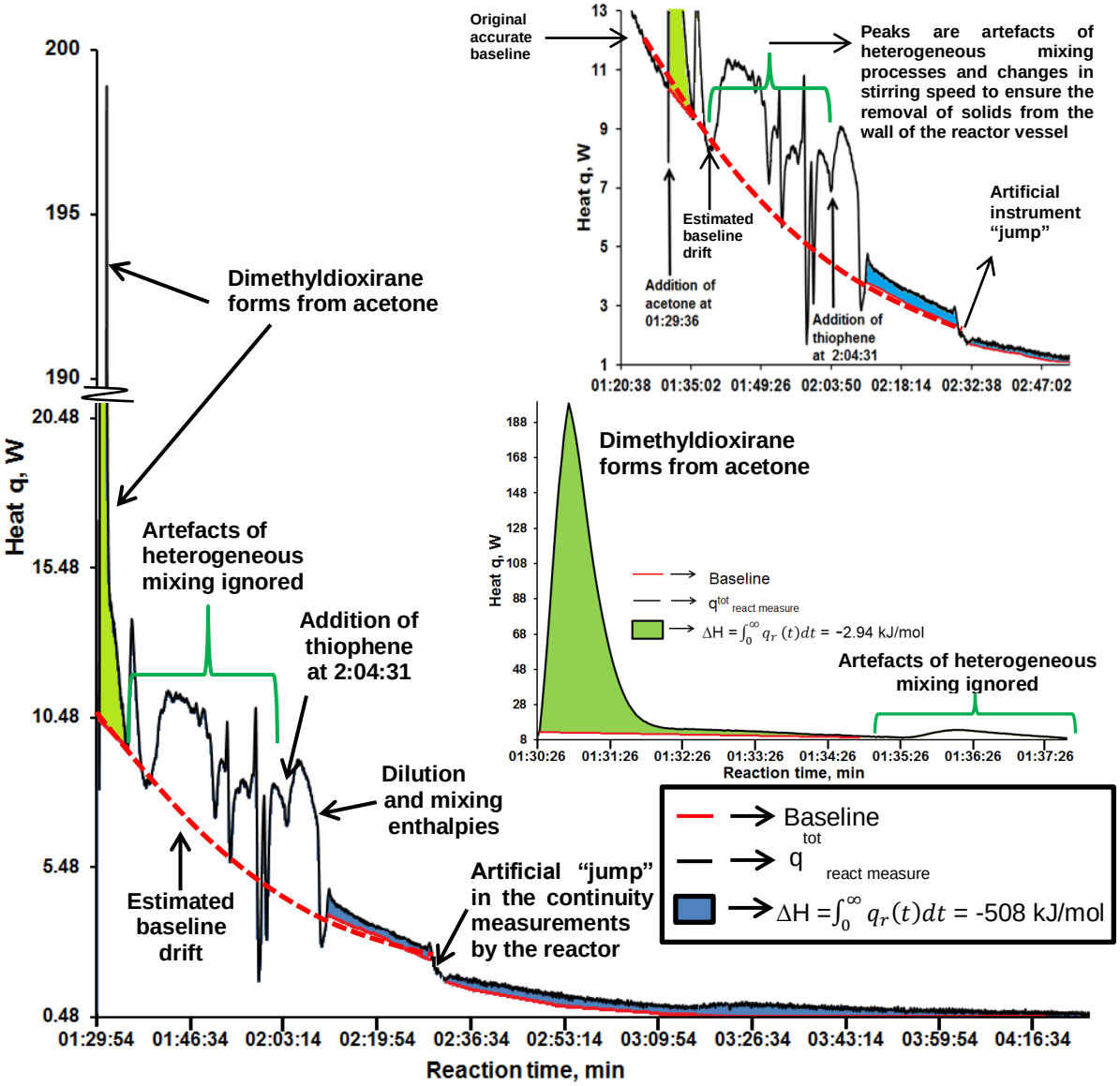

Figure 3.10: Heat profile for the formation of dimethyldioxirane from acetone (conditions as per reaction 3 in Table 3.3, green shaded area in thermogram above), followed by the oxidation of 2,5-dihexylthiophene, **5**, to 2,5-dihexylthiophene-1,1-dioxide, **6**. The heat evolved for the oxidation reaction is shown in blue. Dimethyldioxirane formation was deemed complete after ca. 7 minutes **(middle right insert)**, although heat evolution was only significant in the first four minutes. 2,5-Dihexylthiophene was only added to the reaction mixture ca. 35 minutes after acetone was added. The blue and green shaded areas, the surfaces under the heat line, represent ΔH. The **top insert** highlights the estimation of the baseline that was deemed to drift through the entire reaction. Judgment of a scientifically justifiable baseline was the biggest challenge in these experiments. Important: Note scale chances on the y-axis to prevent confusions.

For reaction 3 (Table 3.3), the measured ΔH value for the dimethyldioxirane formation (the blue area under the graph of Figure 3.10) was -6.0 kJ applicable to 2.04 mole of acetone used. This leads to an experimental molar ΔH value of -6.0/2.04 = -2.94 kJ/mol. As will be seen in the DFT calculations below (section 3.4.1), the theoretical molar ΔH value is actually -57.2

kJ/mol. This implies that the "apparent" yield of dimethyldioxirane that formed in step 1, Scheme 3.10, is only -2.94/-57.2 x 100 = 5.1%. This estimated yield will be used as representative in all further evaluation of results.

After dimethyldioxirane formed in all reactions (as indicated by a "zero" heat flow on the reactor, 7 minutes for reaction 3, see in Figure 3.10 insert bottom right), the appropriate thiophene derivatives were added to the reaction vessel to allow formation of either 2,5-dihexylthiophene-1,1-dioxide, **6**, or 2,5-didodecylthiophene-1,1-dioxide, **14**. As the reaction was slow (5 to 18 hours was allowed), and because of the small amount of heat flow involved, calorimetric measurements were very difficult for the thiophene derivative oxidation process. The blue highlight in the main graph of Figure 3.10 shows measurements for reaction 3 (Table 3.3) in the formation of 2,5-dihexylthiophene-1,1-dioxide, **6**. The measured ΔH value (the blue area under the graph of Figure 3.10) was -1.641 kJ applicable to 6.2 mmol of 2,5-dihexylthiophene used. This converts to an experimental molar ΔH of -264 kJ/mol provided the yield of oxidized product was 100%. However, the yield of isolated 2,5-dihexylthiophene-1,1-dioxide, **6**, was only 52%. Allowing for the lower yield, the experimentally determined molar enthalpy of the oxidation of 2,5-dihexylthiophene with dimethyldioxirane is ΔH_{molar} = 100/52 x (-264) = -507 kJ/mol. In section 3.4.1, the theoretical molar enthalpy for this reaction was determined as -211 kJ/mol. The measured enthalpy therefor differs from the theoretical enthalpy by only a factor of 507/211 = 2.4. This is a remarkably good correlation under the extreme non-ideal experimental conditions used.

The biggest problem to obtain an accurately determined experimental enthalpy is associated with the construction of a scientifically justifiable baseline for heat evolution for the oxidation of thiophene derivatives, **5** and **13**. For these experiments (e.g. Figure 3.9), the baseline was consider to drift non-linearly from the original measured baseline in the same fashion till the end of the reaction. The shown baseline is crudely estimated by the software of the instrument, but manual corrections were performed to adjust for obvious errors or mathematical artefacts in the instrument-determined drifting baseline.

A similar approach was utilized to determine the evolved heat and molar reaction enthalpies for all other reactions and results were summarized in Table 3.3. It is clear that reaction 3 gave the best result (in terms of reproducing the DFT calculated enthalpies), but reactions 4 and 6 also gave reasonable values in that they deviated not more than 4 fold (not even one

order of magnitude) from the theoretical value. Again, the extreme non-ideal conditions for the measurements, as described on page 63, leads the author to regard the experimentally obtained oxidation enthalpies (summarized in Table 3.3) as correlating remarkably well with the DFT-calculated results. To refresh the memory of the reader, the calculated results refer to a gas phase reaction, the discussion of these results are shown in section 3.4.1. Reactor conditions included 150 cm^3 H_2O and 220 cm^3 DCM as immiscible solvents; 210 g of solids were suspended in the reaction mixture, and concentrations of some reactants, like acetone exceeded 3 M.

It is concluded that, despite the extreme non-ideal conditions under which the reactions were performed, an unusually good correlation between experimental and theoretical molar enthalpies of reaction exists. A full discussion of the correlation between theoretical and experimental enthalpies will be presented in section 3.4.3.1.

B. <u>Kinetics</u>

The RC1 reactor has not only calorimetric measuring capability. In the system used, an ATR-IR probe (ATR = attenuated total reflectance) with Si crystal as active surface material was used. The probe is linked by optical fibre to the reactor vessel and can monitor reactions that involve IR active reactants or products up to 40 bar. All measurements are made at the surface of the Si crystal from a thin layer (film thickness is in the range of only a few μm) in the liquid phase. Any solids that do not dissolve in the solvents utilized in the reaction mixture will not be detected by this measuring technique. It was therefore attempted to utilize some of the reactions 1 to 6 listed in Table 3.3 on which the calorimetric measurements were made to simultaneously obtain kinetic results by utilizing ATR-IR probe. Components that could also be uniquely identified in this study were acetone and dimethyldioxirane, and they could also be measured with only a little interference during the course of reactions. It was found that acetone (the precursor to dimethyldioxirane) exhibits an IR C=O stretching frequency signal at 1715 and a CH bending frequency signal at 1366 cm^{-1}. Water, the inorganic co-solvent in the reaction medium, exhibits an O-H bending mode frequency at 1640 cm^{-1} and DCM (the organic co-solvent for the reaction medium) exhibits a HC-Cl wagging movement frequency at 1267 cm^{-1}. Although the film constitution at the surface of the Si crystal may not have been constant in terms of *all* components in the reaction mixture, it was constant for the identification of the desired dissolved species and

measured products because of efficient stirring. It was not possible to uniquely identify S=O signals of the 2,5-dihexyl- or 2,5-didodecylthiophene-1,1-dioxide, **6** and **14**, in this biphasic reaction mixture due to signal overlapping, but fortunately dimethyldioxirane, **15**, showed two uniquely identifiable C-O stretching frequency peaks at 1063 to 1068 and 1208 to 1248 cm^{-1}. It was decided to monitor the formation of dimethyldioxirane with time from acetone in the first step of the reaction (Scheme 3.10) by recording overlay spectra in the region 1000 to 1800 cm^{-1} and then extract kinetic parameters from the 1063 to 1068 and 1208 to 1248 cm^{-1} bands. The second step (Scheme 3.10) involving oxidation of thiophene derivatives to thiophene-1,1-dioxide derivatives was studied by monitoring the disappearance of the dimethyldioxirane peaks at 1063 to 1068 and 1208 to 1248 cm^{-1}. All data were fitted to the first order integrated rate law:

$$A_{obs} = A_1\text{-}(A_1\text{-}A_0)(\exp^{-k(obs).t})$$

Equation 3.1.

Kinetics results from three reactions are discussed below. Reaction 1 (Table 3.3) gave kinetic data for the formation of dimethyldioxirane, **15**, from acetone in the absence of any thiophene derivatives. This gave the rate of formation for dimethyldioxirane under the most ideal conditions employed. No disappearance of dimethyldioxirane, **15**, was observed, i.e. dimethyldioxirane does not naturally decompose under the conditions used. Reaction 4 of Table 3.3 allowed the measurement of dimethyldioxirane formation, and thereafter, the rate of disappearance of dimethyldioxirane which is, by virtue of a 2:1 stoichiometric ratio, equivalent to double the rate of formation of 2,5-dihexylthiophene-1,1-dioxide, **6**, from the stoichiometry shown in Scheme 3.10.

$$-\frac{1}{2}\frac{\mathrm{d}[\mathrm{dimethyldioxirane}]}{\mathrm{dt}} = +\frac{\mathrm{d}[2{,}5-\mathrm{dihexylthiophene}-1{,}1-\mathrm{dioxide}]}{\mathrm{dt}}$$

Equation 3.2

Reaction 6 of Table 3.3 allowed the measurement of dimethyldioxirane, **15**, formation, and thereafter, the rate of disappearance of dimethyldioxirane, **15**. This time the latter measurement is equivalent to double the rate of formation of 2,5-didodecylthiophene-1,1-dioxide, **14**.

The reaction profile of reaction 1, the formation of dimethyldioxirane in the absence of thiophene derivatives, is shown in Figure 3.11, *left*. This profile was obtained by plotting IR data from the overlayed spectra utilizing the 1208 cm^{-1} C-O vibrational peak of dimethyldioxirane. A selection of the IR spectra used is shown in Figure 3.11 *right*. Spectra were recorded at intervals of 60 seconds for almost two half-lives of the reaction. Fitting of the data to Equation 3.1 gave pseudo first order rate constant for the growth of the peaks at 1063 and 1208 cm^{-1} of k_{obs} = 0.00203 and 0.00376 s^{-1}, respectively. The rate constants are considered "pseudo first order" because [dimethyldioxirane] < 5% of [acetone] and 7 times less than [$KHSO_5.KHSO_4.K_2SO_4$] at dynamic equilibrium see Scheme 3.10. Taking into account the extreme non-ideal kinetic conditions for the reaction (the system contained more than three heterogeneous phases viz. liquid organic (DCM), inorganic liquid (water) and several solid phases ($KHSO_5.KHSO_4.K_2SO_4$ and $NaHCO_3$), the two observed rate constants are regarded as mutually consistent.

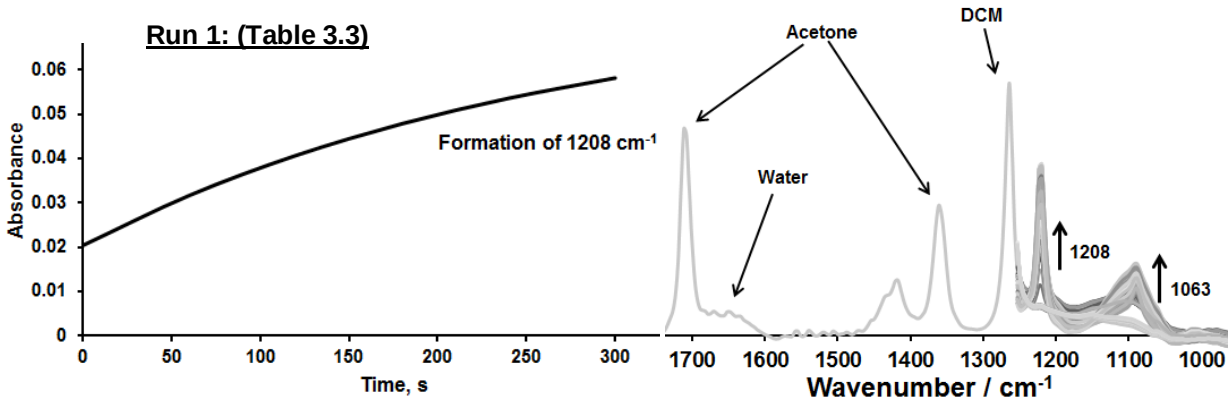

Figure 3.11: Left: The rate of formation of the dimethyldioxirane. **Right:** The overlayed IR-spectra between 950 and 1730 cm^{-1} which shows the formation of signals 1063 and 1208 cm^{-1}.

For reaction runs 4 and 6 in Table 3.3, dimethyldioxirane, **15**, was allowed to form completely before the appropriate thiophene derivative, **5** and **13**, was added to the reaction mixture. This implies that the first reaction step in these two reactions duplicate the conditions used in reaction run 1. The second reaction step involving the oxidation thiophene derivatives can then be followed and interpreted using single reaction kinetic models rather than consecutive reaction kinetic models. Figure 3.12 *left*, main graph, shows the reaction profile of the formation of dimethyldioxirane, **15**, while the insert on the right shows the depletion of dimethyldioxirane during the formation of 2,5-dihexylthiophene-1,1-dioxide, **14**. Some of the overlayed spectra required to generate the formation reaction profile at 1063 cm^{-1} are shown in Figure 3.12 on the *on top*.

Run 4: (Table 3.3)

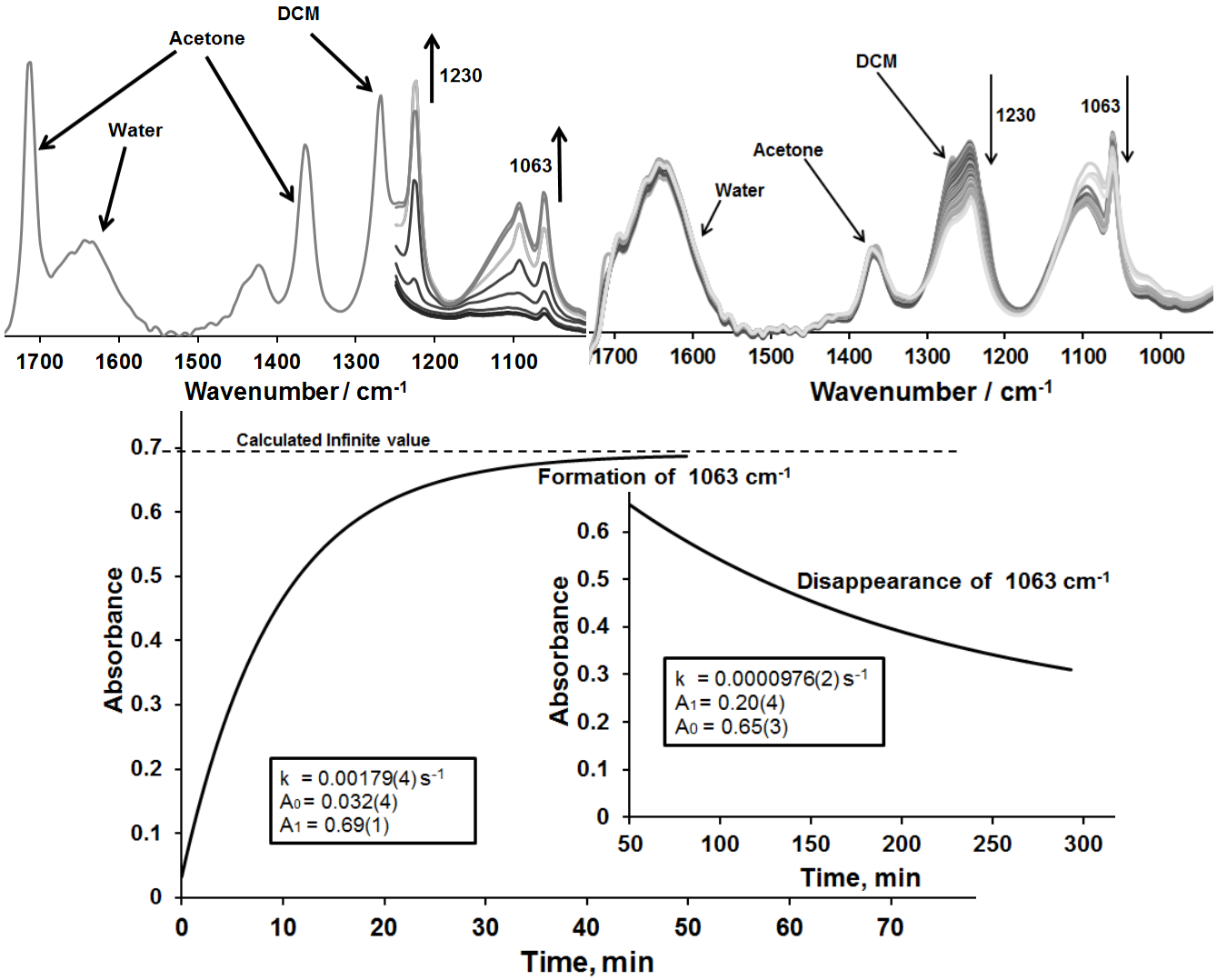

Figure 3.12: Top Left: IR spectra between 950 and 1710 cm^{-1} for the formation of dimethyldioxirane, **15**, for the second 2,5-dihexylthiophene reaction, run 4. **Top Right:** IR spectra between 950 and 1710 cm^{-1} for the disappearance of dimethyldioxirane for the fourth 2,5-dihexylthiophene reaction, run 4. **Bottom**: The rate of formation of the dimethyldioxirane in the fourth 2,5-dihexylthiophene, **5**, reaction, while the **bottom right insert** shows the rate of disappearance of the dimethyldioxirane.

The obtained rate constant for dimethyldioxirane formation utilizing the 1063 cm^{-1} vibrational band was k_{obs} = 1.79 x 10^{-3} s^{-1} while it was 4.83 x 10^{-3} s^{-1} utilizing the 1208 cm^{-1} band. The rate constant for dimethyldioxirane disappearance, 1063 cm^{-1} band, was found to be k_{obs} 9.76 x 10^{-5} s^{-1}. It can be seen that the formation of the oxidizing agent is approximately 1.79 x 10^{-3}/9.76 x 10^{-5} = 18 times faster than the rate at which it was consumed in the oxidation reaction. Obtained rate constants are summarized in Table 3.3.

Observed rate constants were not sufficiently accurate to interpret in terms of stirrer speed or the presence or absence of a baffle.

Figure 3.13 gives reaction profiles and overlay spectra for reaction 6 (Table 3.3) related to dimethyldioxirane formation and the subsequent formation of didodecylthiophene-1,1-dioxide, **14**.

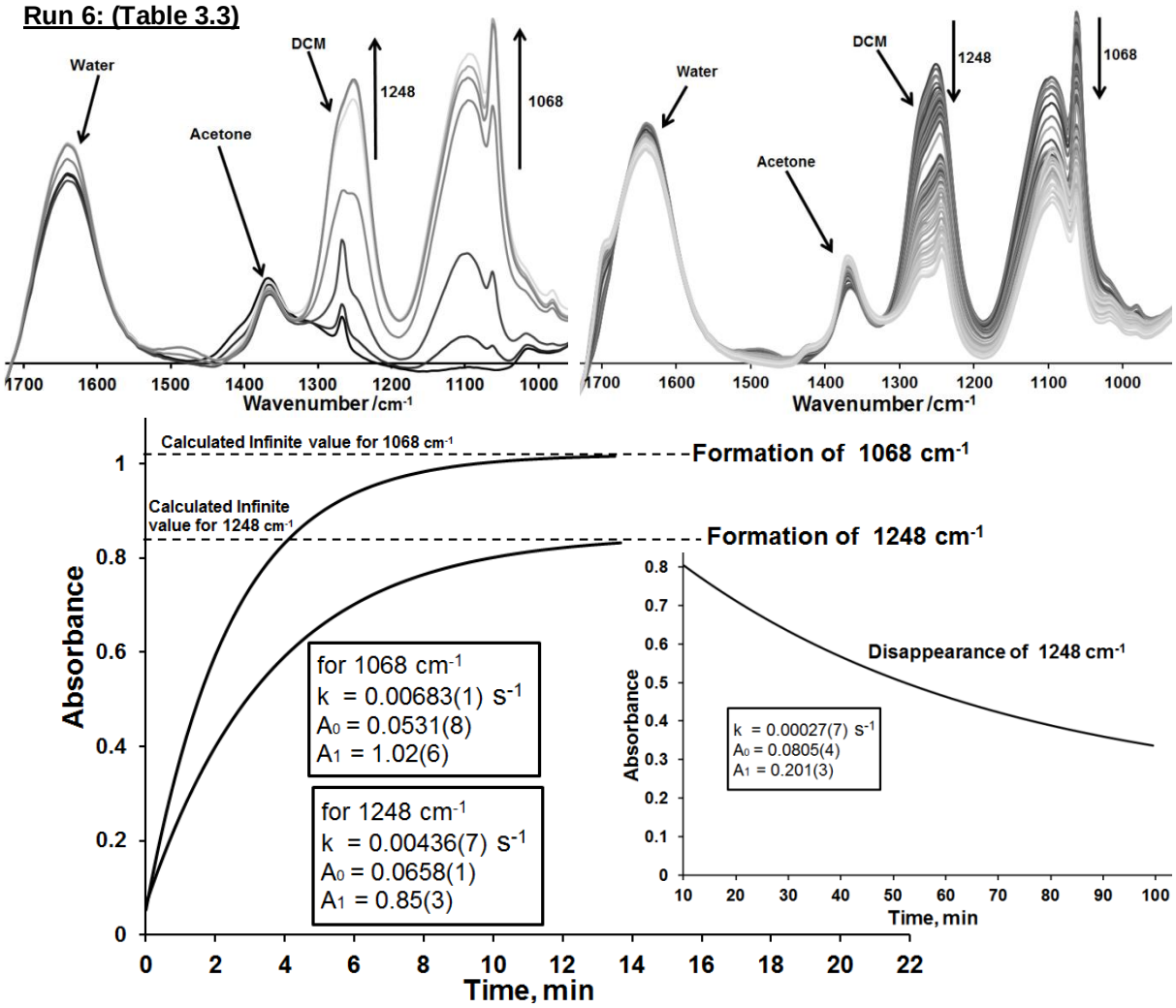

Figure 3.13: Top Left: IR spectra between 950 and 1710 cm^{-1} for the formation of dimethyldioxirane for the second 2,5-didodecylthiophene reaction, run **6**. **Top Right:** IR spectra between 950 and 1710 cm^{-1} for the disappearance of dimethyldioxirane for the second 2,5-didodecylthiophene reaction, run **6**. **Bottom:** The rate of formation of the dimethyldioxirane in the second 2,5-didodecylthiophene, **13**, reaction, while the **bottom right insert** shows the rate of disappearance of the dimethyldioxirane.

The dimethyldioxirane, **15**, formed quickly and the observed rate of formation from the 1068 and 1248 cm^{-1} bands were k_{obs} = 6.829 x 10^{-3} and 4.635 x 10^{-3} s^{-1} respectively. The consumption of dimethyldioxirane, **15**, to generate 2,5-didodecylthiophene-1,1-dioxide, **14**, was found to give rate constants for the disappearance of dimethyldioxirane of

k_{obs} = 3.67 x 10^{-4} s^{-1} utilizing the 1068 cm^{-1} band and k_{obs} = 2.7 x 10^{-4} s^{-1} utilizing the 1248 cm^{-1} vibrational band. This means 2,5-didodecylthiophene, **13**, oxidation by dimethyldioxirane occurs 16 to 20 times slower than dimethyldioxirane formation.

Again, as described on page 63, the kinetics studies were done under far from ideal conditions. Thus, the rate constants for these heterogeneous kinetic studies cannot be compared to any rate constants obtained under homogeneous (ideal) experimental conditions, and thus cannot be compared to any data found in literature.

The activation energy, E_a, for the oxidation of 2,5-dihexylthiophene, **5**, in principle can be determined by utilizing the Arrhenius equation discussed in section 2.9.2. The temperature range that could be used to determine E_a, for **5** is, however, because of the properties of reactants and reaction media, limited to between 0 °C (the freezing point of the co-solvent water) and 8 °C (the boiling point of the oxidant, dimethyldioxirane). This small temperature range to determine E_a cast doubt on its accuracy, but despite this, the result that was obtained is taken at the least as to estimate the activation energy of 2,5-dihexylthiophene oxidation. Figure 3.14 shows the relationship between ln(k_{obs}) (the rate constants for the disappearance of the oxidizing agent at 1063 cm^{-1} was used) and 1/T (in Kelvin) for reaction runs 2, 3 and 4 (Table 3.3).

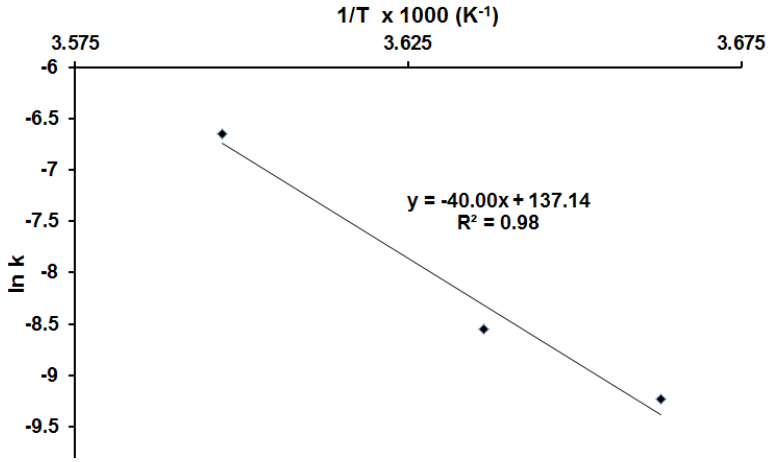

Figure 3.14: A graph to determine the activating energy, E_a, by means of the Arrhenius equation for the oxidation of 2,5-dihexylthiophene, **5**, by dimethyldioxirane, **15**.

Using the slope from the graph displaying the trend line it was found that the slope is

$$\text{Slope} = -40.00\ \text{K} \times 1000 = -40000\ \text{K}$$

However, according to Arrhenius this "slope" = $-E_a/R$

This implies E_a = -Slope x R = -(-40000 K x 8.314 J/mol.K)

E_a = 332560 J/mol

= 332 kJ/mol

This activation energy, E_a = 332 kJ/mol, is large which explains the slow rate of 2,5-dihexylthiophene oxidation. For example, at 0 °C the half-life of reaction 4 is

$t_{1/2}$ = ln2/k

= 0.693/9.76 x 10^{-5}

= 7100 s

= ca. 2 hours.

3.3.4.2 Reaction kinetics and thermodynamics for the reduction of 4-nitrophthalonitrile, 16

In this, last, study on the RC1 reactor, the hydrogenation of 4-nitrophthalonitrile to 4-aminophthalonitrile, **17**, was investigated at 50 ^{0}C under a 1 bar H_2 atmosphere in 170 cm^3 methanol.

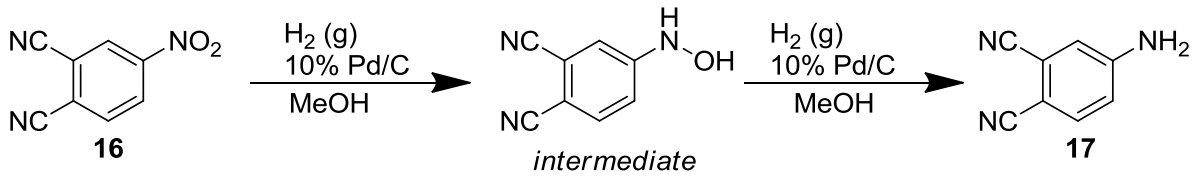

Scheme 3.11: The hydrogenation reaction of 4-nitrophthalonitrile, **16**, illustrating the intermediate product that forms during the reaction.

The thermogram of the reaction is shown in Figure 3.15. Two distinct separate thermal events were observed that, combined, liberated -3.86 kJ for 5.78 mmole 4-nitrophthalonitrile reduced. The two peaks are consistent with a two-step process involving 4-(hydroxyamino)phthalonitrile as intermediate, see Scheme 3.11. The overall molar reaction enthalpy for the conversion of 1 mole of 4-nitrophthalonitrile, **16**¸ to 4-aminophthalonitrile, **17**, is therefore -3.86/0.0058 = -668 kJ/mol.

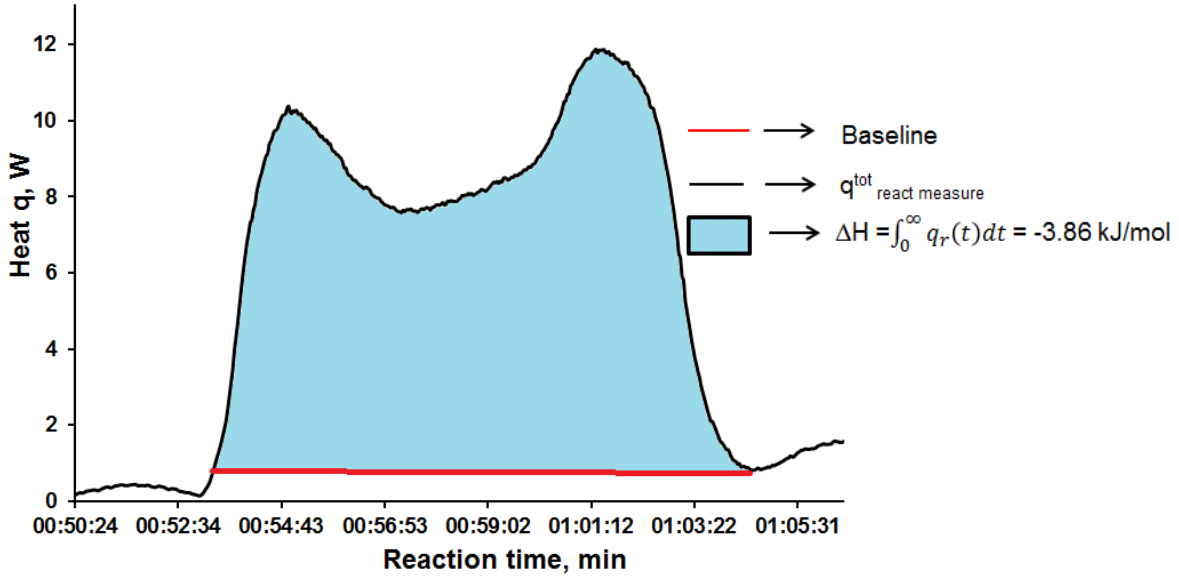

Figure 3.15: Heat profile for the formation of 4-aminophthalonitrile, **16**, from 4-nitrophthalonitrile, **17**, (Table 3.3 , light blue shaded area in thermogram above). 4-Aminophthalonitrile formation was deemed complete after ca. 12 minutes.

In literature, the experimental enthalpy values for the reduction of nitrobenzene, **18** to aniline, **19** and ethyl 4-nitrobenzoate **20** to ethyl 4-aminobenzoate, **21**; has been reported as -530 and -559 kJ/mol. An experimental enthalpy value of -668 kJ/mol for the reduction of 4-nitrophthalonitrile, **16,** was obtained during this study on the RC1 reactor (the volume of the reaction mixture was 210 cm^3). This is a remarkably comparable value to the similar compound **19**, since the CRC.v4 reactor (utilized in literature for the reduction of nitrobenzene, **18** and ethyl 4-nitrobenzoate, **20**) has a working volume of between 25 to 45 cm^3.[4]

This experimental value (-668 kJ/mol), determined under very non-ideal conditions (solid catalyst, gas reactant, H_2, that has to absorb on Pd particles on C, substrate dissolved in the solution phase) corresponds remarkably well with the DFT calculated gas phase reaction molar enthalpy of -424 kJ/mol, see section 3.3.3.2 for the DFT discussion. The results for the hydrogenation reaction are summarized in Table 3.4.

Table 3.4: The summary for the reaction conditions and reaction enthalpies (kJ/mol) for the 4-nitrophthalonitrile, **16**, including rate of formation and disappearance.

Compound	Reaction Temp. (Tr, °C)	Stirrer Speed (rpm)	ΔH, (kJ)[a]	ΔH, (kJ/mol)[b]	1350 cm^{-1}	1555 cm^{-1}
			4-amino-phthalonitrile, **17**	4-amino-phthalonitrile, **17**	Disappea-rance (k_{obs}) ($x10^{-3}$ s^{-1})	Disappearance (k_{obs}) ($x10^{-3}$ s^{-1})
4-nitro-phthalonitrile, **16**	50	400	-3.86	-668	7.92	6.26

[a] Enthalpy, ΔH measured for the masses used in the reactor. [b] ΔH_{meas} converted to be in units of kJ/mol.

Kinetically, the reaction was followed by measuring the disappearance of the NO_2 group of 4-nitrophthalonitriles vibrational signals at 1350 (symmetric band) and 1555 cm^{-1} (the asymmetric N=O band). Figure 3.16 shows relevant portions of IR overlayed spectra as well as the reaction profile obtained from the 1350 cm^{-1} vibrational band with time.

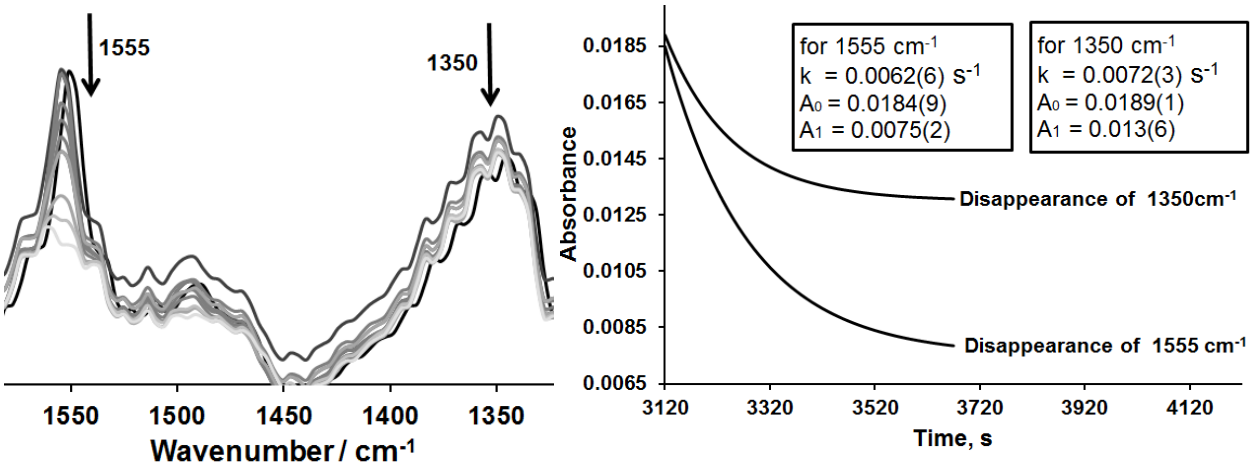

Figure 3.16: Left: Overlayed IR spectra for run **18** between 1325 and 1580 cm^{-1}. **Right:** The rate of disappearance for the NO_2 group vibrational peaks at 1350 (symmetric N=O band) and 1555 cm^{-1} (asymmetric N=O band).

The rate of disappearance of 4-nitrophthalonitrile was determined by means of Equation 3.1 to be k_{obs} = 7.2 x 10^{-3} s^{-1} utilizing data from the 1350 cm^{-1} symmetric IR vibrational band and k_{obs} = 6.2 x 10^{-3} s^{-1} for the 1555 cm^{-1} asymmetric IR vibrational band. This rate constant translates to a half-life of $t_{1/2}$ = ln2/0.0062 = 112 seconds. It follows that 98.2% conversion is obtained after 6 half-lives, that is, after 672 seconds. This time frame corresponds well with the calorimetric time frame of heat evolution as shown in Figure 3.15.

3.4 Computational Chemistry

A computational study was done to calculate the enthalpies involved in the oxidation and reduction reactions done on the RC1 reactor as discussed in section 3.3. In order to determine the enthalpy change involved in these chemical reactions, the geometries of all the reactants and products need to be optimized, followed by a frequency calculation on the optimized geometries.

The output file of the geometry optimization give the total bonding energy and the output file of a frequency calculation give the entropy, S, and internal energy at 298 K. From this information the enthalpy, H, and the Gibbs free energy, G, can be calculated, utilizing the following equations:

$$G = H - TS$$

Equation 3.3

$$H = U + RT$$

Equation 3.4

where U is the total bonding energy plus the internal energy. The reaction enthalpy, ΔH, and the change in the Gibbs free energy, ΔG, can be calculated using Equation 3.5 and Equation 3.6 given below.

$$\Delta G = \Delta G_{products} - \Delta G_{reagents}$$

Equation 3.5

$$\Delta H = \Delta H_{products} - \Delta H_{reagents}$$

Equation 3.6

All compounds were optimized by means of DFT calculations using the ADF program with the OLYP functional and Slater-type TZP basis set.

3.4.1 Oxidation of thiophene derivatives

The Gibbs free energies and reaction enthalpies for the oxidation reaction of various thiophene derivatives was calculated by means of DFT calculations. In order to investigate

the oxidation reaction, the formation of the oxidizing agent was studied first. Experimentally (section 3.3.4.1), the oxidizing agent, **15**, forms *in situ*, which then oxidizes 2,5-dihexylthiophene, **5**, to 2,5-dihexylthiophene-1,1-dioxide, **6** and 2,5-didodecylthiophene, **13**, to 2,5-didodecylthiophene-1,1-dioxide, **14**, respectively. The Gibbs free energy and enthalpy for the formation of the oxidizing agent (Scheme 3.12) was calculated.

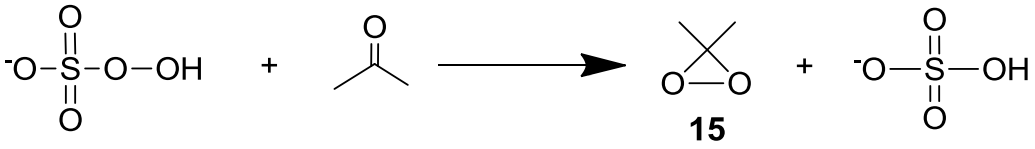

Scheme 3.12: The formation of the oxidizing agent, dimethyldioxirane, **15**, from acetone (from Scheme 3.10, step 1 in the reaction).

Acetone reacts with peroxymonosulfate to form dimethyldioxirane (oxidizing agent). Table 3.5 shows the calculated energies, free energy G (Equation 3.3) and enthalpy H (Equation 3.4), for each compound participating in the reaction, as well as the change in reaction enthalpy, ΔH, and Gibbs free energy, ΔG, for the total reaction using Equation 3.5 and Equation 3.6. The reaction is an exothermic, with calculated ΔH and ΔG, of -57.20 and -59.23 kJ/mol, respectively.

Table 3.5: The reaction enthalpy and Gibbs free energy of compounds utilized during oxidizing agent formation, using the ADF program with the OLYP functional and Slater-type TZP basis set.

	H (Enthalpy), kJ/mol	**G (Gibbs Free Energy), kJ/mol**
Acetone	-3664.4	-4961.97
HSO_5^-	-4876.1	-3761.89
Dimethyldioxirane	-5311.9	-5403.91
HSO_4^-	-3285.9	-3379.18
Overall reaction according to scheme 3.6	**ΔH = -57.20**	**ΔG = -59.23**

The Gibbs free energies and reaction enthalpies for the oxidation reaction of, 2,5-dihexylthiophene, **5** and 2,5-didodecylthiophene, **13**, with dimethyldioxirane, **15**, as oxidizing agent (as depicted in

Scheme **3.13**) was determined by means of DFT calculations. The results of the computed energies found in this section and the experimental data obtained (in section 3.3.3.1), will be compared in section 3.4.3.1.

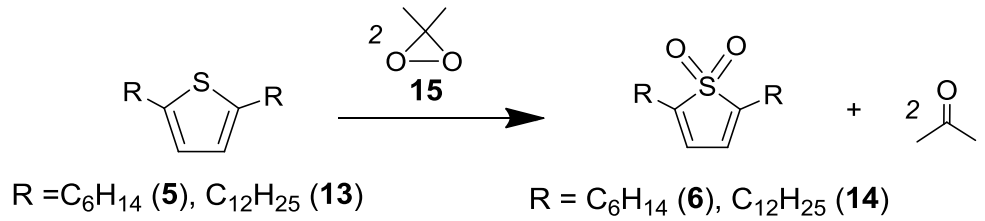

Scheme 3.13: Oxidation of 2,5-dihexylthiophene, **5**, and 2,5-didodecylthiophene, **13**, by means of dimethyldioxirane, **15,** (from scheme 3.5, secondary reaction).

The summarized change in reaction enthalpy, ΔH, and change in free energy, ΔG, calculated with Equation 3.5 and Equation 3.6, for the formation of 2,5-dihexylthiophene-1,1-dioxide, **6**, and 2,5-didodecylthiophene-1,1-dioxide, **14**, are showed in Table 3.6.

Table 3.6: The change in reaction enthalpy, ΔH and free energy change for reaction, ΔG, for various thiophene-1,1-dioxide, **6** and **14**, using the ADF program with the OLYP functional and Slater-type TZP basis set.

Oxidation reaction of	**ΔH, kJ/mol**	**ΔG, kJ/mol**
2,5-dihexylthiophene, **5**, to 2,5-dihexylthiophene-1,1-dioxide, **6**	-210.89	-209.56
2,5-didodecylthiophene, **13**, to 2,5-didodecylthiophene-1,1-dioxide, **14**	-211.65	-205.59

It was found that there was not a noticeably big difference in the Gibbs free energies and the reaction enthalpies for the formation of 2,5-dihexylthiophene-1,1-dioxide, **6**, from 2,5-dihexylthiophene, **5**, and 2,5-didodecylthiophene-1,1-dioxide, **14**, from 2,5-didodecylthiophene, **13**. These compounds have never been optimized using DFT calculations, thus it could not be compared to any literature data.

3.4.2 Reduction of nitrobenzene and 4-nitrophthalonitrile

The Gibbs free energies and reaction enthalpies for the reduction of nitrobenzene, **18**, 4-nitrophthalonitrile, **16**, and ethyl-4-nitrobenzoate, **20**, (see Scheme 3.14) was determined by means of DFT calculations.

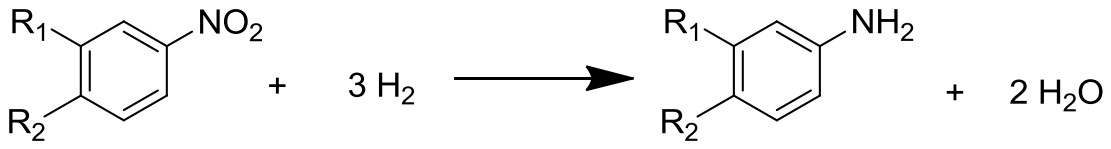

$R_1 = R_2 = CN$ (**16**), $R_1 = R_2 = CN$ (**17**),
$R_1 = R_2 = H$ (**18**), $R_1 = R_2 = H$ (**19**),
$R_1 = H$; $R_2 = COOCH_2CH_3$ (**20**) $R_1 = H$; $R_2 = COOCH_2CH_3$ (**21**)

Scheme 3.14: The reduction reaction of nitrobenzene derivatives, **16**, **18**, and **20**.

The calculated reaction enthalpy values, ΔH, and the Gibbs free energies, ΔG, for the reduction reactions are summarized in Table 3.7. The intermediate products that form during the synthesis, as shown in Scheme 3.11 (section 3.3.4.2), did not affect the calculated reaction enthalpy values and the Gibbs free energies. The calculations for these reactions were done under gas phase conditions with Equation 3.3-Equation 3.6.

Table 3.7: The reaction enthalpy and Gibbs free energies for the reduction of nitrobenzene derivatives, **16**, **18**, and **20**, using the ADF program with the OLYP functional and Slater-type TZP basis set.

Reduction reaction of	**ΔH kJ/mol**	**ΔG, kJ/mol**
4-Nitrophthalonitrile, **16**, to 4-aminophthalonitrile, **17**	-424	-410
Nitrobenzene, **18**, to aniline, **19**	-390	-375
Ethyl 4-nitrobenzoate, **20**, to ethyl 4-aminobenzoate, **21**	-404	-398

The Gibbs free energies and reaction enthalpy ΔH, for the reduction of 4-nitrophthalonitrile, **16**, to 4-Aminophthalonitrile, **17**, are the most negative followed by ethyl 4-aminobenzoate, **21**, and aniline, **19**, (Table 3.7).

3.4.3 Comparison of Computational and RC1 study

3.4.3.1 Thermodynamic relationships for oxidation reactions

The experimental enthalpy values, ΔH, for the formation of only the oxidizing agent, **15**, was compared with the computed (theoretical) enthalpy, ΔH as summarized in Table 3.8. Based on the calculated enthalpy for the formation of **15**, the conversion of step 1 of the reaction in Scheme 3.10 (the formation of **15**) is estimated as 5.1%, see Table 3.3 and the discussion in Section A.

Table 3.8: The experimental and computed enthalpies for the oxidation reaction of thiophene derivatives, utilizing dimethyldioxirane as oxidizing agent.

[a] Run	Experimental Enthalpy, ΔH, kJ/mol	Computed Enthalpy, ΔH, kJ/mol
	[d]Dimethyldioxirane enthalpy (for 5.1% conversion)	[e]Dimethyldioxirane enthalpy (100% conversion)
2[b]	-4.8[d]	-57.20[e]
3[b]	-2.9[d]	[e]
4[b]	-3.8[d]	[e]
5[c]	-3.1[d]	[e]
6[c]	-3.8[d]	[e]
Average ΔH, kJ/mol	-3.232	-57.20

[a] The experimental reaction enthalpies for runs **2** to **6**, given in section 3.3.4.1, Table 3.3, not considering the oxidation of the thiophene derivatives, **5** and **13**.
[b] The experimental reaction enthalpy for the formation of dimethyldioxirane, **15**, for subsequent oxidation of the 2,5-dihexylthiophene, **5**.
[c] The experimental reaction enthalpy for the formation of dimethyldioxirane, **15**, for subsequent oxidation of the 2,5-didodecylthiophene, **13**.
[d] The calculated reaction enthalpy for the formation of only dimethyldioxirane, **15**, not considering the oxidation of the thiophene derivatives, **5** and **13**.
[e] The calculated reaction enthalpy for the formation of only dimethyldioxirane, **15**, not considering the oxidation of the thiophene derivatives, **5** and **13**.

In Table 3.9, the experimental enthalpy values (section A) and the computed (theoretical) enthalpy (section 3.4.1) for the formation of 2,5-dihexylthiophene-1,1-dioxide, **6**, and 2,5-didodecylthiophene-1,1-dioxide, **14**, are summarized.

Table 3.9: The experimental and computed enthalpy for the formation of thiophene-1,1-dioxide derivatives, **6** and **14**, according to

Scheme **3.13**.

[a]Run	Experimental Enthalpy, ΔH, kJ/mol	Computed Enthalpy, ΔH, kJ/mol
	[b]thiophene-1,1-dioxide derivatives enthalpy	thiophene-1,1-dioxide derivatives enthalpy
3 and 4: 2,5-dihexylthiophene, **5**, to 2,5-dihexylthiophene-1,1-dioxide, **6**	Ranges from (-508 to -830)	-210.89
5 and 6: 2,5-didodecylthiophene, **13**, to 2,5-didodecylthiophene-1,1-dioxide, **14**	-860	-211.65

[a] The experimental reaction enthalpies for runs **3** to **6**, given in section 3.3.4.1, Table 3.3.
[b] The experimental enthalpy for oxidized thiophene derivatives, **6** and **14** showed in section 3.3.4.1.
[c] The computed enthalpy for oxidized thiophene derivatives, **6** and **14**, showed in section 3.4.1.

The experimental enthalpies for all the reactions summarized in Table 3.9 are in good correlation with the computed enthalpy values. The experimental enthalpy values deviated

between 2.4 and 4 fold (not even one order of magnitude) from the DFT calculated enthalpy values. These are exceptional results since the experimental enthalpies were obtained in extremely non-ideal experimental conditions, section 3.3.4.1 (page 63).

3.4.3.2 Reaction enthalpies relationships for reduction reactions

The experimental enthalpy values, ΔH, (section 3.3.4.2) of the reduction reactions of nitrobenzene derivatives with their respective computed (theoretical) enthalpy, ΔH (section 3.4.2) are summarized in Table 3.10.

Table 3.10: The experimental and computed enthalpies for various nitrobenzene derivatives.

	Computed Enthalpy, ΔH, kJ/mol	**Experimental Enthalpy, ΔH, kJ/mol**
4-Aminophthalonitrile, **17**	-424	-668
Aniline, **19**	-390	-530[a]
Ethyl 4-aminobenzoate, **21**	-404	-559[a]

[a] Experimental values from literature done on pressure-resistant reaction calorimeter (CRC.v4) reactor, reference 4.
[a] The experimental enthalpy for 4-Aminophthalonitrile, **17**, showed in section 3.3.4.2.

The experimental enthalpy values obtained during the reduction of 4-nitrophthalonitrile, **16** to 4-aminophthalonitrile **17**; nitrobenzene, **18** to aniline, **19** and **20** to ethyl 4-aminobenzoate, **21**; are in good correlation with the computed enthalpy values. The experimental enthalpy values deviated not more than 1.5 fold (not even one order of magnitude) from the DFT calculated enthalpy values. The result for the reduction of 4-nitrophthalonitrile, **16,** are remarkable, since the CRC.v4 reactor (utilized for the reduction of nitrobenzene, **18** and ethyl 4-nitrobenzoate, **20**) has a working volume of between 25 to 45 cm^3 and the reduction of 4-nitrophthalonitrile, **16**, was done in the RC1 reactor that has a working volume of 1200 cm^3 (the volume of the reaction mixture was 210 cm^3).

3.5 Electrochemistry

3.5.1 General

The cyclic voltammetry study of the phthalocyanine derivatives, **9-12** and **23-29**, in this study was investigated in either, dichloromethane (DCM), dimethyl sulfoxide (DMSO) or acetonitrile (CH_3CN) at 25 °C in a glovebox. Measurements were made on 0.5 mM solutions of the compounds, **9-12** and **23-29**. The solutions also contained 0.5 mM of the internal

reference (ferrocene, FcH or decamethyl ferrocene, Fc*) with 0.1 M tetrabutylammonium tetrakis(pentafluorophenylborate), **22**. The choice of solvent was determined by the solubility of the compound under investigation. The electrochemical experiment employed a three-electrode system, consisting of a platinum auxiliary electrode, a silver wire reference electrode and a glassy carbon working electrode with a surface area of 0.1257 cm^2.

Decamethyl ferrocene was used as the internal reference in most cases, as some of the redox waves of the phthalocyanine compounds overlapped with the redox wave of ferrocene (FcH/FcH^+). Figure 3.17 shows the voltammograms at scan rates, 100 to 500 mV/s in DMSO. The Fc^*/Fc^{*+} couple was measured at -480 mV relative to the FcH/FcH^+ in DMSO.

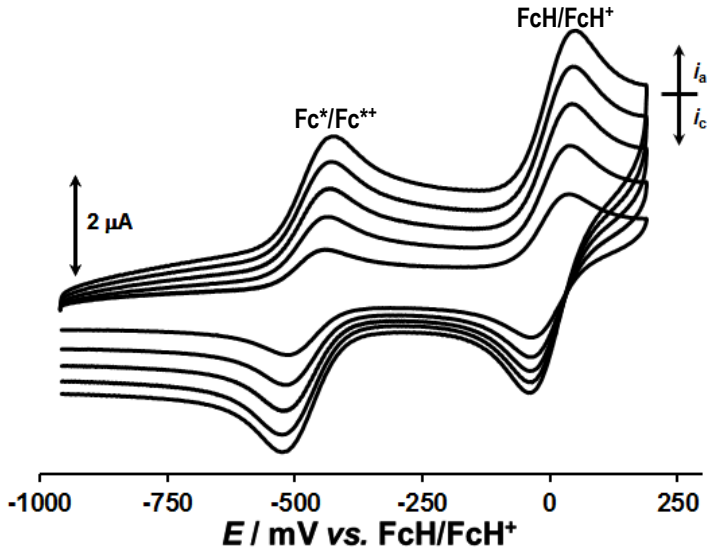

Figure 3.17: The overlayed cyclic voltammograms of 0.5 mM DMSO solution of Fc* and FcH in the presence of $[NBu_4][B(C_6F_5)_4]$ at 25 °C, at a scan rates of 100, 200, 300, 400 and 500 mV/s (largest scan rate).

Figure 3.18 shows the voltammograms at scan rates, 100 to 500 mV/s in DCM. The Fc^*/Fc^{*+} couple was measured at -610 mV relative to the FcH/FcH^+ in DCM.

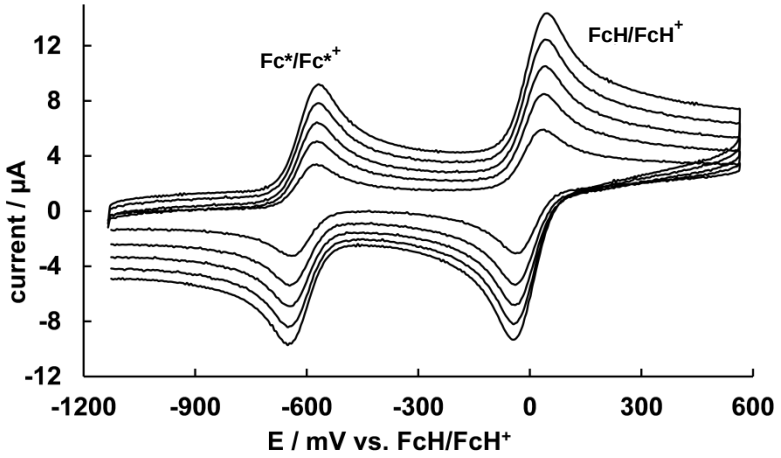

Figure 3.18: The overlayed cyclic voltammograms of 0.5 mM DCM solution of Fc* and FcH in the presence of $[NBu_4][B(C_6F_5)_4]$ at 25 °C, at a scan rates of 100, 200, 300, 400 and 500 mV/s (largest scan rate).

3.5.2 Metal-free phthalocyanines with various ethylene glycol and alkyl substituents, 9, 11-12

3.5.2.1 Electrochemistry of symmetrically substituted phthalocyanines, 9

The electrochemical study for metal-free phthalocyanines containing ethylene glycol substituents, **9**, tetra[2-(2-hydroxyethoxy)ethoxy]phthalocyanine, were performed in 0.5 mM DMSO solutions, because it is insoluble in other suitable electrochemical solvents (DCM and CH_3CN). Figure 3.19 shows the cyclic voltammogram of **9**, tetra[2-(2-hydroxyethoxy)ethoxy]phthalocyanine, at a scan rate of 100 mV/s, with decamethyl ferrocene as internal standard.

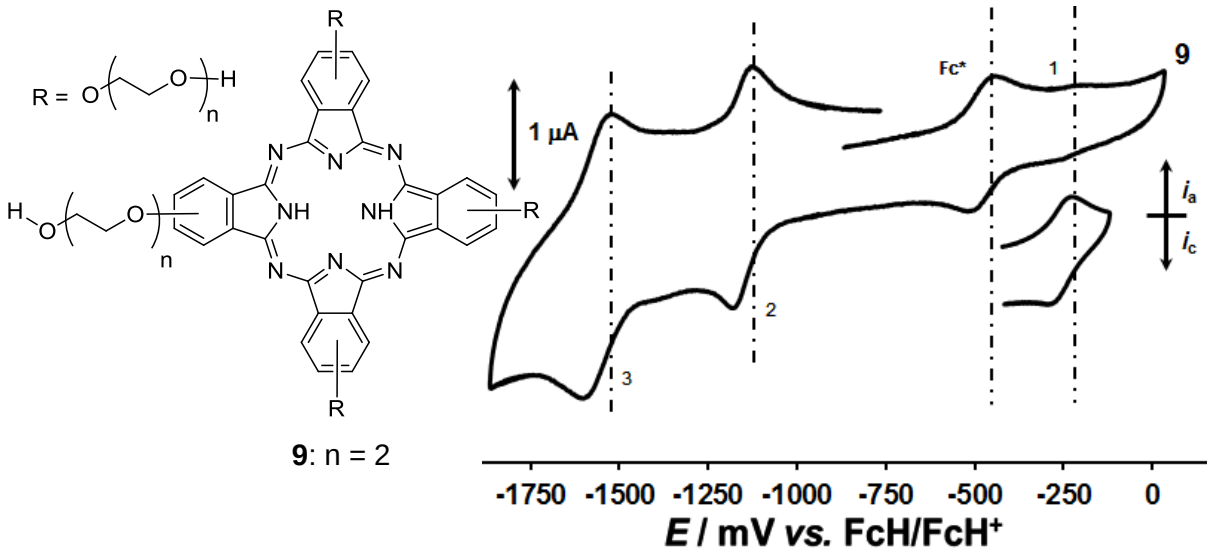

Figure 3.19: Left: The structure of **9**. **Right:** Cyclic voltammogram of a 0.5 mM DMSO solution of **9** containing 0.1M $[N(^nBu)_4][B(C_6F_5)_4]$, obtained at a scan rate of 100 mV/s. **Right bottom:** Cyclic voltammogram of a 0.5 mM DMSO solution of **9** containing 0.1M $[N(^nBu)_4][B(C_6F_5)_4]$, without internal standard for wave 1 with a y-axis scale of 1µA.

Waves 1 were assigned to the first oxidation peak of the compound, while waves 2 and 3 were assigned to the first and second reduction peaks. Table 3.11 summarized all CV data for scan rates 100 to 500 mV/s of compound **9**. Wave 1 is chemically reversible and electrochemically irreversible. Waves 2 and 3 indicate these reductive redox processes are chemically and electrochemically reversible. Results summarized in Table 3.11, show the currents of wave 2 and 3 are twice as large as the currents in wave 1. The electrochemical scheme that best resemble the electrochemical behaviour of this compound, **9**, is given below,

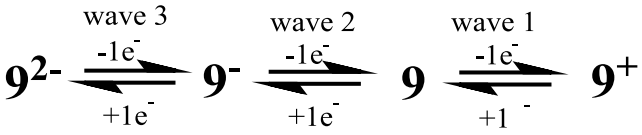

Scheme 3.15: The possible electrochemical scheme for **9**, tetra[2-(2-hydroxyethoxy)ethoxy]phthalocyanine.

The cyclic voltammograms in Figure 3.19 for this compound, **9**, show no signs of any structural isomers. Table 3.11 summarized all CV data for scan rates 100 to 500 mV/s of compound **9** as well as the half-wave potentials of H_2Pc as found in literature.

Table 3.11: Cyclic voltammetry data of 0.5 mmol dm^{-3} solutions at scan rate 100 mV/s of **9**, in pure DMSO at 25 ^{o}C, supporting electrolyte 0.1 mol dm^{-3} $[N(^{n}Bu)_4][B(C_6F_5)_4]$.

	(mV/s)	Wave 1					Wave 2				
		E_{pa}, mV	$E^{0'}$, mV	ΔE_p, mV	i_{pa}, µA	i_{pc}/i_{pa}	E_{pa}, mV	$E^{0'}$, mV	ΔE_p, mV	i_{pa}, µA	i_{pc}/i_{pa}
9	**100**	-213	-263 (-660)[d]	100	0.68	0.98	-1125	-1155 (-1060)[d]	60	1.24	1.07
	200	-207	-261	109	0.95	0.96	-1121	-1154	65	1.66	1.02
	300	-203	-260	115	1.08	0.96	-1118	-1154	72	1.99	1.01
	400	-198	-258	121	1.24	0.93	-1114	-1152	76	2.40	1.04
	500	-204	-265	121	1.33	0.94	-1115	-1156	81	2.58	1.01
		Wave 3									
9	**100**	-1527	-1566 (-1930)[d]	79	1.16	1.07					
	200	-1520	-1563	85	1.57	1.06					
	300	-1518	-1563	89	2.07	1.00					
	400	-1515	-1561	93	2.49	0.97					
	500	-1514	-1563	98	2.89	0.95					

[a] E_{pc} values are given. [b] i_{pc} values are given. [c] i_{pa}/i_{pc} values are given. [d] Half-Wave Potentials (V versus SCE) of H_2Pc in DMF containing 0.1 M TEAP at 100 mV/s as found in literature [ref 5].

3.5.2.2 Electrochemistry of asymmetrically substituted phthalocyanines, 11 and 12

The cyclic voltammogram at a scan rate of 100 mV/s in 0.5mM DCM solutions of tetrahexyl-di-[2-(2-hydroxyethoxy)ethoxy]-phthalocyanine, **11**, are showed in Figure 3.20.

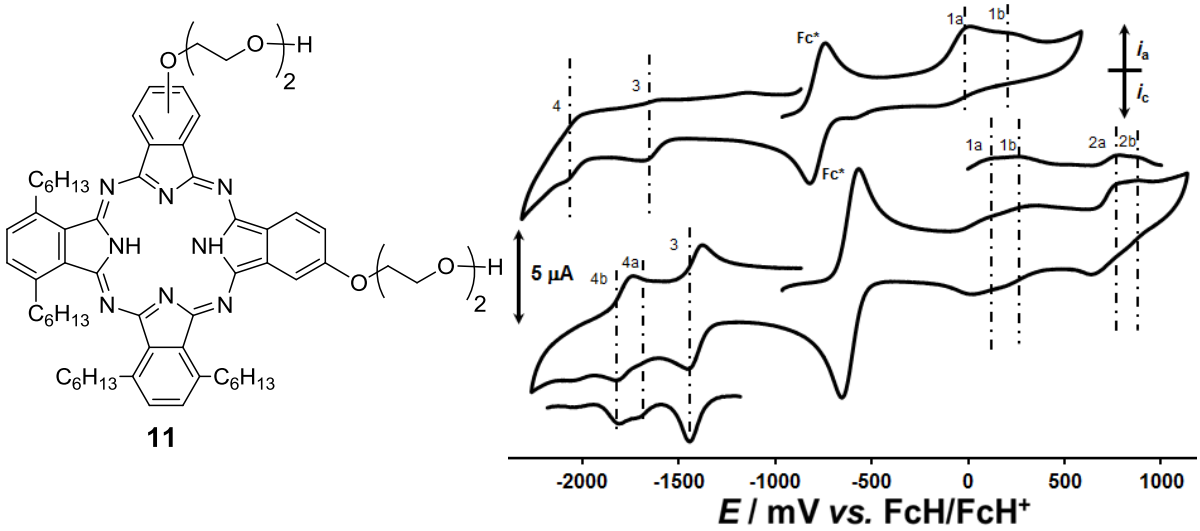

Figure 3.20: Left: The structure of **11**. **Right middle:** Cyclic voltammogram of a 0.5 mM DCM solution of **11** containing 0.1M $[N(^nBu)_4][B(C_6F_5)_4]$, obtained at a scan rate of 100 mV/s. **Right middle and bottom:** The square waves for anodic and cathodic processes of **11** at scan rates of 20 Hz, respectively. **Right at the top**: Cyclic voltammogram of a 0.5 mM THF solution of **11** containing 0.1M $[N(^nBu)_4][B(C_6F_5)_4]$, obtained at scan rates of 100 mV/s.

Two oxidative processes were identified, both were split into two components on the CV of **11**, Figure 3.20 (*middle*), these are labelled 1a, 1b and 2a and 2b. Two observed reductive processes are labelled 3 and 4, on the CV. These processes were observed as single redox processes, i.e. no splitting of peaks. On the SW, however it was possible to identify wave 4 consisting out of an a and b component. Two explanations for the observed peak splitting are possible. The first involves dimerization, and the second explanation implies it was possible to identify two isomers electrochemically. No reason for the possibility of dimerization could be identified (normally metals like Cd is required to induce phthalocyanine dimerization), thus the peak splitting is interpreted as the presence of different structural isomers of the AABB and ABABA type as discussed in section 3.2.2.3 for **11**. For compound **11**, the redox processes are chemically reversible ($i_{pc}/i_{pa} \rightarrow 1$), while wave 1b, 2a and 2b are not electrochemically reversible ($\Delta E > 90$ mV). Table 3.12 summarized all CV data for scan rates 100 to 500 mV/s of compound **11**.

Table 3.12: Cyclic voltammetry data of 0.5 mmol dm^{-3} solutions at scan rates 100-500 mV/s of **11**, tetrahexyl-di-[2-(2-hydroxyethoxy)ethoxy]-phthalocyanine, in pure DCM at 25 ^{o}C, supporting electrolyte 0.1 mol dm^{-3} $[N(^{n}Bu)_4][B(C_6F_5)_4]$.

	(mV/s)	Wave 1a					Wave 1b					Wave 2a				
		E_{pa}, mV	$E^{0'}$, mV	ΔE_p, mV	I_{pa}, µA	I_{pc} /I_{pa}	E_{pa}, mV	$E^{0'}$, mV	ΔE_p, mV	I_{pa}, µA	I_{pc} /I_{pa}	E_{pa}, mV	$E^{0'}$, mV	ΔE_p, mV	I_{pa}, µA	I_{pc} /I_{pa}
	100	110	60	101	1.46	1.12	303	257	93	2.47	0.82	777	707	140	2.47	0.82
	200	138	73	130	1.62	1.22	325	258	133	2.70	0.85	805	715	180	2.70	0.85
11	**300**	153	79	147	2.02	1.17	373	279	188	2.92	1.08	833	726	213	2.92	1.08
	400	173	88	170	2.47	1.09	380	273	213	3.15	1.14	860	739	242	3.15	1.14
	500	193	97	193	2.70	1.08	407	280	253	3.37	1.22	867	742	250	3.37	1.22
		Wave 2b					**Wave 3**									
	100	870	838	63	1.29	[d]	-1381[a]	-1412	63	3.49[b]	0.97[c]					
	200	875	840	70	1.39	[d]	-1375[a]	-1415	80	4.61[b]	0.93[c]					
11	**300**	883	843	80	[d]	[d]	-1371[a]	-1416	90	5.28[b]	0.98[c]					
	400	890	845	90	[d]	[d]	-1367[a]	-1417	100	5.96[b]	0.98[c]					
	500	900	847	107	[d]	[d]	-1364[a]	-1417	106	6.63[b]	0.98[c]					
		Wave 4a					**Wave 4b**									
	100	-1730[a]	-1675	120	[d]	[d]	-1743[a]	-1780	73	3.60[b]	0.94[c]					
	200	-1730[a]	-1668	133	[d]	[d]	-1735[a]	-1778	87	3.82[b]	0.94[c]					
11	**300**	-1727[a]	-1662	140	[d]	[d]	-1727[a]	-1774	93	4.27[b]	0.97[c]					
	400	-1723[a]	-1657	143	[d]	[d]	-1723[a]	-1773	100	4.72[b]	0.95[c]					
	500	-1720[a]	-1653	143	[d]	[d]	-1720[a]	-1773	107	5.17[b]	0.96[c]					

[a] E_{pc} values are given. [b] i_{pc} values are given. [c] i_{pa}/i_{pc} values are given.

The electrochemical scheme that best resemble the electrochemical behaviour of this compound, **11**, according to the study in DCM, is given below. The use of notation AABB and ABAB is made, to differentiate the isomers.

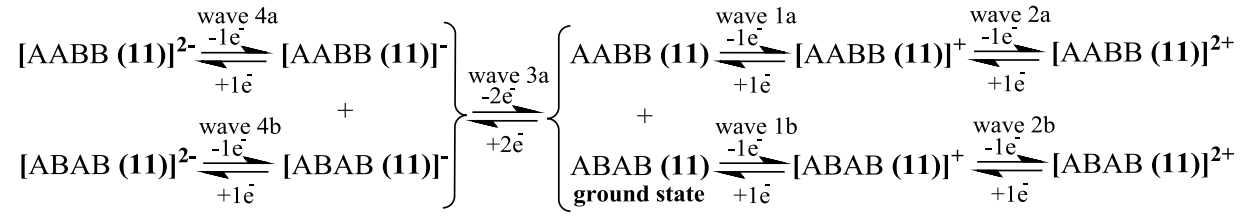

Scheme 3.16: An electrochemical scheme that explains the observed electrochemical behaviour of tetrahexyl-di-[2-(2-hydroxyethoxy)ethoxy]-phthalocyanine, **11**. AABB and ABAB are respectively two structural isomers of **11**. Note that wave 3 has no a and b component. This means the isomers were reduced at the same potential. Wave 4 was assigned an a and a b component because of the SW observation.

The study was repeated for a 0.5 mM THF solution of **11**, Figure 3.20 (*top*). The second oxidation wave, **11**, was not visible in the solvent window; however the oxidation wave 1a and 1b associated with first oxidation still indicated the presence of isomers. The reduction waves, 3 and 4 was observed. The cyclic voltammogram at a scan rate of 100 mV/s in 0.5mM DCM solutions of tetrahexyl-di-{2-[2-(2-hydroxyethoxy)-ethoxy]-ethoxy}-phthalocyanine, **12**, are show in Figure 3.21.

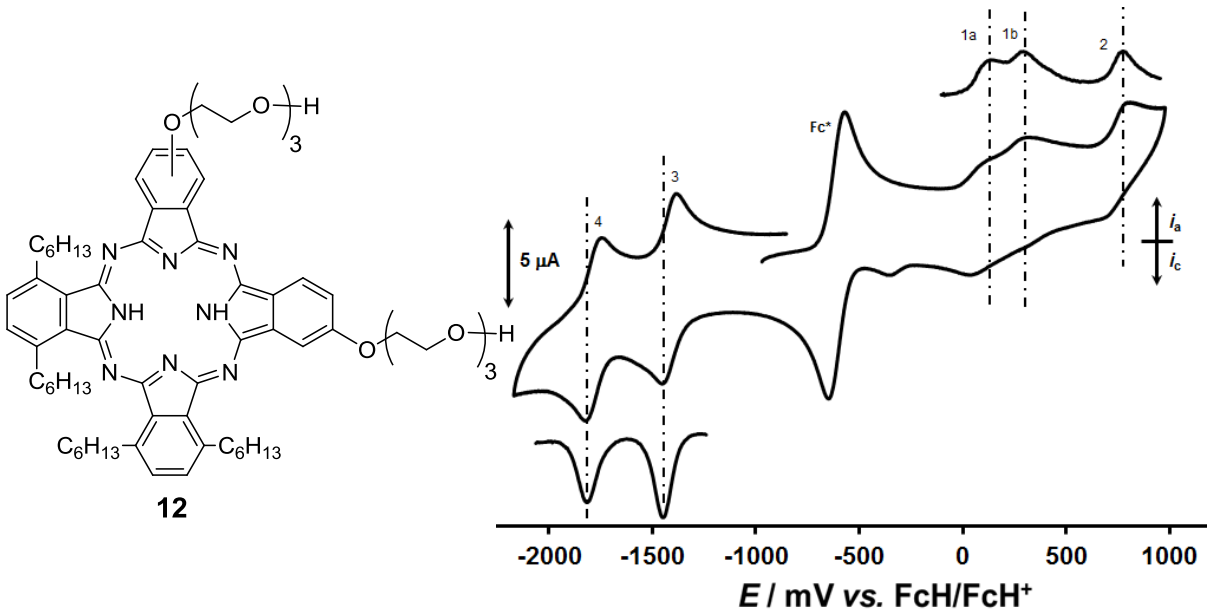

Figure 3.21: Left: The structure of **12**. **Middle:** Cyclic voltammogram of a 0.5 mM DCM solution of **12** containing 0.1M $[N(^nBu)_4][B(C_6F_5)_4]$, obtained at a scan rate of 100 mV/s. **Top and bottom:** The square waves for anodic and cathodic processes of **12** at scan rates of 20 Hz, respectively.

Two oxidative processes were identified, both were split into two components on the CV of **12**, Figure 3.21 (*middle*), these are labelled 1a, 1b and 2. Two observed reductive processes are labelled 3 and 4, on the CV. These processes were observed as single redox processes, i.e. no splitting of peaks. On the SW, it confirms the single redox processes for 3 and 4. Two explanations for the observed peak splitting are possible. The first involves dimerization, and the second explanation implies it was possible to identify two isomers electrochemically. No reason for the possibility of dimerization could be identified (was mentioned, normally metals like Cd is required to induce phthalocyanine dimerization), thus the peak splitting is interpreted as the presence of different structural isomers of the AABB and ABABA type as discussed in section 3.2.2.3 for **12**. For compound **12**, the system is chemically reversible

($i_{pc}/i_{pa} \rightarrow 1$), expect for wave 1a, while wave 1b and 2 are not electrochemically reversible ($\Delta E > 90$ mV). The sum of the peak currents for wave 1a and 1b, and wave 2 are in good correlation with the peak currents of wave 3 and 4. Table 3.13 summarized all CV data for scan rates 100 to 500 mV/s of compound **12**.

Table 3.13: Cyclic voltammetry data of 0.5 mmol dm^{-3} solutions at scan rates 100-500 mV/s of **12** tetrahexyl-di-{2-[2-(2-hydroxyethoxy)-ethoxy]-ethoxy}-phthalocyanine, in pure DCM at 25 °C, supporting electrolyte 0.1 mol dm^{-3} $[N(^nBu)_4][B(C_6F_5)_4]$.

	(mV/s)	Wave 1a					Wave 1b					Wave 2				
		E_{pa}, mV	$E^{0'}$, mV	ΔE_p, mV	i_{pa}, µA	i_{pc}/i_{pa}	E_{pa}, mV	$E^{0'}$, mV	ΔE_p, mV	i_{pa}, µA	i_{pc}/i_{pa}	E_{pa}, mV	$E^{0'}$, mV	ΔE_p, mV	i_{pa}, µA	i_{pc}/i_{pa}
	100	114	81	84	0.67	1.10	299	257	83	1.04	0.91	806	751	107	0.93	1.02
	200	120	78	99	0.95	1.03	344	272	140	1.51	0.88	807	745	118	1.23	1.00
12	**300**	122	73	110	1.23	0.96	353	265	169	1.89	0.75	804	737	126	1.47	0.97
	400	131	73	124	1.42	0.93	380	268	212	1.80	0.84	813	734	146	1.89	1.05
	500	132	70	136	1.51	0.94	386	261	241	1.85	0.83	829	736	178	1.97	1.01
		Wave 3					**Wave 4**									
	100	-1383[a]	-1425	86	1.42[b]	1.03[c]	-1759[a]	-1794	72	1.18[b]	1.04[c]					
	200	-1392[a]	-1433	86	1.85[b]	1.02[c]	-1762[a]	-1802	84	1.47[b]	1.05[c]					
12	**300**	-1399[a]	-1440	90	2.37[b]	1.01[c]	-1763[a]	-1808	96	1.99[b]	1.05[c]					
	400	-1403[a]	-1445	95	2.73[b]	1.01[c]	-1777[a]	-1815	88	2.37[b]	1.04[c]					
	500	-1396[a]	-1448	111	3.05[b]	1.03[c]	-1774[a]	-1825	111	2.75[b]	1.01[c]					

[a] E_{pc} values are given. [b] i_{pc} values are given. [c] i_{pa}/i_{pc} values are given. [d] Not observed

The electrochemical scheme that best resemble the electrochemical behaviour of this compound, **12**, is given below. The use of notation AABB and ABAB is made, to differentiate the isomers.

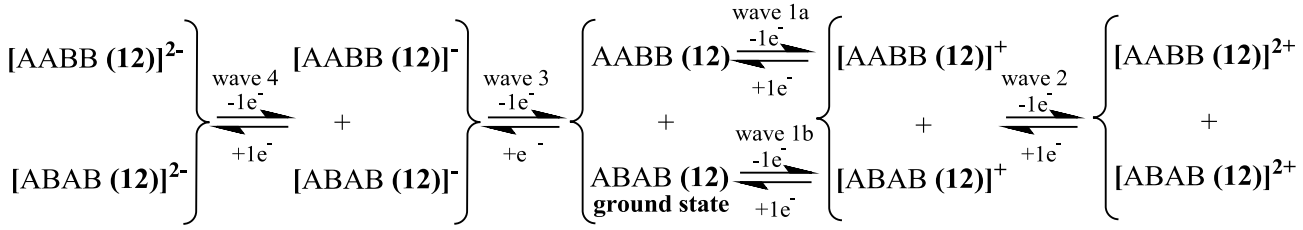

Scheme 3.17: An electrochemical scheme that explains the observed electrochemical behaviour of tetrahexyl-di-{2-[2-(2-hydroxyethoxy)-ethoxy]-ethoxy}-phthalocyanine, **12**. AABB and ABAB are respectively two structural isomers of **12**. Note that wave 3 and 4 has no a and b component. This means the isomers were reduced at the same potential.

When the half-wave potentials ($E^{0'}$-values), in Table 3.12 and Table 3.13, of **12** for wave 3 and 4b, -1425 and -1794 mV, were compared to the values of **11** for wave 3 and 4, -1412 and -1780 mV, it is clear that the redox processes for **11** occur at more negative potentials than that of **12**. Thus, the diethylene glycol groups on compound **11** increases electron density on the macrocycle more than the triethylene glycol groups on compound **12**.

Due to lack of data for asymmetrically substituted phthalocyanines in literature, the half-wave potentials for compounds **11** and **12**, were compared to that of $H_2Pc(OC_5H_{11})_4$ and $H_2Pc(OC_5H_{11})_8$ at 100 mV/s.

Table 3.14: Half-wave redox potentials of **11** and **12** compared to $H_2Pc(OC_5H_{11})_4$ and $H_2Pc(OC_5H_{11})_8$ at 100 mV/s.

Compounds	(mV/s)	Wave 1	Wave 2	Wave 3	Wave 4
		$E^{0'}$, mV	$E^{0'}$, mV	$E^{0'}$, mV	$E^{0'}$, mV
11[a]	**100**	60	707	-1412	-1780
12[a]		81	751	-1425	-1794
$H_2Pc(OC_5H_{11})_4$[b]		850	1220	-1310	-1580
$H_2Pc(OC_5H_{11})_8$[b]		720	1190	-970	-1250

[a] $E^{0'}$-values of **11** and **12** in DCM containing 0.1 mol dm^{-3} $[N(^nBu)_4][B(C_6F_5)_4]$.
[b] $E^{0'}$-values (V vs SCE) of $H_2Pc(OC_5H_{11})_4$ and $H_2Pc(OC_5H_{11})_8$ in DCM containing 0.1 mol dm^{-3} TBAP.

The half-wave potentials of $H_2Pc(OC_5H_{11})_4$ and $H_2Pc(OC_5H_{11})_8$ shows the effect of the four additional substituents on the electron density of the macrocycle. Upon comparing the $E^{0'}$-values of **11** and **12** to the phthalocyanines containing four or eight pentoxy groups, it is clear that the pentoxy groups increases the electron density on the macrocycle more than the glycol groups.

3.5.3 Various ruthenium phthalocyanines with carbonyl axial ligand, 23-29

Section 3.5.3 provides the results of an electrochemical study of a series of ruthenium phthalocyaninato complexes, **23-29**. The cyclic voltammetry study (which also includes square wave voltammetry and linear sweep voltammetry) of the phthalocyanine derivatives, **23-29**, in this study was investigated in either, dichloromethane (DCM), dichloromethane (DCM) with a drop of acetonitrile (CH_3CN) and/or acetonitrile (CH_3CN). The author acknowledges PhD student Johannes H. van Tonder that synthesized these compounds.

3.5.3.1 *np*-$(C_6H_{13})_8$-PcRu(CO), 23

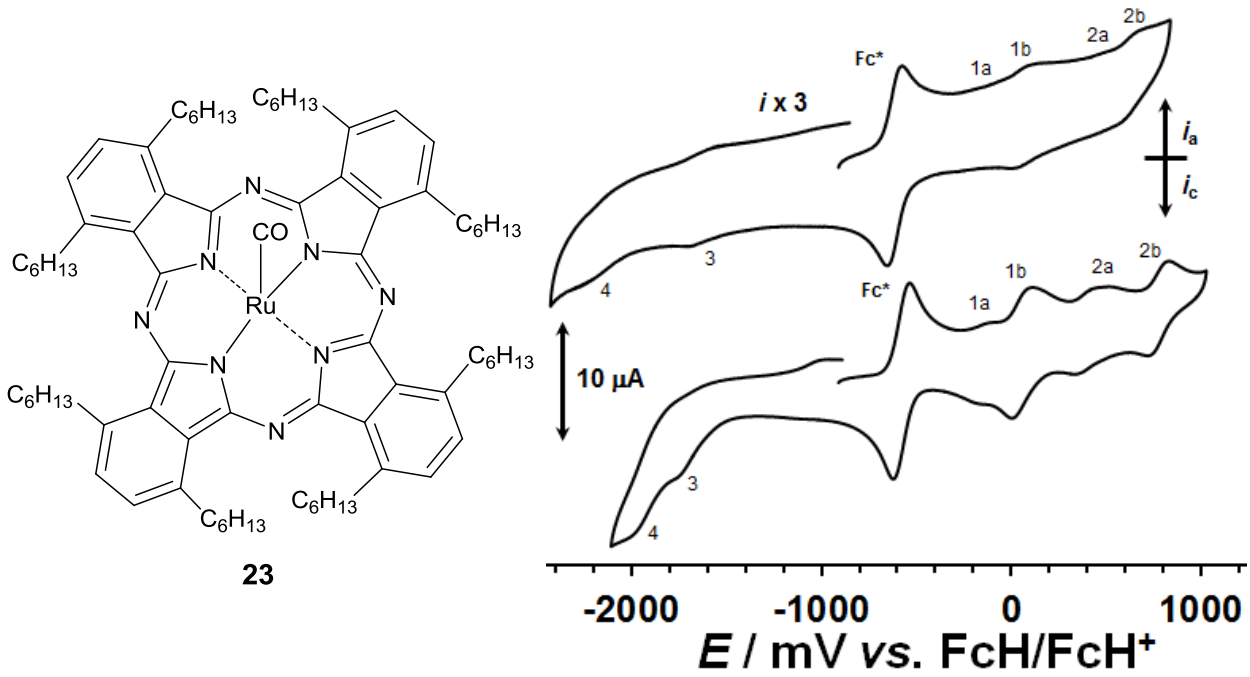

Figure 3.22: Left: The structure of **23**. **Right bottom:** CV of a 0.5 mM DCM solution of **23** containing 0.1M $[N(^nBu)_4][B(C_6F_5)_4]$ obtained at a scan rate of 100 mV/s. **Right top:** CV of **23** in pure CH_3CN obtained at a scan rate of 100 mV/s. To make peaks more observable, currents were multiplied with 3.

In DCM, the compound showed more oxidation waves than expected, waves 1a, 1b, 2a and 2b, as was indicated in Figure 3.22, *right top* and *bottom*. The poor resolution of waves 1a and 2a disallowed measurements of these waves. The addition of a drop of CH_3CN or repeating the experiment in pure CH_3CN, did not remove any satellite (small) peaks, waves 1a and 2a, Figure 3.22, *top*. This may suggest an impure compound. Main oxidation waves 1b and 2b in pure DCM represented an electrochemical ($\Delta E < 90$ mV) and chemical ($i_{pc}/i_{pa} \rightarrow 1$) reversible process at slow scan rates. Waves 3 and 4 are the reduction waves and are poorly resolved in both experiments, DCM and DCM with a drop of CH_3CN. They cannot be interpreted compared to compounds **24** to **29**. Table 3.15 summarizes all CV data for the 100 mV/s scan rate (see Appendix C for larger scan rates).

3.5.3.2 *p*-[OPh(o,p-tert(Butyl)$_2$)]$_8$-PcRu(CO), 24

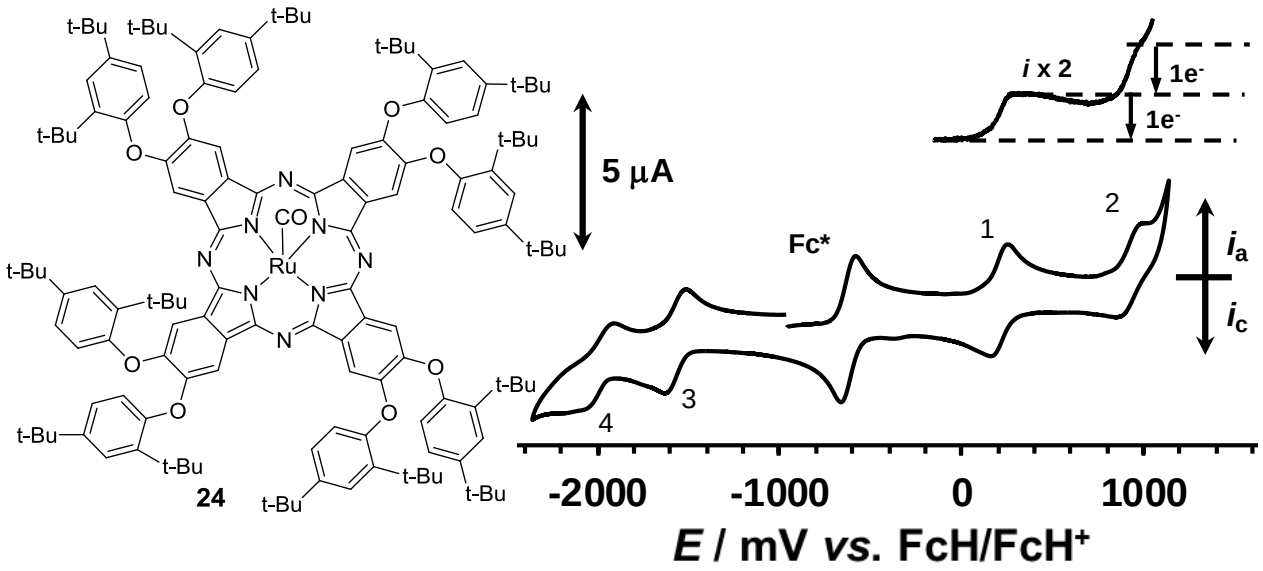

Figure 3.23: Left: The structure of **24**. **Right bottom:** CV of a 0.5 mM DCM solution of **24** containing 0.1M $[N(^nBu)_4][B(C_6F_5)_4]$ obtained at a scan rate of 100 mV/s. **Right top:** LSV at 1 mV s' showing waves 1 and 2 both represented processes in which the same number ($1e^-$) of electrons are being transferred, because the CV $\Delta E < 90$ mV for wave 1.

Waves 1 and 2, in Figure 3.23, represent the oxidative processes, while waves 3 and 4 are representing reductive redox processes. Expect for wave 2, the system is chemically reversible ($i_{pc}/i_{pa} \rightarrow 1$), but only wave 1 is electrochemically reversible ($\Delta E < 90$ mV). No dimerization, aggregation or impurity of this compound was observed at CV concentration level, 0.5 mM. This compound with the bulky *tert*-butyl substituents on the phenoxy groups at the peripheral position gave ideal CV's. Table 3.15 summarizes all CV data for the 100 mV/s scan rate (see Appendix C for larger scan rates). The electrochemical Scheme 3.18 that best resemble the electrochemical behaviour of this compound, **24**, is given below. This is a typical one electron transfer process.

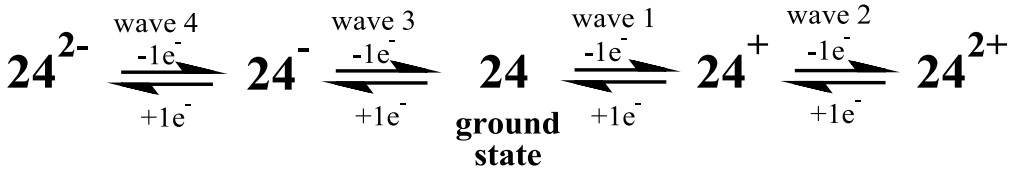

Scheme 3.18: An electrochemical scheme explaining the redox properties of the compound *p*-[OPh(*o,p*-tert(Butyl)$_2$)]$_8$-PcRu(CO), **24**.

3.5.3.3 *p*-(C_6H_{13})$_8$-PcRu(CO), 25

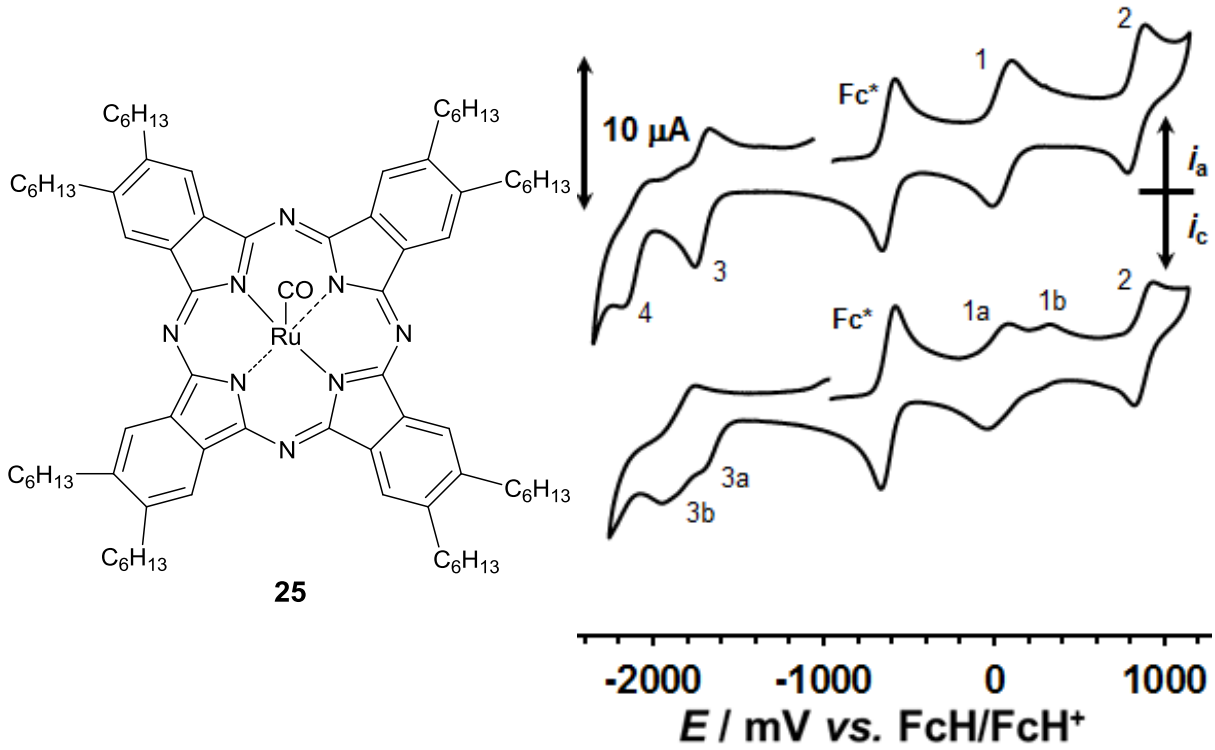

Figure 3.24: Left: The structure of **25**. **Right bottom:** Cyclic voltammogram of a 0.5 mM DCM solution of **25** containing 0.1M [N(^{n}Bu)$_4$][B(C_6F_5)$_4$] obtained at a slow scan rate of 100 mV/s. **Right top:** Cyclic voltammogram of **25** after the addition of a drop of CH_3CN obtained at 100 mV/s.

Waves 1 and 2 represent the oxidative processes, while waves 3 and 4 are representing reductive redox processes in Figure 3.24, *right top*. The electrochemical scheme below is proposed to explain the observed redox behaviour of compound **25** in DCM. There are signs of dimerization for this compound. By comparing results to that of **25**, dimerization (or at least partial dimer, i.e. aggregation) is a feasible explanation for the observed electrochemical fingerprint.

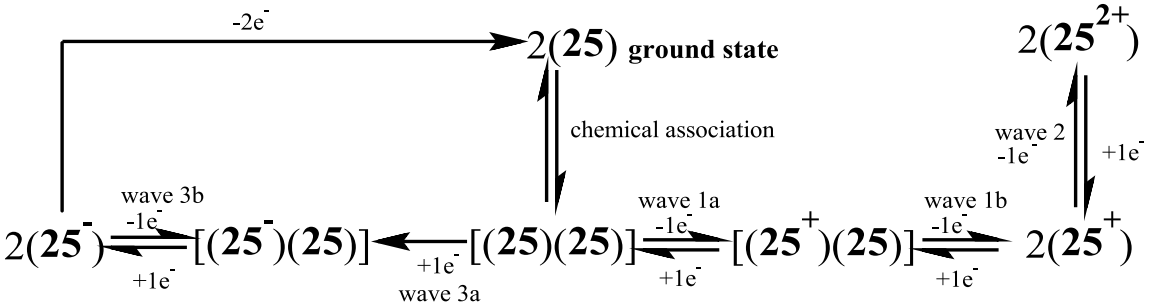

Scheme 3.19: An electrochemical scheme explaining the dimerization or at least partial dimer i.e. aggregation of *p*-(C_6H_{13})$_8$-PcRu(CO), **25**, in DCM.

The addition of a drop of CH_3CN broke the coordinative or aggregative dimerization as indicated by the absence of wave 1b and 3b. A second reduction wave, 4, is detected. All processes except the oxidative process associated with wave 1b are electrochemically irreversible ($\Delta E > 90$ mV). In both solvents, oxidation processes (wave 1, 2) are more chemically reversible ($i_{pc}/i_{pa} \rightarrow 1$), than reduction processes. In the presence of CH_3CN, the electrochemical scheme of **25** is the same as that of complex **24** in DCM. Table 3.15 summarizes all CV data for the 100 mV/s scan rate (see Appendix C for larger scan rates).

3.5.3.4 *np*-$(OC_5H_{11})_8$-PcRu(CO)(CH_3CN), 26

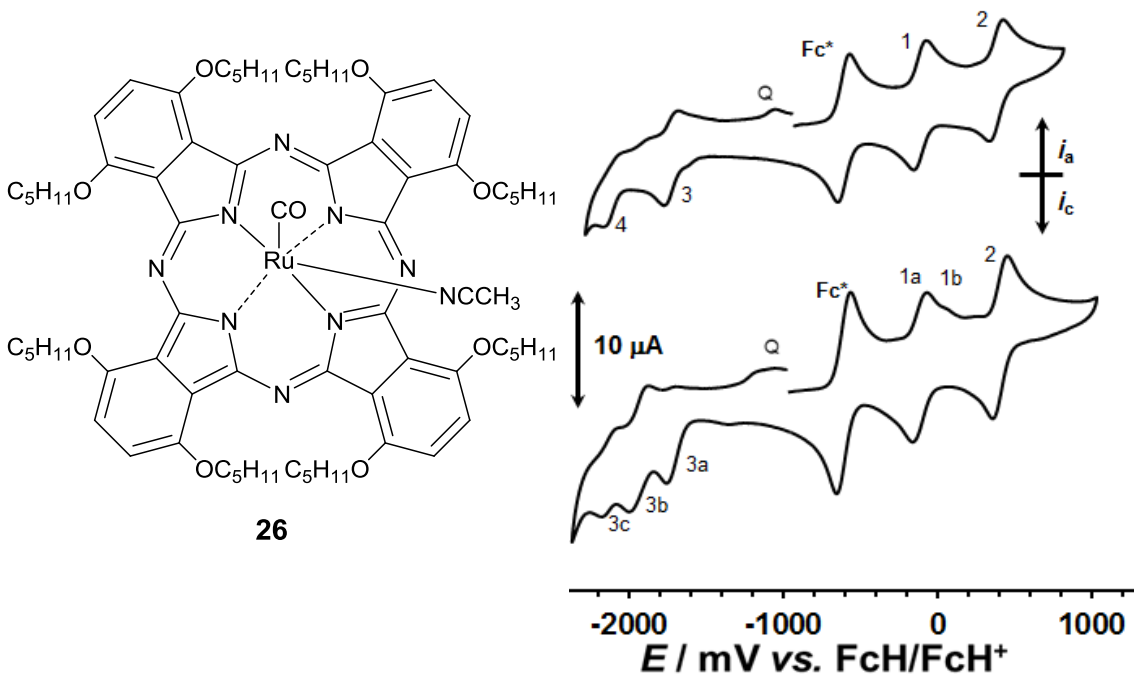

Figure 3.25: Left: The structure of **26**. **Right bottom:** CV of a 0.5 mM DCM solution of **26** containing 0.1M $[N(^nBu)_4][B(C_6F_5)_4]$ obtained at a slow scan rate of 100 mV/s. **Right top:** CV of **26** after the addition of a drop of CH_3CN obtained at 100 mV/s.

In pure DCM, oxidation processes represented by, wave 1 and 2, approached chemical ($i_{pc}/i_{pa} \rightarrow 1$) and electrochemically reversibility ($\Delta E \rightarrow 59$ mV), as shown in Figure 3.25, The reduction half wave 1b associated with the oxidative half wave 1b, was not detected in DCM. If overlapped with reductive half wave 1a, cathodic reduction processes, in DCM, were more complex, wave 3b and 3c approached chemical reversibility ($i_{pc}/i_{pa} \approx 1$), while wave 3a were chemically irreversible ($i_{pc}/i_{pa} < 1$). In DCM containing a drop of CH_3CN, oxidation processes which are associated with waves 1 and 2 were electrochemically ($\Delta E < 90$ mV) and chemically ($i_{pc}/i_{pa} \rightarrow 1$) reversible, while reduction processes were electrochemically quasi

reversible ($90 < \Delta E < 110$ mV) (wave 3) or irreversible ($\Delta E > 90$ mV) (wave 4). It is clear that for wave 3, addition of a drop of CH_3CN simplified the electrochemical response, when compared to that observed in pure DCM. Waves 3a, 3b and 3c, in pure DCM, coalesced into one single wave 3 in the mixed solvent system. In addition, in the mixed solvent system, a second reductive process could be clearly identified and is labelled wave 4. The electrochemical path this compound follows in the presence of CH_3CN duplicates that observed for **24** in pure DCM. Table 3.15 summarizes all CV data for the 100 mV/s scan rate (see Appendix C for larger scan rates).

The electrochemical scheme showed below are suggested to explain the redox properties of *np*-$(OC_5H_{11})_8$-PcRu(CO)(CH_3CN), **26**, in pure DCM, where x is the relative fraction of **26** that possibly losing its axial ligands and "b" represents the branch of oxidize **26**, $\mathbf{26}^+$ that dimerize with still un-oxidized **26** to generate a dimer, [(**26**)($\mathbf{26}^+$)].

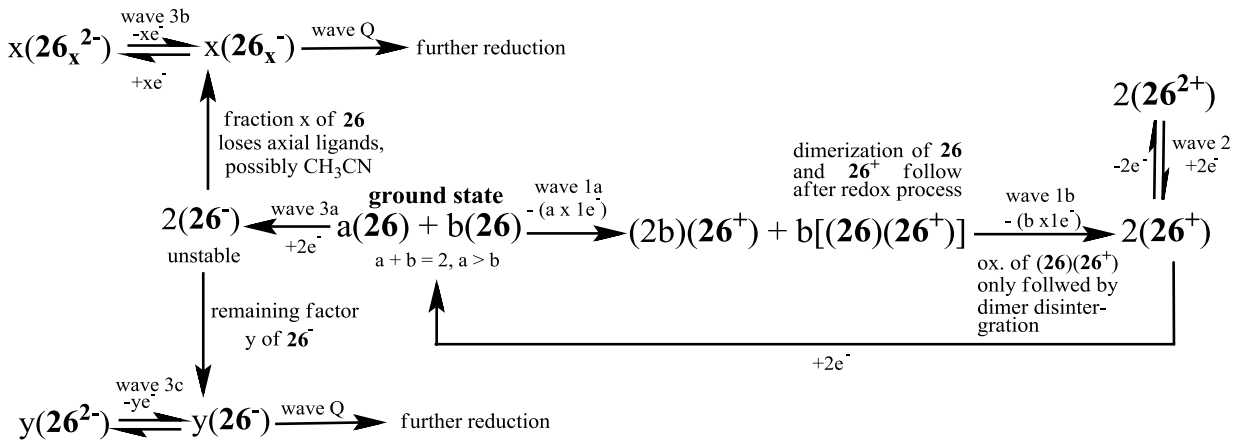

Scheme 3.20: The electrochemical redox sequence of *np*-$(OC_5H_{11})_8$-PcRu(CO)(CH_3CN), **26**, in DCM (in the absence of only CH_3CN added).

3.5.3.5 *p*-$(OC_5H_{11})_8$-PcRu(CO), 27

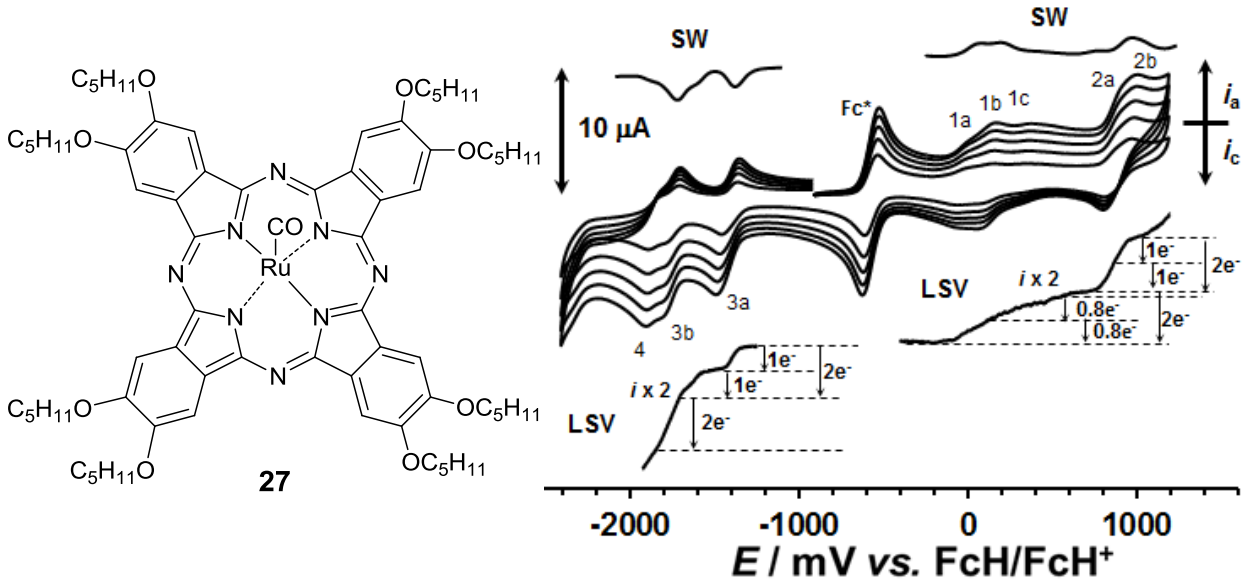

Figure 3.26: Left: The structure of **27**. **Right: Top:** Square wave voltammograms for cathodic and anodic processes at scan rates of 20 Hz, respectively, for **27** in DCM. **Right: Middle:** CV, at 100 (smallest current), 200, 300, 400 and 500 mV/s for a 0.5 mM DCM solution of **27** containing 0.1M $[N(^nBu)_4][B(C_6F_5)_4]$. **Right: Bottom:** LSV of **27** in DCM at 1 mV/s. The anodic and cathodic processes show the sum of the same amount of electrons being transferred.

Figure 3.26 shows compound **27** in DCM, where the oxidation processes which are associated with waves 1a and 1 b were chemically ($i_{pc}/i_{pa} \approx 1$) and electrochemically reversible ($\Delta E < 90$ mV), although wave 1c was not. Wave 2b is only chemically reversible and electrochemically irreversible ($\Delta E > 90$ mV). The reduction processes of waves 3a, 3b and 4 were electrochemically reversible and chemically irreversible. Compound **27** gave clear indication of dimerization in DCM, (by virtually add a, b and c components in the redox processes associated with waves 1, 2 and 3). The scheme below shows the electrochemical sequence that is assigned to clarify the observed redox processes for this compound in the DCM experiment.

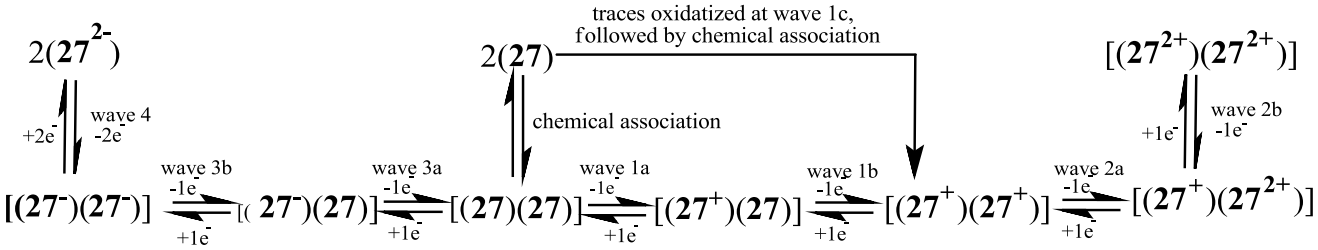

Scheme 3.21: The electrochemical scheme for *p*-$(OC_5H_{11})_8$-PcRu(CO), **27**, in DCM

Figure 3.27 shows that in the case where a drop of CH_3CN was added to the DCM solution, compound **27**, undergoes oxidation processes (wave 1 and 2) that approaches chemical reversibility ($i_{pc}/i_{pa} \rightarrow 1$). They were however, electrochemically irreversible ($\Delta E > 90$ mV). The reduction process of wave 3 was chemically and electrochemically reversible. Wave 4 was chemically reversible and electrochemically irreversible.

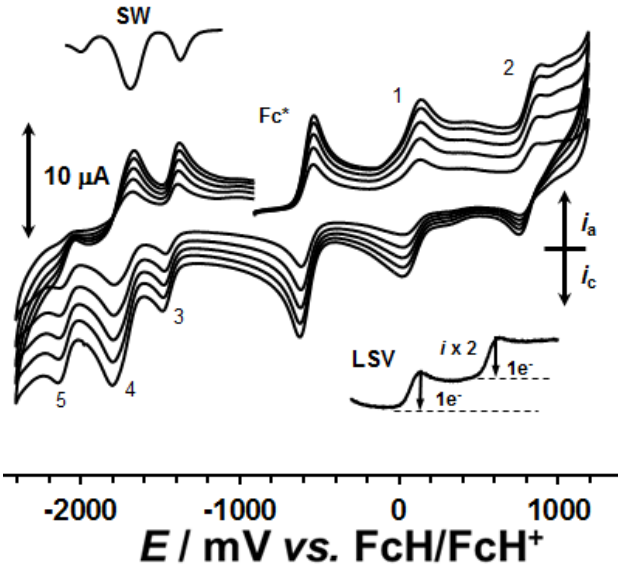

Figure 3.27: Top: Square wave voltammogram of the cathodic process of **27** at a scan rate of 20 Hz. **Middle:** Overlayed cyclic voltammograms of **27** after the addition of a drop of CH_3CN at different scan rates (100, 200, 300, 400 and 500 mV/s). **Bottom:** LSV of waves 1 and 2, at 1 mV/s. Both waves represent a one electron transfer process.

The electrochemical sequence on the next page is an illustration of what was observed in the CV's of **27** in DCM containing a drop of CH_3CN.

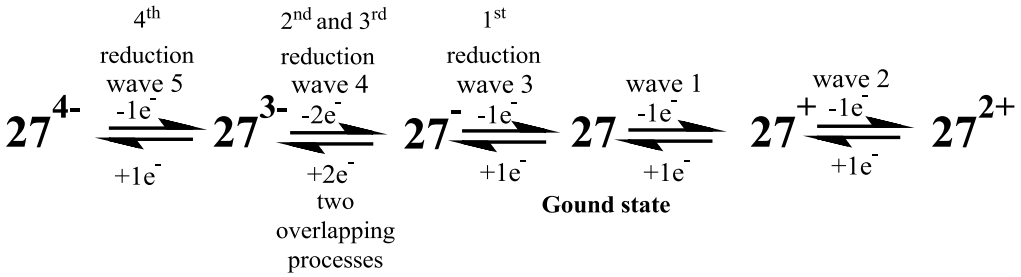

Scheme 3.22: The electrochemical schematic for the redox process of *p*-$(C_5H_{13}O)_8$-PcRu(CO), **27**

It is unclear why the 2rd and 3rd reduction is observable at wave 4 under these experimental conditions. Once a drop of CH_3CN was added, association to dimeric species is prevented by axial ligation of CH_3CN. Waves 1a, 1b, and 1c coalesce to form, in the presence of CH_3CN, predominantly a single wave, wave 1. The same happens to waves 2a, 2b and wave 3. Table 3.15 summarizes all CV data for the 100 mV/s scan rate (see Appendix C for larger scan rates).

3.5.3.6 *np*-$(OC_4H_9)_8$-PcRu(CO)(R), 28 where the second axial ligand, py, is pyridine

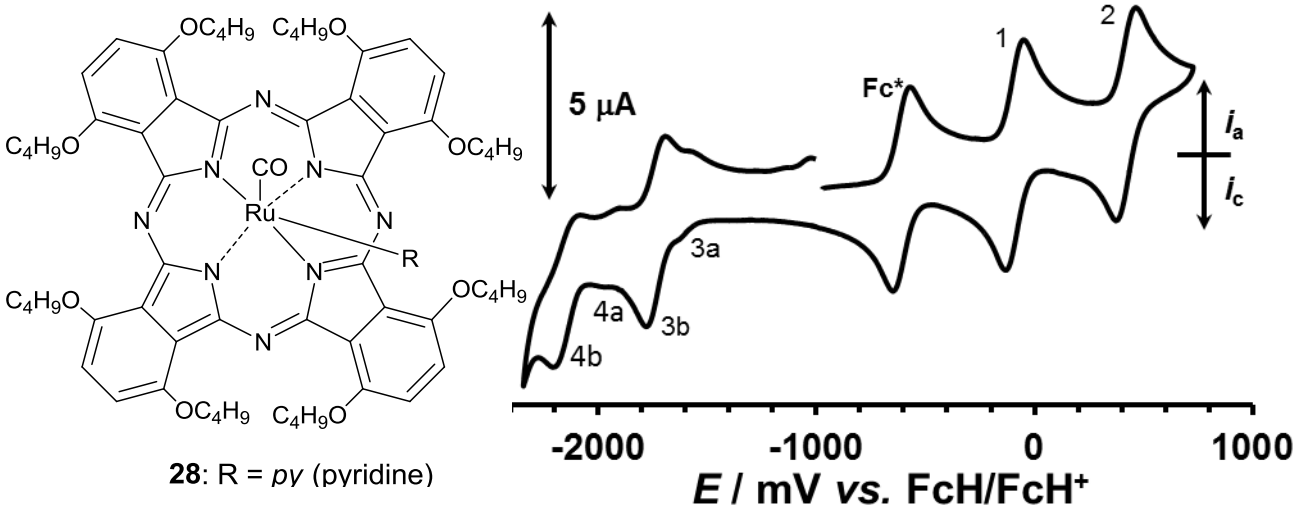

Figure 3.28: Left: The structure of **27**. **Right:** The cyclic voltammogram of a 0.5 mM DCM solution of **28** containing 0.1M $[N(^nBu)_4][B(C_6F_5)_4]$ obtained at a scan rate of 100 mV/s.

In pure DCM, the observed oxidation processes of wave 1 was chemically ($i_{pc}/i_{pa} \approx 1$) and electrochemically ($\Delta E < 90$ mV) reversible, while that of wave 2 was electrochemically irreversible ($\Delta E > 90$ mV) and chemically reversible. For the reduction processes, waves 3b and 4b were considered as the main peaks. Waves 3a, 3b and 4a were electrochemically reversible ($\Delta E < 90$ mV), while wave 4b was electrochemically irreversible ($\Delta E > 90$ mV).

Waves 3b and 4b were chemically irreversible ($i_{pc}/i_{pa} > 1$), while waves 3a and 4a is chemically reversible ($i_{pc}/i_{pa} \approx 1$).

If one ignores the smaller waves 3a and 4a, the electrochemical scheme, associated with the CV of this compound, replicates that of **24**. *np*-$(OC_4H_9)_8$-PcRu(CO)(py), is the first compound, after **26**, which exhibited ideal electrochemical behaviour. The presence of CO axial ligands can be related to waves 3a and 4a, while wave 3b and 4b is consistent with just pyridine as axial ligand. Table 3.15 summarizes all CV data for the 100 mV/s scan rate (see Appendix C for larger scan rates).

3.5.3.7 *np*-$(OC_4H_9)_8$- PcRu(CO)(R), 29 where the second axial ligand, R, is $NH(CH(CH_3)_2)_2$

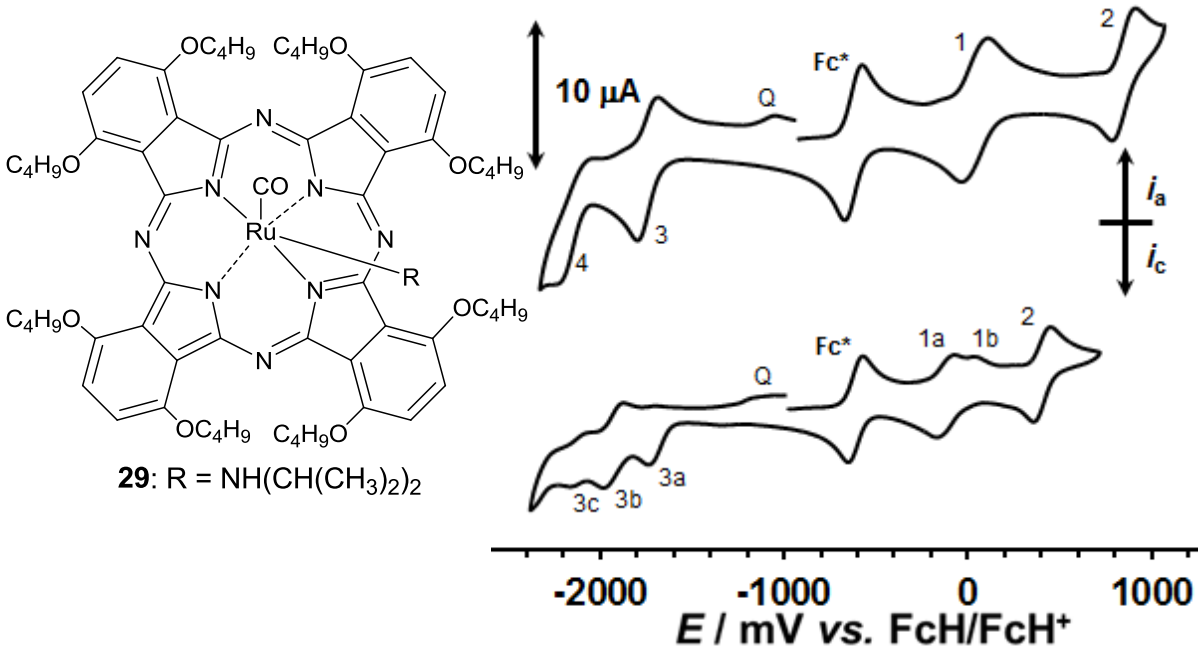

Figure 3.29: Left: The structure of **29**. **Right bottom:** CV of a 0.5 mM DCM solution of **29** containing 0.1M $[N(^nBu)_4][B(C_6F_5)_4]$ obtained at a scan rate of 100 mV/s. **Right top:** CV of **29** after the addition of a drop of CH_3CN at a scan rate of 100 mV/s.

Figure 3.29 shows the voltammograms of **29** in pure DCM (*right bottom*) and in DCM containing a drop of CH_3CN (*right top*). In pure DCM, wave 1 split into two components (a) and (b) which most likely indicates dimerization after a first portion of **29** was oxidized. The observed reduction processes, as illustrated by the CV, are comparatively the same as **24**. The oxidation processes in pure DCM, waves 1a and 2, were electrochemically reversible ($\Delta E \rightarrow 59$ mV) and approached chemically reversible ($i_{pc}/i_{pa} \rightarrow 1$). For the reduction

processes, waves 3b and 3c, by virtue of larger than ideal ΔE values were electrochemically quasi reversible (90 < ΔE < 110 mV) and only weakly approaches chemical reversibility (0.8 < i_{pc}/i_{pa} < 0.9 µA). The position of the oxidative half wave of wave 3a is an artefact of the smallness of i_{pa} relative to the i_{pa} of 3b, causing a false "measured" E_{pa} giving ΔE = 42 < 59 mV. This is electrochemically impossible; implying the species that was oxidized in the forward scan is not exactly the same as the species that generates wave 3a upon reduction during the reverse scan. Alternatively the oxidative peak potential of wave 3a is shifted due to media property changes upon generating different redox species. The electrochemical fingerprint of **29** duplicates that described for **24** in DCM.

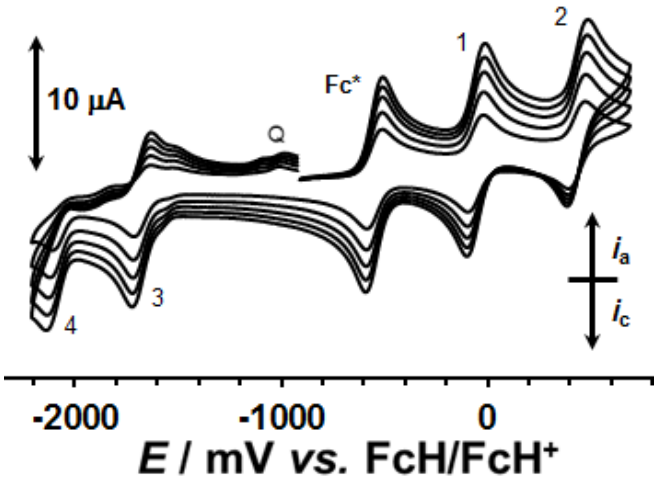

Figure 3.30: Overlayed voltammograms of **29** after addition of a drop of CH_3CN at varying scan rates (100, 200, 300, 400 and 500 mV/s.)

Figure 3.30 shows the overlayed cyclic voltammograms of **29**, in DCM containing a drop of CH_3CN at scan rates 100 to 500 mV/s. In, the oxidation processes, waves 1 and 2, and the reduction processes, waves 3 and 4, were electrochemically irreversible (ΔE > 90 mV). Waves 1 and 2 approached chemical reversibility ($i_{pc}/i_{pa} \rightarrow 1$), while waves 3 and 4 were chemically irreversible ($i_{pc}/i_{pa} < 1$). In the presence of a drop of CH_3CN, an electrochemical scheme equivalent to that of **24** in DCM is valid. Table 3.15 summarizes all CV data for the 100 mV/s scan rate (see Appendix C for larger scan rates) as well as the half-wave potentials ($E^{0'}$-values) for [(*t*-Bu)$_4$PcRu(CO)] and [PcRu(py)(CO)], related two compounds found in literature.[6, 7]

Table 3.15: Cyclic voltammetry data of 0.5 mmol dm^{-3} solutions at scan rate 100 mV/s of **23-29** in pure DCM (left) or containing a drop of CH_3CN (right), at 25 °C, supporting electrolyte 0.1 mol dm^{-3} $[N(^nBu)_4][B(C_6F_5)_4]$.

Wave	E_{pa}, mV	ΔE_p, mV	$E^{o'}$, mV	i_{pa}, µA	i_{pc} / i_{pa}	Wave	E_{pa}, mV	ΔE_p, mV	$E^{o'}$, mV	i_{pa}, µA	i_{pc} / i_{pa}
***np*-$(C_6H_{13})_8$-PcRu(CO), 23, in DCM**						[a] ***np*-$(C_6H_{13})_8$-PcRu(CO), 23, in CH_3CN**					
1a [g]						1a [g]					
1b	110	94	63	0.99	0.94	1b	93	76	55	0.18	1.01
2a [g]						2a [g]					
2b	830	104	778	0.72	0.96	2b	672	75	634	0.21	0.97
3 [g]	-1776 [b]					3	-1614 [b]	76	-1654	0.18 [c]	0.87 [d]
4 [g]	-1887					4	-2090 [b]	106	-2143	0.20 [c]	0.81 [d]
***p*-[OPh(*o*,*p*-$^tBu_2$)]$_8$-PcRu(CO), 24, in DCM**						[e] ***p*-[OPh(*o*,*p*-$^tBu_2$)]$_8$-PcRu(CO), 24, in DCM with a drop of CH_3CN**					
1	234	86	191(130) [h]	3.85	1.04	1a					
2	990	118	931	2.30	1.24	1b					
3	-1501 [b]	112	-1552 (-1100) [h]	2.30 [c]	1.24 [d]	2	Not performed				
4	-1898 [b]	250	-2020	*1.8* [c]	0.60 [d]	3a					
***p*-$(C_6H_{13})_8$-PcRu(CO), 25, in DCM**						***p*-$(C_6H_{13})_8$-PcRu(CO), 25, in DCM with a drop of CH_3CN**					
1a	102	96	54	1.96	0.95	1	95	90	45	1.96	0.98
1b	287	89	332	1.6	0.94	1b [f]					
2	883	110	938	1.87	0.94	2	882	90	837	2.45	0.98
3a [g]	-1685					3	-1685 [b]	81	-1726	2.76 [c]	1.10 [d]
3b	-1947 [b]	202	-1866	2.28 [c]	0.94 [d]	3b [f]					
4 [f]						4	-2034 [b]	98	-2083	2.31 [c]	1.08 [d]
***np*-$(OC_5H_{11})_8$-PcRu(CH_3CN)(CO), 26, in DCM**						***np*-$(OC_5H_{11})_8$-PcRu(CH_3CN)(CO), 26, in DCM with a drop of CH_3CN**					
1a	-79	94	-126	2.04	1.08	1a	119	109	64	2.57	1.02
1b [g]	61			0.82		1b [f]					
2	462	90	418	2.25	1	2	912	102	861	2.77	0.96
3a	-1701 [b]	67	-1735	2.44 [c]	0.74 [d]	3	-1635 [b]	99	-1685	3.25 [c]	0.97 [d]
3b	-1894 [b]	109	-1949	1.63 [c]	0.98 [d]	4	-2000 [b]	172	-2087	2.74 [c]	1.03 [d]
3c	-2094 [b]	114	-2126	1.63 [c]	0.81 [d]						
***p*-$(OC_5H_{11})_8$-PcRu(CO), 27, in DCM**						***p*-$(OC_5H_{11})_8$-PcRu(CO), 27, in DCM with a drop of CH_3CN**					
1a	13	70	-22	1.78	1.07	1	125	91	79	1.89	0.94
1b	151	63	119	1.62	1	1b [f]					
1c [g]	362					1c [f]					
2a [g]	884					2	845	90	800	1.78	1.02
2b	954	141	884	1.48	1.03	2b [f]					
3a	-1360 [b]	92	-1406	2 [c]	0.87 [d]	3	-1390 [b]	79	-1430	1.48 [c]	0.99 [d]
3b	-1709 [b]	97	-1758	1.63 [c]	1.09 [d]	3b [f]					
4	-1801 [b]	81	-1841	2.59 [c]	0.49 [d]	4	-1675 [b]	184	-1767	2.88 [c]	0.97 [d]
5						5	-2044 [b]	82	-2085	1.48 [c]	1.05 [d]
***np*-$(OC_4H_9)_8$-PcRu(CO)(py), 28, in DCM**						[e] ***np*-$(OC_4H_9)_8$-PcRu(CO)(py), 28, in DCM with a drop of CH_3CN**					
1	12	83	-30	2.79	1.03	1					
2	528	92	482 (450) [i]	2.59	1.05	2					
3a	-1510 [b]	75	-1547	0.58 [c]	1.11 [d]	3	Not performed				
3b	-1625 [b]	88	-1669	2.79 [c]	1.05 [d]						
4a	-1846 [b]	64	-1878	0.49 [c]	1.07 [d]	4					
4b	-2025 [b]	112	-2081	1.79 [c]	1.09 [d]						
***np*-$(OC_4H_9)_8$-PcRu(CO)(D), 29, in DCM**						***np*-$(OC_4H_9)_8$-PcRu(CO)(D), 29, in DCM with a drop of CH_3CN**					
1a	-44	93	-90	2.22	1.01	1	-30	85	-72	2.81	1.01
1b [g]	74					1b [f]					
2	450	67	416	3.11	0.98	2	430	77	392	2.81	1
3a	-1608 [b]	62	-1639	2.48 [c]	0.75 [d]	3	-1636 [b]	69	-1671	2.88 [c]	0.97 [d]
3b	-1847 [b]	96	-1895	2.00 [c]	0.96 [d]	3b [f]					
3c	-2047 [b]	97	-2096	1.63 [c]	0.66 [d]	4	-2033 [b]	65	-2066	1.63 [c]	0.66 [d]

[a] The data was collected in pure CH_3CN. [b] E_{pc} values are given. [c] i_{pc} values are given. [d] i_{pa}/i_{pc} values are given.
[e] This experiment wasn't done. [f] The waves was not observed. [g] Poor resolution disallowed further measurements.
[h] The data of a 0.01mmol dm^{-3} solution of [(*t*-Bu)4PcRu(CO)] in DCM and TBAP as supporting electrolyte at a scan rate of 100 mV/s^{-1}, as found in reference 6.
[i] The data of a 0.05 mmol dm^{-3} solution of [PcRu(py)(CO)] in 0.05M DCM and $[^tBu_4N][PF_6]$ as supporting electrolyte at a scan rate of 100 mV/s^{-1}, as found in reference 7.

The half-wave potentials of compounds *p*-[OPh(*o*,*p*-$^tBu_2$)]$_8$-PcRu(CO), **24** and *np*-$(OC_4H_9)_8$-PcRu(CO)(py), **28** showed good correlations between that of (*t*-Bu)$_4$-PcRu(CO)[6] and PcRu(py)(CO)[7].

3.5.3.8 The influence of substituent or ligand changes

The influence of the type and position of substituent and ligand changes of compounds **23-29** are discussed by utilizing Table 3.15 and Figure 3.31.

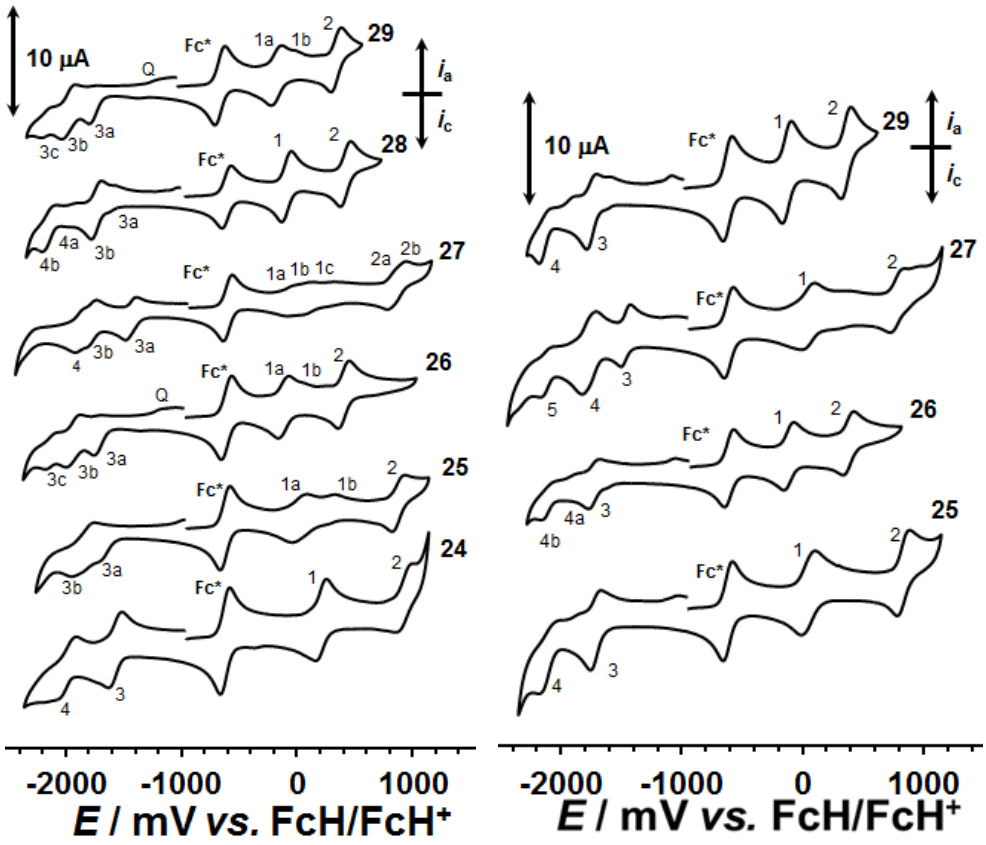

Figure 3.31: Left: Cyclic voltammograms of **24-29** in pure DCM, **Right:** Cyclic voltammograms of **25-27** and **29** in DCM containing a drop of CH_3CN, obtained at a scan rate of 100 mV/s.

1) By comparing peak potentials of **23** (CV not shown in Figure 3.31, but in Figure 3.22) and **25**, the influence of the position of the 8 non-peripheral or 8 peripheral alkyl (hexyl) groups can be assessed. By comparing results in DCM it is found that wave 2 oxidation potential for **25** is larger than that of **23** by 160 mV. When the results of **23** (in CH_3CN) are compared to that of **25** (in DCM containing a drop of CH_3CN) the oxidation potentials for **25** are more positive than that of **23**. From these results it appears that the peripheral alkyl substituents pumps electron density (e.g. ± 200 mV) more effectively into the macrocycle, although literature suggests that a larger increase in electron density should be suspected from an electron-donating substituent

on the non-peripheral position.[8] Possibly the Ru (II) coordination is the reason the respected trend was reversed. It is likely that the Ru^{II}-CO pumps so much electron density into the macrocycle that the alkyl groups become relatively electron with-drawing compared to Ru^{II}-CO. In such a case the observed trend of higher redox potentials for **25** would fit and the non-peripheral position would allow better electronic communication with the macrocycle than the peripheral position.

2) For compounds **24** and **25**, by replacing 8 peripheral phenoxy groups with 8 peripheral alkyl (hexyl) groups, the electron-donating effect between the phenoxy and alkyl substituents can be compared. The peripherally substituted hexyl groups increases the electron density of the macrocycle more than the phenoxy groups substituents, thus causing a shift to the less positive potentials for waves 1, 2 and 3 with 132, 107 and 184 mV, respectively.
3) The difference between peripheral substituents in **24** and **27** reports a switch from an aromatic (phenoxy) substituent to an aliphatic (pentoxy) substituent. This resulted in the lowering of formal oxidation potentials of wave 1 with approximately 220 mV in **27** compared to **24**. Wave 2 oxidation potentials were almost unchanged ($\Delta E^{o'}$ = 47 mV). Wave 3a, the first reduction process, moved with 146 mV and wave 4 moved 179 mV to more positive potentials in **27**. From the change in the formal oxidation potentials, it can be concluded that the aromatic substituent more effectively stabilizes the reduced macrocyclic core, but less effectively stabilizes the oxidized macrocyclic core.
4) By comparing peak potentials of **25** and **27**, the influence of an alkyl (hexyl) and alkoxide (pentoxy) peripheral substituents, respectively, may be assessed. Comparing results in DCM it was found that the alkoxide substituted derivative **27** exhibited first peak oxidation potentials smaller than the alkyl substituted derivatives **25** as follows: wave 1, (-76 mV). The reduction peak potentials were shifted the opposite direction. The negative potential shift was 107 mV (wave 3b). Comparing results in DCM containing a drop of CH_3CN, it was found that the alkoxide substituted derivative **27** exhibited first peak oxidation potentials slightly larger than the alkyl substituted derivatives **25** as follows: wave 1, (+30 mV). However, peak reduction potentials were shifted the opposite direction compared to DCM. Here, the alkyl derivative **25** showed $E^{o'}$ values at larger potentials. These negative potential shifts were -296 mV (wave 3) and -316 mV (wave 4). From the results in DCM containing a drop of

CH_3CN, it can be concluded that the alkoxide substituted compound **27** are less electron-donating than the alkyl substituted compound **25**.

5) By comparing **26** (axial ligands CO and CH_3CN) with **28** (axial ligands CO and pyridine), in pure DCM, the peak oxidation potentials of **28** exhibited peak potentials more positive than those of **26**. The peak reduction potentials of **26** were more negative than that of **28**. If wave 3a of **28** is ignored, wave 3a, 3b and 3c of compound **26** and wave 3b, 4a and 4b of compound **28** showed a difference of between 48 and 75 mV. From the results it can be concluded that the acetonitrile axial ligand for **26** are stronger electron-donating ligand, which increases the electron density of the macrocycle more than the pyridine axial ligand of **28**, because all potentials of **26** are smaller (less negative) than those of **28**.
6) By comparing **26** (axial ligands CO and CH_3CN) with **29** (axial ligands CO and (-$NH(CH(CH_3)_2)_2$), the influence of the addition of CH_3CN on the different axial ligands can be compared. Comparing results in DCM containing a drop of CH_3CN it was found that **26** exhibited peak oxidation potentials larger than **29**, with wave 1, +149 mV, and wave 2, +482 mV. However, peak reduction potentials of **29** were more negative or the same (with wave 3, -1 mV) as that of **26**, and wave 4, -33 mV. Comparing results in DCM for **26** (axial ligands CO and CH_3CN) and **29** (axial ligands CO and (-$NH(CH(CH_3)_2)_2$), it was found that **26** exhibited peak oxidation and reduction potentials smaller than **29** (wave 1b was ignored), with differences of -35, -12, -93, -47 mV for waves 1, 2 and 3a-c, respectively. The results in DCM showed that the tertiary amine (-$NH(CH(CH_3)_2)_2$) axial ligand of **29** are less electron-donating than the acetonitrile axial ligand, however only the oxidation peak potentials of the results in DCM containing a drop of CH_3CN, showed the same trend.
7) The difference in axial ligands of **28** (axial ligands CO and pyridine) and **29** (axial ligands CO and (-$NH(CH(CH_3)_2)_2$), was compared in pure DCM. Results showed that waves 1, 2, 3b, 4a and 4b of compound **28** shifted to more positive (larger) potentials with 56, 78, 16, 1 and 22 mV, respectively, in comparison to waves 1, 2, 3b, 3b and 3c of **29**. The tertiary amine (-$NH(CH(CH_3)_2)_2$) axial ligand of **29** is more electron-donating, which increases the electron density of the macrocycle more than the pyridine axial ligand of **28**.

3.6 Computational study of the ruthenium phthalocyanines, 23-29

To determine the optimized geometry and properties of the series of (CO)RuPcs, **23-29**, of which the electrochemistry was presented in section 3.5.3, a computational chemistry study was done. The structures and complex numbers are given in Scheme 3.23.

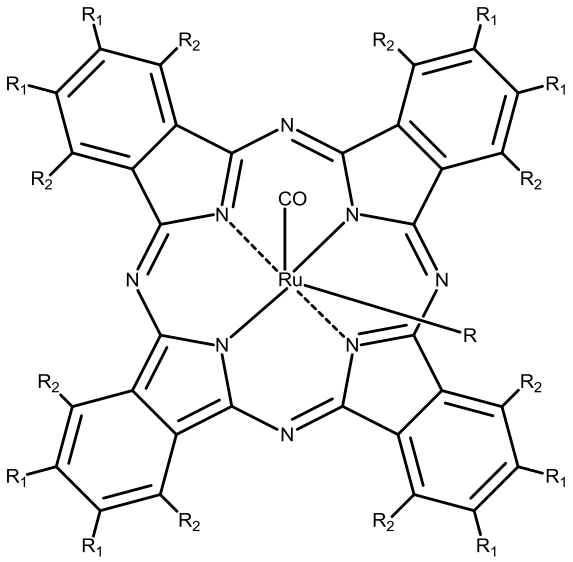

(23) R = no axial ligand; R_2 = -C_6H_{13}; **(23a) R = no axial ligand; R_2 = -C_2H_{13};**
(24) R = no axial ligand; R_1 = -OPh(o.p-Me)]; **(24a) R = no axial ligand; R_1 = -OPh;**
(25) R = no axial ligand; R_1 = -C_6H_{13}; **(25a) R = no axial ligand; R_1 = -C_2H_5;**
(26) R = $NCCH_3$; R_2= -O(C_5H_{11}); **(26a) R = $NCCH_3$; R_2 = -OCH_3;**
(27) R = no axial ligand; R_1= -O(C_5H_{11}); **(27a) R = no axial ligand; R_2 = -OCH_3;**
(28) R = pyridine; R_2 = -O(C_4H_9); **(28a) R = pyridine; R_2 = -OCH_3;**
(29) R = N($CH(CH_3)_2$)$_2$; R_2 = -O(C_4H_9); **(29a) R = N($CH(CH_3)_2$)$_2$; R_2 = -OCH_3**

Scheme 3.23: (CO)RuPcs, **23-29** and **23a-29a** with various substituents and secondary axial ligands, R = $NCCH_3$, pyridine and N($CH(CH_3)_2$)$_2$.

Compounds, **23-29** (Scheme 3.23), were optimized utilizing B3LYP functional and the 6-311G(d,p) basis set on all atoms except Ru for which the def2tzvpp basis set was used. Simplified ruthenium phthalocyanine structures, **23a-29a**, were also optimized in order to compare them to the more complex ruthenium phthalocyanine structures, **23-29**.

The geometry for the optimized structures, **23a-29a** and **23-29**, will be discussed in sections 3.6.1 and 3.6.2, respectively. The reliability of the optimized geometry obtained by means of DFT calculations utilizing the B3LYP functional, was confirmed by comparing it to the geometry of an X-ray crystal structure[9] for a related PcRu($HNQu)_2$ found in literature.

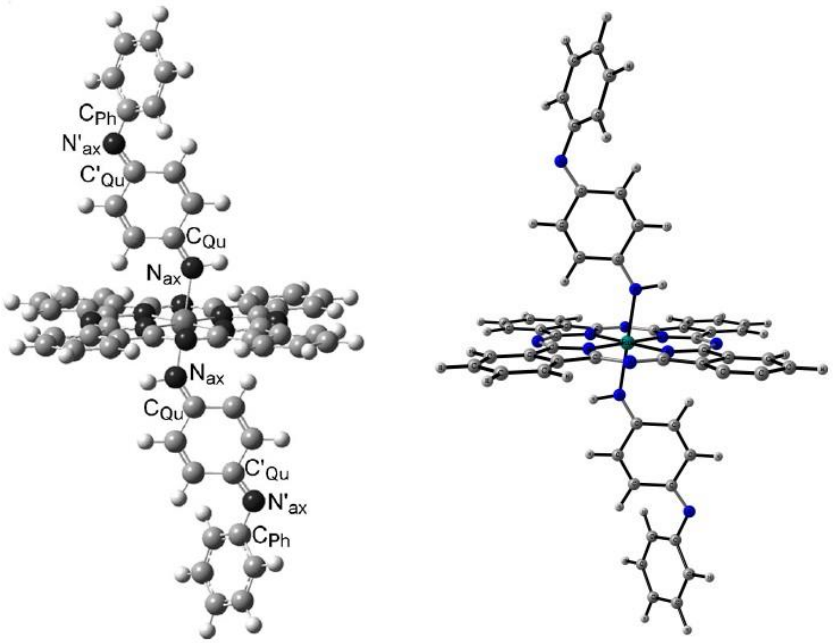

Figure 3.32: Left: The structure of $PcRu(HNQu)_2$ with labelled atoms[9] **Right:** The DFT-optimized structure of $PcRu(HNQu)_2$ using B3LYP.

The DFT optimized structure of $PcRu(HNQu)_2$ using B3LYP/6-311G(d,p) are showed on the right-hand side and the relevant nitrogen and carbon atoms for $PcRu(HNQu)_2$ are labelled on the left of Figure 3.32. Table 3.16 shows the bond lengths and angles, of $PcRu(HNQu)_2$, determined X-ray crystal analysis[9] and the DFT-optimized structure.

Table 3.16: Selected bond lengths [Å] and angles [°] in DFT-optimized $PcRu(HNQu)_2$ structure using the B3LYP/6-311G(d,p) functional.

$PcRu(HNQu)_2$	**Experimental[a]**	**Calculated**	**Difference between experimental and calculated data**
$d(Ru\text{-}N_{iso})$[b] [Å]	1.992, 2.005	2.014	0.022, 0.009
$d(Ru\text{-}N_{py})$ [Å]	2.075	2.068	0.007
$d(C_{Qu}\text{-}N_{py})$ [Å]	1.294	1.309	0.015
$d(N'_{ax}\text{-}C'_{Qu})$ [Å]	1.311	1.298	0.013
$d(N_{ax}\text{-}C_{Ph})$ [Å]	1.430	1.394	0.036
Angle ($Ru\text{-}N_{ax}\text{-}C_{Qu}$ [°]	139.8	141.5	1.7
Angle ($C'_{Qu}\text{-}N'_{ax}\text{-}C_{Ph}$) [°]	122.4	123.9	1.5

[a] Determined by X-ray crystal structure analysis from literature.[9] [b] N_{iso} coordinated N atoms of the Pc ligand.

The axial ligands are slightly non-linear with respect to the ruthenium metal centre with the average angle (N_{ax}-Ru-N_{ax}) of 170.2° (experimental) and 179.6° (calculated). The bond lengths and angles of the DFT-optimized structure using B3LYP are in agreement with those determined by X-ray crystal analysis of $PcRu(HNQu)_2$.[9] It can be concluded that the geometry determined by DFT calculation utilizing the B3LYP functional are reliable and can be extended to the geometries determined for **23a-29a** and **23-29**.

3.6.1 Simplified phthalocyanines, 23a-29a

Figure 3.33 below indicates the nitrogen and carbon atoms and their descriptions (where N_{ax} is the coordinated N atom of the axial ligand, N_{iso} is the coordinated N atom of the Pc ring and C_{ax} is the coordinated C atom of the axial ligand) which will be used throughout the geometry discussion of the various ruthenium phthalocyanine compounds, **23a-29a** and **23-29**.

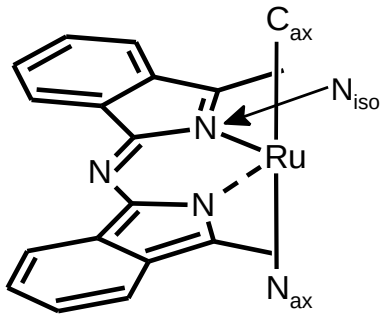

Figure 3.33: The relevant nitrogen and carbon atoms and their description.

Firstly, the bulky hexyl, pentoxy, butoxy and *tert*-butylphenoxy groups on the (CO)RuPcs, **23-29**, were replaced with similar but simpler substituents, namely ethyl, methoxy and phenoxy to give simplified models, **23a-29a**. This simplification to **23a-29a** was done to reduce CPU time needed to optimize the central structure of the molecules before adding the bulky substituents to the complexes. By comparing the optimized geometries and molecular orbital energies of the simplified complexes, **23a-29a** to that of **23-29,** the effect of the substituents on the phthalocyanine ring as well as the secondary axial ligand on the ruthenium metal of the complex ruthenium phthalocyanines can be discussed and better understood. Optimized geometries of the simplified structures **23a-29a** are shown in Figure 3.34.

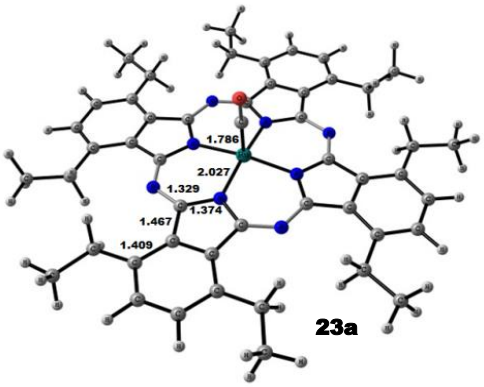

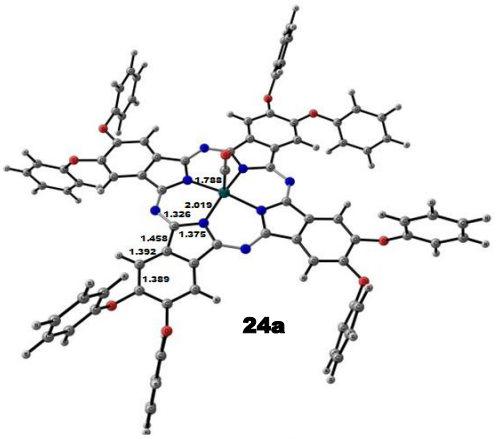

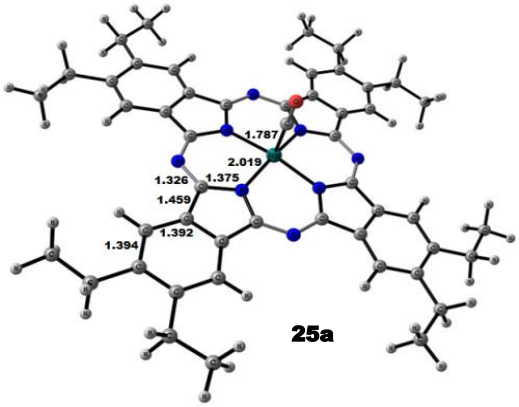

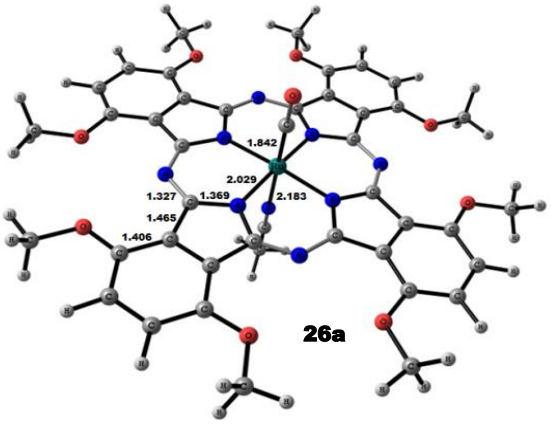

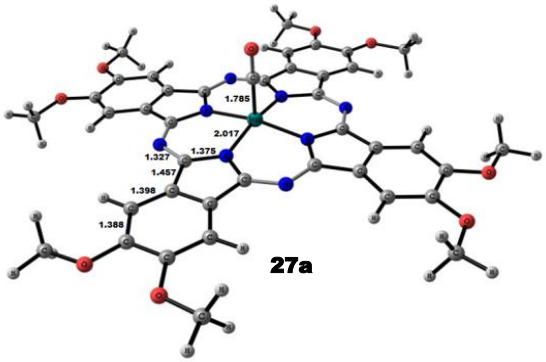

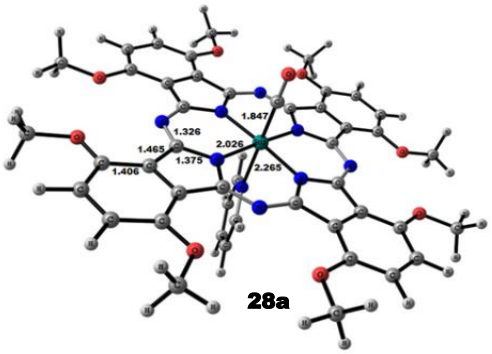

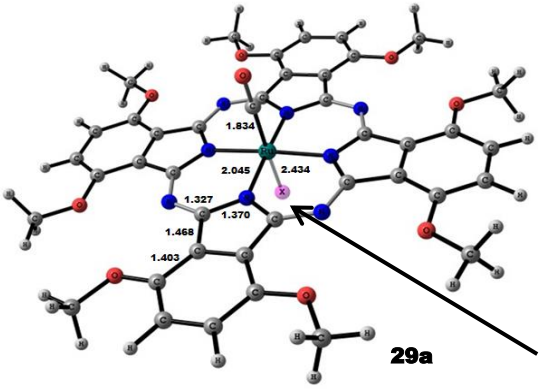

The axial ligand **X**, for **29a** is given below, to clarify structure:

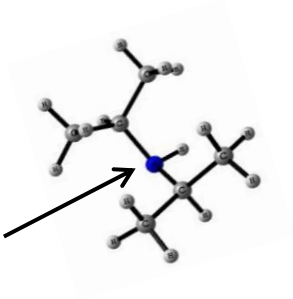

Nitrogen atom (right) bonds to Ru, bond indicated by Ru-X bond (left)

Figure 3.34: Selected bond distances (Å) of the B3LYP/6-311G(d,p) optimized complexes **23a-29a**, respectively.

From an input without any symmetry, compounds **23a-29a** spontaneously optimized to nearly C_s-symmetry. All bond lengths and angles for the optimized structures of **23a-29a** are showed in Table 3.18, section 3.6.2.

The optimized structural data for **23a-29a** revealed that the macrocycle for all these compounds assumes a flat conformation. The Ru-N_{iso} distances for **23a-29a** are similar to the Ru-N_{iso} distances found in the X-ray diffraction data for PcRu(HNQu)$_2$ and PcRu(4-Mepy)$_2$.[9, 10] From literature the X-ray diffraction data of PcRu(4-Mepy)$_2$ showed a Ru-N_{iso} distance of 1.991 and 1.985 Å, and PcRu(HNQu)$_2$ showed a Ru-N_{iso} distance 1.992 and 2.005 Å, while the Ru-N_{iso} distances for **23a-29a**, were found to be between 2.017 and 2.028 Å. No significant changes in the C-N_{iso} bond lengths (where C is the carbon in the Pc ring bound to N_{iso}) were observed for all the (CO)RuPcs, **23a-29a**.

The distance of Ru-C_{ax} remains unchanged at ~ 1.785(2) Å for the 5-coordinated complexes **23a-25a** and **27a**. The Ru-N_{ax} bond lengths for PcRu(4-Mepy)$_2$ showed a distance of 2.101 Å for the two identical 2-methylpyridine axial ligands, while PcRu(HNQu)$_2$ showed a Ru-N_{ax} distance of 2.075 Å,[9, 10] which is smaller than the Ru-N_{ax} bond in complexes **26a**, **28a** and **29a**. The Ru-N_{ax} bond lengths of the 6-coordinated compounds, **26a**, **28a** and **29a**, having a CO ligand as the fifth ligand, the effect of the different secondary axial ligands (the sixth ligand) namely acetonitrile (-$NCCH_3$), pyridine (-NC_5H_5) and tertiary amine (-$NH(CH(CH_3)_2)_2$), showed an increase in Ru-N_{ax} length. The Ru-N_{ax} bond length for the bulky tertiary amine ligand, **29a**, is the longest, followed by pyridine, **28a**, and then the acetonitrile ligand, **26a**, with bond lengths of 2.434, 2.266 and 2.183 Å, respectively. The increase in Ru–N_{ax} distances for *np*-$(OC_5H_{11})_8$PcRu(CO)($NCCH_3$), **26a**, **28a** and **29a** can be due to the contribution of the π-back bonding from Ru to the carbonyl axial ligand, weakening the opposite Ru-N_{ax} bond. The longer Ru–N_{ax} bond lengths are related to ease of replacement, thus tertiary amine ligand of **29a** should be displaced the easiest. The Ru-C_{ax} bond for complexes **26a**, **28a** and **29a** are stretched, to 1.842, 1.847 and 1.834 Å, respectively.

3.6.2 Full experimental phthalocyanines, 23-29

After optimization of compounds **23-29**, the macrocycle of complexes **23**, **26**, **28**, and **29** containing non-peripheral substituents became slightly non-planar molecules. The non-planar deformation observed for **23**, **26**, **28**, and **29** are called saddled and the degree of

saddling are measured by the CCCC torsion angle illustrated in Figure 3.35 for *np*-$(OC_4H_9)_8$-PcRu(CO)(N(CH$(CH_3)_2)_2$, **29**.

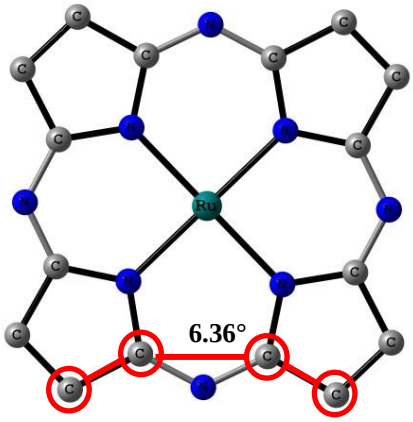

29

Figure 3.35: A simplified structure of *np*-$(OC_4H_9)_8$PcRu(CO)(N(CH$(CH_3)_2)_2$, **29**, showing the average of the saddling dihedral angles.

A saddled conformation can be described when the isoindole rings of the macrocycle are tilted alternately up and down, almost as rigid bodies. The dihedral angle, formed by the isoindole units on either side of the phthalocyanine core for **29** for example, is on average 6.36°, Figure 3.35. The non-planar conformations and dihedral angles of compounds **23a-29a** and **23-29** are summarized in Table 3.17. The distortions from planar for the ruthenium phthalocyanines were due to steric interactions between non-peripheral substituents. For compounds **23**, **26**, **28** and **29**, the dihedral angle increased when the bulkier substituents were introduced on the Pc-ring of the compounds, however no significant change was observed for the complexes having peripherally substituted ligands.

The saddled conformation have been observed, for example, in *np*-$(Ph)_8$-PcZn by Fukuda and co-workers,[11] and also Jinwan and co-workers.[12] Recently, Huang and co-workers reported a planar phthalocyanine ring, for three phosphine complexes of ruthenium phthalocyanines through X-ray crystallography.[13]

Table 3.17: Summary of non-planar conformations and their dihedral angles for the peripherally and non-peripherally substituted ruthenium phthalocyanines, **23a-29a** (**bottom**) and **23-29** (**top**).

Full experimental compounds	**Dihedral Angle (°)**	**Conformation**
23, *np*-$(C_6H_{13})_8$-PcRu(CO)	2.39	Saddled
24, *p*-[OPh(o,p-Me)]$_8$PcRu(CO)	0.36	Flat
25, *p*-$(C_6H_{13})_8$-PcRu(CO)	0.02	Flat
26, *np*-$(OC_5H_{11})_8$PcRu(R)(CO), R = $NCCH_3$	3.58	Saddled
27, *p*-$(OC_5H_{11})_8$-PcRu(CO)	0.36	Flat
28, *np*-$(OC_4H_9)_8$PcRu(CO)(R), R = Pyridine (py)	6.90	Saddled
29, *np*-$(OC_4H_9)_8$PcRu(CO)(R), R=$NH(CH(CH_3)_2)_2$	6.36	Saddled
Simplified compounds	**Dihedral Angle (°)**	**Conformation**
23a, *np*-$(CH_3)_8$-PcRu(CO)	0.18	Flat
24a, *p*-$(OPh)_8$PcRu(CO)	0.36	Flat
25a, *p*-$(CH_3)_8$-PcRu(CO)	0.08	Flat
26a, *np*-$(OCH_3)_8$PcRu(R)(CO), R = $NCCH_3$	0.02	Flat
27a, *p*-$(OCH_3)_8$-PcRu(CO)	0.03	Flat
28a, *np*-$(OCH_3)_8$PcRu(CO)(R), R = Pyridine (py)	0.03	Flat
29a, *np*-$(OCH_3)_8$PcRu(CO)(R), R=$NH(CH(CH_3)_2)_2$	0.75	Flat

Selected geometry parameters of the optimized geometries of **23a-29a** and **23-29**, are shown in Table 3.18.

Table 3.18: The bond lengths (Å) and angles (°) of compounds **23a-29a** (**bottom**) and **23-29** (**top**).

Full experimental compounds	**Bond lengths (Å)**			**Angles (°)**		
	d(Ru-N_{iso})	**d(Ru-C_{ax})**	**d(Ru-N_{ax})**	**Cax-Ru-N_{iso}**	**N_{ax}-Ru-C_{ax}**	**Nax-Ru-N**
23, *np*-$(C_6H_{13})_8$-PcRu(CO)	2.026	1.786	n/a	95.83	n/a	n/a
24, *p*-[OPh(o,p-Me)]$_8$PcRu(CO)	2.018	1.788	n/a	96.28	n/a	n/a
25, *p*-$(C_6H_{13})_8$-PcRu(CO)	2.019	1.787	n/a	96.26	n/a	n/a
26, *np*-$(OC_5H_{11})_8$PcRu(R)(CO), R = $NCCH_3$	2.028	1.843	2.185	92.59	179.720	87.753
27, *p*-$(OC_5H_{11})_8$-PcRu(CO)	2.018	1.785	n/a	96.59	n/a	n/a
28, *np*-$(OC_4H_9)_8$PcRu(CO)(R), R = Pyridine (py)	2.027	1.847	2.267	92.16	179.791	88.738
29, *np*-$(OC_4H_9)_8$PcRu(CO)(R), R=$NH(CH(CH_3)_2)_2$	2.022	1.831	2.440	91.77	174.747	91.328
Simplified compounds	**Bond lengths (Å)**			**Angles (°)**		
	d(Ru-N_{iso})	**d(Ru-C_{ax})**	**d(Ru-N_{ax})**	**Cax-Ru-N_{iso}**	**N_{ax}-Ru-C_{ax}**	**Nax-Ru-N**
23a, *np*-$(CH_2CH_3)_8$-PcRu(CO)	2.027	1.786	n/a	95.77	n/a	n/a
24a, *p*-$(OPh)_8$PcRu(CO)	2.019	1.788	n/a	96.21	n/a	n/a
25a, *p*-$(CH_2CH_3)_8$-PcRu(CO)	2.019	1.787	n/a	96.27	n/a	n/a
26a, *np*-$(OCH_3)_8$PcRu(R)(CO), R = $NCCH_3$	2.029	1.842	2.183	92.55	179.981	87.435
27a, *p*-$(OCH_3)_8$-PcRu(CO)	2.017	1.785	n/a	96.49	n/a	n/a
28a, *np*-$(OCH_3)_8$PcRu(CO)(R), R = Pyridine (py)	2.026	1.847	2.265	92.11	180.0	87.877
29a, *np*-$(OCH_3)_8$PcRu(CO)(R), R=$NH(CH(CH_3)_2)_2$	2.028	1.834	2.434	91.83	174.377	84.733

The Ru-N_{iso} and Ru-C_{ax} bond lengths, for **23-29**, remained unchanged when compared to that of **23a-29a**. Similar to section 3.6.1, the Ru-N_{iso} distances for **23-25** and **27** are longer than Ru-C_{ax}, while the Ru-N_{iso} and Ru-C_{ax} distances are shorter than Ru-N_{ax} in cases, **26**, **28** and **29**. The bond angle **(**C_{ax}-Ru-N_{iso}) for **26**, **28** and **29** remained similar to that of **26a**, **28a** and **29a**. The axial ligands were linear with respect to the ruthenium metal centre with an angle (N_{ax}-R-C_{ax}) of ~180°, for **26** and **28**; however the angle for **29** were slightly non-linear with a value of 175°. In the crystal structure of PcRu(py)(CN), diffraction studies showed that the axial ligands were slightly non-linear with respect to the ruthenium metal, with an average angle (N_{ax}-R-C_{ax}) of 175°.[10] From the structural data collected, on the simplified and more complex ruthenium phthalocyanines, it becomes clear that the non-peripheral position on the phthalocyanine rings have a larger effect on the dihedral angle than the peripheral position.

After comparing the geometries of the simplified compounds, **23a-29a**, to that of **23a-29a**, it can be concluded that the simplified model, **23a-29a**, gave reliable insight into the possible bond lengths and bond angles of the full experimental model, **23-29**. However, the influence of the substituents on the on the deformation of the macrocycle could only be comprehended when the full experimental model, **23-29**, was optimized.

3.6.3 Frontier Orbital Energies

The energies of the HOMO (highest occupied molecular orbital) and LUMO (lowest unoccupied molecular orbital) of the optimized ruthenium phthalocyanines structure, **23a-29a**, and **23-29** are summarized in Table 3.19.

Upon comparing the HOMO-LUMO gap of the simplified compounds, **23a-29a**, to that of **23-29**, it can be concluded that the simplified models only give a reliable value if the substituents are on the peripheral position. However, the contributions of the bulkier substituents at non-peripheral positions on the macrocycle cannot be understood without the full experimental model, **23**, **26**, **28** and **29**.

Table 3.19: The HOMO and LUMO energies for **23-29** (**left**) and **23a-29a** (**right**).

Compounds	HOMO (eV)	LUMO (eV)	HOMO-LUMO gap (eV)	Compounds	HOMO (eV)	LUMO (eV)	HOMO-LUMO gap (eV)
23, *np*-$(C_6H_{13})_8$-PcRu(CO)	-5.07	-2.9	2.17	**23a**, *np*-$(C_2H_5)_8$-PcRu(CO)	-5.04	-2.82	2.22
24, *p*-[OPh(o,p-Me)]$_8$-PcRu(CO)	-5.22	-2.97	2.28	**24a**, *p*-$(OPh)_8$-PcRu(CO)	-5.31	-3.03	2.28
25, *p*-$(C_6H_{13})_8$-PcRu(CO)	-4.92	-2.63	2.29	**25a**, *p*-$(C_2H_5)_8$-PcRu(CO)	-4.96	-2.67	2.29
26, *np*-$(OC_5H_{11})_8$-PcRu(R)(CO), R = $NCCH_3$	-4.65	-2.51	2.14	**26a**, *np*-$(OCH_3)_8$-PcRu(R)(CO), R = $NCCH_3$	-4.26	-2.10	2.16
27, *p*-$(OC_5H_{11})_8$-PcRu(CO)	-4.80	-2.50	2.30	**27a**, *p*-$(OCH_3)_8$-PcRu(CO)	-4.88	-2.58	2.30
28, *np*-$(OC_4H_9)_8$-PcRu(CO)(R), R = Pyridine (py)	-4.64	-2.53	2.11	**28a**, *np*-$(OCH_3)_8$-PcRu(CO)(R), R = Pyridine (py)	-4.73	-2.36	2.37
29, *np*-$(OC_4H_9)_8$-PcRu(CO)(R), R=$NH(CH(CH_3)_2)_2$	-4.70	-2.61	2.09	**29a**, *np*-$(OCH_3)_8$-PcRu(CO)(R), R=$NH(CH(CH_3)_2)_2$	-4.80	-2.44	2.36

The combined molecular orbital (MO) energy level diagram, for compounds **23-29**, is illustrated in Figure 3.36. The MO energy level diagram shows the HOMO-LUMO gap, HOMO-1 and LUMO+1. The LUMO and LUMO+1 are well separated for compounds **25** and **27**, while the LUMO and LUMO+1 separation for compounds **23**, **24**, **28** and **29** are notably smaller. The LUMO+1 for **26** are nearly degenerate with the LUMO. The HOMO and HOMO-1 separation for **24** and **27** are small in comparison to that of the remaining compounds. The near-degeneracy of the LUMO and the LUMO+1 for all complexes except **25**, is in agreement with the Gouterman four-orbital model of a typical metalloporphyrin.[14, 15] According to this model, the two highest occupied molecular orbitals (HOMOs) and two of the lowest unoccupied molecular orbitals (LUMOs) are near degenerate, located on the metalloporphyrin macrocycle, and these four molecular orbitals (MOs) are energetically well separated from the other MOs. The LUMO and LUMO+1 for complexes **23**, **25-29** are indeed also energetically well separated from the other MOs and located on the macrocycle of the phthalocyanine (see Section 3.6.4). The HOMO and HOMO-1 of complexes **23-29** are not near degenerate. The large % Ru on the HOMO-1 of complexes **23-29** (see Section 3.6.4) causes the energy of the HOMO-1 to be much lower than the energy of the HOMO that is phthalocyanine based. DFT calculations on (^{t}BuNC)$_2$FePc and (FcNC)$_2$FePc by Nemykin and co-workers, also found that the LUMO and LUMO+1 were nearly degenerate and located on the phthalocyanine, while the HOMO-1 was of Fe-metal character and of lower energy

than the HOMO that was phthalocyanine based where the lowest unoccupied molecular and LUMO-1 were nearly degenerate.[16]

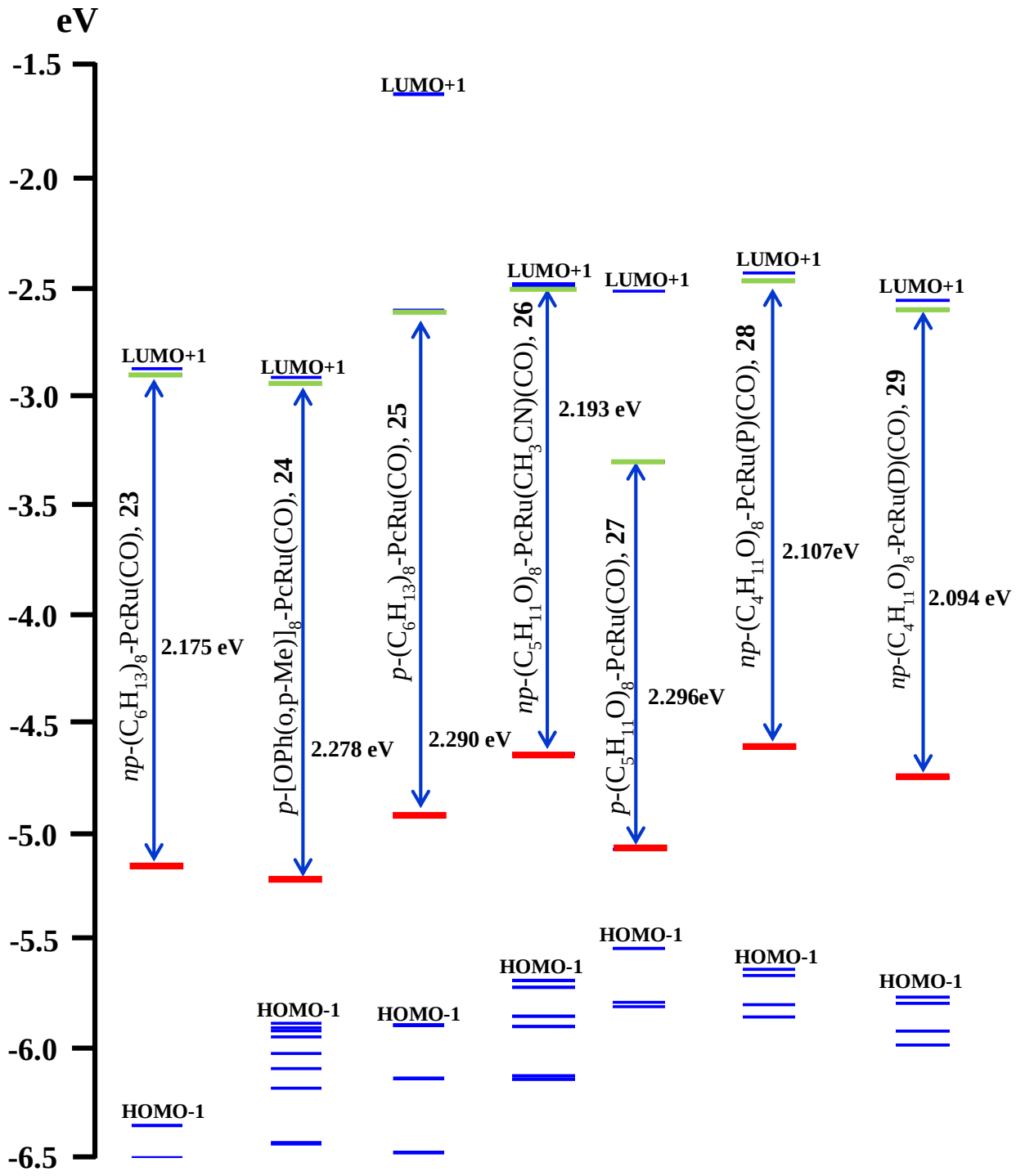

Figure 3.36: The energy level diagram of **23-29**, where the HOMO-LUMO gap energy, HOMO and LUMO are indicated in red and green, respectively. Note that the second axial ligands; P for **28** and D for **29** are pyridine and $NH(CH(CH_3)_2)_2$, respectively.

3.6.4 Molecular Orbital view of phthalocyanines, 23a-29a

Table **3.20** shows a depicted of the molecular orbital views of compound **26a** and **26**. It is clear that the depiction that the addition of the substituents have no big effect on the character of the HOMO or LUMO of this compound. According to the classic Gouterman's four orbital model, the frontier molecular orbitals should be π-orbital of a_{1u}, a_{2u} (both occupied) and e_g (unoccupied) symmetries. The HOMO for compound **26**, as well as **26a** are located on the phthalocyanine ring and have an a_{1u} π-orbital character, while the LUMO and LUMO+1 showed an e_g π-orbital character.

Table 3.20: The molecular orbitals for PcRu(R)(CO) compounds **26a** and **26**, where R = CH_3CN.

Compound	HOMO -1	HOMO	LUMO	LUMO +1
26a, *np*-$(CH_3O)_8$-PcRu(R)(CO) R = CH_3CN	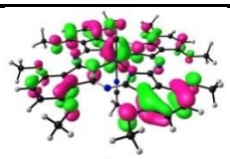	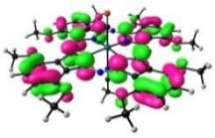	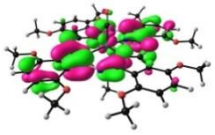	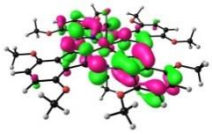
26, *np*-$(C_5H_{11}O)_8$-PcRu(R)(CO) R = CH_3CN	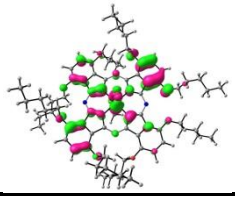	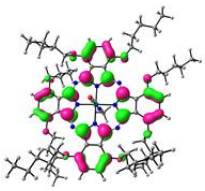	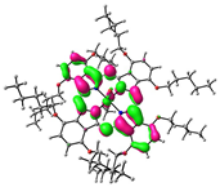	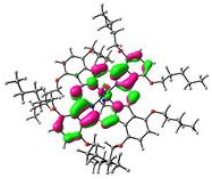

The HOMO, LUMO or LUMO+1 for compounds **23-29** (see Appendix D), give the same results as **23a-29a**. In the DFT calculations presented in Table 3.21, the HOMO has a_{1u} π-orbital character while the LUMO and LUMO+1 e_g π-orbital character for all complexes, **23a-29a**. These results are in agreement with the classic Gouterman's orbital model. The HOMO for **23a-29a** are exclusively located on the phthalocyanine ring, with a nearly C_4-symmetry. The LUMO and LUMO+1 of **23a-29a** indicated a small additional contribution by the CO-axial ligand while the majority are located on the phthalocyanine ring with a small which have an equivalent C_2-symmetry.

The HOMO-1 of compounds, **23a-29a**, shows a large contribution by the Ru-metal (d_π-orbital character). Compound **23a** shows the largest Ru d_π-orbital character by HOMO-1 (28%), while **26a** and **27a** both show a contribution of 14%. An a_{2u} π-orbital character was showed by HOMO-1 for **29a** with a 27% Ru d_π-character. The character of the frontier molecular

orbitals (MOs) of the experimental complexes **23-29** (Appendix D) is similar to the frontier MOs of **23a-29a** (Table 3.21).

Table 3.21: The molecular orbitals for compounds **23a-29a**.

Compound	HOMO -1	HOMO	LUMO	LUMO +1
23a, *np*-$(CH_2CH_3)_8$-PcRu(CO)		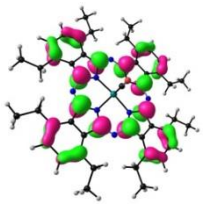	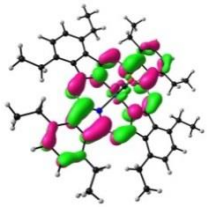	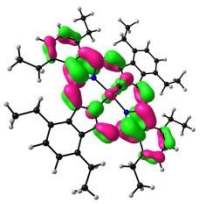
24a, *p*-$(PhO)_8$-PcRu(CO)	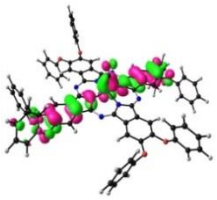	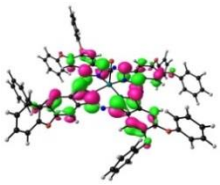	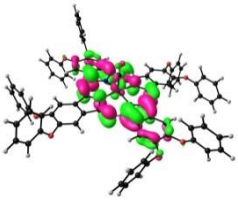	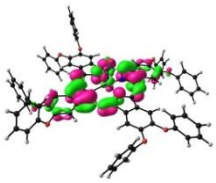
25a, *p*-$(CH_2CH_3)_8$-PcRu(CO)	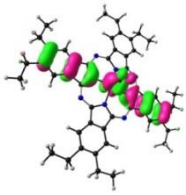	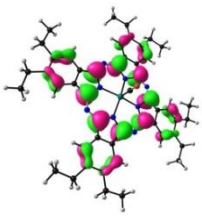	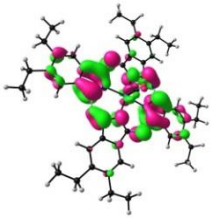	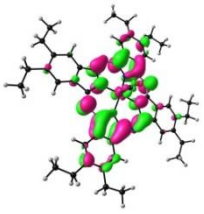
26a, *np*-$(CH_3O)_8$-PcRu(CO)(CH_3CN)	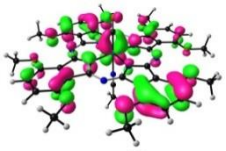	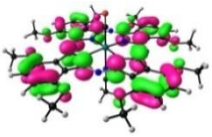	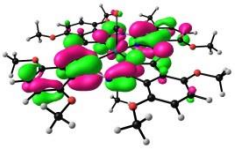	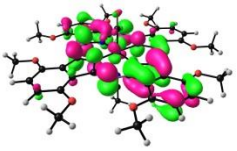
27a, *p*-$(CH_3O)_8$-PcRu(CO)	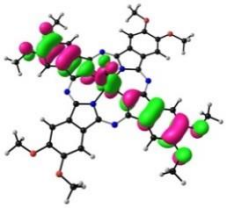	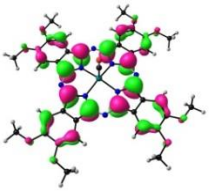		
28a, *np*-$(CH_3O)_8$-PcRu(CO)(py)	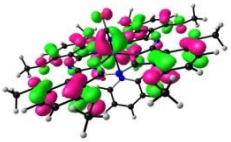		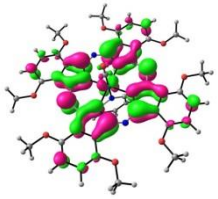	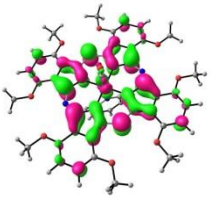
29a, *np*-$(CH_3O)_8$-PcRu(CO)($NH(CH(CH_3)_2)_2$)		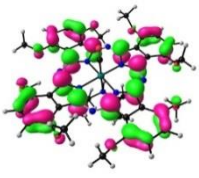	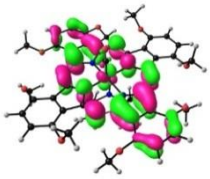	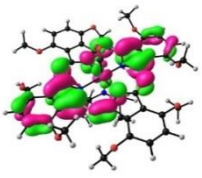

The HOMO for compounds **23-29** (as seen in Appendix D) are located on the phthalocyanine ring and has an a_{1u} π-orbital character. The LUMO and LUMO+1 showed an e_g π-orbital character for all complexes, **23-29**, and are phthalocyanine centred. The HOMO-1 for **23** and

26-29 shows d_π-orbital character, the ruthenium metal for **23** contributes the largest percentage of d_π-orbital character, 27%. The HOMO-1 for compound **24**, only consist out of a_{2u} π-orbital and no d_π-orbital character. The d_π-orbital contribution for **29** was reduced from 27% to 17% when compared to that of **29a**. The depiction of the LUMO-1 and LUMO for ruthenium phthalocyanine compounds **26**, **28** and **29**, with two axial ligands, are similar to work done on iron (II) phthalocyanines, due to the molecular orbital degeneracy that were mostly Pc-centered.[13]

3.7 Comparison of the ruthenium phthalocyanine derivatives

3.7.1 Oxidation potential relationships

The HOMO energy (section 3.6.2) was expected to have a relationship with the experimental E_{pa} value (section 3.5) since the electron that the phthalocyanine lost during oxidation would go out of the HOMO, which would be become the new LUMO. The oxidation potential (E_{pa}) and the formal reduction potential $E^{0'}$ of the first oxidation process of the various ruthenium phthalocyanines, **23-29** with their respective HOMO energies are summarized in Table 3.22.

Table 3.22: A summary of the calculated HOMO energy and the electrochemical first oxidation energy.

Compounds	**[a]HOMO (eV)**	**[b]E_{pa}(V) First Oxidation**	**[c]$E^{0'}$ (V)**
23, *np*-$(C_6H_{13})_8$-PcRu(CO)	-5.071	0.120	0.063
24, *p*-[OPh(o,p-Me)]$_8$-PcRu(CO)	-5.218	0.234	0.191
25, *p*-$(C_6H_{13})_8$-PcRu(CO)	-4.924	0.102	0.054
26, *np*-$(OC_5H_{11})_8$-PcRu(R)(CO), where R = $NCCH_3$	-4.649	-0.079	-0.126
27, *p*-$(OC_5H_{11})_8$-PcRu(CO)	-4.797	0.013	-0.022
28, *np*-$(OC_4H_9)_8$-PcRu(CO)(R), where R = Pyridine (py)	-4.640	0.012	-0.030
29, *np*-$(OC_4H_9)_8$-PcRu(CO)(R), where R=$NH(CH(CH_3)_2)_2$	-4.703	-0.044	-0.090

[a] Calculated HOMO energy .
[b] E_{pa} (first oxidation potential) for electrochemical experiment in DCM versus FcH/FcH^+.
[c] The formal reduction potential $E^{0'}$ for electrochemical experiment in DCM versus FcH/FcH^+.

When the first oxidation peak energy, E_{pa} and the formal reduction potential $E^{0'}$ were compared to the HOMO energy, a linear correlation was found (Figure 3.37). The linear correlation shows a fit, R^2 above 0.88. Good linear trends between HOMO energies and

oxidation potentials are often obtained between a series of related complexes.[17] Given the variety of phthalocyanines in this study, namely 5-coordinated and 6-coordinated metal centres, peripheral and non-peripheral substituted with alkyl or ethoxy chains, the correlation found here are exceptional.

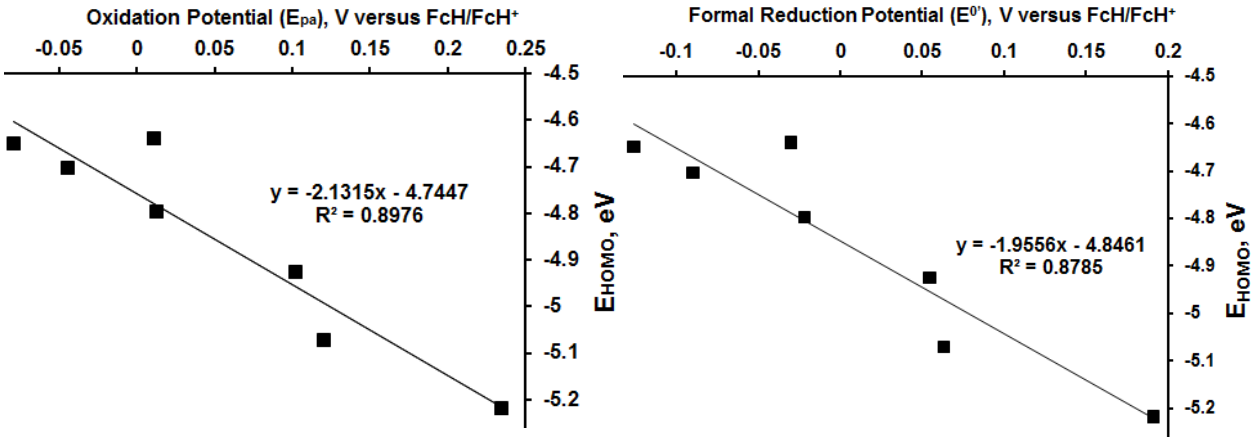

Figure 3.37: The comparison of the computational and electrochemical study of **23-29** in DCM

The first reduction peak energy, E_{pc} and the LUMO energy showed no relationship, due to the observed dimer formation of some of the compounds during the electrochemistry.

3.8 Conclusion

Asymmetrically and symmetrically substituted phthalocyanines containing hexyl and glycol groups were successfully synthesized and characterized. By utilizing a RC1-reactor for the study of selected hydrogenation and oxidation reactions, kinetic (rate constants) and thermodynamic (reaction enthalpies) data was obtained. Upon comparing the experimental reaction enthalpies to DFT calculated reaction enthalpies, a good correlation was found. The DFT study for the phthalocyanato ruthenium metal complexes also included a comprehensive study into the geometries and molecular orbitals of these compounds. The electrochemical and computational studies done on a serious of peripherally and non-peripherally substituted phthalocyanato ruthenium metal complexes, showed a linear correlation between formal reduction potential $E^{0'}$ and the HOMO energy.

[1] Tuncel, S., Dumoulin, F., Gailer, J., Sooriyaarachchi, M., Atilla, D., & Durmus, M.; *Dalton Trans.*, 2011, 40, 4067.

[2] Karabork, M., & Serin, S.; *Synth. React. Inorg., Met.-Org., Nano-Met. Chem.*, 2002, 32, 1635.

[3] McKeown, N. B., Chambrier, I., & Cook, M. J.; *J. Chem. Soc., Perkin Trans*. 1,. 1990, 1169.

[4] Visentin, F., Puxty, G., Kut, O. & Hungerbühler, K.; *Ind. Eng. Chem. Res,*. 2006, 45, 4544.

[5] Meray, M., Louati, A., Simon, J., Andre, J.J., Kadish, K.M., Gross, M. & Giraudeau, A.; *Inorg. Chem*., 1985, 24, 1175.

[6] Manowong, M., Van Caemelbecke, E., Rodríguez-Morgade, M., Bear, J., Kadish, K., & Torres, T.; *J. Porphyrins Phthalocyanines*., 2014, 18, 49.

[7] Dolphin, D., James, B., Murray, A., & Thornback, J.; *Can J. Chem.*, 1980, 58, 1125.

[8] Li, R.; Zhang, X..; Zhu, P.; Ng, D.K.P.; Kobayashi, N.; & Jiang, J., *Inorg. Chem.*, 2006, 45, 2327.

[9] Huang, J., Wong, K., Chan, S., Tso, K., Jiang, T., & Che, C.; *Asian J. Chem.*,2014, 9, 338.

[10] Rawling, T.; *Coord. Chem. Rev.*, 2007, 251, 1128.

[11] Fukuda, T., Homma, S., & Kokayashi, N.; *Chem. Eur. J.*, 2005, 11, 5205.

[12] Jinwan, C., Judong, W., Jinling, H., & Naisheng, C.; *Chin. Sci. Bull.*, 2002, 47, 644.

[13] Huang, J. S., Yu, G.A, Xie, J., Wong, K.M., Zhu, N., & Che, C.M.; *Inorg. Chem.*, 2008, 47, 9166.

[14] Gouterman, M.; *J. Mol. Spectrosc*. 1961, 6, 138.

[15] Gouterman M., *The Porphyrins*, Academic Press, New York, 1978, 3, 1-165.

[16] Nemykin, V. N., Purchel, A. A., Spaeth, A. D., Barybin, M. V.; *Inorg. Chem.*, 2013, 52, 11004.

[17] (a) Conradie, J.; *Dalton Trans.*, 2015, 44, 1503. (b) Van As, A., Joubert, C., Buitendach, B.E., Erasmus, E., Conradie, J., Cammidge, A., Chambrier, I., Cook, M. & Swarts, J.; *Inorg. Chem.*, 2015, 54, 5329. (c) Conradie, M.M. & Conradie, J.; *Electrochim. Acta*, 2015, 152, 512.

CHAPTER 4

EXPERIMENTAL

4.1 Introduction

In this chapter all experimental procedures, reaction conditions and techniques are described.

4.2 Materials

Solid reagents (Merck, Aldrich) employed in preparations were used without further purification. Liquid reagents were purchased from Aldrich and used without further purification. Solvents were distilled prior to use and water was double distilled. Organic solvents were dried according to published methods.[1] Silica and basic Alumina was used as the stationary phase in chromatography.

4.3 Spectroscopic measurements

^{1}H NMR-spectra at 298 K was recorded on a Bruker Advance CPX 600 instrument for the phthalocaynine structures. Chemical shifts are reported as δ-values (ppm) relative to $SiMe_4$ at 0.00 ppm utilizing $CDCl_3$ and DMSO as solvent. Infrared spectra (cm^{-1}) were recorded on a Bruker Tensor 27 spectrometer (with a Pike MIRacle ATR-attachment). Optical spectra in the UV-visible region were recorded with a Shimadzu spectrophotometer using a 1 cm path length cuvette at room temperature.

4.4 Synthesis

Section 4.4 describes the stepwise synthesis all the precursors as well as the metal-free phthalocyanine.

4.4.1 Phthalonitrile derivatives

4.4.1.1 4-[2-(2-hydroxyethoxy)ethoxy]phthalonitrile[2], 1

4-nitrophthalonitrile (1.047 g, 6.5 mmol) was added to the solution of diethylene glycol (1.5 cm^3, 1.68 g, 12.4 mmol) in DMF (20 cm^3). To this reaction mixture anhydrous K_2CO_3 (4.27 g, 30.9 mmol) was added portion wise over 2 hours. The mixture was stirred continuously over a period of 24 hours under an argon atmosphere. The reaction mixture was filtered, put through a short silica gel column using dichloromethane (DCM) as eluent and evaporated under reduced pressure, to yield the product as a pure oil, **6**. Yield: 0.85 g, (3.66 mmol, 49.5%); δ_H (300 MHz, $CDCl_3$, Spectrum A1)/ppm 7.74 (1H, d, Ar-H), 7.33 (1H, d, Ar-H), 7.255 (1H, dd, Ar-H), 4.25 (2H, t, Ar-OCH_2), 3.92 (2H, t, -OCH_2), 3.78 (2H, t, -OCH_2), 3.68 (2H, t, -OCH_2-OH).

4.4.1.2 4-[2-(2-(2-hydroxyethoxy)ethoxy)ethoxy]phthalonitrile[2], 2

4-nitrophthalonitrile (1.257 g, 7.39 mmol) was added to the solution of triethylene glycol (2.3 cm^3, 1.5 g, 16.85 mmol) in DMF (20 cm^3). To this reaction mixture anhydrous K_2CO_3 (4.115 g, 29.77 mmol) was added portion wise over 2 hours The mixture was stirred continuously over a period of 24 hours under an argon atmosphere. The reaction mixture was filtered, evaporated under reduced pressure to yield the product as a yellow oil, **7**. Yield: 0.925 g (45.25%, 3.348 mmol); δ_H (300 MHz, $CDCl_3$, Spectrum A2)/ppm 7.73 (1H, d, Ar-H), 7.35 (1H, d, Ar-H), 7.255 (1H, dd, Ar-H), 4.25 (2H, t, Ar-OCH_2), 3.92 (2H, t, -OCH_2), 3.74 (6H, t, 3 x -OCH_2), 3.64 (2H, t, -OCH_2-OH).

4.4.1.3 4-(2-(2-((tetrahydro-2H-pyran-2-yl)oxy)ethoxy)ethoxy)phthalonitrile, 4

(i) *4.4.1.3.1 2-[2-(Tetrahydropyranyloxy)ethoxy]ethanol[3],**3***

A DCM solution (200 cm^3) of 3,4-dihydro-2H-pyran (25.792 g, 306 mmol) with pyridinium *p*-toluenesulfonate (7.592 g, 30 mmol) was slowly added to a solution of diethylene glycol (46.68 g, 411 mmol, 1.34 eq) in DCM (500 cm^3). The reaction mixture was stirred for 4 hours at room temperature. The mixture was washed with H_2O (4 x 50 cm^3), dried over $MgSO_4$, filtered and the

solvent removed under reduced pressure to afford an off-white crude product. The crude product was then purified by silica column chromatography (diethyl ether as eluent, R_f = 0.40) to yield pure, **8**, as a colourless oil. Yield: 29 g, (152 mmol, 49.78%); δ_H (300 MHz, $CDCl_3$, Spectrum A3)/ppm 4.65 (1H, t, OC<u>H</u>O), 3.90-3.40 (10H, m, OC<u>H</u>$_2$), 1.90-1.50 (6H, m, C<u>H</u>$_2$).

(ii) *4.4.1.3.2 4-(2-(2-((tetrahydro-2H-pyran-2-yl)oxy)ethoxy)ethoxy)phthalonitrile, **4***

4-nitrophthalonitrile (1.257 g, 7.39 mmol) was added to a solution of 2-[2-(tetrahydropyranyloxy)ethoxy]ethanol (3.089 g, 16.26 mmol) in DMF (40 cm^3). To this reaction mixture anhydrous K_2CO_3 (4.115 g, 29.77 mmol) was added in four portions over 2 hours. The mixture was stirred continuously over a period of 24 hours under an argon atmosphere. The reaction mixture was filtered, and then diluted with DCM (100 cm^3) and washed with distilled H_2O (3 x 50 cm^3). The organic layer was dried over $MgSO_4$ filtered and the solvent evaporated. The oily brown crude product was then purified by silica gel column using DCM as eluent (R_f = 0.65) to yield a pure yellow oil, **9**. Yield: 0.153 g (0.48 mol, 6.56%); δ_H (300 MHz, $CDCl_3$, Spectrum A4)/ppm 7.73 (1H, d, Ar-<u>H</u>), 7.34 (1H, d, Ar-<u>H</u>), 7.27-7.22 (1H, dd, Ar-<u>H</u>), 4.65 (1H, t, -OC<u>H</u>$_2$), 3.90-3.80 (4H, m, -OC<u>H</u>$_2$), 3.8-3.7 (2H, t, -OC<u>H</u>$_2$), 3.7-3.48 (2H, m, -OC<u>H</u>$_2$), 1.90-1.65 (2H, m, C<u>H</u>$_2$), 1.58-1.45 (4H, m, C<u>H</u>$_2$).

4.4.1.4 3,6-dihexylphthalonitrile[4, 5], 7

(i) *4.4.1.4.1 2,5-dihexylthiophene, **5***

To a solution of thiophene (8.4 g, 150 mmol) in dry THF (25 cm^3), ooled to between -75 °C and -60 °C in an acetone/liquid nitrogen bath, 144 cm^3 of 2.5 M of n-butyl lithium in hexane (360 mmol) was added slowly under inert atmosphere. After the addition, the reaction was allowed to reach room temperature immediately while stirring continuously for 24 hours. The reaction mixture was then cooled to -70 °C again, before adding a slight excess of 1-hexylbromide (52.82 g, 320 mmol) over a period of 30 minutes. The mixture was allowed to reach room temperature while stirring for 24 hours. The mixture was poured onto ice and extracted with diethyl ether (4 x 200 cm^3). The combined organic extracts were dried over $MgSO_4$, filtered and the solvent removed under reduced pressure at 75 °C to afford brown oil as crude product. The crude brown

oil was fractionally distilled under reduced pressure (< 1 mmHg) at 105 °C. The residue was put through a short silica column using hexane as eluent to remove impurities to yield pure 2,5-dihexylthiophene as a light orange-yellow oil. Yield: 32.1 g (76.49 mmol, 76.56%); δ_H(300 MHz, $CDCl_3$, Spectrum A5)/ppm 6.58 (2H, s, $C_4\underline{H}_2S$), 2.75 (4H, t, 2 x -$C\underline{H}_2$-), 1.67 (4H, m, 2 x -$C\underline{H}_2$-), 1.29 (12H, s, 2 x (-$C\underline{H}_2)_3$-), 0.88 (6H,t, 2 x (-$C\underline{H}_3$); ν_{max}/cm^{-1} 2963 (C-H) and 1463 (-CH_3).

(ii) *4.4.1.4.2 2,5-dihexylthiophene-1,1-dioxide[4], **6***

A solution of 2,5-dihexylthiophene (8.455 g, 33 mmol) in 100 cm^3 DCM was stirred with 50±60% m-chloroperoxybenzoic acid (15.1 g, 87 mmol) at 0 °C in the presence of an excess of $NaHCO_3$ (14 g, 166 mmol). The heterogeneous mixture was left standing for 16 hours at 5 °C before all solids were filtered and washed with DCM (2 x 100 cm^3). The combined organic phases were washed with 20% NaOH (2 x 100 cm^3), H_2O (2 x 100 cm^3) and dried ($MgSO_4$) to give the crude product. After solvent removal and recrystallization of the crude product from ethanol (EtOH), the product, 2,5-dihexylthiophene-1,1-dioxide **12**, was obtained as a white solid. Yield: 3.0 g (10.55 mmol, 31.69%); δ_H(300 MHz, $CDCl_3$, Spectrum A6)/ppm 6.28 (2H, s, $C_4\underline{H}_2SO_2$), 2.48 (4H, t, 2 x -$C\underline{H}_2$-), 1.67 (4H, m, 2 x -$C\underline{H}_2$-), 1.38 (4H, m, -$C\underline{H}_2$-), 1.29 (8H, s, 2 x (-$C\underline{H}_2)_2$-), 0.86 (6H,t, 2 x (-$C\underline{H}_3$); ν_{max}/cm^{-1} 1275 and 1140 (-SO_2).

(iii) *4.4.1.4.3 3,6-dihexylphthalonitrile[4], **7***

2,5-dihexylthiophene-1,1-dioxide (3.464 g, 12.2 mmol) and fumaronitrile (0.954 g, 12.7 mmol) were washed into a glass tube with a minimal amount of chloroform (less than 2 cm^3). The glass tube was sealed and heated to 160 °C over 18 hours.* After the tube was cooled to room temperature, the contents were washed out with chloroform. The solvent was removed from the residue under reduced pressure at 90 °C until no further gas evolution was observed. The residue was then purified by silica column chromatography (toluene as eluent), collecting the second band (R_f = 0.73). The product was recrystallized from EtOH to give pure 3,6-dihexylphthalonitrile.

* The sealed glass tube is placed in a sand-filled steel tube to protect the oven against damage should the tube explode due to pressure build-up.

Yield: 1.7 g (5.98 mmol, 49.13%); δ_H(300 MHz, $CDCl_3$, Spectrum A7)/ppm 7.47 (2H, s, $C_6\underline{H}_2$), 2.86 (4H, t, 2 x -$C\underline{H}_2$-), 1.67 (4H, m, 2 x -$C\underline{H}_2$-), 1.35 (12H, s, 2 x (-$C\underline{H}_2$)$_3$-), 0.85 (6H,t, 2 x (-$C\underline{H}_3$); ν_{max}/cm^{-1} 2228 (C≡N).

4.4.2 Synthesis of Metal-free substituted phthalocyanines

4.4.2.1 1,4,8,11,15,18,22,25-Octahexylphthalocyanine, 8

3,6-Dihexylphthalonitrile (40 mg, 0.14 mmol) was dissolved in 1-pentanol (0.5 cm^3) under inert conditions. An excess of clean lithium metal (4.8 mg, 0.69 mmol) was added to the solution and brought to reflux. The mixture was refluxed for 16 hours under inert atmosphere. The deep green coloured suspension was cooled to room temperature before stirring for 10 minutes with acetone (15 cm^3). The solids were filtered off and washed with acetone (15 cm^3) before the combined acetone fractions were concentrated to 7.5 cm^3. Acetic acid (15 cm^3) was added to the filtrate and stirred for 30 minutes. The resulting precipitate was filtered off and washed first with acetone (20 cm^3) followed by methanol (MeOH) (20 cm^3). The dark green solid was air dried. Yield: 16.8 mg (0.014 mmol, 10.10%); δ_H(300 MHz, $CDCl_3$, Spectrum A8)/ppm 7.89 (8H, s, Ar-$\underline{H}$), 4.47 (16H, s, 8 x Ar-$C\underline{H}_2$-), 2.10 (19H, m, 8 x -$C\underline{H}_2$-), 1.19 (45H, m, 8 x (-$C\underline{H}_2$)$_3$-), 0.84 (24H,t, 8 x (-$C\underline{H}_3$); ν_{max}/cm^{-1} (Spectrum B1) 3294.32 (N-H); UV-vis (THF) λ_{max} (log ε): 356 (4.54),697 (4.78), 728 (4.85).

4.4.2.2 2,9,16,23-Tetra[2-(2-hydroxyethoxy)ethoxy]phthalocyanine, 9

4-[2-(2-hydroxyethoxy)ethoxy]phthalonitrile, **1**, (116 mg, 0.5 mmol) and hydroquinone (66 mg, 0.6 mmol) were placed in a thick-walled tube and flushed with argon. The tube was sealed and heated to 160 °C for 22 hours. To the deep-green waxy solid reaction mixture hot EtOH (5 cm^3) was added. The solution was kept in the freezer overnight. The product precipitates from the solution as a black solid. The resulting precipitate was filtered off and rinsed with diethylether and dried under vacuum. Yield: 108 mg (0.110 mmol, 20.06%); δ_H(600 MHz, DMSO, Spectrum A9)/ppm 7.5 (12H, s, Ar-$\underline{H}$), 3.06-2.8 (32H, m, -$C\underline{H}_2$-), 1.48-1.40 (2H, s, -O$\underline{H}$); ν_{max}/cm^{-1} (Spectrum B2) 3290.86 (N-H); UV-vis (DMSO) λ_{max} (log ε): 337 (4.62), 673 (4.67), 706 nm (4.64).

4.4.2.3 2,9,16,23-Tetra[2-(2-(2-hydroxyethoxy)ethoxy)ethoxy]phthalocyanine, 10

4-[2-(2-(2-hydroxyethoxy)ethoxy)ethoxy]phthalonitrile, **2**, (138 mg, 0.5 mmol) and hydroquinone (66 mg, 0.6 mmol) were placed in a thick-walled tube and flushed with argon. The tube was sealed and heated to 160 °C for 22 hours. The dark reaction mixture was rinsed with hot EtOH to wash off brown-yellow side products together with residual amounts of hydroquinone and quinone. The resulting black powder was dried under vacuum, before the product was recrystallized from the mixture of hot MeOH and triethylamine (NEt_3) (1% of amine) by precipitating it with diluted HCl (3% in H_2O).Yield: 123 mg (0.106 mmol, 21.29%); δ_H(600 MHz, DMSO, Spectrum A10)/ppm 7.54-6.646 (12H, s, Ar-H), 3.577-3.204 (48H, m, -CH_2-), 1.505-1.377 (2H, s, -OH); ν_{max}/cm^{-1} (Spectrum B3) 3202.36 (N-H); UV-vis (DMSO) λ_{max} (log ε): 334 (4.55), 676 (3.99),705 nm (4.00).

4.4.2.4 Tetrahexyl-di-[2-(2-hydroxyethoxy)ethoxy]-phthalocyanine, 11

3,6-Dihexylphthalonitrile (176 mg, 0.59 mmol) and 2-(2-hydroxyethoxy)ethoxyphthalonitrile (137 mg, 0.59 mmol) were placed in a thick-walled glass tube and flushed with argon. 1-pentanol (3 cm^3) was added to the tube, and gently heated to ensure a homogeneneous mixture before the addition of lithium metal (83 mg, 11.9 mmol). The reaction was heated to 140 ºC and kept for 20 hours. The reaction mixture was allowed to cool to before adding acetone (15 cm^3). After 30 min the deep-green suspension was filtered and washed with DCM. The filtrate was evaporated to dryness to yield a green residue. The residue was chromatographed on neutral alumina using pure DCM to elute the A4-type phthalocaynine. The eluents polarity was then increased DCM: MeOH to collect the third fraction. The fraction was evaporated to dryness and rinsed with MeOH to yield blue solids. The solids were redissolved in small amount of DCM and loaded on preparative SiO_2 TLC (eleunts include DCM: MeOH: NEt_3 (98.5: 1: 0.5) (R_f = 0.69), which eluted the A_2B_2-type product. Yield: 12 mg (0.011 mmol, 2%); δ_H(600 MHz, $CDCl_3$, Spectrum A11)/ppm 8.55 (1H, s, Ar-H), 8.05 (1H, s, Ar-H), 7.95 (1H, s, Ar-H), 7.9 (2H, s, Ar-H), 7.8 (1H, s, Ar-H), 7.75 (1H, s, Ar-H), 7.64 (1H, s, Ar-H), 7.60 (1H, s, Ar-H), 7.55(1H, s, Ar-H), 4.45-4.35 (4H, m, OCH_2), 4.35-4.30 (2H, t, -OCH_2), 4.30-4.20 (2H, t,-OCH_2), 4.15-4.10 (2H, t, -OCH_2), 4.05-3.95 (2H, t, -OCH_2), 3.95-3.90 (2H, t, -OCH_2), 3.90-3.85 (2H, t, -OCH_2), 2.35 (10H, m, C-H), 1.75-1.65 (4H, m, C-H), 1.45-1.15 (26H, m, C-H), 0.9-0.8 (13H, m, C-H), -1.6 (2H, s, N-H);

ν_{max}/cm^{-1} (Spectrum B4) 3279.84 (N-H); UV-vis (THF) λ_{max} (log ε): 331 (4.70), 684 (4.87), 717 nm (4.92).

4.4.2.5 Tetrahexyl-di-{2-[2-(2-hydroxyethoxy)-ethoxy]-ethoxy}-phthalocyanine, 12

3,6-Dihexylphthalonitrile (354 mg, 1.20 mmol) and 2-[2-(2-hydroxyethoxy)-ethoxy]-ethoxyphthalonitrile (330 mg, 1.20 mmol) were placed in a thick-walled glass tube and flushed with argon. 1-pentanol (3 cm^3) was added to the tube, and gently heated to ensure a homogeneneous mixture. Lithium metal (185 mg, 26 mmol) was added to the reaction mixture in 6 pieces over 5 min. The reaction was heated to 140 ºC and kept for 21 hours. The reaction mixture was cooled down, and transferred to a flask using DCM and MeOH. The mixture evaporated to dryness. The solids were suspended in hexane and sonicated to remove A4 phthalocyanine and side-products. The remaining mixture was loaded on preparative SiO_2 TLC plate and A_2B_2 was eluted with DCM: MeOH: NEt_3 (94: 5.5: 0.5) which yielded the product . Yield: 18 mg (0.016 mmol, 2.66%); δ_H(600 MHz, $CDCl_3$, Spectrum A12)/ppm 8.5-7.4 (10H, m, Ar-H), 4.45-4.39 (2H, s, OCH_2), 4.38-4.29 (4H, s, -OCH_2), 4.28-4.18 (4H, s,-OCH_2), 4.15-4.10 (2H, t, -OCH_2), 3.95-3.91 (4H, m, -OCH_2), 3.90-3.80 (2H, t, -OCH_2), 3.77-3.72 (2H, t, -OCH_2), 2.20-2.10 (4H, m, C-H), 2.10-2.00 (8H, m, C-H), 1.70-1.64 (4H, m, C-H), 1.62-1.45 (16H, m, C-H), 1.40-1.25 (26H, m, C-H), 0.90-0.80 (16H, m, C-H), -1.72 (2H, s, N-H); ν_{max}/cm^{-1} (Spectrum B5) 3692.51 and 3281.22 (N-H); UV-vis (THF) λ_{max} (log ε): 341 (4.89),684 (4.89),718 (4.93).

4.5 RC1 Reactor synthesis

4.5.1 General

The RC1 reactor used during this experiment is a medium pressure Mettler Toledo reactor (MP10-1- RTC), measuring both the traditional heat flow calorimetry and heat flow in real time using RTCal™. This reactor is equipped with a 10 bar glass reactor vessel with a capacity of 1000 cm^3. T he reactor uses iControl RC1e™ Software integrated with iC IR™ software and an iCIR-sensor to record data every 30 seconds.

4.5.2 Experimental determination of Mass Transfer coefficient, k_La

To the reactor vessel 700 cm^3 of solvent (THF or Toluene) was added. The vessel was filled with 4 bar N_2 gas. When the gas level was constant, the stirrer was turned on at 600 rpm. The decrease in gas pressure level in the reactor vessel was tracked and quantified until it reached a dynamic equilibrium. The after a dynamic equilibrium was reached, the solvent was removed from the reactor vessel and degassed for 5 minutes. The experiment was repeated at 700 and 800 rpm before a different solvent was used.

4.5.3 Oxidation of thiophene derivatives

4.5.3.1 2,5-dihexylthiophene-1,1-dioxide[5], 6

To the RC1-reactor vessel a mixture of water (137.5 cm^3) and DCM (198.1 cm^3), and an excess of $NaHCO_3$ (73.95 g, 880.3 mmol) was added. T he mixture was stirred at 1000 rpm while kept at 15 °C. The heterogeneous mixture was cooled to, 0, 2 or 5 °C , respectively depending on reaction run, before the addition of oxone® (127 g, 412.6 mmol). Acetone (99.03 cm^3) was added to the mixture and the system was allowed to stabilize, before the addition of the suitable thiophene, 2,5-dihexylthiophene (1.389 g, 5.502 mmol) . The heterogeneous mixture was stirred at 1000 rpm for 16 hours at at. The temperature was kept constant (at the chosen temperature) with a variation of no more than 0.1 °C. The reaction mixture was removed from the reaction vessel by vacuum and rinsed with water. All solids were filtered and washed with DCM (2 x 100 cm^3). The crude product was extracted from the water with DCM (3 x 300 cm^3). The combined organic phases were washed with 20% NaOH (2 x 100 cm^3), H_2O (2 x 100 cm^3) and dried ($MgSO_4$) to give 2,5-dihexylthiophene 1,1-dioxide, **6**, as a white solid, after solvent removal and recrystallization from EtOH. Yield: 1.267 g (4.46 mmol, 81.1%); δ_H (300 MHz, $CDCl_3$, Spectrum A6)/ppm 6.28 (2H, s, $C_4\underline{H}_2SO_2$), 2.48 (4H, t, 2 x -$C\underline{H}_2$-), 1.67 (4H, m, 2 x -$C\underline{H}_2$-), 1.38 (4H, m, -CH_2-), 1.29 (8H, s, 2 x (-$C\underline{H}_2)_2$-), 0.86 (6H,t, 2 x (-$C\underline{H}_3$); ν_{max}/cm^{-1} 1275 and 1140 cm^{-1} (-SO_2).

4.5.3.2 2,5-didodecylthiophene-1,1-dioxide[5], 14

The same procedure as described in section 4.5.3.1 was followed with a mixture of water (129 cm^3), DCM (186 cm^3), acetone (93 cm^3), $NaHCO_3$ (69.58 g, 0.8283 mol), oxone® (119.5 g, 0.3883 mol) and 2,5-didodecylthiophene, **13**, (2.174 g, 5.177 mmol). The synthesis yielded 2,5-didodecylthiophene-1,1-dioxide, **14**, as a white needle-like solid. Yield: 1.765 g (3.905 mmol, 81.21%); δ_H (300 MHz, $CDCl_3$, Spectrum A13)/ppm 6.28 (2H, s, $C_4\underline{H}_2SO_2$), 2.48 (4H, t, 2 x -$C\underline{H}_2$-), 1.67 (4H, m, 2 x -$C\underline{H}_2$-), 1.38 (4H, m, -$C\underline{H}_2$-), 1.29 (32H, s, 2 x (-$C\underline{H}_2$)$_8$-), 0.86 (6H,t, 2 x (-$C\underline{H}_3$); ν_{max}/cm^{-1} (Spectrum B6) 1282 and 1137 ($-SO_2$).

4.5.4 Reduction of 4-nitrophthalonitrile, 16

4-nitrophthalpnitrile, **16**, (1.035 g, 5.978 mmol) was dissolved in MeOH (200 cm^3), heated to 50 °C and flushed with N_2 to remove all O_2. To the mixture 10% Pd/C (1 g, 9.397 mmol) was added with MeOH (10 cm^3). The system was closed, and filled with 1 bar H_2. The mixture was stirred at 400 rpm at 50 °C under 1 bar H_2 for 1 hour. The temperature was kept constant at 50 °C with a variation of no more than 0.5 °C. The system was flushed with N_2 before opening the reactor vessel. The compound, **17**, was isolated. Yield: 0.735 g (5.13 mmol, 85.88%); δ_H (300 MHz, $CDCl_3$, Spectrum A)/ppm 7.59-7.51 (1H, d, Ar-$\underline{H}$), 6.99-6.92 (1H, d, Ar-$\underline{H}$), 6.92-6.82 (1H, dd, Ar-$\underline{H}$).

4.6 Thermal analysis with the RC1 calorimeter

An RC1 reactor from Mettler Toledo interfaced with a ReactIR 45 m utilising a probe with SiComp ATR tip and 6.3 mm AgX fiber conduit for IR measurements were used. A baffler was installed for more efficient stirring. Stirring speeds are as indicated in the relevant sections. Solvents that were used include THF, ethanol, DCM, water and acetone or toluene. Temperatures were controlled to within 0.1 ^oC, and pressure was never allowed to exceed 4 bar. Exact conditions may be found in Chapter three for each experiment.

4.7 Computational Chemistry

4.7.1 Method

4.7.1.1 Phthalocyanines

Density Functional Theory (DFT) calculations were performed using the Gaussian 09 program with B3LYP functional and def2tzvpp basis set, as well as tight criteria for SCF convergence and geometry optimization. No symmetry limitations were imposed, in other words, all calculations were done in the C1 (no symmetry) mode.

4.7.1.2 Oxidation and hydrogenation reactions

Density Functional Theory (DFT) calculations were performed using the Amsterdam Density Functional 2014 (ADF) program with the OLYP functional and Slater-type TZP basis set, as well as tight criteria for SCF convergence and geometry optimization. No symmetry limitations were imposed, in other words, all calculations were done in the C1 (no symmetry) mode.

4.8 Electrochemistry

Cyclic voltammetry (CV), linear sweep voltammetry (LSV) and square wave voltammetry (SWV) was carried out using a Princeton Applied Research PARSTAT 2273 voltammograph and recorded using PowerSuite (Version 2.58). A three electrode cell configuration was used. A glassy carbon working electrode (surface area 0.1257 cm^2) was pre-treated by polishing on a Buehler polishing mat first with 1 micron and then with ¼ micron diamond paste. A platinum and silver wire was used for auxiliary and reference electrodes, repectively. Voltammograms in this study were performed inside an M Braun Lab master SP glovebox filled with high purity argon (H_2O and O_2 < 5 ppm). Spectrochemical grade DCM, acetonitrile (CH_3CN), DMSO and THF (Aldrich) was used in a 1 cm^3 cell. Tetrabutylammonium tetrakis(pentafluorophenyl)borate, $[NBu_4][B(C_6F_5)_4]$, was used as a supporting electrolyte (0.1 M). The concentration of all analyte solutions was 0.5 mM. Analysis was performed at room temperature.

4.8.1 Synthesis of Tetrabutylammonium tetrakis(pentafluorophenyl)borate, $[^{n}Bu_4N][B(C_6F_5)_4]$, 22

Lithium tetrakis(pentafluorophenyl)borate (10 g, 18.23 mmol) was dissolved in MeOH (20 cm^3). Tetrabutylammonium bromide (5.1 g, 15.8 mmol) dissolved in MeOH (10 cm^3) was added drop-wise at room temperature over 30 minutes, while stirring, to the lithium tetrakis(pentafluorophenyl)borate solution. The solution was closed with a septum and kept at 0 °C for 30 minutes. Thereafter the solution was left overnight at -25 °C. An off-white precipitate was obtained by filtration and washed with MeOH (10 cm^3 at -25 °C). The solid was dissolved in dry DCM (30 cm^3), $MgSO_4$ added and the mixture, covered with a septum, stirred for 2 hours at room temperature. The $MgSO_4$ was filtered off, washed with DCM and the solvent removed under vacuum to yield white crystals. Yield: 5.6 g (6.08 mmol, 38.5%); ^{1}H NMR δ_H (300MHz, $CDCl_3$, Spectrum A15)/ppm: 3.01 (8H, t, 4 x -C$\underline{H}_2$), 1.54 (8H, m, 4 x -C$\underline{H}_2$), 1.35 (8H, m, -C$\underline{H}_2$-), 0.97 (12H, t, 4 x -C$\underline{H}_3$).

---

[1] B.S. Furniss, A.J. Hannaford, P.W.G. Smith and A.R. Tatchell, *Vogel's Textbook of Practical Organic Chemistry*, 4th Edition, Longman, New York, p 264-318.

[2] Tuncel, S., Dumoulin, F., Gailer, J., Sooriyaarachchi, M., Atilla, D., Durmus, M.; *Dalton Trans.*, 2011, 40, 4067.

[3] Allcock, H. R., & Kim, C.; *Macromolecules*, 1991, 2846.

[4] McKeown, N. B., Chambrier, I., & Cook, M. J.; *J. Chem. Soc.: Perkin Trans. 1*,. 1990, 1169.

[5] Swarts, J. C., Langner, E. H., Krokeide-Hoveb, N., & Cook, M. J.; *J. Mater. Chem.*, 2001, 11, 434.

CHAPTER 5

SUMMARY, CONCLUSIONS AND FUTURE PERSPECTIVES

5.1 Summary and Concluding remarks

In this study, peripherally substituted tetra[2-(2-hydroxyethoxy)ethoxy]phthalocyanine, $((HO(CH_2CH_2O)_2)_4$-PcH_2, and tetra[2-(2-(2-hydroxyethoxy)ethoxy)ethoxy]phthalocyanine, and $(HO(CH_2CH_2O)_3)_4$-PcH_2; was successfully synthesized through tetramerization of 4-(2-(2-hydroxyethoxy)ethoxy)phthalonitrile and 4-[2-(2-(2-hydroxyethoxy)ethoxy)ethoxy]phthalonitrile, respectively. Asymmetrically substituted tetrahexyl-di-[2-(2-hydroxyethoxy)ethoxy]-phthalocyanine, $((C_6H_{13})_4(HO(CH_2CH_2O)_2)_2$-$PcH_2$ and tetrahexyl-di-{2-[2-(2-hydroxyethoxy)-ethoxy]-ethoxy}-phthalocyanine, $(C_6H_{13})_4(HO(CH_2CH_2O)_3)_2$-$PcH_2$, was also successfully synthesized through statistical condensation of 3,6-dihexylphthalonitrile with 4-(2-(2-hydroxyethoxy)ethoxy)phthalonitrile or 4-[2-(2-(2-hydroxyethoxy)ethoxy)ethoxy]phthalonitrile, respectively. All synthesized compounds were characterized by ^{1}H NMR, IR and UV/vis spectroscopy or a combination of these techniques.

The electrochemistry of these ethylene glycol substituted phthalocyanines (symmetrically substituted ethylene glycolated phthalocyanines and asymmetrically substituted tetrahexyl-di-[2-(2-hydroxyethoxy)ethoxy]-phthalocyanine and tetrahexyl-di-{2-[2-(2-hydroxyethoxy)-ethoxy]-ethoxy}-phthalocyanine) were studied in CH_2Cl_2 and DMSO containing tetrabutylammonium tetrakis(pentafluorophenylborate) as supporting electrolyte. The cyclic voltammograms showed up to four macrocycle-based redox processes.

Utilizing the RC1 reactor, we were able to study the calorimetric and kinetic profile of various oxidation and reduction reactions in real-time for the first time. Oxidation of 2,5-dihexylthiophene and 2,5-didodecylthiophene, was carried out accoriding to known methods using *in situ* prepared dimethyldioxirane as oxidant, but for the first time studied kinetically and thermodynamically. The *in situ* formation of dimethyldioxirane, as well as the disappearance of dimethyldioxirane, i.e. the formation of the desired oxidized 2,5-dihexylthiophene and 2,5-didodecylthiophene could be followed with great accuracy. Reaction enthalpies, rate constants and activation energy were experimentally acquired during this study, under real conditions. The reduction of 4-nitrophthalonitrile to 4-aminophthalonitrile was also studied using the RC1 reactor, yielding calorimetric and kinetic data.

The computational chemistry of the above mentioned oxidation and hydrogenation reactions was done to obtain the computed enthalpies. This enabled the comparison of the computed enthalpies to the experimentally obtained enthalpy values from RC1 reactor. Theoretical enthalpy and experimental enthalpy results for the oxidation reactions, showed no more than a 4 fold difference. The experimental enthalpy and theoretical enthalpy results for the hydrogenation reactions, showed a difference of 1.5 fold. The good correlation obtained between the experimental en theorectcal study of these reaction (oxidation and hydrogenation reactions), are considered as very impressive, since the theoretical enthalpy optimization was done in ideal gas-phase and the experimental enthalpy values obtained was done under extremely non-ideal conditions.

An electrochemical and computational study was done on a series of ruthenium containing phthalocyanines with a CO-axial ligand. Variations in peripheral and non-peripheral substituents as well as secondary axial ligands were investigated. In most cases the electrochemical study for these (CO)RuPc compounds were performed in both dichloromethane and dichloromethane containing a drop of acetonitrile with tetrabutylammonium tetrakis(pentafluorophenylborate) as supporting electrolyte. The electrochemistry of these compounds, showed up to four macrocycle-based redox processes. A drop of acetonitrile was added to the dichloromethane solvent in order to disrupt any possible dimer formation and thus simplified the voltammograms significantly. The computational study investigated the effect of varying substituents (shorter or longer alkyl or ethoxy chains) and ligands (carbonyl and/or acetonitrile, pyridine and tertiary amine) on the geometries and molecular orbital energies of the phthalocyanine copounds. Upon comparing the first oxidation process obtained experimentally and the highest occupied molecular orbitals (HOMO), a linear correlation was found. Given the variety of phthalocyanines in this study, namely 5-coordinated and 6-coordinated metal centres, and peripheral or non-peripheral substituents the correlation found here was considered exceptional.

5.2 Future perspectives

In this study, we were able to successfully synthesize asymmetrically substituted phthalocyanines containing both ethylene glycol and hexyl groups. Due to time constraints, however, we were not able to optimize this step and and very low yields of 2 to 3 % were

obtained. Future work on this project should definitely aim to optimize the synthetic and purification steps in order to improve yields.

Future work on this project will also include the metal insertion e.g. Zn or Al, as well as anchoring of these asymmetrically substituted phthalocyanines containing both ethylene glycol and hexyl groups to a biogradable, water soluble polymers, to enchance properties for possible biomedical applications, (e.g. photodynamic theraphy for cancer treatment).

In this study the RC1 reactor was ulitized for the optimization of the oxidation and hydrogenation reactions as well as the the collection of never before seen thermodynamic and kinetic information for these reactions. Due to the vast amount of information that can be obtained by the RC1 reactor, futher work on this part of the project should include testing the reproducibility and optimization of the reaction conditions, as well as thermodynamic and kinetic data obtained for these, and any future work on similar reactions.

Computational chemistry was utilized to compliment the experimentally obtained thermodynamic data of the above mentioned oxidation and reduction reactions, as well as the geometries and molecular orbital energies of the ruthenium containing phthalocyanines. Further work on this project should include testing the reproducibility of the DFT methods used, by enlarging the series of oxidation and reduction reactions as well as the ruthenium containing phthalocyanines.

APPENDIX A

^{1}H NMR SPECTRA

Spectrum A1: 4-[2-(2-hydroxyethoxy)ethoxy]phthalonitrile, 1

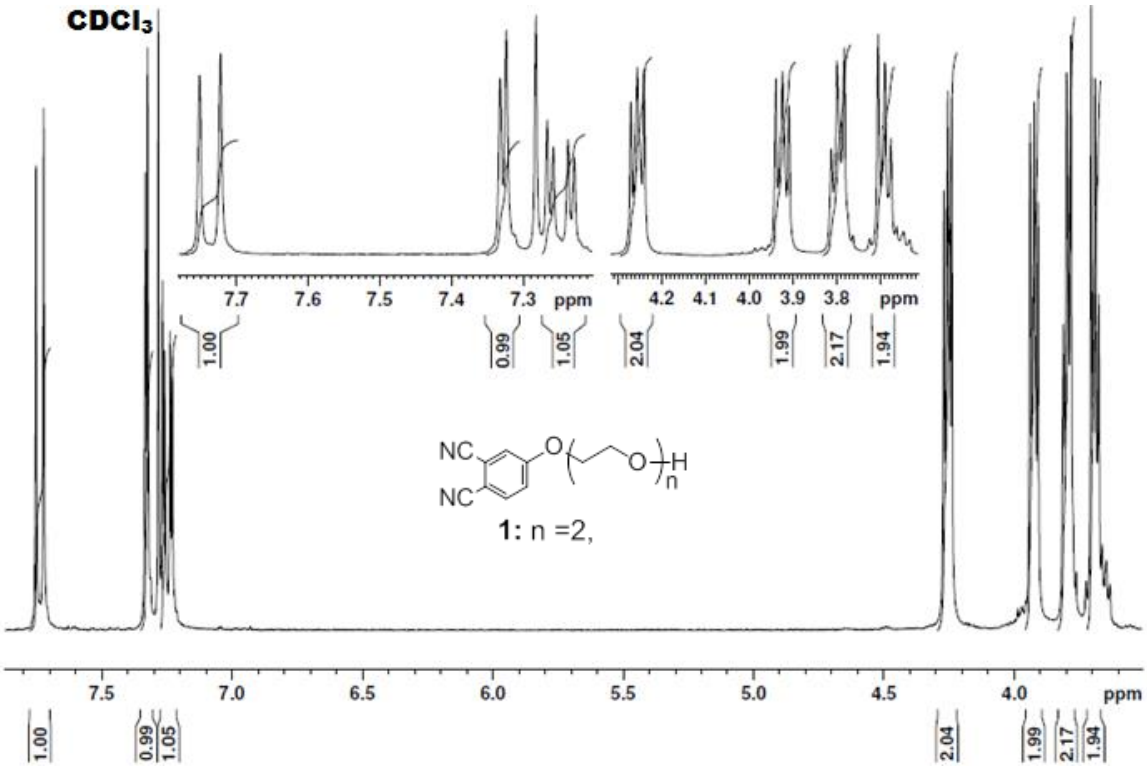

Spectrum A2: 4-[2-(2-(2-hydroxyethoxy)ethoxy)ethoxy]phthalonitrile, 2

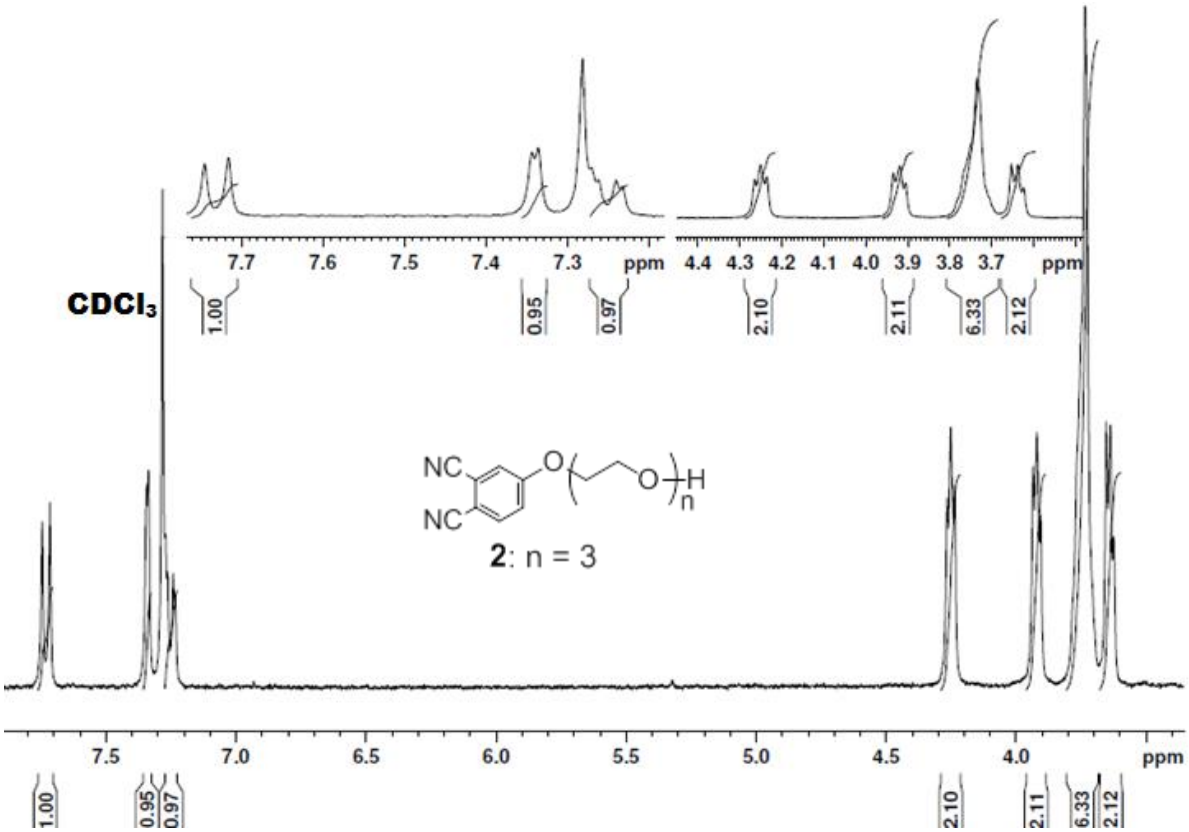

Spectrum A3: 2-[2-(Tetrahydropyranyloxy)ethoxy]ethanol, 3

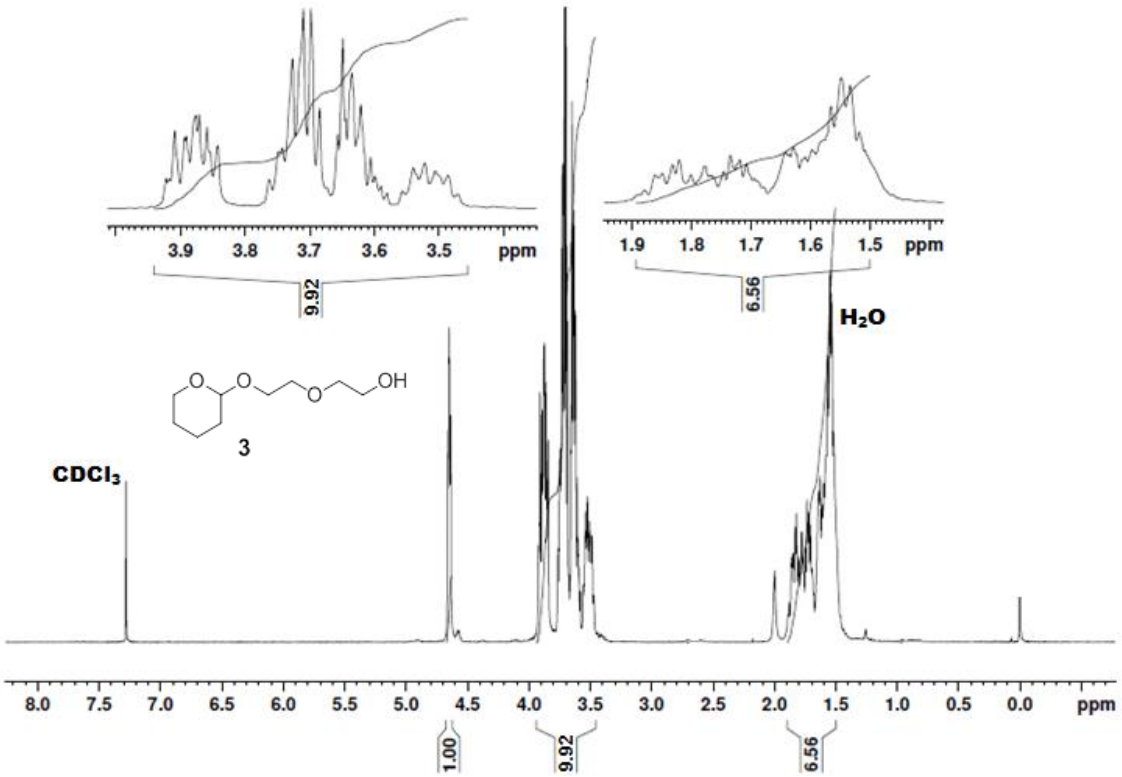

Spectrum A4: 4-[2-(2-(2-pyranethoxy)ethoxy)ethoxy]phthalonitrile, 4

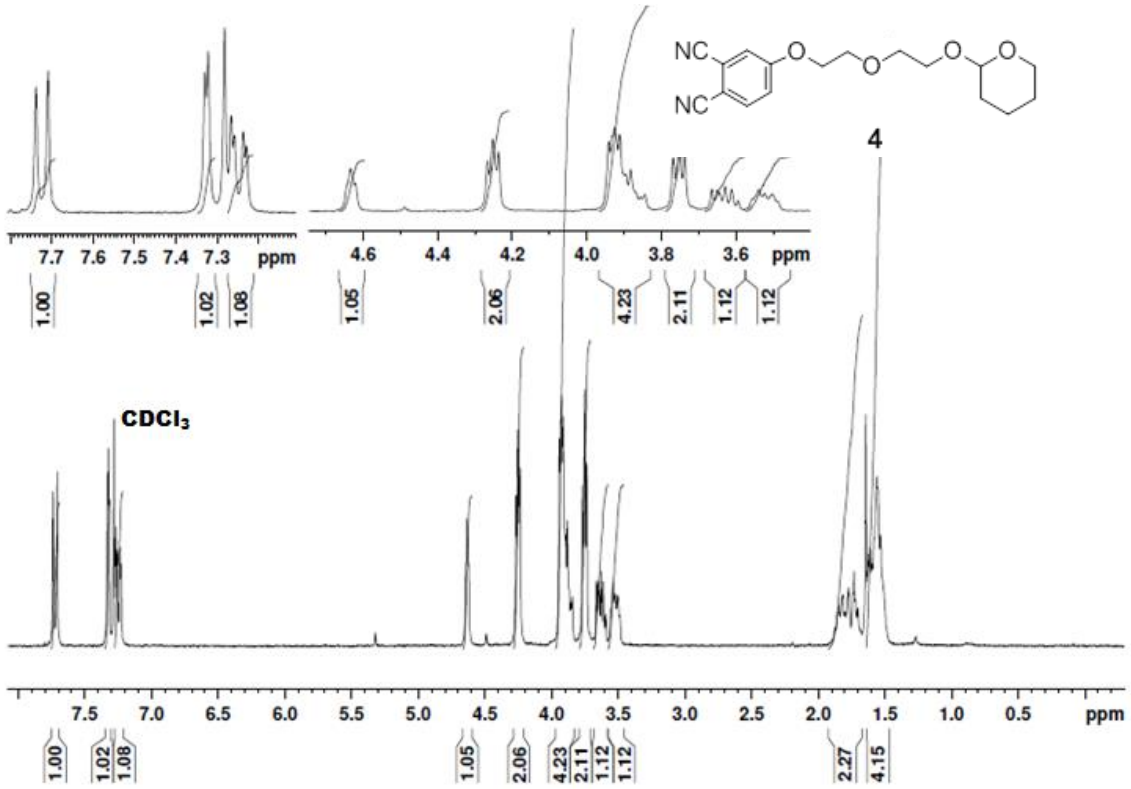

Spectrum A5: 2,5-dihexylthiophene, 5

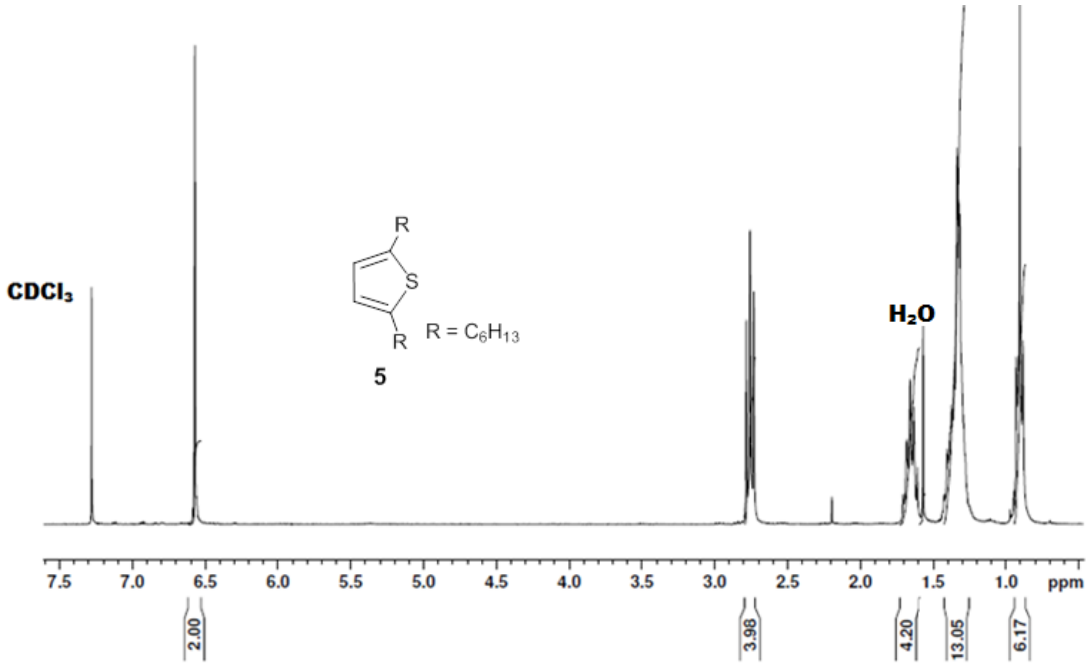

Spectrum A6: 2,5-dihexylthiophene-1,1-dioxide, 6

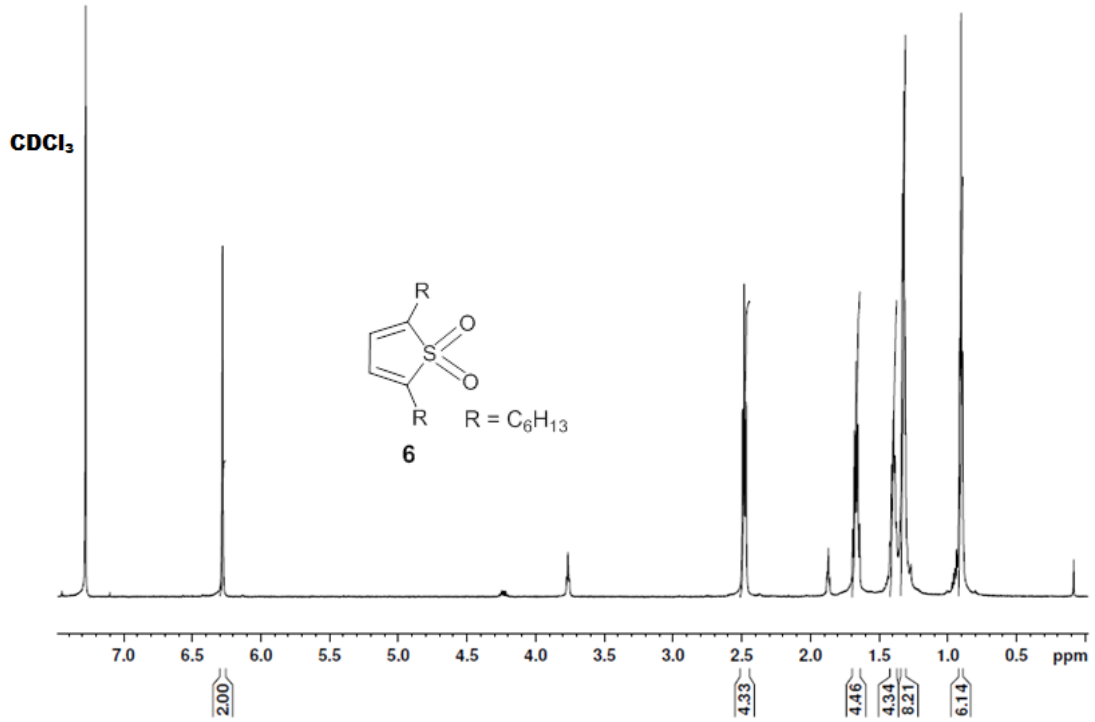

Spectrum A7: 3,6-dihexylphthalonitrile, 7

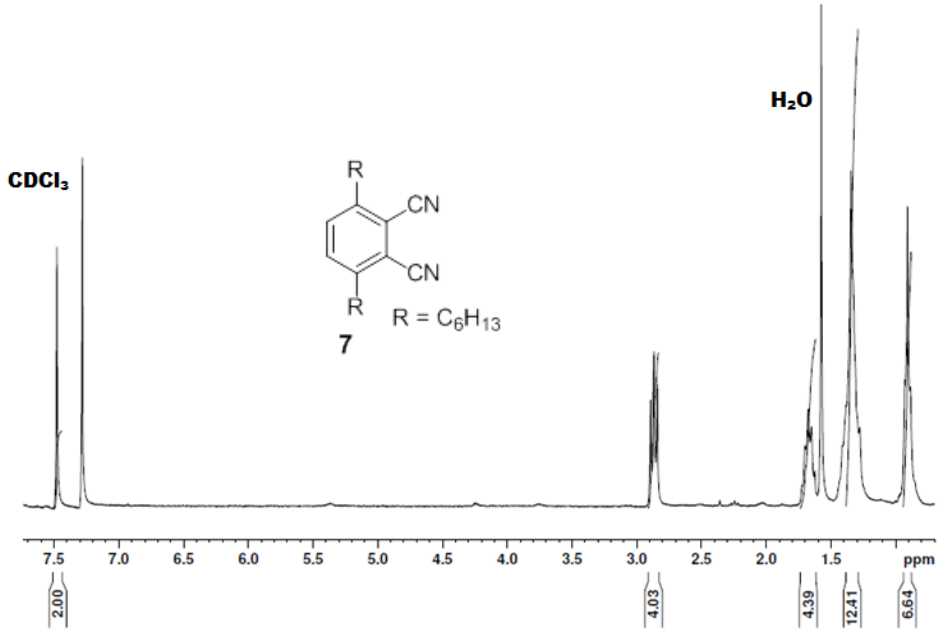

Spectrum A8: 1,4,8,11,15,18,22,25-Octahexylphthalocyanine, 8

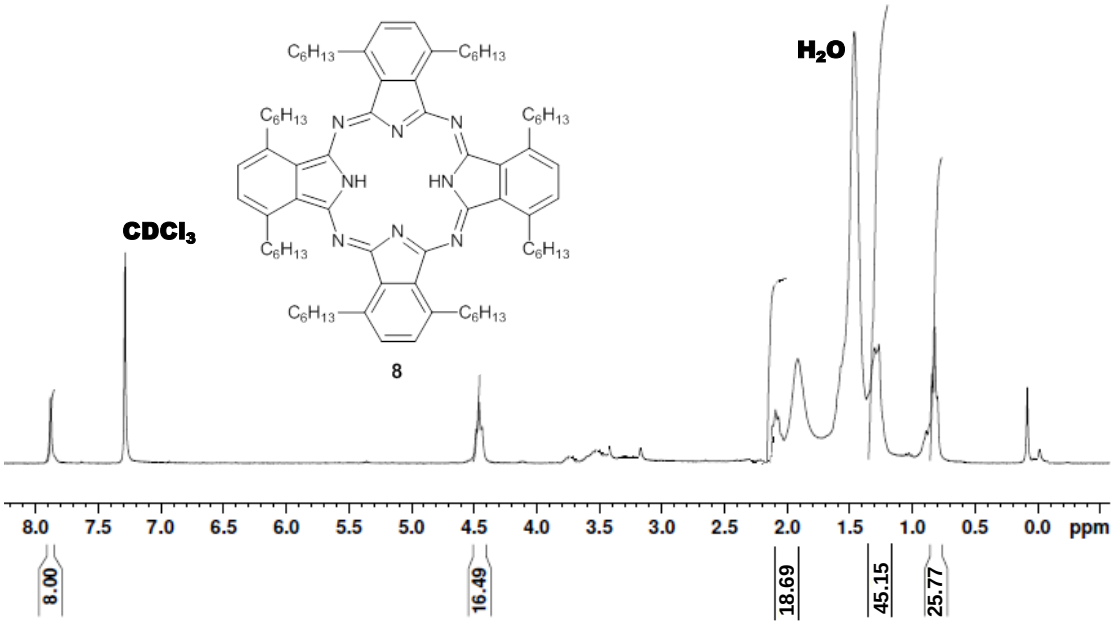

Spectrum A9: 2,9,16,23-Tetra[2-(2-hydroxyethoxy)ethoxy]phthalocyanine, 9

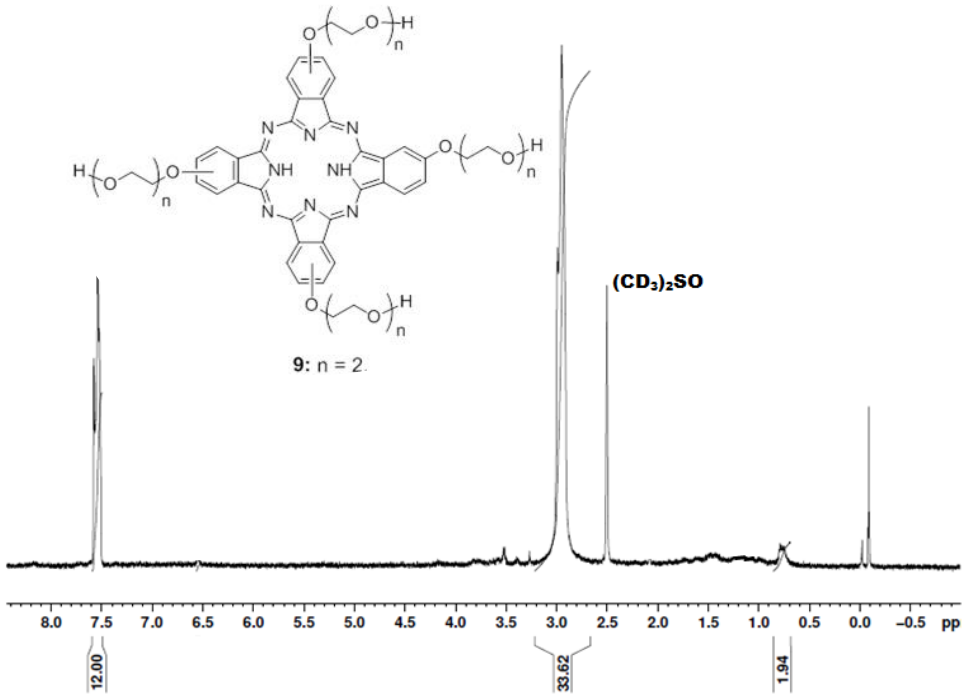

Spectrum A10: 2,9,16,23-Tetra[2-(2-(2-hydroxyethoxy)ethoxy)ethoxy]phthalocyanine, 10

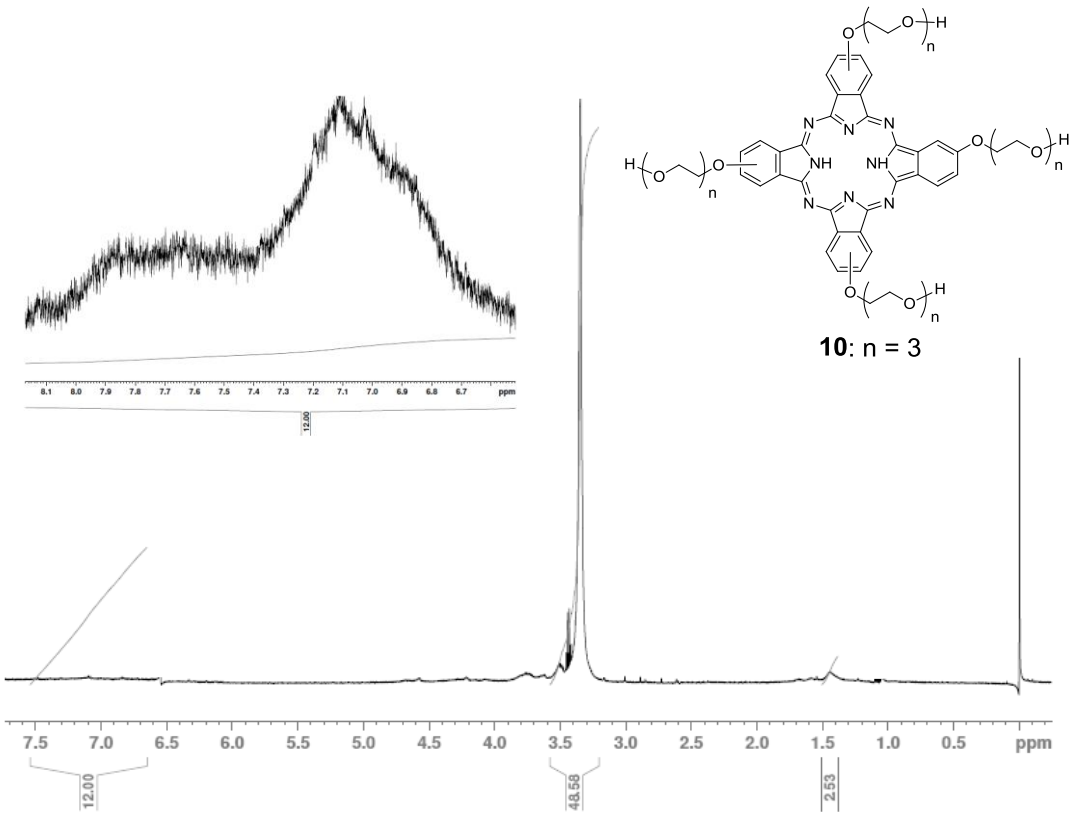

Spectrum A11: Tetrahexyl-di-[2-(2-hydroxyethoxy)ethoxy]-phthalocyanine, 11

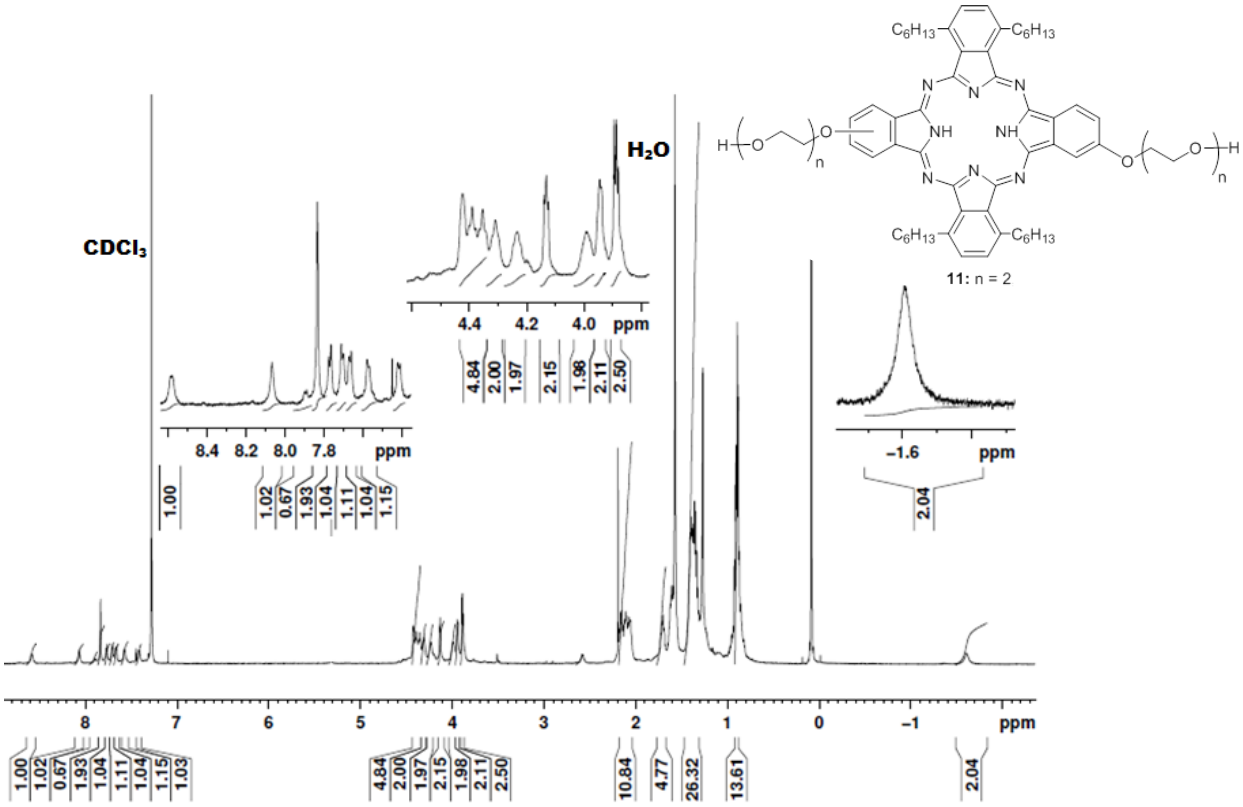

Spectrum A12: Tetrahexyl-di-{2-[2-(2-hydroxyethoxy)-ethoxy]-ethoxy}-phthalocyanine, 12

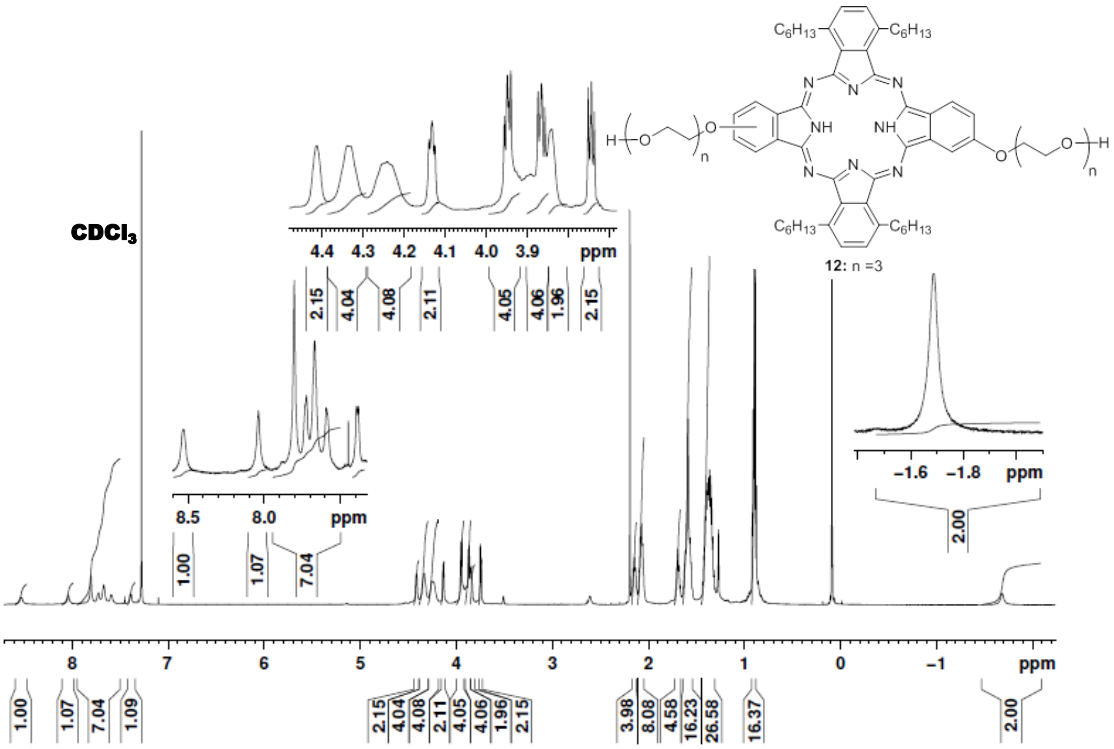

Spectrum A13: 2,5-dodecylthiophene-1,1-dioxide, 14

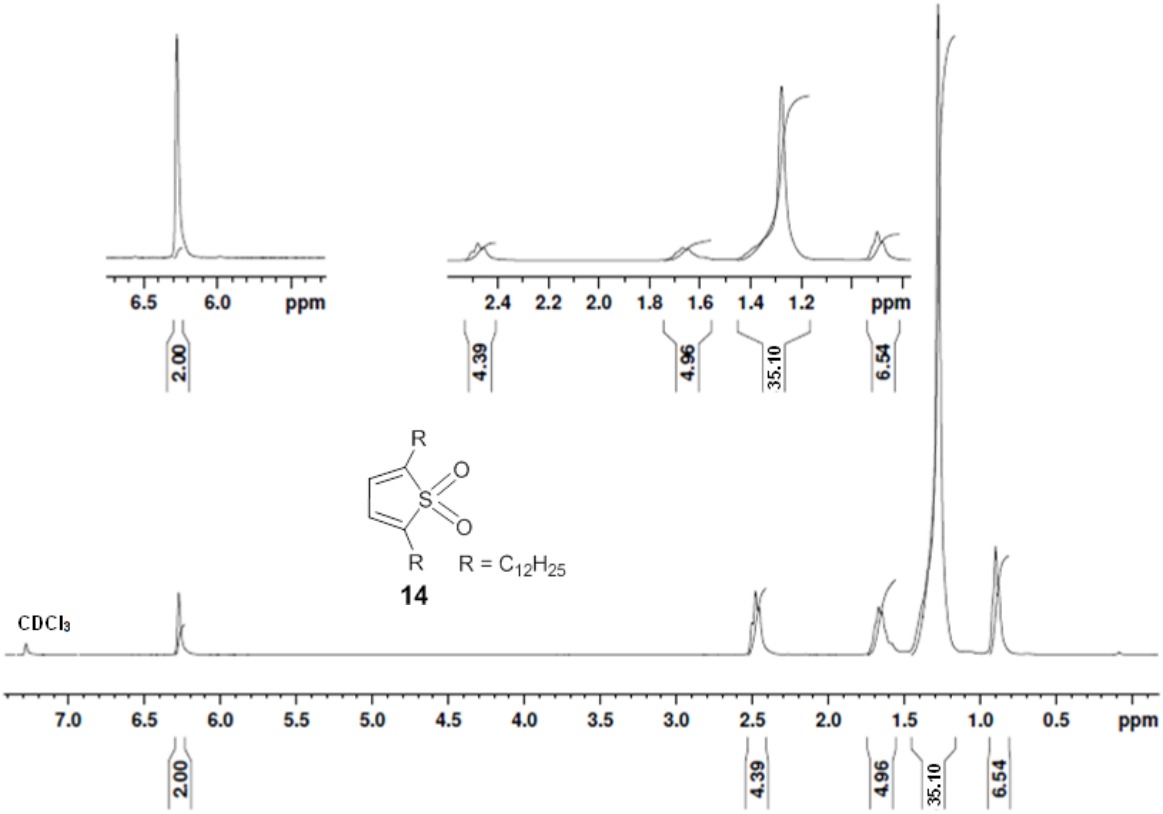

Spectrum A14: 4-Aminophthalonitrile, 17

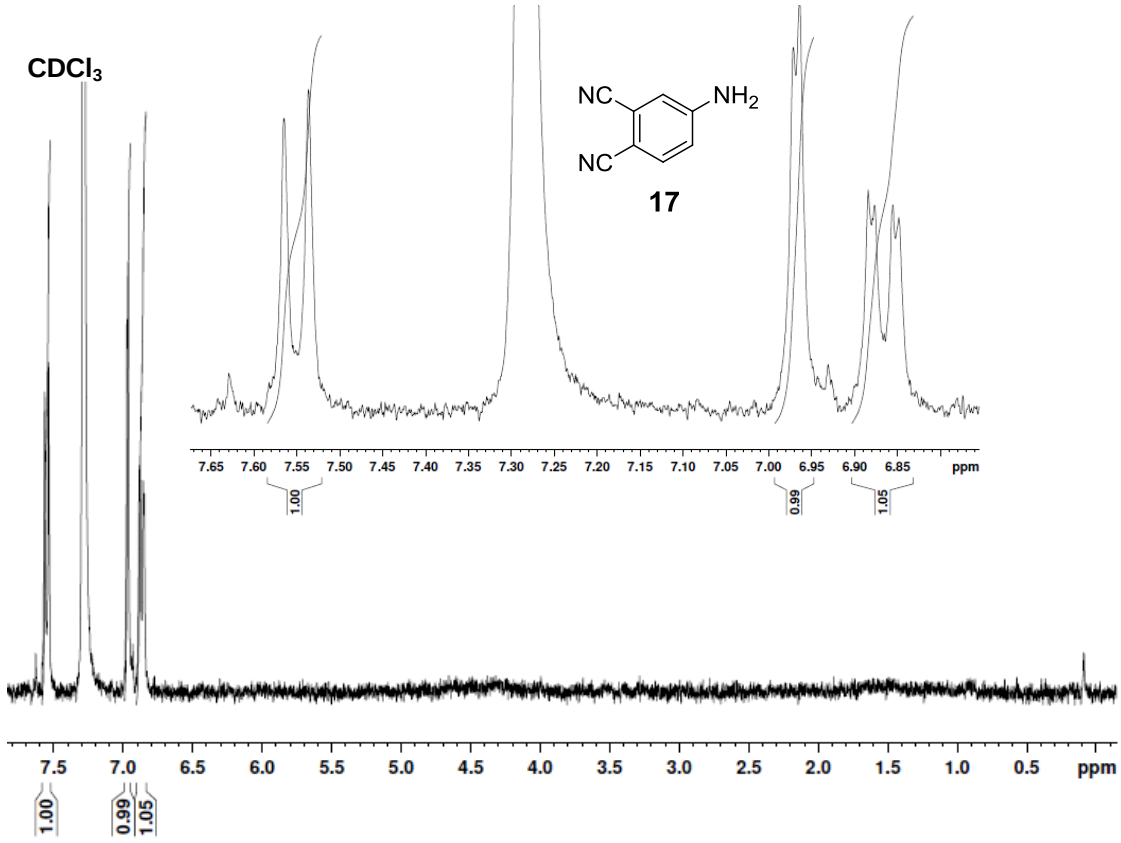

Spectrum A15: Tetrabutylammonium tetrakis(pentafluorophenyl)borate, $[NBu_4][B(C_6F_5)_4]$, 22

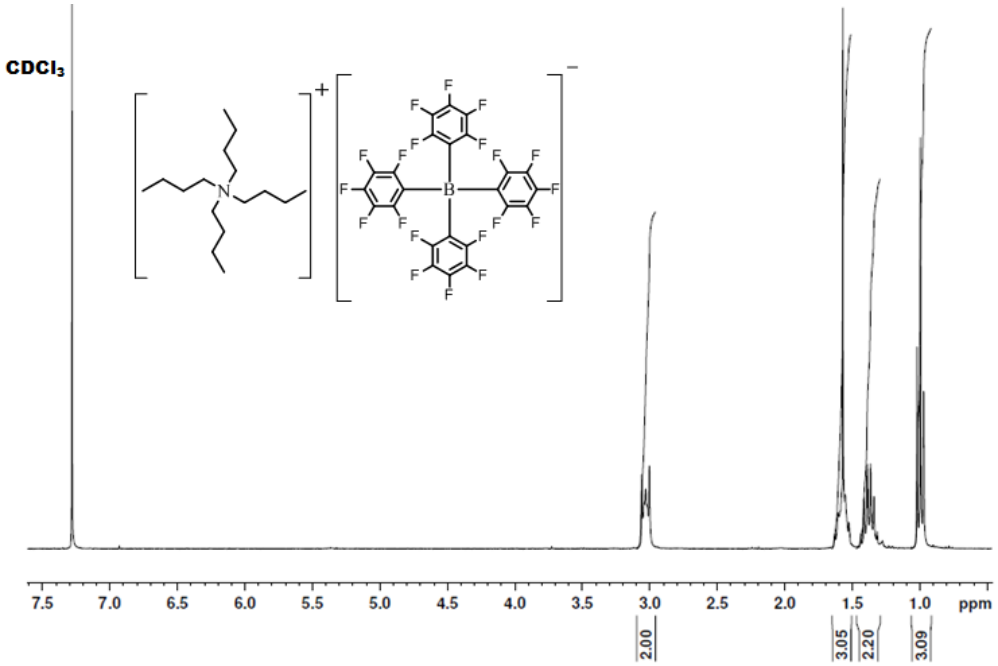

APPENDIX B

FT-IR SPECTRA

Spectrum B1: 1,4,8,11,15,18,22,25-Octahexylphthalocyanine, **8**

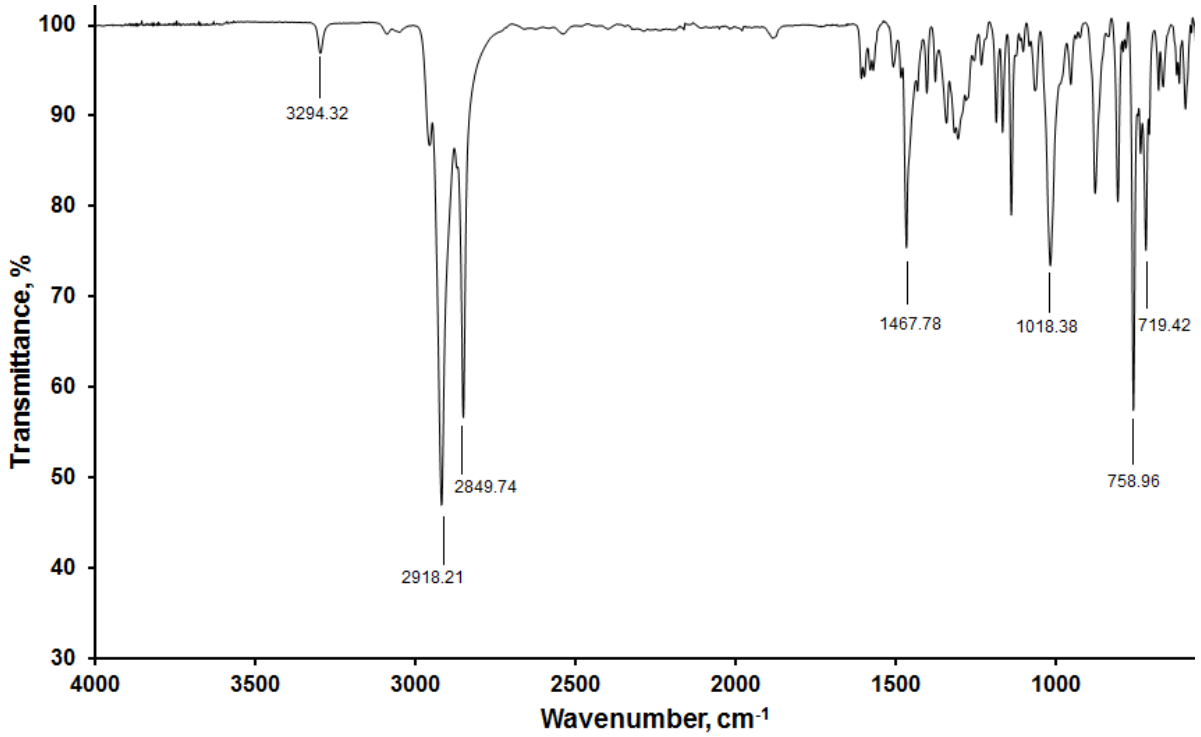

Spectrum B2: Tetra[2-(2-hydroxyethoxy)ethoxy]phthalocyanine, **9**

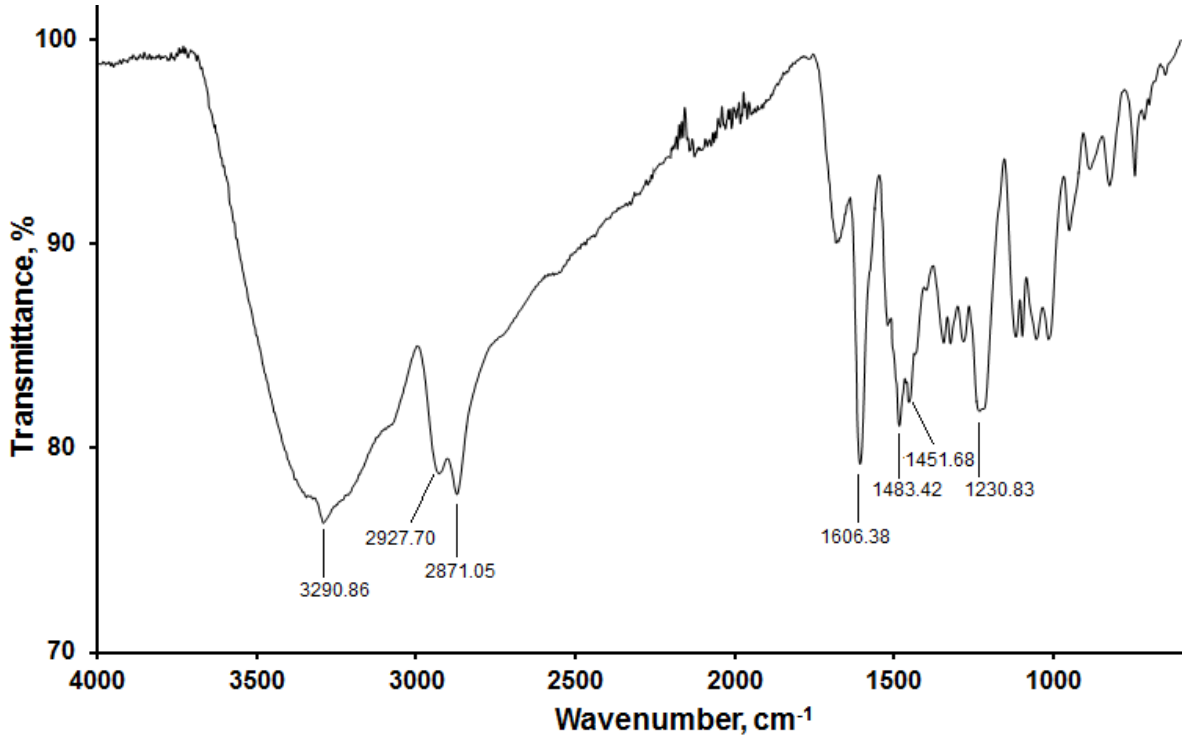

Spectrum B3: Tetra[2-(2-(2-hydroxyethoxy)ethoxy)ethoxy]phthalocyanine, **10**

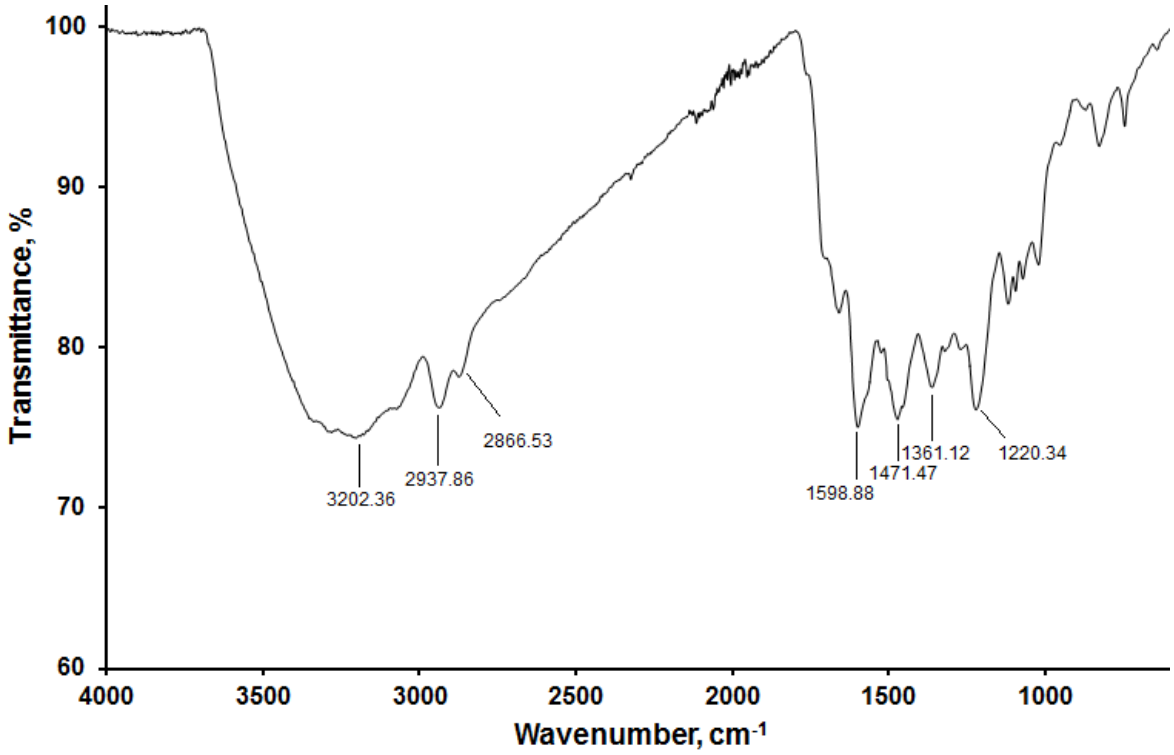

Spectrum B4: tetrahexyl-di-[2-(2-hydroxyethoxy)ethoxy]-phthalocyanine, **11**

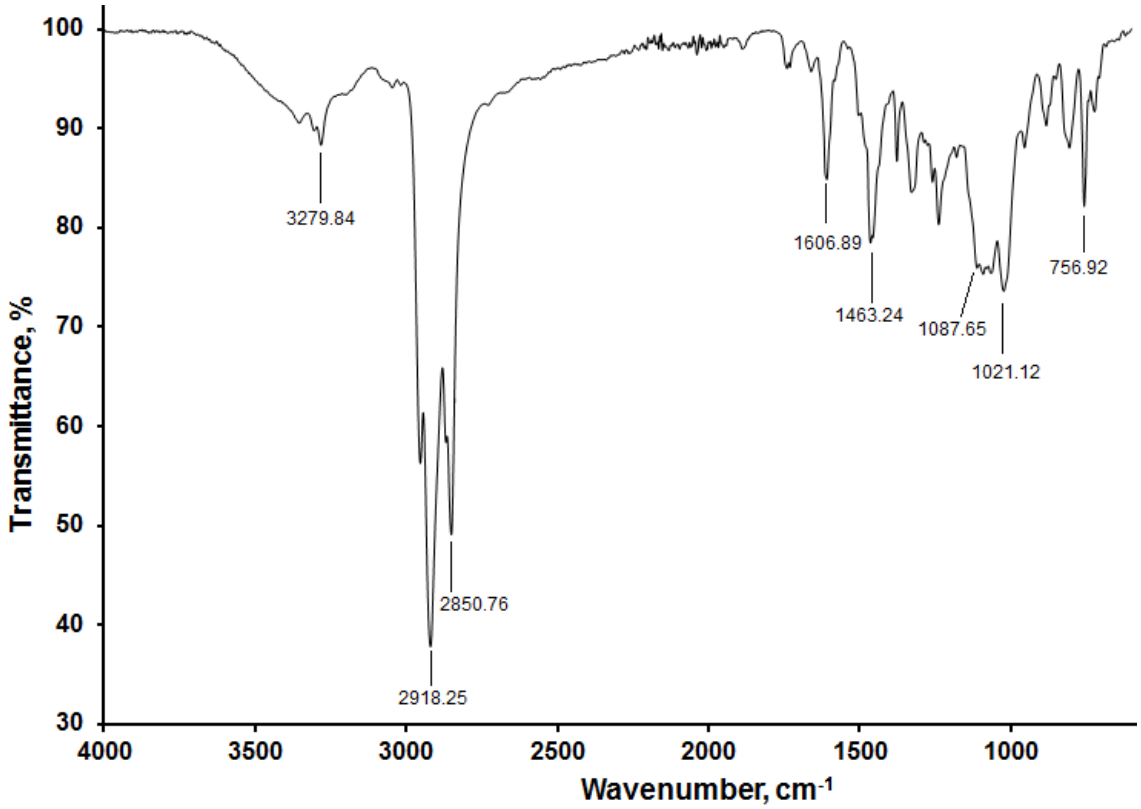

Spectrum B5: tetrahexyl-di-{2-[2-(2-hydroxyethoxy)-ethoxy]-ethoxy}-phthalocyanine, **12**

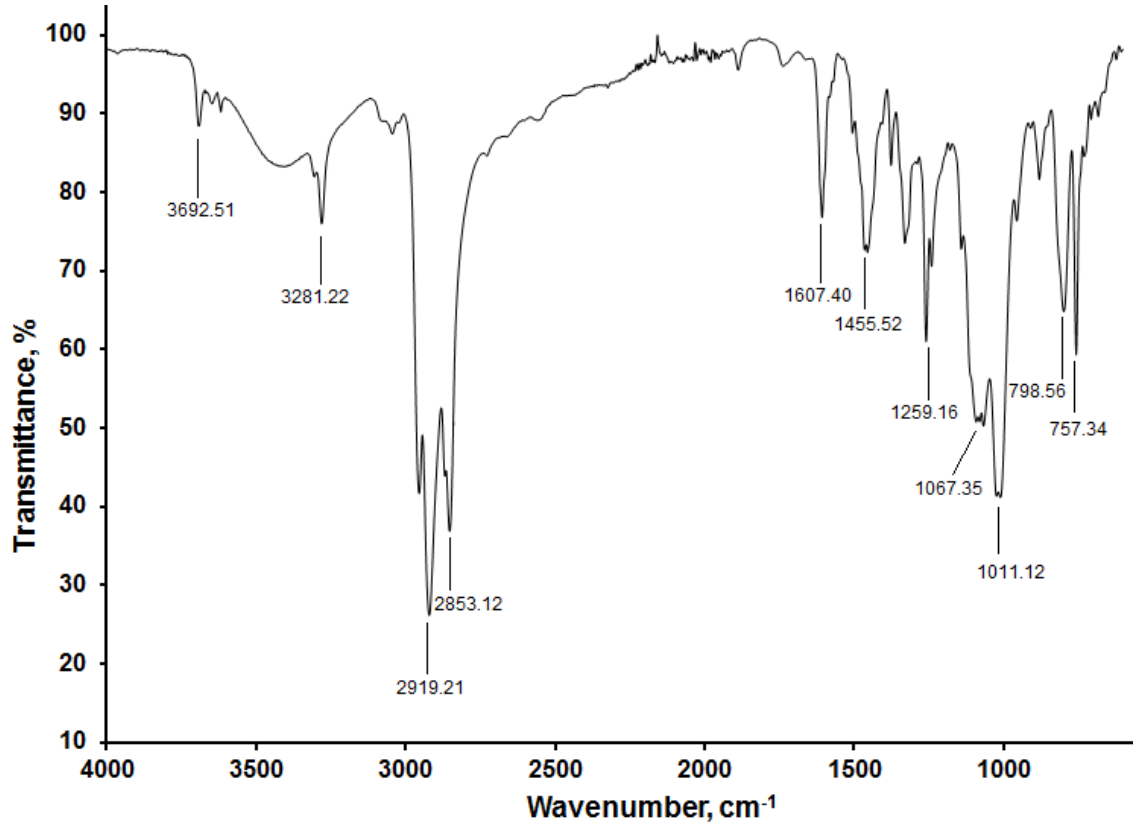

Spectrum B6: 2,5-didodecylthiophene-1,1-dioxide, **14**

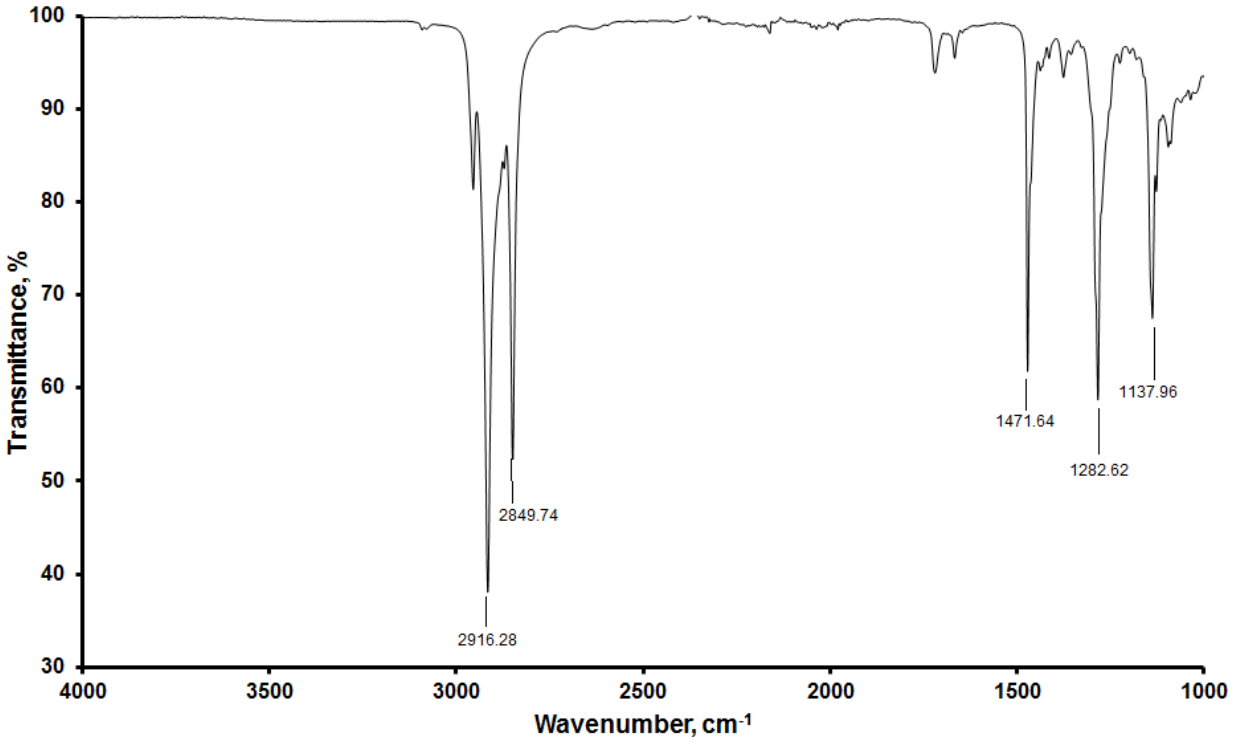

APPENDIX C

CYCLIC VOLTAMMETRY DATA

Appendix C1:

Cyclic voltammetry data of 0.5 mmol/dm^3 solutions at scan rate 100 to 500 mV/s of **23-29** in pure CH_2Cl_2, at 25 ^oC, supporting electrolyte 0.1 mol/dm^3 $[N(^nBu)_4][B(C_6F_5)_4]$, for the oxidation waves.

	mV/s	Wave 1b					Wave 2b									
		E_{pa} (mV)	$E^{0'}$ (mV)	ΔE_p (mV)	I_{pa} (µA)	I_{pc}/I_{pa}	E_{pa} (mV)	$E^{0'}$ (mV)	ΔE_p (mV)	I_{pa} (µA)	I_{pc}/I_{pa}	E_{pa} (mV)	$E_{0'}$ (mV)	ΔE_p (mV)	I_{pa} (µA)	I_{pc}/I_{pa}
23	**100**	110	63	94	0.99	0.94	830	778	104	0.72	0.96	-	-	-	-	-
	200	118	65	106	1.57	0.88	837	781	112	0.99	0.97	-	-	-	-	-
	300	122	61	122	1.87	0.82	845	785	120	1.19	0.95	-	-	-	-	-
	400	126	61	130	2.09	0.84	849	786	126	1.30	0.96	-	-	-	-	-
	500	130	61	138	2.3	0.90	853	787	131	1.60	0.97	-	-	-	-	-
		Wave 1					**Wave 2**									
24	**100**	234	191	86	3.85	1.04	990	931	118	2.30	1.24	-	-	-	-	-
	200	239	191	95	5.65	1.00	996	932	128	3.45	1.09	-	-	-	-	-
	300	239	186	105	7.1	0.99	999	932	135	4.40	1.05	-	-	-	-	-
	400	239	183	112	8.3	0.99	1003	932	141	5.24	1.01	-	-	-	-	-
	500	239	180	118	9.2	0.99	1010	934	151	6.04	0.99	-	-	-	-	-
		Wave 1a					**Wave 1b**					**Wave 2**				
25	**100**	102	54	96	1.96	0.95	287	332	89	1.60	0.94	883	938	110	1.87	0.94
	200	112	57	110	2.49	0.96	283	332	99	2.31	1.04	886	946	121	2.84	0.97
	300	121	51	140	2.76	1.06	285	336	103	2.84	1.03	886	951	128	3.38	0.95
	400	135	60	151	3.16	1.07	286	338	104	2.84	1.19	886	955	136	3.73	0.95
	500	142	67	151	3.56	1.06	286	341	110	3.20	1.17	886	957	143	4.27	0.92
		Wave 1a					**Wave 1b**					**Wave 2**				
26	**100**	-79	-126	94	2.04	1.08	61	418	90	2.25	1.00	462	418	90	2.25	1.00
	200	-75	-126	102	2.93	1.03	65	418	102	3.33	1.02	469	418	102	3.33	1.02
	300	-68	-125	112	3.51	1.04	71	422	114	3.84	1.03	479	422	114	3.84	1.03
	400	-61	-121	123	3.95	1.05	75	424	127	4.42	1.01	487	424	127	4.42	1.01
	500	-58	-121	129	4.36	1.05	79	425	136	4.90	1.03	493	425	136	4.90	1.03
		Wave 1a					**Wave 1b**					**Wave 1c**				
27	**100**	13	-22	70	1.78	1.07	151	119	63	1.63	1.00	362	-	-	-	-
	200	13	-25	77	2.37	1.13	154	117	73	2.22	1.03	366	-	-	-	-
	300	17	-25	83	3.11	1.02	161	119	85	2.51	1.03	375	-	-	-	-
	400	24	-26	100	3.40	1.04	165	112	106	2.88	1.05	376	-	-	-	-
	500	31	-26	114	3.70	1.06	168	112	113	3.48	0.94	380	-	-	-	-
		Wave 2a					**Wave 2b**									
27	**100**	884	-	-	-	-	954	884	141	1.48	1.03	-	-	-	-	-
	200	898	-	-	-	-	982	892	180	2.51	1.01	-	-	-	-	-
	300	912	-	-	-	-	989	894	190	3.11	1.00	-	-	-	-	-
	400	926	-	-	-	-	993	895	195	3.85	0.99	-	-	-	-	-
	500	954	-	-	-	-	1003	899	208	4.59	0.98	-	-	-	-	-
		Wave 1					**Wave 2**									
28	**100**	12	-30	83	2.82	0.97	528	482	92	2.59	1.05	-	-	-	-	-
	200	17	-28	92	3.89	0.99	532	482	100	3.66	1.06	-	-	-	-	-
	300	22	-29	101	4.67	0.99	538	484	108	4.42	1.03	-	-	-	-	-
	400	26	-28	108	5.31	0.99	544	486	116	5.15	1.02	-	-	-	-	-
	500	29	-27	112	5.90	0.99	551	488	125	5.54	1.01	-	-	-	-	-
		Wave 1a					**Wave 1b**					**Wave 2**				
29	**100**	-44	-90	93	2.22	1.01	74	-	-	-	-	450	416	67	3.11	0.98
	200	-42	-91	97	2.85	0.99	80	-	-	-	-	453	417	71	3.59	1.02
	300	-41	-91	101	4.02	0.99	85	-	-	-	-	455	418	75	4.33	1.02
	400	-38	-93	109	5.03	0.97	96	-	-	-	-	461	420	82	5.03	0.98
	500	-33	-91	118	5.51	0.99	101	-	-	-	-	466	421	90	5.47	1.00

[a] The data was collected in pure CH_3CN. [b] E_{pc} values are given. [c] i_{pc} values are given. [d] i_{pa}/i_{pc} values are given.
[e] This experiment wasn't done. [f] The waves was not observed. [g] Poor resolution disallowed further measurements.

Appendix C2:

Cyclic voltammetry data of 0.5 mmol/dm^3 solutions at scan rate 100 to 500 mV/s of **23-29** in pure CH_2Cl_2, at 25 ^oC, supporting electrolyte 0.1 mol/dm^3 $[N(^nBu)_4][B(C_6F_5)_4]$, for the reduction waves.

	mV/s	Wave 3					Wave 4									
		E_{pa} (mV)	$E^{0'}$ (mV)	ΔE_p (mV)	I_{pa} (µA)	I_{pc}/I_{pa}	E_{pa} (mV)	$E^{0'}$ (mV)	ΔE_p (mV)	I_{pa} (µA)	I_{pc}/I_{pa}	E_{pa} (mV)	$E_{0'}$ (mV)	ΔE_p (mV)	I_{pa} (µA)	I_{pc}/I_{pa}
23	**100**	-1776 [b]	-	-	-	-	1887	-	-	-	-	-	-	-	-	-
	200 [g]	-1784	-	-	-	-	-1904	-	-	-	-	-	-	-	-	-
	300 [g]	-1791	-	-	-	-	-1917	-	-	-	-	-	-	-	-	-
	400 [g]	-1799	-	-	-	-	-1931	-	-	-	-	-	-	-	-	-
	500 [g]	-1803	-	-	-	-	-1803	-	-	-	-	-	-	-	-	-
		Wave 3					**Wave 4**									
24	**100**	-1501 [b]	-1552	112	2.85 [c]	0.81 [d]	-1898 [b]	-2020	250	3.00 [c]	0.60 [d]	-	-	-	-	-
	200	-1512 [b]	-1568	122	3.75 [c]	0.92 [d]	-1895 [b]	-2028	270	3.20 [c]	0.97 [d]	-	-	-	-	-
	300	-1512 [b]	-1571	128	4.6 [c]	0.96 [d]	-1899 [b]	-2036	280	3.30 [c]	0.89 [d]	-	-	-	-	-
	400	-1512 [b]	-1572	132	5.3 [c]	0.99 [d]	-1902 [b]	-2040	283	3.50 [c]	0.80 [d]	-	-	-	-	-
	500	-1514 [b]	-1577	135	6 [c]	1.01 [d]	-1904 [b]	-2043	283	3.60 [c]	0.73 [d]	-	-	-	-	-
		Wave 3a					**Wave 3b**									
25	**100**	-1685	-	-	-	-	-1784 [b]	-1865	202	2.13 [c]	1.07 [d]	-	-	-	-	-
	200	-1695	-	-	-	-	-1772 [b]	-1865	226	3.38 [c]	1.03 [d]	-	-	-	-	-
	300	-1700	-	-	-	-	-1766 [b]	-1871	250	4.53 [c]	0.94 [d]	-	-	-	-	-
	400	-1705	-	-	-	-	-1769 [b]	-1875	253	5.33 [c]	0.95 [d]	-	-	-	-	-
	500	-1715	-	-	-	-	-1769 [b]	-1879	260	6.31 [c]	0.96 [d]	-	-	-	-	-
		Wave 3a					**Wave 3b**					**Wave 3c**				
26	**100**	-1701 [b]	-1735	67	1.80 [c]	1.36 [d]	-1894 [b]	-1949	109	1.60 [c]	1.02 [d]	-2094 [b]	-2126	114	1.33 [c]	1.23 [d]
	200	-1702 [b]	-1739	74	2.42 [c]	1.35 [d]	-1882 [b]	-1949	135	2.65 [c]	1.03 [d]	-2097 [b]	-2134	140	2.20 [c]	1.23 [d]
	300	-1699 [b]	-1739	81	2.95 [c]	1.34 [d]	-1878 [b]	-1952	149	3.27 [c]	1.02 [d]	-2098 [b]	-2140	154	2.72 [c]	1.23 [d]
	400	-1696 [b]	-1742	91	3.44 [c]	1.35 [d]	-1868 [b]	-1949	163	3.54 [c]	1.04 [d]	-2106 [b]	-2146	168	2.99 [c]	1.23 [d]
	500	-1694 [b]	-1743	98	4.08 [c]	1.30 [d]	-1865 [b]	-1955	180	3.95 [c]	1.03 [d]	-2110 [b]	-2155	185	3.31 [c]	1.23 [d]
		Wave 3a					**Wave 3b**					**Wave 4**				
27	**100**	-1360 [b]	-1406	92	1.74 [c]	1.15 [d]	-1709 [b]	-1758	97	1.78 [c]	0.92 [d]	-1801 [b]	-1841	81	1.78 [c]	1.46 [d]
	200	-1357 [b]	-1413	113	2.44 [c]	1.15 [d]	-1705 [b]	-1760	109	2.51 [c]	0.97 [d]	-1797 [b]	-1845	95	1.92 [c]	1.50 [d]
	300	-1354 [b]	-1414	120	2.93 [c]	1.11 [d]	-1702 [b]	-1764	123	2.96 [c]	0.98 [d]	-1783 [b]	-1839	113	2.22 [c]	1.47 [d]
	400	-1350 [b]	-1416	132	3.39 [c]	1.09 [d]	-1698 [b]	-1767	137	3.25 [c]	0.95 [d]	-1776 [b]	-1838	123	2.29 [c]	1.52 [d]
	500	-1350 [b]	-1419	138	3.74 [c]	1.11 [d]	-1696 [b]	-1768	144	3.59 [c]	0.99 [d]	-1765 [b]	-1834	137	2.74 [c]	1.51 [d]
		Wave 3a					**Wave 3b**									
28	**100**	-1510 [b]	-1547	75	0.58 [c]	1.11 [d]	-1625 [b]	-1669	88	2.79 [c]	1.05 [d]	-	-	-	-	-
	200	-1507 [b]	-1548	82	0.82 [c]	1.11 [d]	-1622 [b]	-1669	94	3.63 [c]	1.04 [d]	-	-	-	-	-
	300	-1501 [b]	-1546	91	0.97 [c]	1.10 [d]	-1619 [b]	-1671	103	4.54 [c]	1.06 [d]	-	-	-	-	-
	400	-1495 [b]	-1545	100	1.04 [c]	1.10 [d]	-1616 [b]	-1671	109	5.05 [c]	1.06 [d]	-	-	-	-	-
	500	-1492 [b]	-1545	106	1.09 [c]	1.10 [d]	-1615 [b]	-1671	113	5.70 [c]	1.05 [d]	-	-	-	-	-
		Wave 4a					**Wave 4b**									
28	**100**	-1846 [b]	-1878	64	0.49 [c]	1.07 [d]	-2025 [b]	-2081	112	1.79 [c]	1.09 [d]	-	-	-	-	-
	200	-1843 [b]	-1878	70	0.53 [c]	1.10 [d]	-2025 [b]	-2084	119	2.02 [c]	1.09 [d]	-	-	-	-	-
	300	-1840 [b]	-1878	76	0.58 [c]	1.11 [d]	-2024 [b]	-2087	125	2.98 [c]	1.09 [d]	-	-	-	-	-
	400	-1837 [b]	-1878	82	0.65 [c]	1.10 [d]	-2023 [b]	-2091	135	3.69 [c]	1.09 [d]	-	-	-	-	-
	500	-1834 [b]	-1878	88	0.71 [c]	1.09 [d]	-2023 [b]	-2092	139	4.15 [c]	1.09 [d]	-	-	-	-	-
		Wave 3a					**Wave 3b**					**Wave 3c**				
29	**100**	-1608 [b]	-1639	62	2.48 [c]	0.75 [d]	-1847 [b]	-1895	96	2.00 [c]	0.96 [d]	-2047 [b]	-2096	97	1.63 [c]	0.66 [d]
	200	-1607 [b]	-1640	66	3.67 [c]	0.75 [d]	-1838 [b]	-1895	114	2.74 [c]	0.97 [d]	-2050 [b]	-2099	98	2.37 [c]	0.65 [d]
	300	-1604 [b]	-1641	73	4.36 [c]	0.75 [d]	-1832 [b]	-1897	129	3.18 [c]	0.98 [d]	-2053 [b]	-2102	99	2.81 [c]	0.64 [d]
	400	-1599 [b]	-1639	81	4.96 [c]	0.75 [d]	-1829 [b]	-1901	144	3.48 [c]	0.98 [d]	-2056 [b]	-2105	98	3.18 [c]	0.64 [d]
	500	-1593 [b]	-1638	90	5.59 [c]	0.74 [d]	-1823 [b]	-1905	164	3.77 [c]	0.98 [d]	-2058 [b]	-2107	99	3.70 [c]	0.66 [d]

[a] The data was collected in pure CH_3CN. [b] E_{pc} values are given. [c] i_{pc} values are given. [d] i_{pa}/i_{pc} values are given.
[e] This experiment wasn't done. [f] The waves was not observed. [g] Poor resolution disallowed further measurements.

Appendix C3:

Cyclic voltammetry data of 0.5 mmol/dm^3 solutions at scan rate 100 to 500 mV/s of **23-29** in pure CH_2Cl_2 containing a drop of CH_3CN, at 25 ^oC, supporting electrolyte 0.1 mol/dm^3 $[N(^nBu)_4][B(C_6F_5)_4]$.

	mV/s	Wave 1b					Wave 2b									
		E_{pa} (mV)	$E^{\theta'}$ (mV)	ΔE_p (mV)	I_{pa} (µA)	I_{pc}/I_{pa}	E_{pa} (mV)	$E^{\theta'}$ (mV)	ΔE_p (mV)	I_{pa} (µA)	I_{pc}/I_{pa}	E_{pa} (mV)	$E_{\theta'}$ (mV)	ΔE_p (mV)	I_{pa} (µA)	I_{pc}/I_{pa}
23	**100**	93	55	76	0.18	1.01	672	634	75	0.21	0.97	-	-	-	-	-
	200[g]	-	-	-	-	-	-	-	-	-	-	-	-	-	-	-
	300[g]	-	-	-	-	-	-	-	-	-	-	-	-	-	-	-
	400[g]	-	-	-	-	-	-	-	-	-	-	-	-	-	-	-
	500[g]	-	-	-	-	-	-	-	-	-	-	-	-	-	-	-
		Wave 1					**Wave 2**									
25	**100**	95	45	90	1.96	0.98	882	837	90	2.45	0.98	-	-	-	-	-
	200	105	50	99	2.28	0.96	896	843	106	2.67	1.03	-	-	-	-	-
	300	110	53	105	2.61	0.97	911	848	127	3.20	1.03	-	-	-	-	-
	400	114	53	111	3.07	0.96	919	850	138	3.38	1.15	-	-	-	-	-
	500	116	57	110	3.57	0.99	927	852	149	3.77	1.12	-	-	-	-	-
		Wave 1					**Wave 2**									
26	**100**	119	64	109	2.57	1.02	912	861	102	2.77	0.96	-	-	-	-	-
	200	126	66	119	3.76	0.96	923	865	116	3.11	0.96	-	-	-	-	-
	300	129	66	126	4.58	0.97	933	868	129	3.94	0.94	-	-	-	-	-
	400	132	67	131	5.47	0.98	943	870	146	4.49	0.94	-	-	-	-	-
	500	136	68	136	6.46	0.98	953	873	160	4.96	0.95	-	-	-	-	-
		Wave 1a					**Wave 2**									
27	**100**	125	79	91	1.89	0.94	845	800	90	1.78	1.02	-	-	-	-	-
	200	128	76	105	2.70	0.93	860	805	109	2.22	1.02	-	-	-	-	-
	300	132	76	113	3.18	0.93	874	810	127	2.59	1.03	-	-	-	-	-
	400	135	76	120	3.55	0.94	884	816	137	2.96	1.05	-	-	-	-	-
	500	135	74	123	4.14	0.95	888	816	144	3.25	1.05	-	-	-	-	-
		Wave 1					**Wave 2**									
29	**100**	-30	-72	85	2.81	1.01	430	392	77	2.81	1.00	-	-	-	-	-
	200	-27	-72	90	4.07	1.02	435	393	84	3.88	0.96	-	-	-	-	-
	300	-22	-70	96	4.87	1.00	438	393	89	4.73	0.98	-	-	-	-	-
	400	-19	-69	101	5.62	1.00	441	394	93	5.18	0.99	-	-	-	-	-
	500	-17	-69	104	6.21	1.01	446	396	100	5.77	0.99	-	-	-	-	-
		Wave 3					**Wave 4**									
23	**100**	-1614[b]	-1654	76	0.18[c]	0.87[d]	-2090[b]	-2143	106	0.20[c]	0.81[d]	-	-	-	-	-
	200[g]	--	-	-	-	-	-	-	-	-	-	-	-	-	-	-
	300[g]	-	-	-	-	-	-	-	-	-	-	-	-	-	-	-
	400[g]	-	-	-	-	-	-	-	-	-	-	-	-	-	-	-
	500[g]	-	-	-	-	-	-	-	-	-	-	-	-	-	-	-
		Wave 3					**Wave 4**									
25	**100**	-1685[b]	-1726	81	2.76[c]	1.10[d]	-2034[b]	-2083	98	2.49[c]	0.93[d]	-	-	-	-	-
	200	-1679[b]	-1726	93	3.70[c]	1.03[d]	-2028[b]	-2083	109	2.84[c]	0.94[d]	-	-	-	-	-
	300	-1670[b]	-1721	102	4.14[c]	1.05[d]	-2022[b]	-2109	174	3.29[c]	0.92[d]	-	-	-	-	-
	400	-1666[b]	-1720	109	4.89[c]	1.02[d]	-2018[b]	-2110	184	3.56[c]	0.95[d]	-	-	-	-	-
	500	-1663[b]	-1721	115	5.33[c]	1.03[d]	-2015[b]	-2112	194	3.91[c]	0.95[d]	-	-	-	-	-
		Wave 3					**Wave 4**									
26	**100**	-1635[b]	-1685	99	3.25[c]	0.97[d]	-2000[b]	-2087	172	2.74[c]	1.03[d]	-	-	-	-	-
	200	-1628[b]	-1683	109	3.97[c]	1.02[d]	-2002[b]	-2089	174	3.59[c]	1.00[d]	-	-	-	-	-
	300	-1625[b]	-1685	119	4.79[c]	1.03[d]	-2004[b]	-2104	200	4.45[c]	0.92[d]	-	-	-	-	-
	400	-1622[b]	-1686	129	5.43[c]	1.06[d]	-2006[b]	-2112	211	5.05[c]	0.93[d]	-	-	-	-	-
	500	-1618[b]	-1690	143	5.99[c]	1.06[d]	-2013[b]	-2129	232	5.47[c]	0.94[d]	-	-	-	-	-
		Wave 3					**Wave 4**					**Wave 5**				
27	**100**	-1390[b]	-1430	79	1.48[c]	0.99[d]	-1675[b]	-1767	184	2.88[c]	0.97[d]	-2044[b]	-2085	82	1.48[c]	1.05[d]
	200	-1388[b]	-1430	85	1.79[c]	1.01[d]	-1668[b]	-1765	193	3.74[c]	1.01[d]	-2042[b]	-2085	87	1.92[c]	1.04[d]
	300	-1382[b]	-1431	98	2.16[c]	1.01[d]	-1665[b]	-1765	200	4.62[c]	1.01[d]	-2039[b]	-2086	94	2.14[c]	1.03[d]
	400	-1378[b]	-1430	106	2.55[c]	0.99[d]	-1662[b]	-1765	207	5.33[c]	0.97[d]	-2036[b]	-2087	101	2.43[c]	1.04[d]
	500	-1378[b]	-1432	109	2.66[c]	1.08[d]	-1659[b]	-1767	215	5.99[c]	0.99[d]	-2033[b]	-2087	108	2.81[c]	1.05[d]
		Wave 3					**Wave 4**									
29	**100**	-1636[b]	-1671	69	2.88[c]	0.97[d]	-2033[b]	-2066	65	1.63[c]	0.66[d]	-	-	-	-	-
	200	-1635[b]	-1672	73	3.73[c]	1.02[d]	-2028[b]	-2069	82	2.37[c]	0.65[d]	-	-	-	-	-
	300	-1634[b]	-1672	78	5.03[c]	1.05[d]	-2022[b]	-2070	97	2.81[c]	0.64[d]	-	-	-	-	-
	400	-1632[b]	-1675	84	5.61[c]	1.08[d]	-2017[b]	-2072	110	3.18[c]	0.64[d]	-	-	-	-	-
	500	-1629[b]	-1676	93	6.21[c]	1.07[d]	-2011[b]	-2071	120	3.70[c]	0.66[d]	-	-	-	-	-

[a] The data was collected in pure CH_3CN. [b] E_{pc} values are given. [c] i_{pc} values are given. [d] i_{pa}/i_{pc} values are given.
[e] This experiment wasn't done. [f] The waves was not observed. [g] Poor resolution disallowed further measurements.

APPENDIX D

MOLECULAR ORBITAL VIEWS

The molecular orbital views of the HOMO-1, HOMO, LUMO and LUMO+1 orbitals for compounds **23** to **29.**

Compound	HOMO -1	HOMO	LUMO	LUMO +1
23, *np*-$(C_6H_{13})_8$-PcRu(CO)	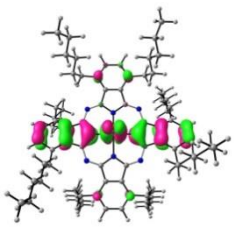	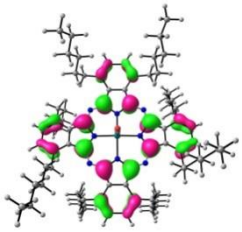	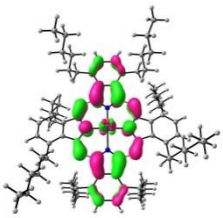	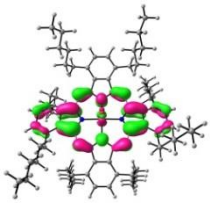
24, *p*-$(CH_3PhO)_8$-PcRu(CO)	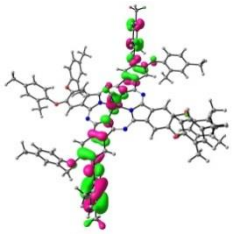	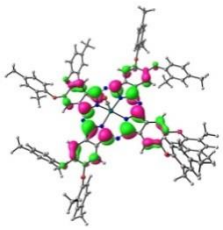	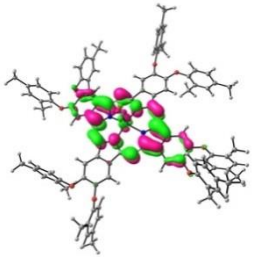	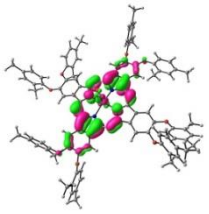
25, *p*-$(C_6H_{13})_8$-PcRu(CO)	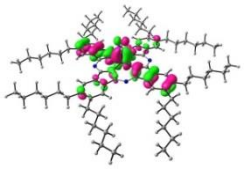	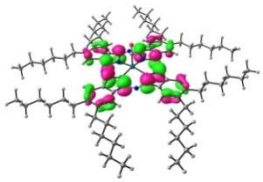	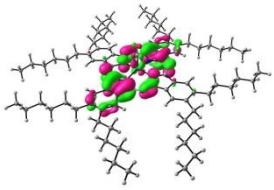	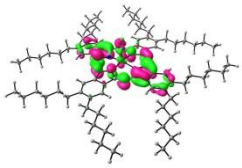
26, *np*-$(OC_5H_{11})_8$-PcRu(R)(CO) R = CH_3CN	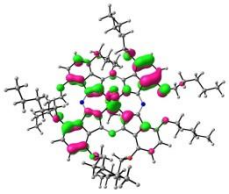	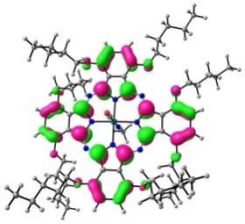	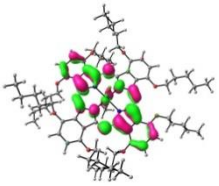	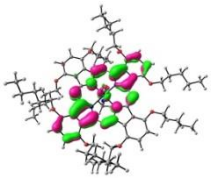
27, *p*-$(OC_5H_{11})_8$-PcRu(CO)	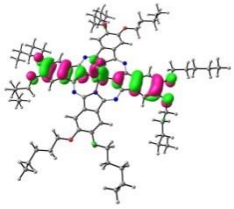	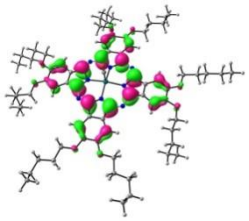	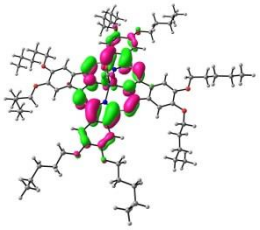	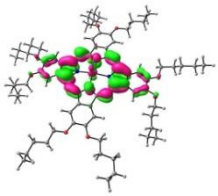
28, *np*-$(OC_4H_9)_8$-PcRu(CO)(R), R = Pyridine (py)	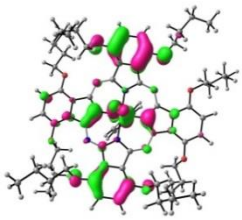	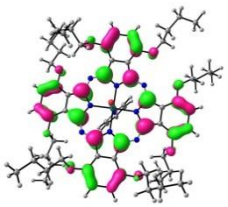	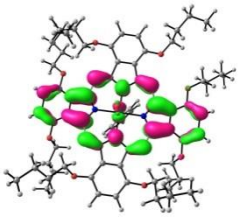	
29, *np*-$(OC_4H_9)_8$-PcRu(CO)(R), R = $N(CH(CH_3)_2)_2$	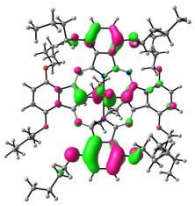	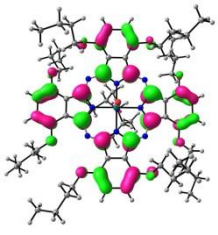	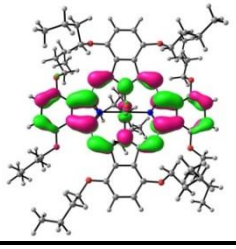	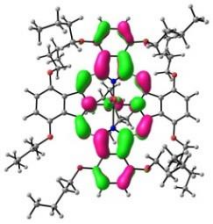

Abstract

A series of metal-free phthalocyanines, with ethylene glycol and alkyl peripheral and non-peripheral substituents, were synthesized and characterized with the aid of ^{1}H NMR, IR and UV/vis spectroscopy. The electrochemical study (cyclic voltammetry) showed smaller peak potentials for phthalocyanines with shorter ethylene glycol substituents, thus the shorter the ethylene glycol chain, the higher the electron density of the macrocycle.

Electrochemical (cyclic, square wave and linear sweep voltammetry) and computational (including the determination of relevant geometries and molecular orbitals) studies were done on a series of ruthenium phthalocyaninato complexes. A comparison of the peak oxidation potential of the first experimental oxidation process and computed energy of the highest occupied molecular orbitals (HOMO) for the series of (CO)RuPc, showed a linear correlation..

An RC1 reactor was used to study the hydrogenation reaction of 4-nitrophthalonitrile as weak as the oxidation reaction of 2,5-dihexylthiophene and 2,5didodecylthiophene utilizing dimethyldioxirane of oxidizing agent. By making use of the RC1 reactor, the reactions were followed kinetically and thermodynamically, yielding rate constants as well as reaction enthalpies. These results were compared to theoretical reaction enthalpies determined by DFT calculations. Good correlation was found between the experimentally obtained reaction enthalpies and theoretical reaction enthalpies.

Keywords: Phthalocyanines, DFT, RC1 reactor, cyclic voltammetry

Opsomming

‘n Reeks van metaal-vrye phthalosianien komplekse met etileen glikol en alkiel periferiese en nie-periferiese substituente, is gesintetiseer en gekarakteriseer met behulp van ^{1}H NMR, IR en UV/vis spektroskopie. ‘n Elektrochemiese studie met behulp van sikliese voltammetrie het gewys dat phthalosianiene met korter etileen glikol kettings kleiner piek potensiale het dus verhoog dit die elektron digtheid van die makrosikliese struktuur .

‘n Elektrochemiese (sikliese, vierkantige golf en lineêre golwing voltammetrie) en berekenings studies is gedoen op ‘n reeks van ruthenium phthalosianienato komplekse. ‘n Reglynige verband is gevind tussen die oksidasie potentiaal van die eerste eksperimentele oksidasie proses en die berekende energie van die hoogste besette molekulêre orbitaal (HOMO).

‘n RC1 reaktor studie iss gedoen op die hidrogeneringsreaksie van 4-nitrophthalonitriel, asook die oksidasie reaksie van 2,5-diheksieltiofeen en 2,5-didodesieltiofeen utilizing dimetieldioksiraan as oksideermiddel. Met behulp van die RC1 reaktor, is tempokonstantes en reaksie entalpieë kon bereken word vir elke reaksie. Hierdie resultate was gevergelyk met teoriese reaksie bereken vir elke reaksie. Die resultate is vergelyk met teoretiese reaksie entalpieë bereken deur DFT. ‘n Goeie verband is gevind tussen die eksperimentele en teoreties berekende reaksie entalpieë.

Sleutelwoorde: Phthalosianiene, sikliese voltammetrie, DFT, RC1 reaktor